Hadronization and Azimuthal Angle Shift in 3-Jet Events at Z^0 Energy

An Alternative Approach to the String Effect

Dissertation

Raimund Vogl

Innsbruck

Mai 1995

Science Is truth for life Watch religion fall obsolete Science Will be truth for life Technology as nature Science Truth for life In fortran tongue the Answer With wealth and prominence Man so near perfection Possession It's an absence of interim Secure no demurrer Defense against divine Defense against his true Image Human conflict number five Discovery Dissolved all illusion Mystery Destroyed with conclusion And illusion never restored Any modern man can see That religion is Obsolete Piety Obsolete Faith Obsolete Ritual Obsolete Martyrdom Obsolete Prophetic vision Obsolete Mysticism Obsolete Commitment Obsolete Sacrament Obsolete Revelation Obsolete.

Planned Obsolescence, 10,000 Maniacs
Hope Chest, The Fredonia Recordings 1982–1983

Contents

Abstract

From the hadronic events collected by the ALEPH experiment at the LEP collider (CERN) at $E_{cm} = 91.2$ GeV in 1992 and 1993, 3-jet events which can be interpreted as hard gluon radiation are selected using a cluster finding algorithm for a range of cut-off values y_{cut}. After projecting the particle momenta into the event plane, the azimuthal momentum flow in the jets is analyzed with respect to the *color string effect*. As a new observable for the string effect, the azimuthal angle shift between the leading particle in a jet and the jet axis is introduced. Results from ALEPH data, corrected for detector effects, are compared with the predictions of different Monte Carlo models for hadron production, taking into account the dependence on the 3-jet kinematics and the cluster algorithm cut-off.

Zusammenfassung

Aus den vom ALEPH Experiment am LEP Speicherring (CERN) bei $E_{cm} = 91.2\,\mathrm{GeV}$ in den Jahren 1992 und 1993 gesammelten hadronischen Ereignissen werden mittels eines Clusteralgorithmus für eine Reihe von Werten des Abschneideparameters y_{cut} 3-Jet Ereignisse ausgewählt, die als harte Gluonabstrahlung interpretiert werden können. Nach Projektion aller Teilchenimpulse in die Ereignisebene wird der azimutale Impulsfluß in den Jets im Hinblick auf den sogenannten *Color String Effekt* untersucht. Als neue Meßgröße für den String Effekt wird die azimutale Winkelverschiebung des führenden Teilchens eines Jets zur Jetachse eingeführt. Die gegen Detektoreffekte korrigierten ALEPH Daten werden, in Abhängigkeit von der 3-Jet Kinematik und dem Wert des Abschneideparameters y_{cut}, mit verschiedenen Monte Carlo Modellen der Hadronproduktion verglichen.

Chapter 1

Introduction

1.1 QCD, Event Generators and the String Effect

In the late 1960s and early 1970s, Quantum Field Theory (QFT) has found renewed interest due to the conception of the Standard Model of Electroweak Interactions by Glashow, Salam and Weinberg and of Quantum Chromodynamics (QCD) as a Quantum Field Theory of strong interactions by Gell-Mann and Fritzsch.

Since this time, Quantum Field Theories with local gauge invariance under non-abelian symmetry groups have become the paradigm for the description of the fundamental constituents of matter.

An introduction to the theory of Quantum Chromodynamics can be found in references [33], [34], [18] and [17] (references ordered with respect to increasing difficulty). A more general introduction to Quantum Field Theory and theoretical particle physics can be found in references [19] and [27].

Eventhough QCD is a fundamental theory that should, in principle, be able to describe all features of strongly interacting matter (hadrons), this is made very complicated by a special property of QCD as a gauge theory with unbroken gauge group $SU(3)$: *confinement*.

The color charges of the elementary fermions (quarks) that constitute the hadronic matter are not macroscopically observable. The color force field does not reach to infinity (like the electromagnetic field) but is confined to regions of the size of nuclei. This is due to the self interaction of the 8 types of force carrying gauge bosons (gluons) of the color field.

The coupling "constant" for strong interactions is not really a constant, but depends on the 4-momentum (Q^2) transfer in the interaction. In leading order, this dependence is of the form

$$\alpha_S(Q) = \frac{12\pi}{(33 - 2n_f)\ln(\frac{Q^2}{\Lambda^2})},$$

where n_f is the number of active quark flavors ($n_f = 5$ for LEP energies) and Λ is a scale parameter that has to be determined experimentally ($\approx 200\,\mathrm{MeV}$; depending on the renormalization scheme).

It is obvious that the QCD coupling constant α_S is divergent for small 4-momentum transfer and will thus render perturbation theory useless in this regime.

For reactions with high 4-momentum transfer, though, QCD perturbation theory is well applicable and in good agreement with experiment (eg. the observation of 3-jet events can be well understood as signature of hard (perturbatively describable) gluon emission off a quark). This property is called "asymptotic freedom".

The process of hadronization, ie. the formation of color neutral observable hadrons from partons (quarks and gluons), is inherently non-perturbative in nature and could not yet be described in the QCD framework.

Nevertheless, some phenomenological models exist for this hadronization process. The oldest model of "independent fragmentation" is due to Feynman and Field. An initial quark is thought to lose energy by the production of a quark antiquark pair (or diquark antidiquark pair) completely independent of the other partons with which it was produced (eg. in a Z^0 decay). The initial quark can then form a meson together with the antiquark while the secondary quark can go on to produce quark antiquark pairs. Gluons are thought to fragment like a quark antiquark pair. The independent fragmentation scheme in its simplest form does not conserve energy, momentum and flavor quantum numbers.

The hadronization scheme that is currently most popular is the so-called "string fragmentation" scheme. It is inspired by ideas from non-perturbative QCD. The color field between the partons is thought to be confined to a quasi-one-dimensional color flux tube (the color string) through the self-interaction of the gluons. The fragmentation is described as the breaking up of this color string by the creation of quark antiquark (or diquark antidiquark) pairs (see section 2.3 for more details; a detailed account of the string fragmentation scheme can be found in reference [9]) from the vacuum which join with the original partons to form hadrons. Clearly, the partons do not fragment independently in this model.

Experimental observations in favour of this view of the hadronization process have been made (see references [20] and [21]). As described in section 2.3, the string fragmentation scheme implies a depletion of particles in the region between the quark and the antiquark jet in 3-jet events compared to the region between the quark and the gluon jet. The standard observable used in the study of this so-called "string effect" is the ratio

$$R_{string} = \frac{N_{12}}{N_{13}}$$

of the number of particles in the interjet region (see figure 2.11) between jets 1 and 2 and those in the region between jets 1 and 3 (integrated over all selected 3-jet events). Here, the two most energetic jets are taken to be the quark jets and the least energetic jet is taken to be the gluon jet. In reference [23], the ALEPH data is analyzed with respect to the string effect using this variable.

In this thesis, alternative observables that allow the study of effects of the hadronization process shall be investigated.

The starting point for this investigation is the observation, that the momentum flow (ie. the azimuthal angle of the particles in the event plane, weighted with the absolute values of their momenta) is asymmetrical with respect to the jet axes. This asymmetry turns out to be dependent on the particle momentum; the momentum flow distributions have different shapes (mean value and RMS) when derived for particles from different momentum intervals.

The peaks of the narrow momentum flow distributions for particles with high momenta around jet 1 and jet 2 are each shifted away from the side to which the third jet lies.

For the momentum flow distributions of low momentum particles, the RMS is larger and the distribution is shifted towards the third jet.

This finding can be interpreted as being caused by the process of fragmentation, as it is described in the string fragmentation scheme: soft particles are produced in the hadronization process along the color string stretching between the color charged partons, while the hard particles go into the direction of the original partons.

Since the jet vector is the momentum sum of the hard and the soft particles assigned to the jet, the azimuthal angles of the leading particles (marking the direction of the original partons) in jet 1 and jet 2 should in the mean be shifted away from the side to which the third (gluon) jet lies.

If one thus compares the jet axes on the parton and on the hadron level, the axes of the two quark jets move closer to the gluon jet direction; the event topology seems to be narrowing.

An observable quantity for this narrowing has already been proposed in reference [32], where the angle shift $\Delta\phi$ of the hadron jet axis with respect to a redefined jet axis which is computed by weighting the particles with their energy squared E^2, was introduced.

But the power of E, with which the normalized direction vectors of the particles are weighted to form the redefined jet axis, can be chosen arbitrarily and thus this specific angle shift variable has no clear interpretation.

A much simpler observable, which is proven by Monte Carlo studies to well approximate the azimuthal shift in the hadronization process, is here introduced in the form of $\langle\Delta\phi(\mathbf{L1})\rangle$, which is defined as the mean value of the distribution of the azimuthal angle $\Delta\phi(\mathbf{L1})$ of the leading particle with respect to the jet axis.

The most important tool for such investigations are Monte Carlo event generators (see reference [8] for an overview over the QCD event generators). These are simulations of multihadronic Z^0 decays based on perturbative QCD and certain model assumptions. The most popular amongst a variety of different event generators is the JETSET model (see [31] for details on the JETSET event generator).

It is designed as a collection of FORTRAN 77 subprograms that have to be called from a user supplied main program. The execution is controlled by parameters and switches arranged in arrays which are accessible via COMMON blocks.

Depending on the settings of these switches, the JETSET event generator calculates a possible decay of a Z^0 boson into a quark/gluon partonic state either via a QCD matrix element (ME) which is exact to second order perturbation theory in α_S or via a parton shower (PS) cascade. In the parton shower, only elementary branchings of the type $q \to qg$, $g \to q\overline{q}$ and $g \to gg$ are considered (leading log approximation LLA). These branchings are described by the Altarelli-Parisi splitting kernels

$$\begin{aligned} P_{q\to qg}(z) &= C_F \frac{1+z^2}{1-z} \\ P_{g\to gg}(z) &= N_C \frac{(1-z(1-z))^2}{z(1-z)} \\ P_{g\to q\overline{q}}(z) &= T_R(z^2+(1-z)^2) \end{aligned}$$

with $C_F = 4/3, N_C = 3$ and $T_R = n_f/2$. z gives the sharing of the original parton's

energy and momentum among the two partons after the branching. Additionally to the energy fraction z of the two daughter particles in the branching, an azimuthal emission angle for one of them with respect to the original parton has to be specified to describe the kinematics. This angle is usually chosen isotropically. In the coherent parton shower approach, the polar emission angles are reduced in subsequent branchings to simulate coherence effects (angular ordering).

The evolution of the parton shower cascade is parametrized by the variable

$$t = \ln(Q^2/\Lambda^2).$$

In the JETSET shower algorithm, the evolution variable Q^2 is associated with the mass of the branching parton: $Q^2 = m_a^2$ for a branching $a \to bc$. Other event generators use different definitions (eg. $Q^2 \approx m^2/(2z(1-z))$ in HERWIG and $Q^2 = p_\perp^2 \approx z(1-z)m^2$ in ARIADNE). The parton shower is allowed to develop until the evolution variable reaches the invariant mass cut-off M_{min}, below which the partons are not assumed to radiate.

For QCD simulations at the Z^0 energy scale, the parton shower prescription of the formation of the partonic final state is prefered to the matrix element formulation, since it describes better the particle multiplicities observed in the experiment.

The fragmentation algorithm is then applied on the partonic state created either by the matrix element or parton shower.

The decays of the hadrons created in the hadronization process are also simulated to produce a final hadronic state as close as possible to that which could be observed in an ideal detector.

1.2 The ALEPH Detector

The ALEPH (Apparatus for LEP Physics) detector is one of the four large experiments at the LEP collider at CERN (see figure 1.1 for an artists impression of the detector). In the LEP accelerator, collisions between electron and positron beams at $E_{cm} = 91.2\,\mathrm{GeV}$ (the Z^0 resonance peak) are produced, resulting in the formation of Z^0 particles (the Z^0 is, together with the W^+ and W^-, an intermediate vector boson of the electroweak interaction) whose decay products are studied in the four detectors.

ALEPH is a multipurpose detector designed for good angular resolution and to cover as much of the 4π solid angle as possible. It consists of several subdetectors which are dedicated for the measurement of certain aspects of the particles produced in the decays of the Z^0 bosons to which e^- and e^+ pair-annihilate. Detailed accounts on the design and functionality of the ALEPH detector can be found in references [1], [2] and [5].

In figure 1.2 the graphical reconstruction of a multihadronic Z^0 decay is shown which was produced using the event display program DALI (Display of ALEPH Interactions; see reference [15]).

This event shows a pronounced 3-jet structure. The three jets of approximately the same energy having angles close to 120° are clearly visible. Events with topologies like this are for obvious reasons called "Mercedes" events.

The picture shows a projection into the plane perpendicular to the beam direction. The particles produced at the vertex of the multihadronic decay of the Z^0 located at the center of the image are directed outward.

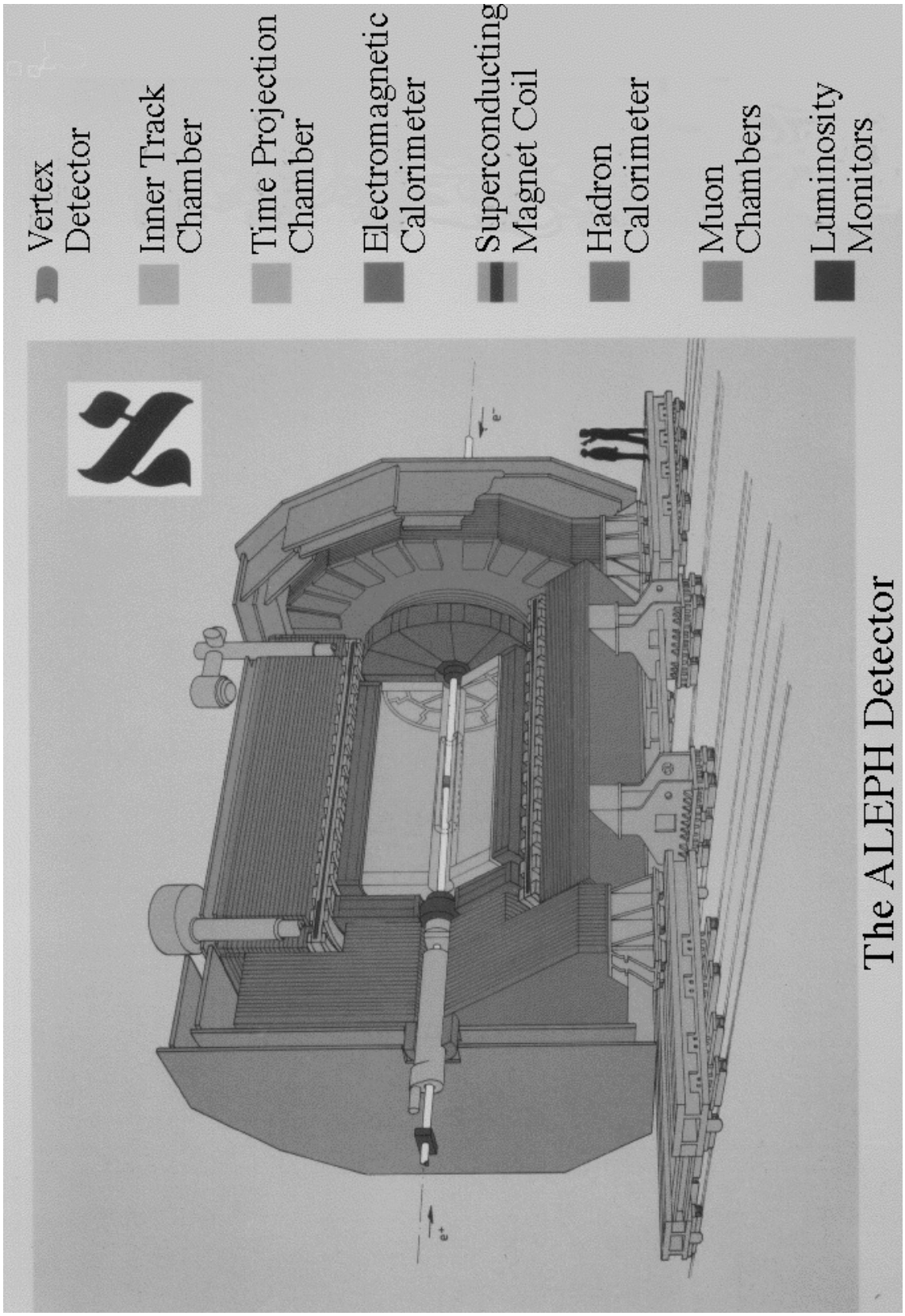

Figure 1.1: Artists impression of the ALEPH detector. The beam pipe with the colliding e^- and e^+ beams can be seen. The subdetectors, which are arranged in onion-like layers around the central interaction vertex, are depicted in different shades of grey. The muon chambers can be seen as the last layer. For comparison of size, two people are shown on the lower right.

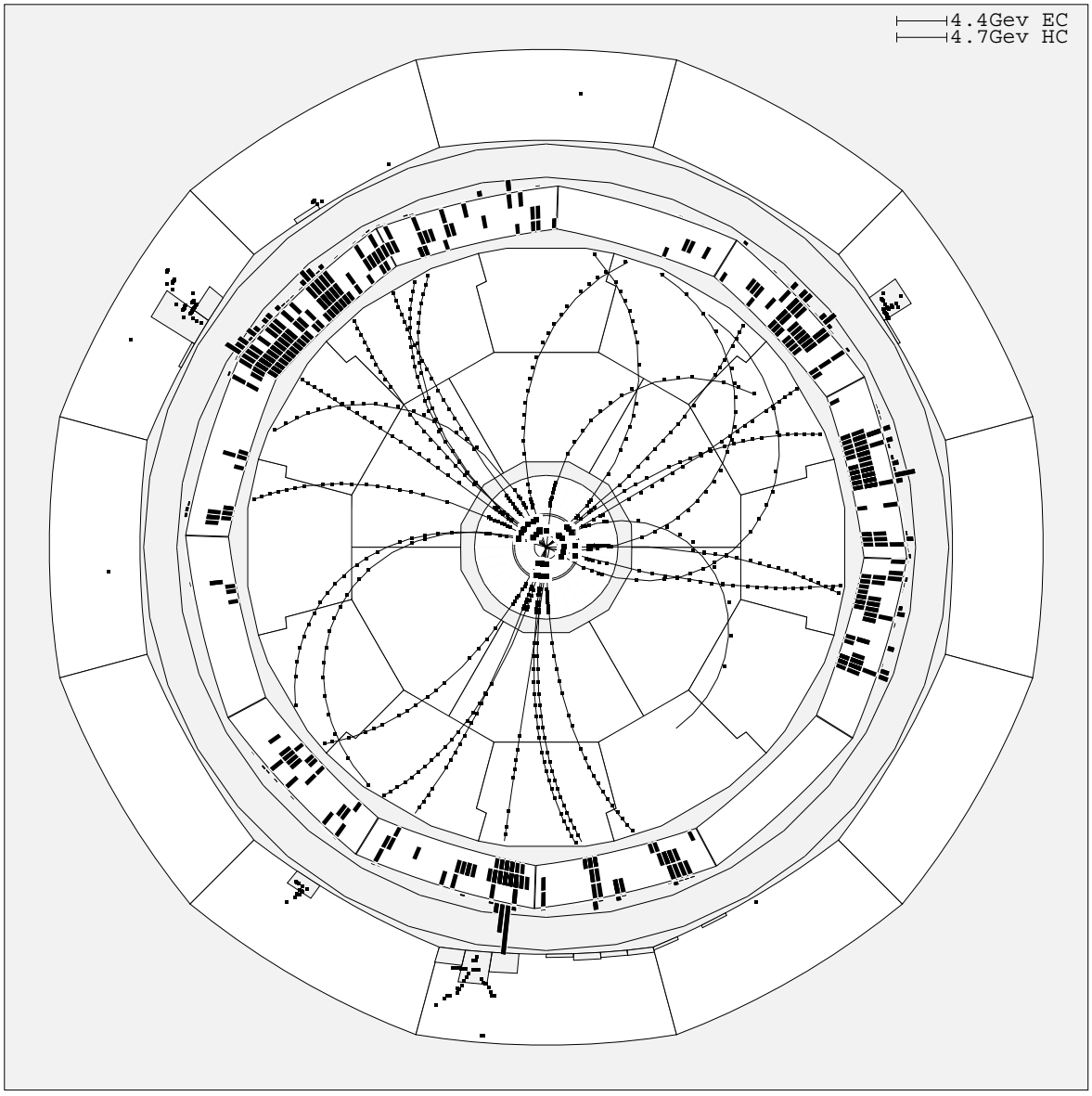

Figure 1.2: Mercedes event as seen in the ALEPH detector. The particle tracks are projected into a the plane perpendicular to the beam direction. The inner part of the detector is magnified (fish-eye view) for better visibility.

The detector part closest to the interaction point, the so-called vertex detector (VDET) consisting of two cylindrical layers formed from 96 silicon micro-strip detector chips sensitive for minimum ionizing radiation, can only be seen as the innermost ring-shape area (with squares indicating hits) in this picture. It has a hit resolution of 12 μm and gives tracking data accurate enough for the reconstruction of secondary vertices from B meson decays (B mesons have mean lifetimes of $\approx 1.5 \cdot 10^{-12}$ s giving a decay length of $\approx 500 \mu$m; see reference [28]).

The vertex detector is surrounded by a cylindrical inner drift chamber (ITC) which can be seen as the second ring-shape area in the picture. It is used for tracking and for the trigger system.

The charged particles leave ionization trails in the cylindrical volume of the TPC (Time Projection Chamber; in the picture visible as the segmented ring-shaped area around the center; the tracks of the charged particles are shown as connected dots). A maximum of 21 3-dimensional hits for a charged particle track can be measured in the TPC.

The charged particles are bend in the 1.5 Tesla field of a superconducting solenoid for momentum determination.

In layers around the TPC, the electromagnetic calorimeter (ECAL; a sampling calorimeter consisting of 45 lead/wire-chamber layers used for the detection of electrons and gamma particles) and the hadronic calorimeter (HCAL; build of 23 layers of plastic streamer tubes separated by iron slabs which also serves as the support structure for the detector) stop the charged and neutral particles by electromagnetic (ECAL; 22 radiation lengths thickness) or strong (HCAL; 7 interaction lengths thickness) interactions and measure the energy deposition through the charged particles produced in showers caused by interactions of the original particle with the lead (ECAL; bremsstrahlung and pair creation reactions) or iron (HCAL; strong interactions with the iron nuclei). The energy deposition in the calorimeters is indicated by radial towers in this picture.

Between ECAL and HCAL, the superconducting coil is located using the iron of the HCAL as a return yoke for the field lines.

To accurately measure the highly penetrating muons which can not be stopped in the calorimeters, two double layers of muon chambers (each double layer consisting of two planes of streamer tubes read out in orthogonal direction to give a space point for the muon hit) are attached outside the HCAL.

For the determination of the total luminosity, which is essential for cross section measurements, luminosity monitors (LCAL; based on the same design as the ECAL) are attached at very small polar angles close to the beam pipe to measure the e^- and e^+ particles deflected in Bhabha scattering. The rate of these elastic e^+e^- t-channel scattering reactions gives a good gauge for the luminosity.

Chapter 2

Monte Carlo Studies on the String Effect

2.1 Synopsis

To study the effect of the string fragmentation scheme on the azimuthal momentum flow in the event plane and on the angle shift of the leading particles with respect to the jet axis, Monte Carlo simulations using the JETSET 7.3 Monte Carlo event generator with best fit parameters are made. If not otherwise stated, all calculations are done at $E_{cm} = 91.2\,\mathrm{GeV}$.

Special 3-jet kinematic configurations with threefold symmetry are produced by starting the event generation from a 3 parton $q\overline{q}g$ initial state instead of the usual $q\overline{q}$ state, anticipating a hard gluon emission in the parton shower.

The azimuthal momentum flow around the quark jet axes is found to be asymmetric, with the peak shifted to the side averted from the gluon jet.

The mean azimuthal angle of the leading particle (or the momentum sum of the two or three leading particles) in a jet reproduces the angle shift of the parton jet axis to the hadron jet axis caused by the hadronization. The mean of the $\Delta\phi$ distribution of the leading particle, $\langle\Delta\phi(\mathbf{L1})\rangle$, is adopted as a new string effect observable.

2.2 Symmetric Events

In order to study the string effect in the context of the JETSET Monte Carlo program and to isolate the parameters of that model that are responsible for it, it is necessary to minimize influences of the event kinematics on the observation of the effect.

The study of the string effect is facilitated if one restricts oneself to Monte Carlo events which fulfil the following criteria:

- Maximally separated jets.
- Identical angles between the jets.
- Possibility to identify the gluon jet in the context of the parton shower Monte Carlo.

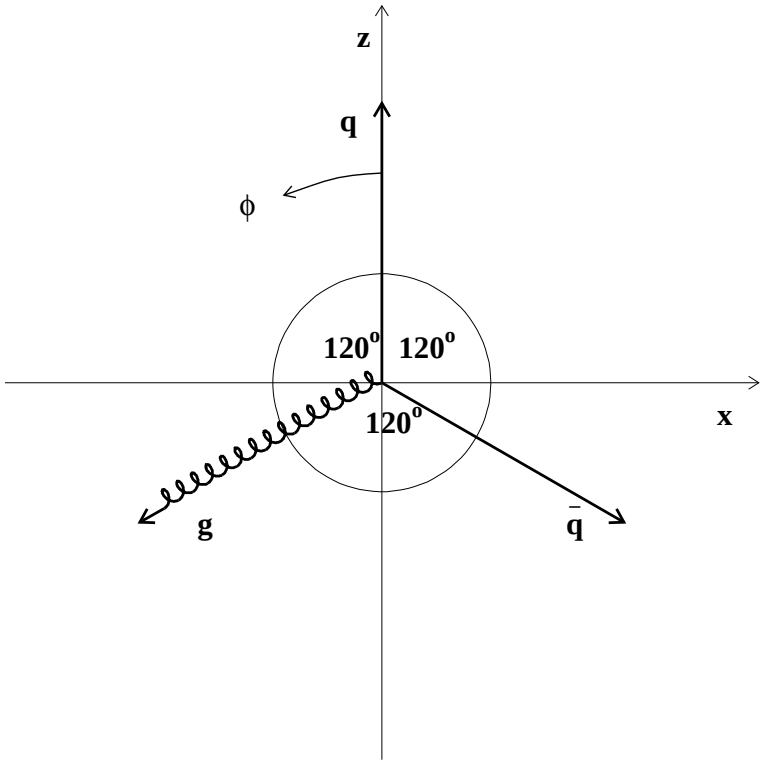

Figure 2.1: Parton configuration from which a TRISTAR Y120 event is generated and its orientation in the event plane

Especially the last point is hard to deal with when operating on all kinematically possible 3-jet configurations.

Symmetric events with the features required above can be produced with the JETSET program, if one defines an initial 3 parton ($q\overline{q}g$) configuration using the subroutine `LU3ENT` and starts the parton shower cascade from this configuration with a call to `LUSHOW` followed by a call to `LUEXEC` (for the hadronization and the decays of the unstable hadrons). This is in contrast to the usual procedure of calling the master routine `LUEEVT` which initiates the parton shower starting from a $q\overline{q}$ configuration. Apart from these differences, the same best fit parameters (parameters of the JETSET Monte Carlo program optimized to describe corrected global event shape distributions derived from ALEPH 1992 data) as for the usual JETSET PSCO2 runs (see section 5.2) are used.

Events of this type shall be named TRISTAR events because of their characteristic three prong star shape. The events with threefold symmetry having 120° angles between all jets are referred to as Y120 events; variations which still have the Y symmetry but larger angles between the original q and the g are called Y140 and Y160 events depending on the size of ϕ_{qg}.

By convention, the momenta of the initial partons are confined to the xz plane with the q parton aligned along the positive z axis. The $\overline{q}$ momentum vector has a 120° angle (for Y120 events) to the q and lies towards the positive x axis (see figure 2.1). The direction of the q parton defines the origin for the azimuthal angle.

Hadronic events with a topology like the one that is artificially introduced into the

JETSET Monte Carlo by the procedure described above can be experimentally observed (see figure 1.2 for a picture of a so-called "Mercedes" event).

2.3 Effect of String Fragmentation on the Particle Momenta

To study the momenta with which particles are produced in the string fragmentation process, it is useful to look at Y120 events in which all processes are switched off that could obscure the directions and absolute values of the particle momenta as they result from the string fragmentation.

The following processes are $p_\perp$ producing processes which have been turned off for this purpose:

- In the parton shower, new additional partons are created which have transverse momentum components. To avoid this, the fragmentation has to start from the initial $q\overline{q}g$ configuration (`LUSHOW` is not called).
- The primary hadrons acquire transverse momenta in the tunnelling process arising in the breaking of the color string. The width σ of the gaussian which determines the spread of this $p_\perp$ distribution (`PARJ(21)`[1]) is set to 0.
- All decays of hadrons are inhibited.

In the string fragmentation, a one-dimensional color string (in the following a coordinate system is chosen, where the string is aligned along the z axis) is thought to stretch from a quark with color charge C to an antiquark with color charge $\overline{C}$ or to a gluon with color charge $C\overline{C}$. Since a gluon carries double color charge, it functions as a node connecting two string pieces.

In the process of fragmentation, this color string breaks up with the production of quark antiquark pair (or a diquark antidiquark pair) out of the vacuum, where the newly produced antiquark joins the original quark to form a meson (in the case of diquark antidiquark pairs produced from the vacuum, three quarks can join to form a baryon) leaving its companion quark behind to continue the fragmentation process.

The fraction (hence the name "fragmentation") of the original quark's energy (or rather $E + p_z$) that the newly produced hadron acquires is determined by a phenomenologically motivated fragmentation function.

To determine E and p_z of the hadron (with the transverse mass $m_\perp^2 := m^2 + p_x^2 + p_y^2$ determined by the mass m of the hadron and the transverse momentum components p_x and p_y acquired in the tunnelling process), only one variable z can be freely chosen, which gives the fraction of the $E + p_z$ of the fragmenting quark that the hadron receives.

It holds that

$$(E + p_z)(E - p_z) = E^2 - p_z^2 = m_t^2$$

[1] The `PARJ` array is used for real-valued parameters and the `MSTJ` array for integer-valued switches for the steering of JETSET program runs. They are both accessible via the `LUJETS` COMMON block.

and the $E+p_z$ and $E-p_z$ left over for subsequent steps of splitting off hadrons are given by

$$(E+p_z)_{new} = (1-z)(E+p_z)_{old},$$
$$(E-p_z)_{new} = (E-p_z)_{old} - \frac{m_\perp^2}{z(E+p_z)_{old}}.$$

A function $f(z)$ giving the probability for a hadron to get fraction z of the quark's $E+p_z$ (the fragmentation function) has still to be specified.

Since the splitting up of the string has to look the same, no matter from what end of the string one starts, this fragmentation function has to be of a special form, which is used in the JETSET Monte Carlo and known as the Lund left-right symmetric fragmentation function:

$$f(z) = \frac{(1-z)^a}{z}\exp(-\frac{bm_\perp^2}{z})$$

where a and b are adjustable parameters (the default values for these two parameters are `PARJ(41)`$= a = 0.5$ and `PARJ(42)`$= b = 0.9$ GeV^{-2}).

The explicit mass dependence of the fragmentation function implies a harder fragmentation function for heavy hadrons.

In the case of events without $p_\perp$ producing processes, the hadrons produced in the string fragmentation have only momentum components parallel to the original color string. Especially for Y120 events with threefold symmetry, the transformation of the chain of particles (originating from the fragmentation of the color string) into the rest frame of the three initial partons is a boost along a direction perpendicular to the string.

A particle in the string with $p = (E, 0, 0, p_z)$ is boosted along the x axis to

$$p' = \Lambda p = \begin{pmatrix} \gamma & \beta\gamma & 0 & 0 \\ \beta\gamma & \gamma & 0 & 0 \\ 0 & 0 & 1 & 0 \\ 0 & 0 & 0 & 1 \end{pmatrix} p = (E\gamma, E\gamma\beta, 0, p_z)$$

in the rest frame. Its momentum vector thus has an angle

$$\phi = \arctan\frac{p_z}{E\beta\gamma}$$

with the line halfway between the directions of the original partons between which the string stretched.

A particle with mass m that is at rest in the string ($p_z = 0$) acquires a momentum

$$p_x' = m\beta\gamma$$

due to the boost. The momentum component parallel to the boost direction is proportional to the mass of the particle.

For high energy particles ($p_z \approx E, m \approx 0$) one can see that the parameter $\beta\gamma$ for the boost is given by

$$\beta\gamma = \cot\frac{\phi_{qg}}{2},$$

thus being only dependent on the angle ϕ_{qg} between the original partons.

In figure 2.2 a scatter plot for the momenta of particles in Y120 events without $p_\perp$ producing processes is shown. The mass bands (particles with different masses get different boosts!) for the predominant hadron species are clearly visible.

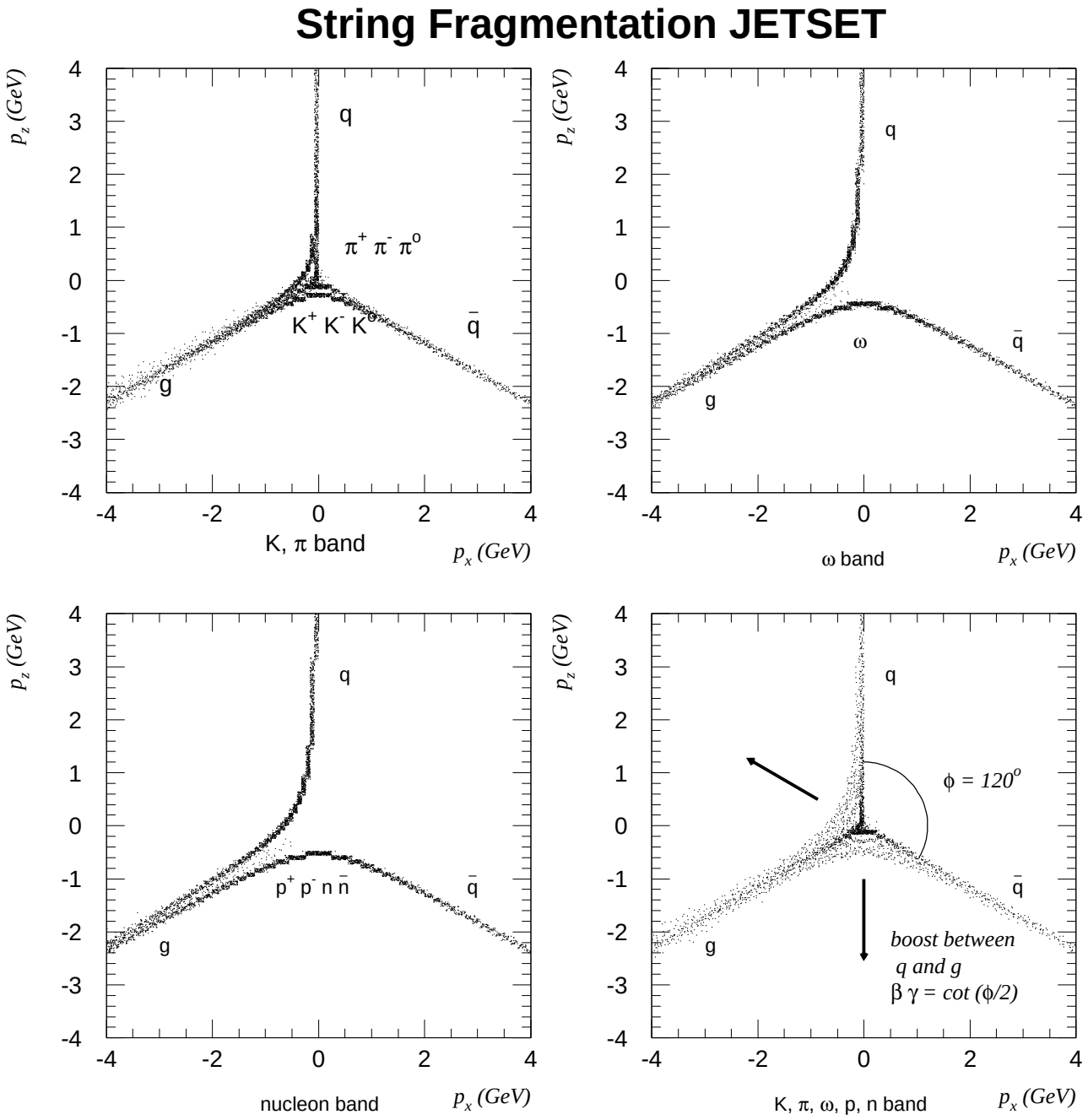

Figure 2.2: Distribution of particle momenta in the xz plane caused by string fragmentation in Y120 events with $p_\perp$ producing processes switched off. The mass bands are hyperboles due to the boost the particles get in the transformation from the string rest system into the lab system.

2.4 Momentum Flow in Symmetric Events

Figure 2.2 clearly demonstrates, that a depletion of particles in the region between the two quark jets results from the fragmentation of a color string stretching from one quark via the gluon (with it's double color charge) to the other quark.

To study the string effect using symmetric events utilizing the knowledge which of the three hadronic jets originated from a gluon, a means of identifying this jet has to be devised. No longer shall the $p_\perp$ generating processes be switched off. This means that the additional partons resulting from branchings in the parton shower process obscure the idea of a color string merely stretching from q to $\overline{q}$ via the g since they are included into the string as further bumps.

Weak decays involving neutrinos will furtheron lead to missing energy. Thus, a common event plane for all particles (excluding neutrinos) has to be defined via the algorithm described in section 4.2.

In order to have a clear assignment of the hadronic jets to one of the three initial partons, the following procedure is applied:

- On the parton level (after the completion of the parton shower), the DURHAM cluster finding algorithm (see section 3.2) with the cut-off parameter $y_{cut} = 0.01$ is applied, assigning each parton to a jet. If an event is not found to be of 3-jet type on the parton level it is discarded.

- The parton jets found by the DURHAM algorithm are matched via minimum angle to the original partons. If one of the matching angles is in excess of 10° the event is discarded. Such cases are possible when a showering parton acquires a high virtuality and thus drastically changes the topology by subsequent branchings.

- On the hadron level, the DURHAM cluster algorithm is also applied with the same cut-off $y_{cut} = 0.01$, assigning each particle to one of the jets. If the event is found to be of 3-jet type, the hadron jets are also matched to the parton jets via minimum angle starting with the most energetic jet. Otherwise, the event is discarded.

In the course of this selection, $\approx 56\%$ of the events are rejected in the case of Y120 topologies.

The distribution of the flow of momentum (ie. the distribution of the azimuthal angle weighted with the momentum of the particle projected into the event plane, denoted by $p * \phi$) in the reconstructed hadron level event plane and around the $q, \overline{q}$ and g jet axes can now be studied. The jet axes are the momentum vectors of the jets, which are the sum of the momentum vectors of the individual particles assigned to the jet.

The hadronic momentum flow in the event plane for Y120 events is shown in figure 2.3.

Figure 2.4 shows that the momentum flow distribution around the q-jet is asymmetric with the peak shifted away from the gluon jet. The gluon jet itself has a symmetric distribution, as expected.

A quantity useful for measuring this is the left-right asymmetry

$$A_{LR} := \frac{R - L}{R + L},$$

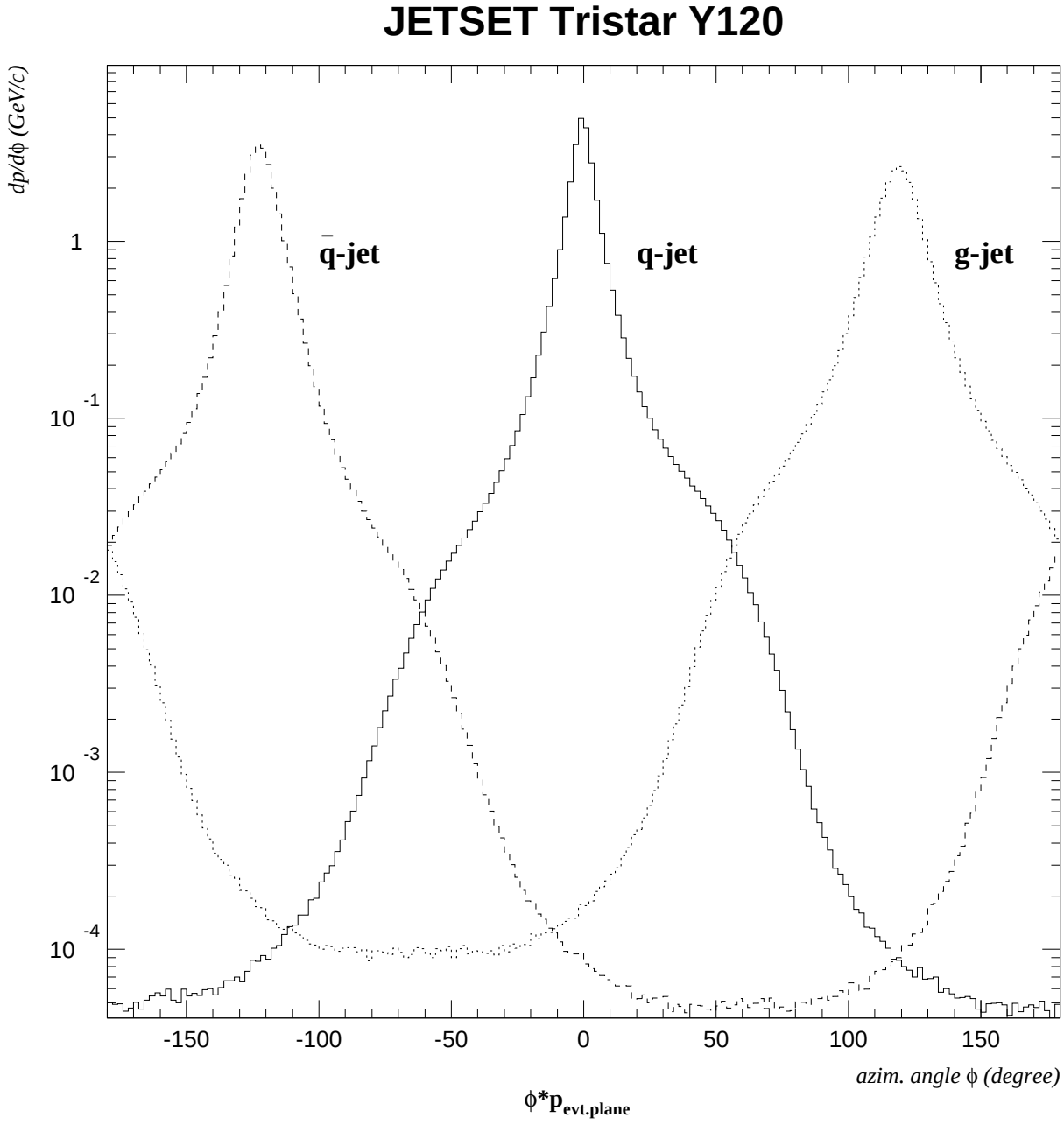

Figure 2.3: Hadronic momentum flow distribution in the event plane for Y120 events with normal flavor mixture. Note that the momentum flow around a given jet is non-vanishing for the whole 360° of the azimuthal angle. The effect of particles with momenta antiparallel to the jet axis (which happen to be assigned to the jet by the DURHAM cluster finding algorithm) is studied using reassignment of particles to jets via minimum angle. The difference of the q and $\overline{q}$ peaks arises from the way the parton shower is generated in JETSET.

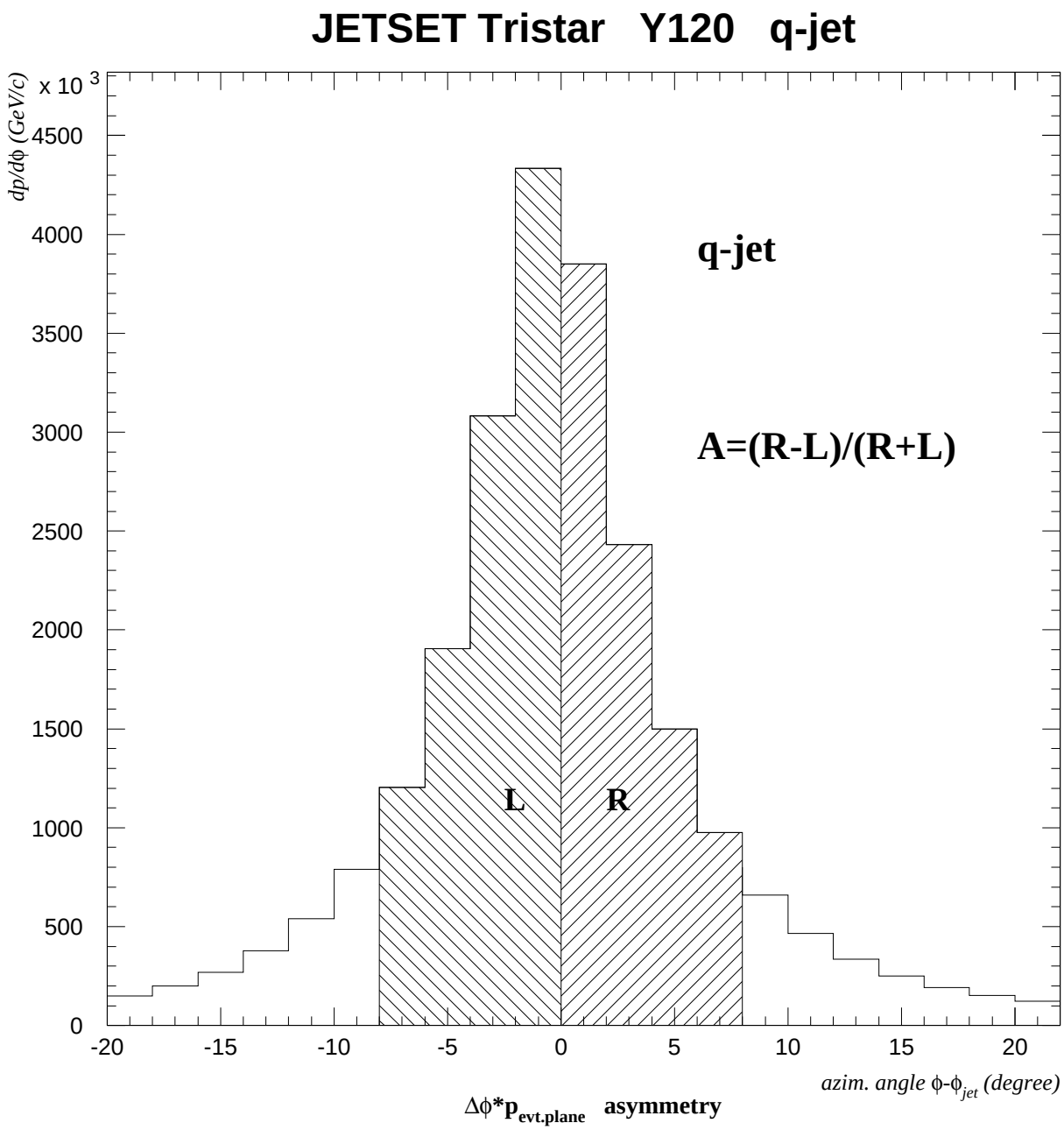

Figure 2.4: Asymmetry of the momentum flow distribution around the q-jet axis. The shaded regions are those used for the definition of the $A_{LR}^{\pm 8}$ asymmetry. For $A_{LR_i}^{detail}$, intervals of 2° lying symmetrically around the jet axis centered at $\pm 1^\circ, \pm 3^\circ, \pm 5^\circ, \ldots$ are used.

where L and R stand for the integrated momentum flow to the left (ie. at negative values of $\phi - \phi_{jet}$) respectively to the right of the jet axis.

There are two useful definitions for this asymmetry:

- The asymmetry $A_{LR}^{\pm 8}$ is calculated from the momentum flow in the regions 8° to the right and 8° to the left of the jet axis. This gives one single number to describe the momentum flow asymmetry for the jet core (here, a definition of the jet core as the azimuthal angle region 8° wide around the jet axis is used).

- The asymmetries $A_{LR_i}^{detail}$ are calculated from the difference in momentum flow in 2° wide regions located symmetrically around the jet axis — thus giving 10 numbers describing the difference of the momentum flow to the left and to the right of the jet axis in increasing distance between 0° and 20° from the axis (the azimuthal spread of a jet is defined as reaching 20% around the jet axis, here. The azimuthal regions farther away from the jet axis are considered as interjet regions).

In figures 2.6, 2.7 and 2.8 the detailed asymmetries around the hadron and the parton jet axes and their dependence on the initial flavor, the center of mass energy and the angle between q and g jet in the symmetric events of types Y120, Y140 and Y160 are shown.

The dependence on the initial flavor (b against the lighter flavors d, u, s, c) is found to be very strong, thus revealing the momentum flow asymmetry A_{LR} as a not overly useful observable for the study of the string effect.

2.5 Effect of Interjet Particles and of the Jet Finding Algorithm on the Momentum Flow Asymmetry

For the analysis of the string effect using the conventional variable $R_{string} = N_{q\overline{q}}/N_{qg}$ (or $R_{string} = N_{12}/N_{13}$ for the analysis of data where one does not know which jet the gluon jet is and therefore has to assume that the least energetic jet is the gluon jet) only the particles in the sparsely populated interjet regions (see figure 2.11) are used.

When using the momentum flow asymmetry, which strongly relies on the definition of the jet axis, as a variable to study the string effect, all particles in the jets (ie. the q and $\overline{q}$ jets) are used.

In order to see how much of the string effect comes from the interjet particles in this definition of the string effect, it is instructive to exclude them from the analysis and recalculate the momentum flow asymmetry.

This is done in the following way:

- Events with 3-jet structure (for the given $y_{cut} = 0.01$ for the DURHAM algorithm) are selected based on all visible particles (ie. with the exclusion of neutrinos).

- The particles whose momenta are within the 40% interjet regions between the jets (see figure 2.11) are tagged for exclusion from the analysis.

- The jet axes used are recalculated (by simply adding the momenta of the particles assigned to the jet) without the interjet particles.

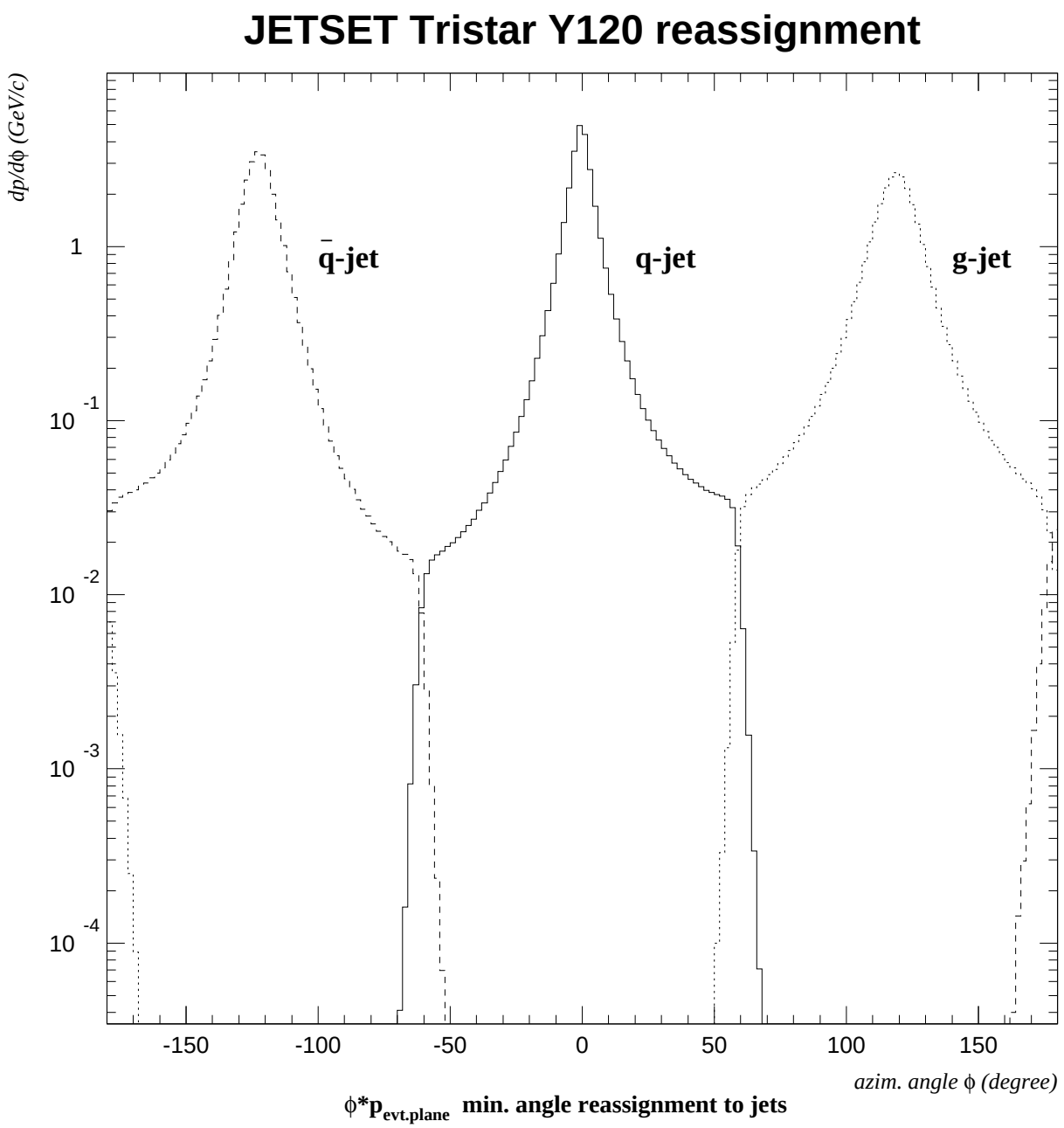

Figure 2.5: Momentum flow distribution in the event plane for Y120 events with reassignment of particles to the closest jet. The momentum flow around all 3-jets is now closely confined to the vicinity of the jet axis with very sharp borders.

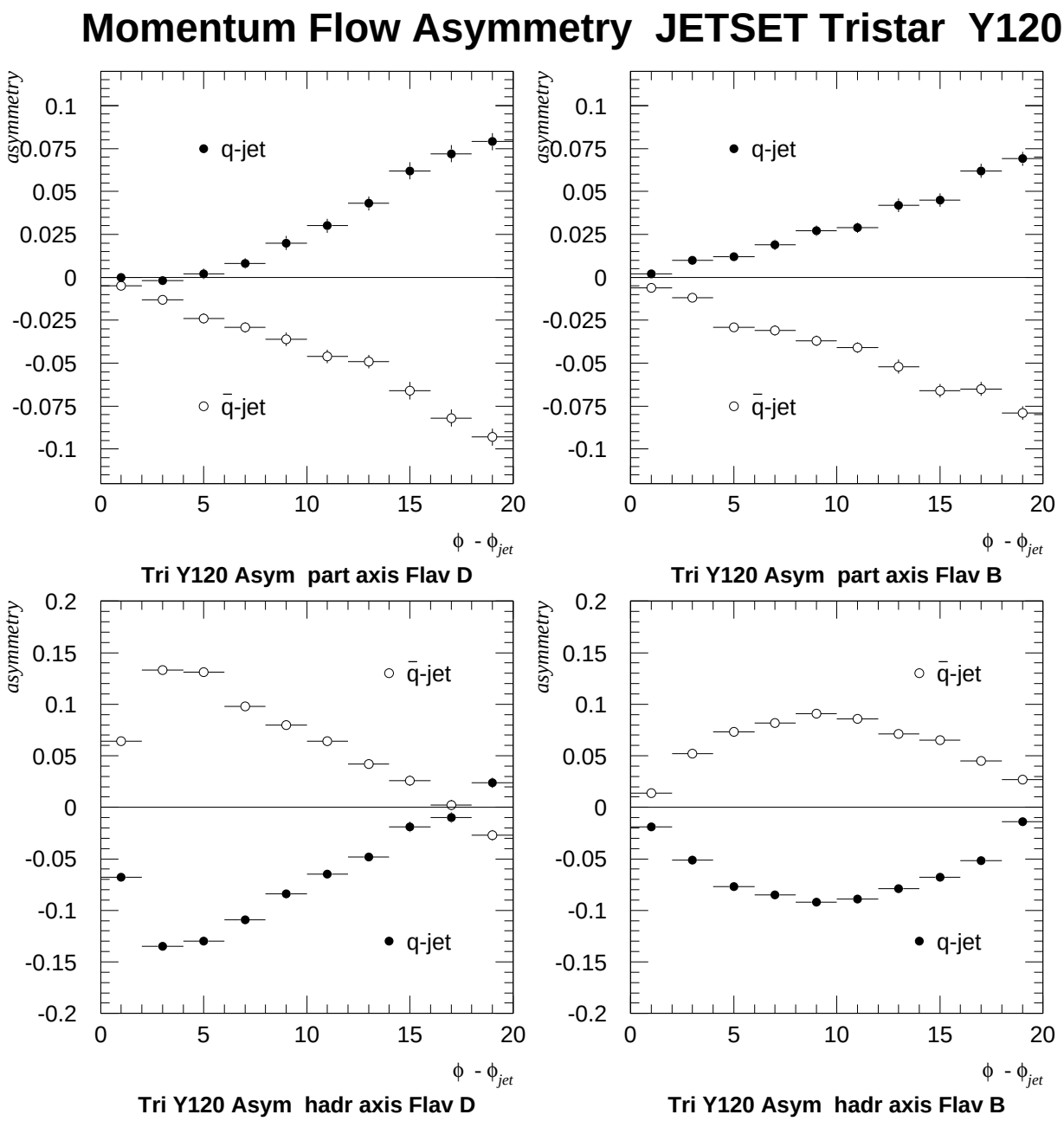

Figure 2.6: Detailed momentum flow asymmetries around the parton and hadron jet for different initial flavors. Close to the jet axis, the asymmetries around the parton jet axis are small while they are large around the hadron jet axis. The asymmetry for b events is much smaller than that for d events.

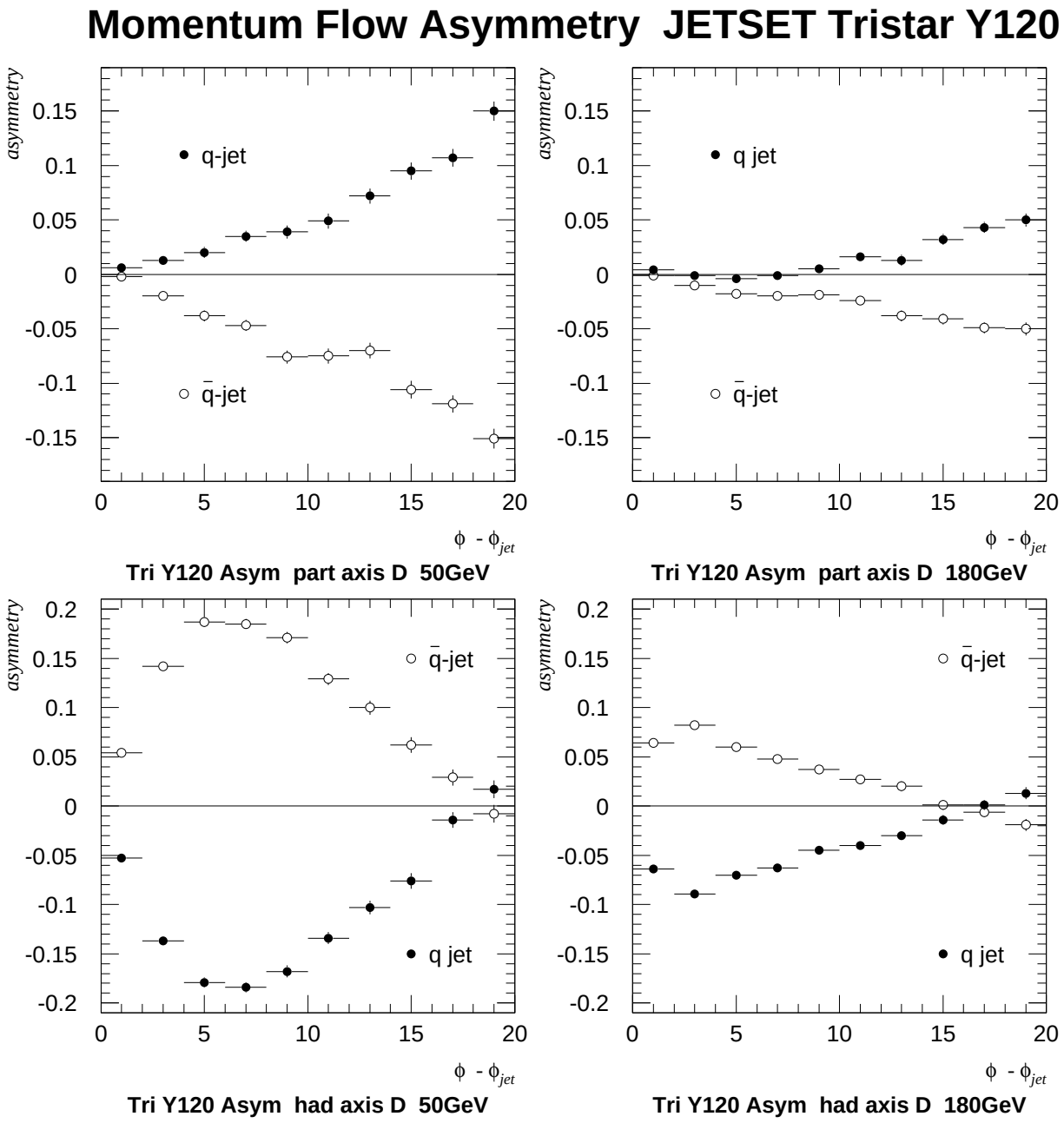

Figure 2.7: Detailed momentum flow asymmetries around the parton and hadron jet in d events for different values of E_{cm}. The asymmetries get smaller with increasing E_{cm}.

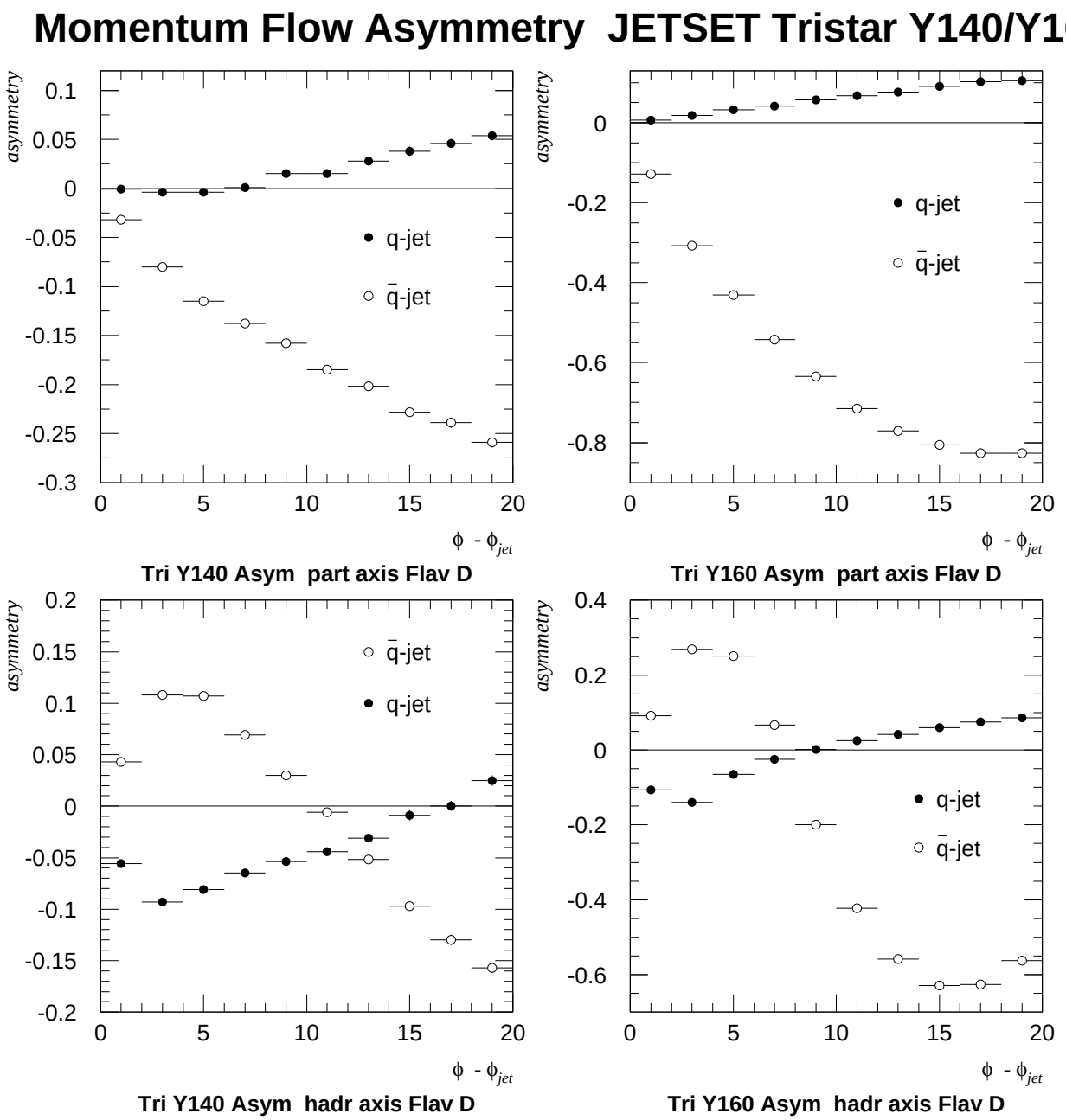

Figure 2.8: Detailed momentum flow asymmetries around the parton and hadron jet for Y140 and Y160 events. For Y events without threefold symmetry, the $\overline{q}$ jet asymmetries are behaving differently from those around the q jet. The asymmetries in the core region ($\pm 8^\circ$) of the q jet get smaller with increasing ϕ_{qg}.

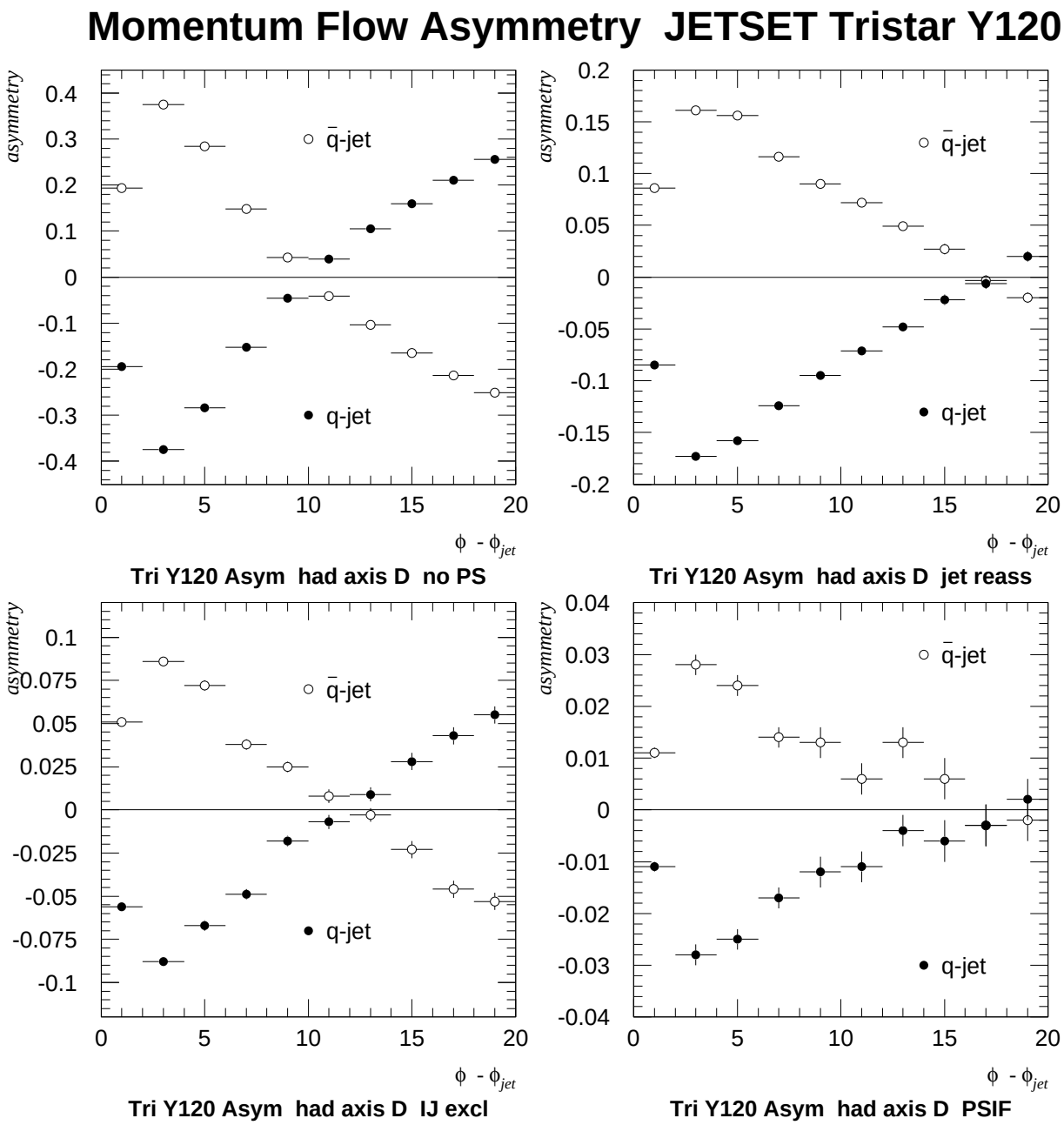

Figure 2.9: Detailed momentum flow asymmetries around the hadron jet for Y120 d events with no parton shower, reassignment of particles to the closest jet, exclusion of interjet particles and for independent fragmentation, respectively. The asymmetries for the no parton shower case are more than twice as large as those for the standard case. The exclusion of interjet particles almost halvens the asymmetries. The reassignment for particles to the closest jet axis makes the asymmetries larger and for the case of independent fragmentation, they are very small.

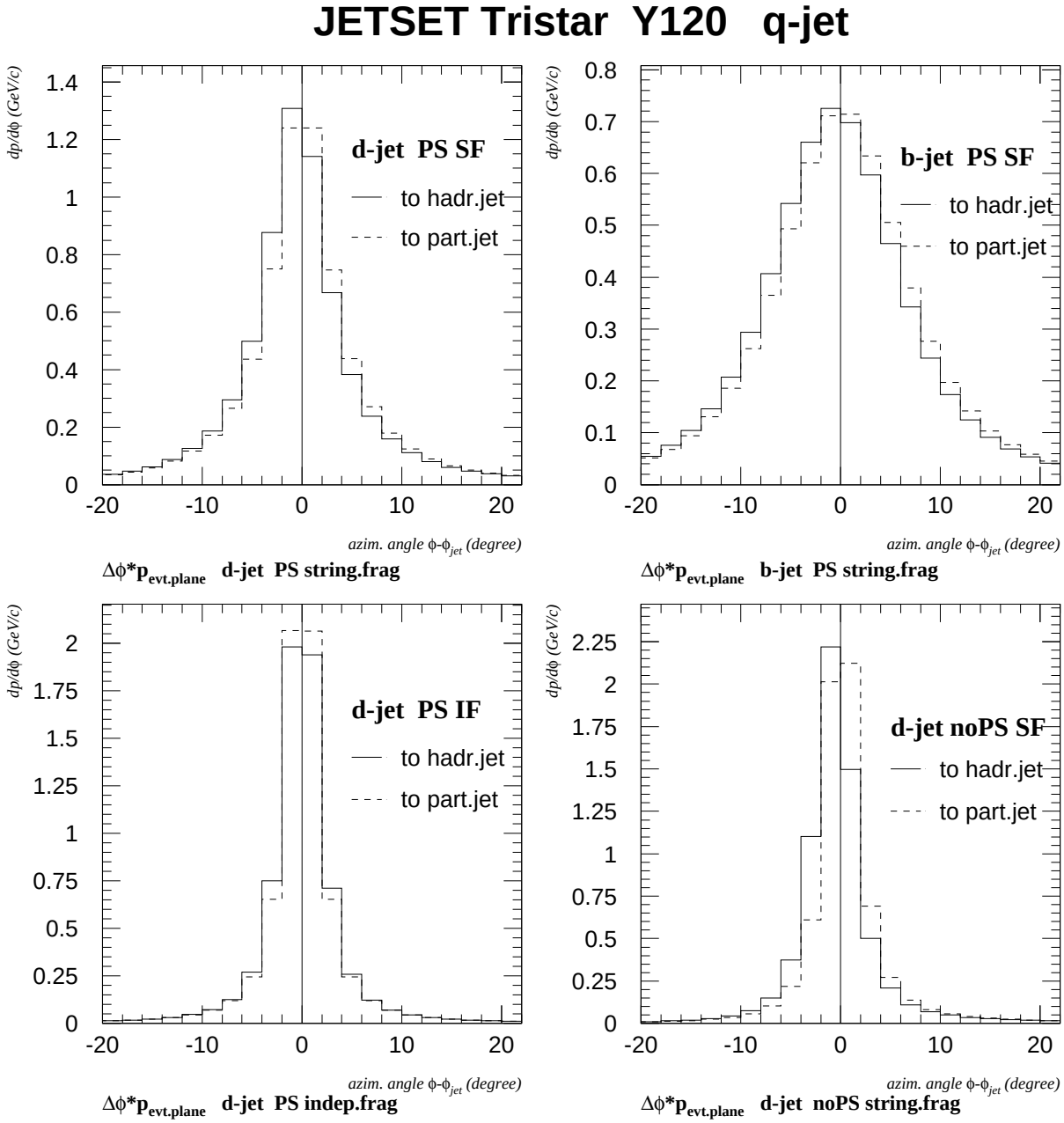

Figure 2.10: Hadronic momentum flow distributions around the q jet axis in Y120 events for flavors d and b in the string fragmentation case. The distributions are much broader for b events and show less asymmetry than for d events. For independent fragmentation, the distribution is narrower than for string fragmentation and shows no asymmetry. For the no parton shower case, the distribution is also narrower but has a stronger asymmetry. The momentum flow distributions with respect to the parton jet are superimposed as dashed lines and show no asymmetry in the jet core.

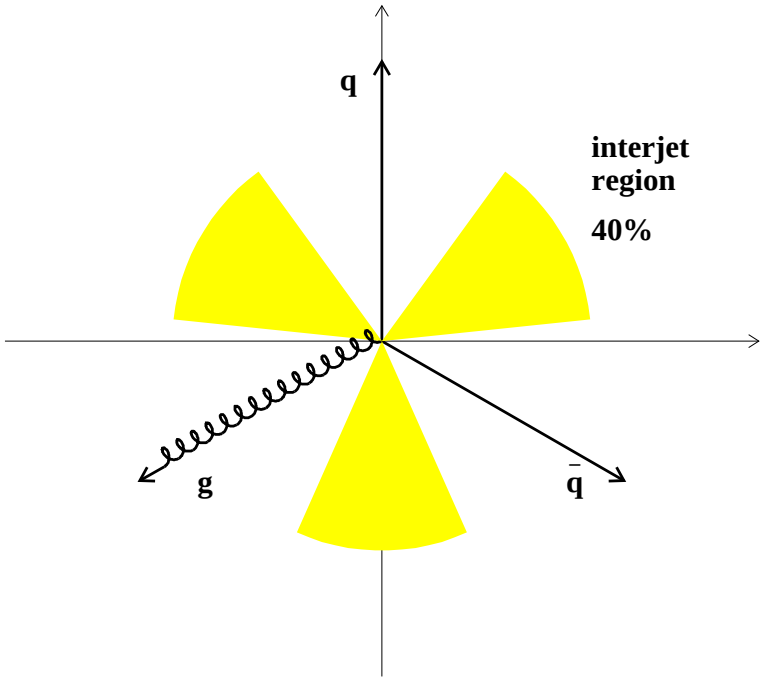

Figure 2.11: Definition of the interjet regions.

The exclusion of the interjet particles reduces the momentum flow asymmetry by $\approx 30\%$ (see figure 2.9 and table 3 in section 2.7).

Since the definition of the string effect via momentum flow asymmetry depends crucially on the jet finding algorithm, variations of this algorithm have to be studied to see how much they influence the magnitude of the effect.

Besides the DURHAM cluster algorithm in the form that is employed here (E-scheme), there exist numerous other algorithms (ie. JADE and LUCLUS) that have different metrics (see section 3.2) and schemes for the combination of particle momenta to form jets. Most of them lead sometimes to the assignment of particles to a jet which have momenta that point into the hemisphere opposite to the jet axis.

To study the influence of these particles on the string effect, an alteration of the DURHAM cluster algorithm is used which reassigns particles to the closest jet in the following way:

- The ordinary DURHAM cluster algorithm (with $y_{cut} = 0.01$) is used to group the particles into jets and to select 3-jet events.
- The angles of the particles momenta to the 3 jet axes are calculated and the particles are reassigned to the jet with which they have the smallest angle and from the momenta of the reassigned particles, new jet axes are calculated.
- The step above is iterated until no more reassignments are made (or at most 5 times).

Figure 2.5 shows the momentum flow in the event plane for the case of reassignment.

The jets have (unphysically) sharp edges. This reassignment results in a 25% increase in $A_{LR}^{\pm 8}$.

2.6 Effect of the Parton Shower and of the Fragmentation Scheme

The TRISTAR model as it has been used up to now involved a three parton initial state from which a parton shower was allowed to develop. The hadronization was done using string fragmentation.

Clearly, the momentum flow asymmetry used to describe the string effect could be dependent on the perturbative (ie. parton shower) as well as the non-perturbative part of the simulation.

To study this dependency, the effects of switching off the parton shower and of an alternative fragmentation scheme, the independent fragmentation, are investigated.

The parton shower is found to reduce the asymmetry by more than a factor of 2 (see figure 2.9 and table 3 in section 2.7).

The independent fragmentation scheme, in which all partons are assumed to fragment independent of each other (in the string fragmentation scheme, they are connected with color strings), shows practically no momentum flow asymmetry (see figure 2.9 and table 3 in section 2.7) as expected.

2.7 Results for the Momentum Flow Asymmetry from TRISTAR Events

The results for the $A_{LR}^{\pm 8}$ asymmetries for the different TRISTAR models are given in the next tables.

1. $A_{LR}^{\pm 8}$ for Y120, Y140 and Y160 events with respect to the parton jet and to the hadron jet axis.

   For the Y120 topology, the $\overline{q}$ jet shows almost identical results as the q jet with reversed sign. Thus, only the q has to be considered.

   The light flavors (u, d, s) show identical values — they don't have to be considered separately. The c and especially the b events show much less asymmetry (only 1/2 in the b case).

   The asymmetry with respect to the parton jet axis in the jet core is very small for the q jet.

$A_{LR}^{\pm 8}$	Y120		Y140		Y160	
q jet	hjet	pjet	hjet	pjet	hjet	pjet
d	-0.101	0.001	-0.070	-0.002	-0.028	-0.003
u	-0.102	-0.001	-0.068	-0.001	-0.029	-0.003
s	-0.106	0.003	-0.071	0.001	-0.030	-0.002
c	-0.091	0.005	-0.063	0.002	-0.027	-0.002
b	-0.052	0.010	-0.041	0.004	-0.021	0.001

$A_{LR}^{\pm 8}$	Y120		Y140		Y160	
$\overline{q}$ jet	hjet	pjet	hjet	pjet	hjet	pjet
$\overline{d}$	0.098	-0.013	0.076	-0.071	-0.054	-0.163
$\overline{u}$	0.099	-0.011	0.076	-0.073	-0.054	-0.163
$\overline{s}$	0.102	-0.014	0.079	-0.076	-0.054	-0.169
$\overline{c}$	0.087	-0.014	0.067	-0.069	-0.053	-0.157
$\overline{b}$	0.050	-0.017	0.021	-0.046	-0.130	-0.087

2. $A_{LR}^{\pm 8}$ for Y120 events at different E_{cm} values. The asymmetries get smaller with increasing E_{cm}.

$A_{LR}^{\pm 8}$	$E_{cm} = 50\,\mathrm{GeV}$		$E_{cm} = 91.2\,\mathrm{GeV}$		$E_{cm} = 130\,\mathrm{GeV}$		$E_{cm} = 180\,\mathrm{GeV}$	
q jet	hjet	pjet	hjet	pjet	hjet	pjet	hjet	pjet
d	-0.121	0.015	-0.101	0.001	-0.085	0.000	-0.071	0.001
c	-0.099	0.021	-0.106	0.005	-0.079	0.000	-0.067	-0.001
b	-0.031	0.022	-0.052	0.010	-0.056	0.004	-0.051	0.000

3. $A_{LR}^{\pm 8}$ for Y120 events without parton shower, with exclusion of interjet particles, with reassignment to closest jet and with independent fragmentation.

$A_{LR}^{\pm 8}$	std		IJ excl		reass	
q jet	hjet	pjet	hjet	pjet	hjet	pjet
d	-0.101	0.001	-0.066	0.001	-0.126	0.001
c	-0.106	0.005	-0.055	0.005	-0.112	0.005
b	-0.052	0.010	-0.028	0.010	-0.062	0.009

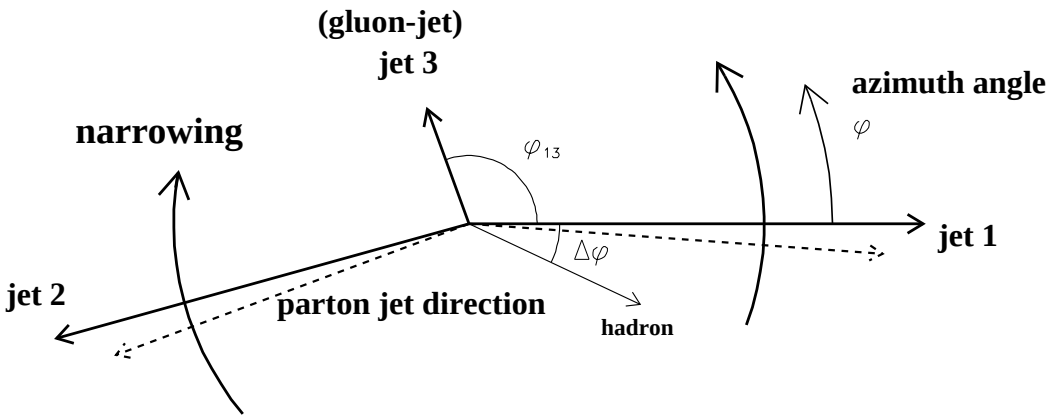

Figure 2.12: Azimuthal angle shift (narrowing) due to the string fragmentation.

$A_{LR}^{\pm 8}$	std		no PS		PSIF	
q jet	hjet	pjet	hjet	pjet	hjet	pjet
d	-0.101	0.001	-0.248	0.045	-0.013	-0.008
c	-0.106	0.005	-0.186	0.048	-0.013	-0.009
b	-0.052	0.010	-0.077	0.031	-0.012	-0.005

2.8 Angle Shift of Leading Particles to the Jet Axis

If one looks at the momentum flow around the q-jet axis as a function of the momentum (see figure 2.13), one finds the distributions to be asymmetric with different averages depending on the momentum interval. Particles with low momenta are predominant on the side adjacent to the gluon jet while high momentum particles cumulate on the side averted from the gluon jet.

This can be understood in the following way: the high momentum particles mark the direction of the parton jets; they are not deflected from the parton jet direction by the boost due to the string fragmentation, while the low momentum particles are strongly deflected.

The event topology is "narrowing" due to the string effect (see figure 2.12 where this is visualized for the case of an event with general kinematics).

This leads to the analysis of the distribution of the azimuthal angles of the high momentum particles (leading particles) in a jet relative to the jet axes.

The mean values of the distributions of

$$\Delta\phi := \phi - \phi_{jet}$$

are referred to as $\langle\Delta\phi\rangle$.

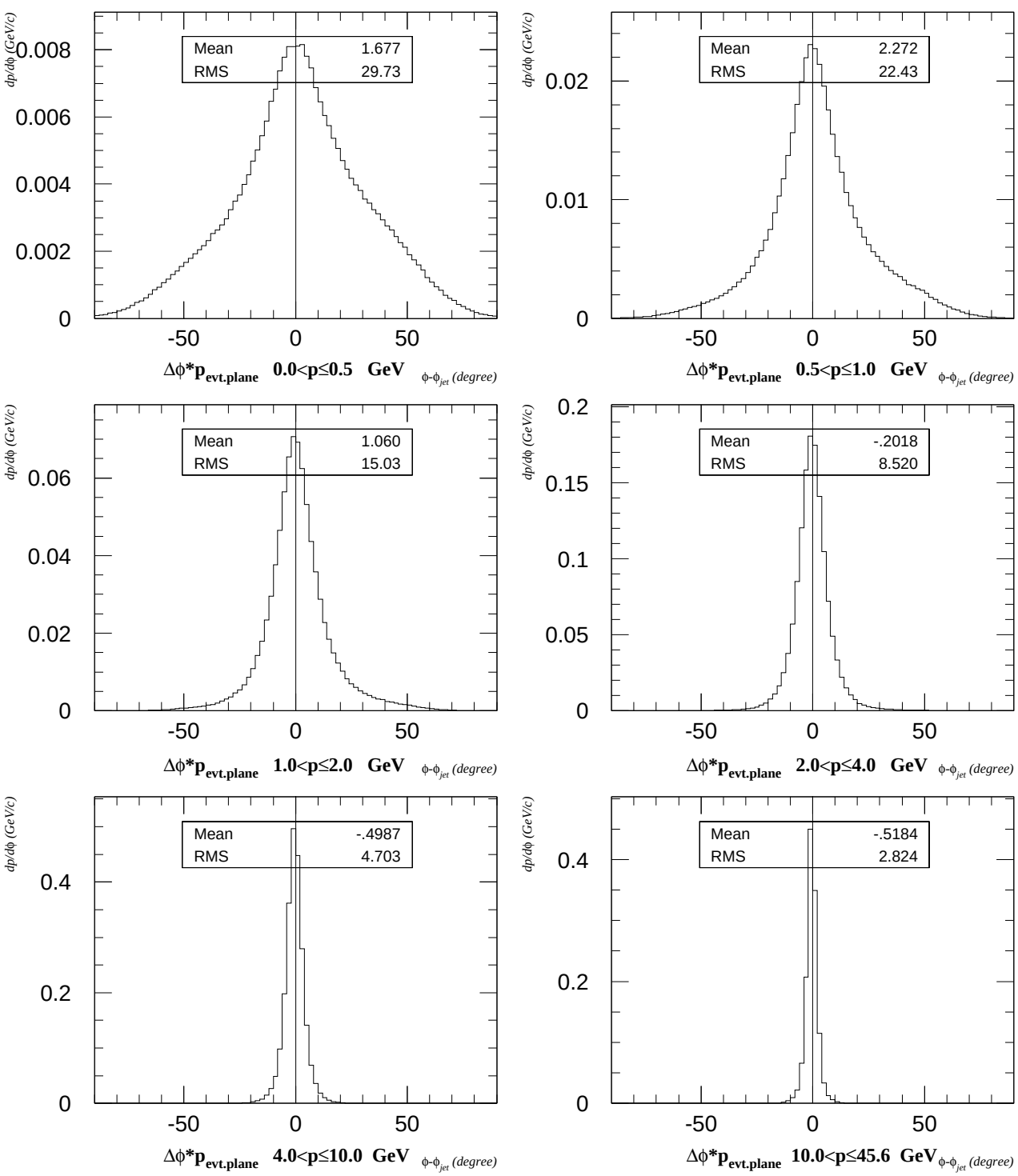

Figure 2.13: Momentum flow distributions for Y120 events relative to the d jet in p intervals.

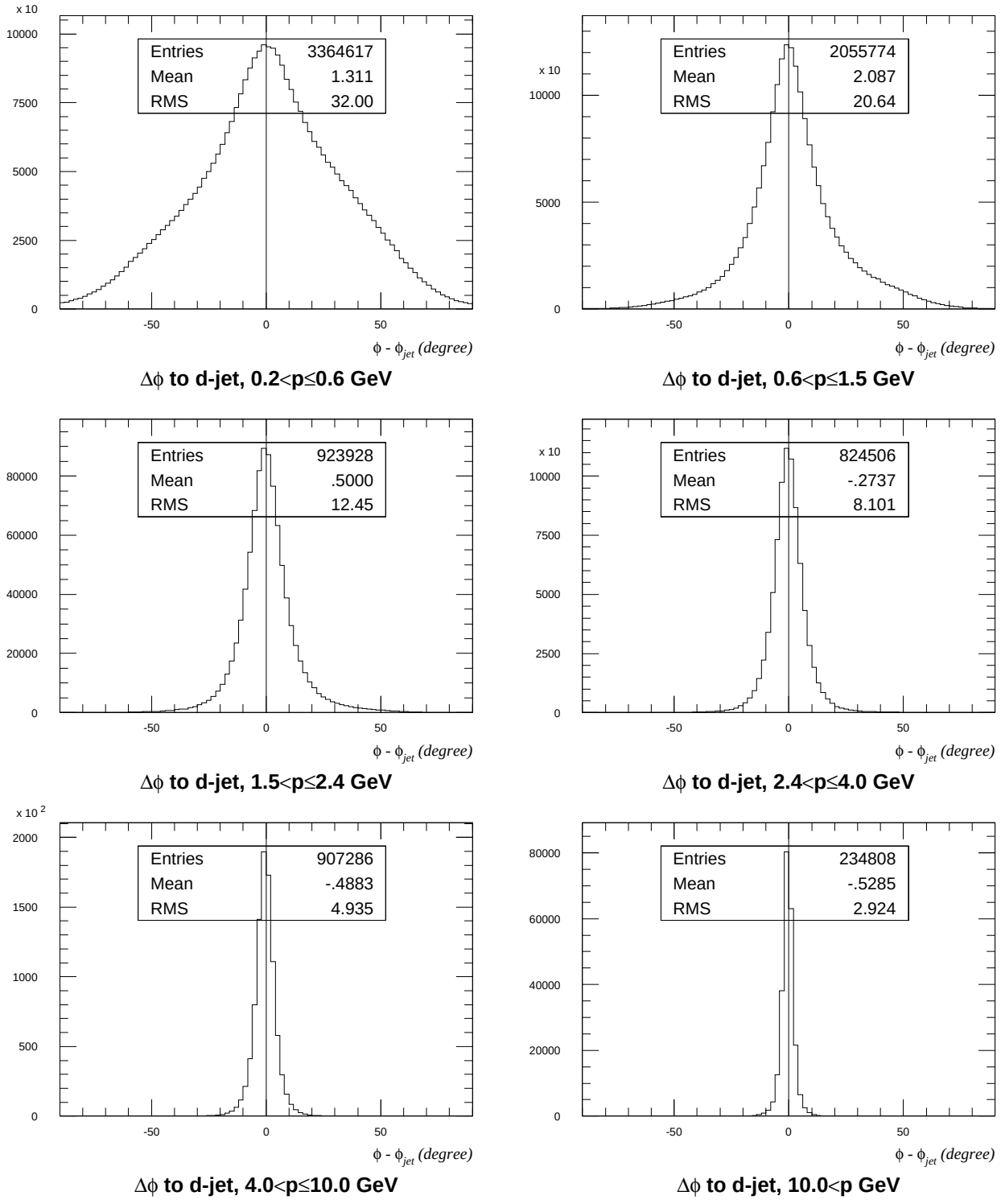

Figure 2.14: $\Delta\phi$ distributions around the d jet in Y120 events for particles from different momentum intervals.

The $\Delta\phi$ distributions relative to the q-jet for particles having momenta in certain p intervals are shown in figure 2.14 for Y120 events with initial flavor d. The distributions get narrower with increasing p; their mean value reaches a maximum of 2° in the interval $0.6\,\mathrm{GeV} < p \leq 1.5\,\mathrm{GeV}$ and goes to $\approx -0.5^\circ$ for large momenta. For Y120 events, the $\Delta\phi$ distributions around the $\overline{d}$ jet show the same behavior with inverted mean values.

In figures 2.15, 2.16 and 2.17 the variation of $\langle\Delta\phi\rangle$ (the mean of the $\Delta\phi$ distribution) with p is shown for the different TRISTAR models considered.

As it was already observed for the case of the momentum flow around the jet axes, the high energetic particles mainly go in the direction of the parton jets; the distributions for the low energy particles are much wider.

Since the momentum of the hadronic jet axis is the sum of the momenta of the low energy and high energy particles, the high energy particles aiming in the direction of the parton jets are shifted to the side averted from the gluon jet (see figures 2.12 and 2.18).

To define an observable to measure the shift of the jet axes caused by the fragmentation process (ie. the azimuthal angle shift between parton and hadron jet axes) one has to look for a quantity proportional to this experimentally unaccessible shift.

Possibilities for approximating the parton jet direction would be:

- The momentum sum of all particles with a momentum larger than some lower limit. Judging from the TRISTAR results for $\langle\Delta\phi\rangle(p)$ shown in figure 2.16, a plausible value for this lower limit could be $p = 4.5\,\mathrm{GeV}$, since for the symmetric configurations considered here the mean of the $\Delta\phi$ distributions reaches its asymptotic value for that momentum.

- The momentum of the most energetic particle in the jet (**L1**), the momentum sum of the two most energetic (**L2**) or of the three most energetic (**L3**) particles in the jet (the particles are ordered according to their momentum; $p_1 > p_2 > p_3 > \ldots > p_n$).

In view of the requirements for the analysis of the data, the choice of a selection of the particles used to approximate the direction of the parton jet based on a cut on the absolute value of their momenta seems unfavourable, since this would introduce a dependence on the description of the momentum spectra of the particles by the fully reconstructed Monte Carlo simulations (including a simulation of particle interactions with the detector material) which are needed for the correction of the results against detector effects (see section 4.7).

For this reason, the second possibility is adopted as an observable to measure the string effect. In order to have a well defined "rest" jet vector to which the angle shift of the leading particle (**L1**) is computed, all jets included in the analysis are required to have at least 3 particles (see reference [30]).

The angle shift of the leading particle with respect to the jet axis is defined as

$$\Delta\phi(\mathbf{L1}) := \phi(\mathbf{L1}) - \phi_{jet}.$$

Figure 2.19 shows the distributions of $\Delta\phi(\mathbf{L1})$, $\Delta\phi(\mathbf{L2})$ and $\Delta\phi(\mathbf{L3})$ in comparison to the distribution of $\phi_{parton\ jet} - \phi_{hadron\ jet}$ as it is found from Y120 events.

The mean values of the distributions for the azimuthal angle shift of the leading particle momentum sums all closely approximate $\phi_{parton\ jet} - \phi_{hadron\ jet}$. But $\Delta\phi(\mathbf{L3})$

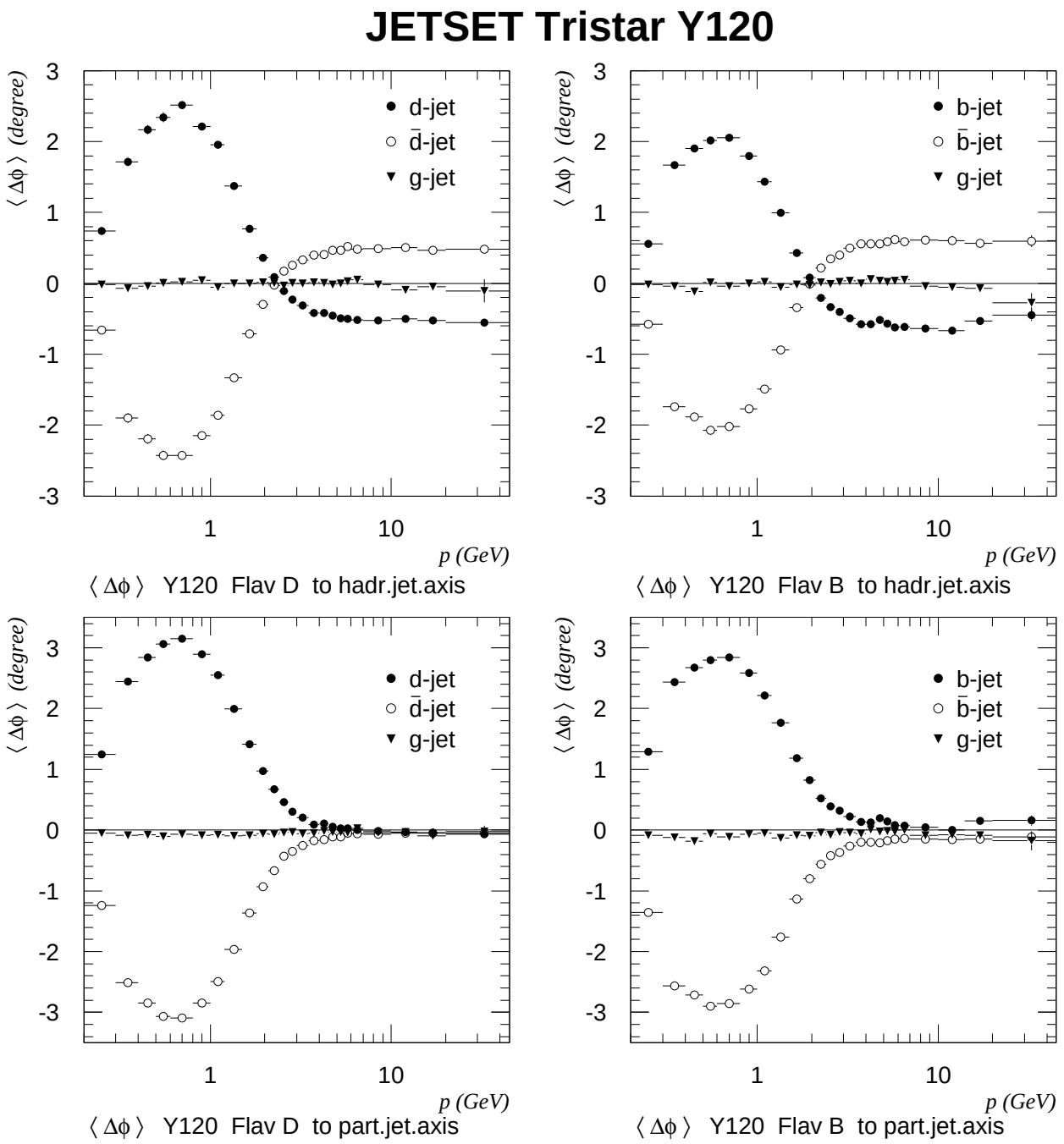

Figure 2.15: Dependence of $\langle\Delta\phi\rangle$ around q,$\overline{q}$ and g parton and hadron jets (for Y120 events and flavors d and b) on the particle momentum p. The $\langle\Delta\phi\rangle$ for particles with large momenta is somewhat larger for b events than for d events, eventhough the difference between the flavors is much smaller in $\langle\Delta\phi\rangle$ than for the momentum flow asymmetries. For events with threefold symmetry, $\langle\Delta\phi\rangle(p)$ for q and $\overline{q}$ are almost mirror images. The g jet shows $\langle\Delta\phi\rangle = 0$ for all p.

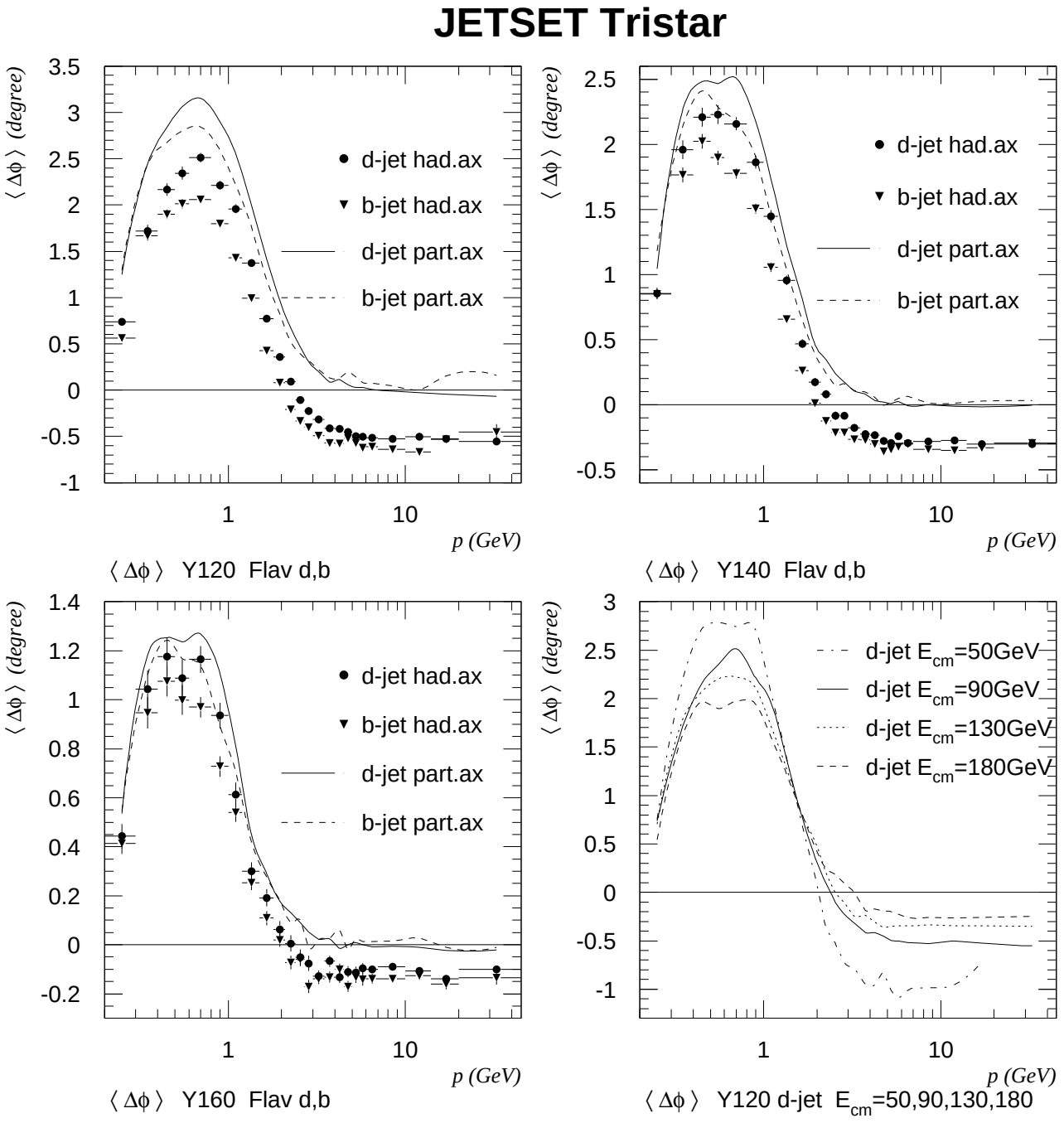

Figure 2.16: $\langle\Delta\phi\rangle(p)$ around q parton and hadron jet axes for Y120, Y140 and Y160 events (flavors d and b) and different values of E_{cm} between 50 GeV and 180 GeV. $\langle\Delta\phi\rangle$ is getting smaller with increasing ϕ_{qg} and with increasing E_{cm}.

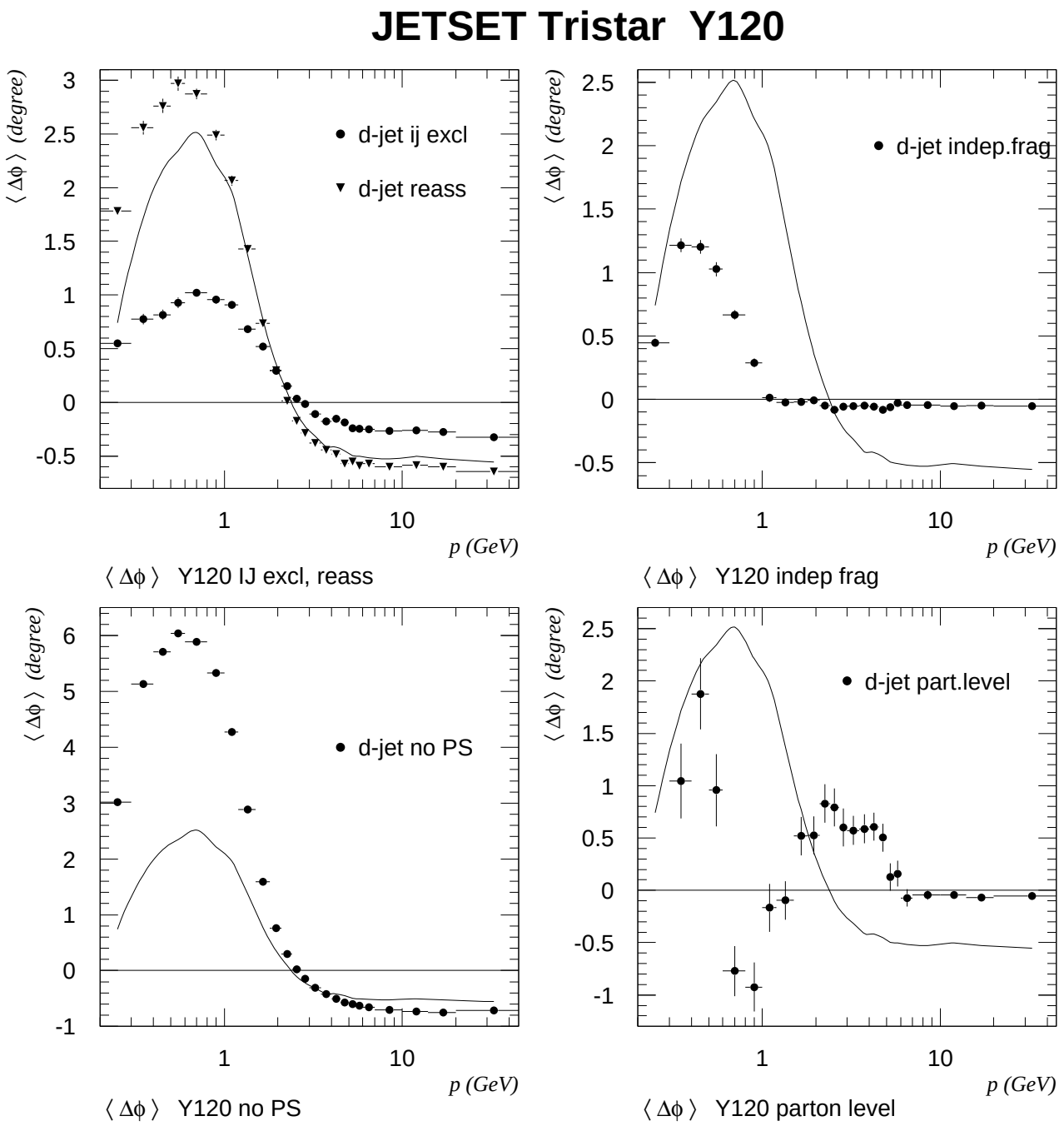

Figure 2.17: $\langle\Delta\phi\rangle$(q) around q hadron jet axis for Y120 events of flavor d (solid line) compared to the case of exclusion of interjet particles, smallest angle reassignment to jets, independent fragmentation, no parton shower and parton level analysis. The exclusion of interjet particles halvens the $\langle\Delta\phi\rangle$ whereas the reassignment increases it by some 20%. Independent fragmentation shows $\langle\Delta\phi\rangle = 0$ for $p > 1\,\mathrm{GeV}$. No parton shower increases the effect and on the parton level, almost no $\langle\Delta\phi\rangle$ effect can be seen.

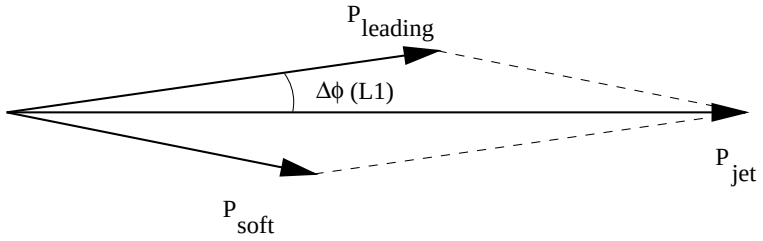

Figure 2.18: Decomposition of the jet vector into a low energy and high energy part. In this special case, the high energy part is taken as the momentum of the most energetic (ie. leading) particle in the jet.

seems favourable since it also shows an RMS that is closer to that of the $\phi_{parton\,jet} - \phi_{hadron\,jet}$ distribution.

Nevertheless, $\langle\Delta\phi(\mathbf{L1})\rangle$ is finally adopted as the prefered observable for the description of the string effect, because Monte Carlo studies on events with general kinematics show that in these cases, $\langle\Delta\phi(\mathbf{L1})\rangle$ best describes $\phi_{parton\,jet} - \phi_{hadron\,jet}$ and that $\langle\Delta\phi(\mathbf{L2})\rangle$ and $\langle\Delta\phi(\mathbf{L3})\rangle$ show a smaller angle shift (see figure 3.8 for a comparison of $\langle\Delta\phi(\mathbf{L1})\rangle$, $\langle\Delta\phi(\mathbf{L2})\rangle$ and $\langle\Delta\phi(\mathbf{L3})\rangle$ at different y_{cut} values for events with general kinematics in JETSET).

The choice of the observable $\langle\Delta\phi(\mathbf{L1})\rangle$ represents a new definition of the string effect.

In the following chapters, the string effect shall be studied in view of this observable. A measurement on data obtained by the ALEPH experiment in the years 1992 and 1993 is made and the corrected results are compared with predictions of various QCD models.

2.9 Results for $\langle\Delta\phi\rangle$ from TRISTAR Events

The results for the observable $\langle\Delta\phi\rangle$ as obtained from JETSET using symmetric (TRISTAR) events under various conditions are given in the next tables. For all Monte Carlo runs, $2 \cdot 10^6$ events were generated. In the case of the standard version of the TRISTAR model, $\approx 56\%$ of the events generated are rejected due to the requirement to have 3 jets for $y_{cut} = 0.01$ on the parton level and on the hadron level and as a consequence of the 10° cut on the matching angle between the original partons and parton jets.

1. The standard version of the TRISTAR model: Y120 events at $E_{cm} = 91.2$ GeV with parton shower. For the different initial flavors, the values of $\langle\Delta\phi(\mathbf{L1})\rangle$ and $\langle\Delta\phi(\mathbf{L3})\rangle$ with respect to the parton jet axis and to the hadron jet axis as well as the value of $\langle\Delta\phi_{pj-hj}\rangle$ are given (with the RMS of the $\Delta\phi$ distributions in brackets).

   The values of $\langle\Delta\phi(\mathbf{L1})\rangle$ reproduce $\langle\Delta\phi_{pj-hj}\rangle$ very well; $\langle\Delta\phi(\mathbf{L1})\rangle$ is a good approximation of the (experimentally unavailable) $\langle\Delta\phi_{pj-hj}\rangle$. For threefold symmetric (Y120) events, $\langle\Delta\phi(\mathbf{L3})\rangle$ also proves to be a good approximation to $\langle\Delta\phi_{pj-hj}\rangle$ and has the additional advantage of having a distribution with lower RMS (closer to that of $\langle\Delta\phi_{pj-hj}\rangle$); in order to have higher statistical significance, a choice of $\langle\Delta\phi(\mathbf{L3})\rangle$ as observable for the string effect thus seems favourable. But for non-symmetric configurations, studies with the JETSET Monte Carlo show that only $\langle\Delta\phi(\mathbf{L1})\rangle$ approximates $\langle\Delta\phi_{pj-hj}\rangle$ well and that $\langle\Delta\phi(\mathbf{L3})\rangle$ fails to do so (see section 3.5).

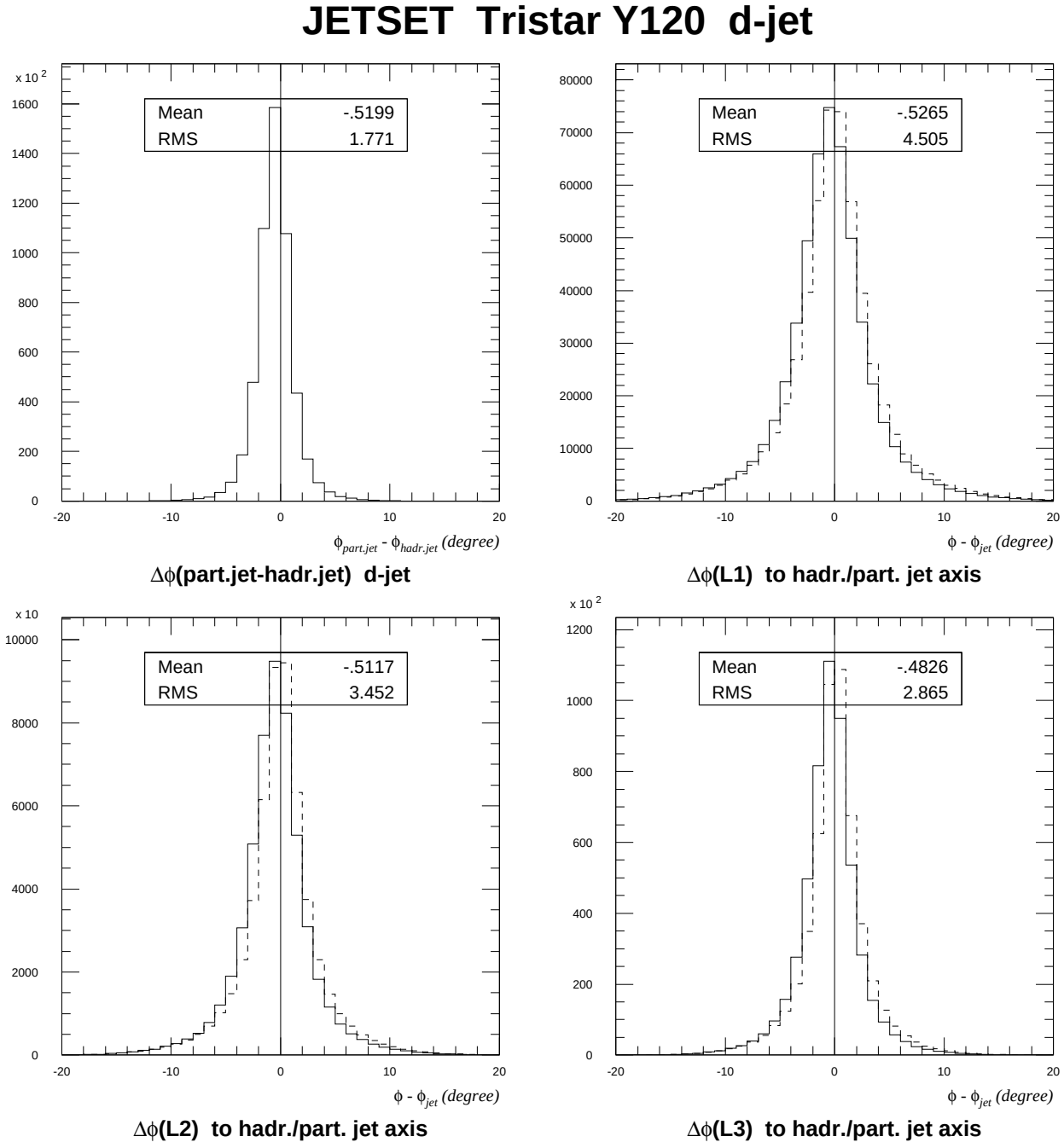

Figure 2.19: Distributions of $\Delta\phi(\mathbf{L1})$, $\Delta\phi(\mathbf{L2})$ and $\Delta\phi(\mathbf{L3})$ compared to $\phi_{parton\ jet} - \phi_{hadron\ jet}$. The $\Delta\phi$ distributions with respect to the parton jet axis are superimposed and show no asymmetry.

The angle shift effect shows some dependence on the initial flavor — it is $\approx 20\%$ larger for b events than for such with light quarks (but also the angle shift with respect to the parton jet axis is larger for b events). The $\Delta\phi$ distributions are broader for b events, which is due to their higher multiplicity and the high p_t decays of b hadrons.

$\Delta\phi(RMS)$		to part.jet		to hadr.jet		
flav	jet	$\langle\Delta\phi(\mathbf{L1})\rangle$	$\langle\Delta\phi(\mathbf{L3})\rangle$	$\langle\Delta\phi(\mathbf{L1})\rangle$	$\langle\Delta\phi(\mathbf{L3})\rangle$	$\langle\Delta\phi_{pj-hj}\rangle$
uds	q	−0.007(4.61)	0.038(3.02)	−0.527(4.50)	−0.483(2.86)	−0.520(1.77)
	$\overline{q}$	−0.064(4.56)	−0.105(2.97)	0.496(4.47)	0.457(2.84)	0.560(1.72)
	g	−0.034(6.28)	−0.041(3.95)	0.018(6.27)	0.012(3.92)	0.052(2.21)
c	q	0.020(4.62)	0.058(3.03)	−0.551(4.56)	−0.514(2.92)	−0.571(1.83)
	$\overline{q}$	−0.083(4.59)	−0.122(2.97)	0.526(4.54)	0.488(2.88)	0.610(1.79)
	g	−0.038(6.26)	−0.042(3.94)	0.006(6.25)	0.004(3.90)	0.046(2.20)
b	q	0.091(6.28)	0.145(3.55)	−0.633(6.17)	−0.578(3.30)	−0.723(2.20)
	$\overline{q}$	−0.165(6.23)	−0.208(3.51)	0.605(6.12)	0.563(3.28)	0.770(2.16)
	g	−0.063(6.18)	−0.054(3.91)	−0.002(6.14)	0.007(3.84)	0.061(2.16)

2. The variation of $\langle\Delta\phi\rangle$ with ϕ_{qg} for the TRISTAR model (ie. the Y120, Y140 and Y160 configurations) at $E_{cm} = 91.2$ GeV with parton shower.

   The symmetry $\langle\Delta\phi(\mathbf{L1})\rangle_{q-jet} \approx -\langle\Delta\phi(\mathbf{L1})\rangle_{\overline{q}-jet}$ only exists for threefold symmetric configurations and vanishes with increasing ϕ_{qg}. The strength of the $\langle\Delta\phi(\mathbf{L1})\rangle$ angle shift effect also diminishes with increasing ϕ_{qg}.

   But still $\langle\Delta\phi_{pj-hj}\rangle$ is well approximated by $\langle\Delta\phi(\mathbf{L1})\rangle$ for Y140 and Y160, at least for the q jet.

$\Delta\phi$		Y120		Y140		Y160	
flav	jet	$\langle\Delta\phi(\mathbf{L1})\rangle$	$\langle\Delta\phi_{pj-hj}\rangle$	$\langle\Delta\phi(\mathbf{L1})\rangle$	$\langle\Delta\phi_{pj-hj}\rangle$	$\langle\Delta\phi(\mathbf{L1})\rangle$	$\langle\Delta\phi_{pj-hj}\rangle$
uds	q	−0.527	−0.520	−0.283	−0.279	−0.122	−0.106
	$\overline{q}$	0.496	0.560	0.382	0.937	−0.211	0.791
	g	0.018	0.051	0.503	−0.299	1.763	0.105
c	q	−0.551	−0.571	−0.288	−0.300	−0.117	−0.118
	$\overline{q}$	0.526	0.610	0.406	1.034	−0.269	0.906
	g	0.006	0.046	0.504	−0.280	1.759	0.160
b	q	−0.633	−0.723	−0.352	−0.374	−0.138	−0.164
	$\overline{q}$	0.605	0.770	0.473	1.196	−0.768	0.055
	g	−0.002	0.061	0.475	−0.311	1.707	−0.110

3. TRISTAR Y120 events at $E_{cm} = 91.2\,\mathrm{GeV}$ and exclusion of interjet particles, reassignment of particles to jets, no parton shower and no fragmentation. The results for $\langle\Delta\phi(\mathbf{L1})\rangle$ are given for the cases of the exclusion of particles in the interjet region (40% definition), the reassignment of particles to the closest jet, the non-parton shower case (the hadronization process starts from the original $q\overline{q}g$ configuration without intermediate parton shower), and the non-fragmentation case (the $\Delta\phi$ analysis is performed on the parton level after the parton shower).

   The exclusion of the particles in the interjet region is found to reduce the effect by $\approx 50\%$ for Y120 events.

   The reassignment of particles to the jet with which they have the smallest angle (thus removing cases of particles being assigned to a jet going in the opposite direction) increases the effect by $\approx 15\%$ for threefold symmetric configurations. For general configurations from ALEPH data, a decrease by $\approx 15\%$ for **R3** events is seen, though.

   Without parton shower, an increase by $\approx 20\%$ is seen for the angle shift; the parton shower therefore smears the effect.

   The $\Delta\phi$ analysis applied on parton level shows less than 10% of the string effect observed after the string fragmentation. This shows that the string effect in its definition via the angle shift $\langle\Delta\phi(\mathbf{L1})\rangle$ is almost entirely due to the string fragmentation. This holds for events with threefold symmetry as they are studied here. This finding is also supported by the study of Y120 events with parton shower together with independent fragmentation, where also no string effect can be seen.

$\Delta\phi$		standard	IJ excl	reassign	no PS	no frag
flav	jet	$\langle\Delta\phi(\mathbf{L1})\rangle$	$\langle\Delta\phi(\mathbf{L1})\rangle$	$\langle\Delta\phi(\mathbf{L1})\rangle$	$\langle\Delta\phi(\mathbf{L1})\rangle$	$\langle\Delta\phi(\mathbf{L1})\rangle$
uds	q	−0.527	−0.264	−0.592	−0.649	−0.045
	$\overline{q}$	0.496	0.250	0.558	0.649	−0.042
	g	0.018	−0.002	0.000	−0.023	0.001
c	q	−0.551	−0.279	−0.622	−0.717	−0.048
	$\overline{q}$	0.526	0.264	0.600	0.713	−0.067
	g	0.006	−0.003	0.004	−0.024	−0.006
b	q	−0.633	−0.301	−0.668	−0.726	−0.086
	$\overline{q}$	0.605	0.290	0.650	0.735	−0.083
	g	−0.002	−0.026	0.013	−0.025	−0.016

4. The dependence of $\langle\Delta\phi(\mathbf{L1})\rangle$ on E_{cm} for Y120 events.

   The strength of the $\Delta\phi$ angle shift is found to decrease with increasing E_{cm} like $1/E_{cm}$. The transverse momentum that a particle of mass m acquires in the string fragmentation was found to be

$$p_\perp = m\beta\gamma$$

where $\beta\gamma$ is a constant which is only determined by the angle between the partons between which the string stretches (see section 2.3) and not dependent on E_{cm}.

The angle shift $\Delta\phi$ of a particle is given by

$$\Delta\phi \approx \sin\Delta\phi = \frac{p_\perp}{p},$$

and since the particle momenta p increase with E_{cm}, one can see that

$$\Delta\phi \propto \frac{1}{E_{cm}}.$$

$\Delta\phi$		50 GeV	91.2 GeV	130 GeV	180 GeV
flav	jet	$\langle\Delta\phi(\mathbf{L1})\rangle$	$\langle\Delta\phi(\mathbf{L1})\rangle$	$\langle\Delta\phi(\mathbf{L1})\rangle$	$\langle\Delta\phi(\mathbf{L1})\rangle$
uds	q	-1.017	-0.527	-0.363	-0.261
	$\overline{q}$	0.997	0.496	0.331	0.234
	g	-0.083	0.018	0.005	0.007
c	q	-1.082	-0.551	-0.389	-0.269
	$\overline{q}$	1.055	0.526	0.324	0.245
	g	-0.100	0.006	0.047	0.032
b	q	-1.000	-0.633	-0.442	-0.291
	$\overline{q}$	0.984	0.605	0.387	0.264
	g	-0.131	-0.002	0.018	0.026

5. The influence of the fragmentation scheme for Y120 events. $\langle\Delta\phi(\mathbf{L1})\rangle$ is studied for independent fragmentation together with parton shower (to see the strength of the effect that is due to the parton shower) and without (to ensure a zero effect). The independent fragmentation is performed without explicit conservation of energy, momentum and flavor. Otherwise, the compensation of the momentum imbalance resulting from the independent fragmentation would lead to a boost and thus obscure the observable $\langle\Delta\phi(\mathbf{L1})\rangle$.

   As in the case of the $\Delta\phi$ analysis on the parton level, only a very small angle shift effect is seen for independent fragmentation, suppressed by more than a factor of 10 relative to the standard case with string fragmentation.

   It should be noted that the combination of parton shower with independent fragmentation is unphysical and requires the introduction of an artificially high parton shower invariant mass cut-off `PARJ(82)`$= M_{min} = 4$ GeV in order to preserve acceptable multiplicities.

   For threefold symmetric configurations, parton shower together with independent fragmentation show that "no string effect" is equivalent to $\langle\Delta\phi(\mathbf{L1})\rangle \approx 0$. For the case of general kinematics, this can *not* be assumed.

If no parton shower is invoked (ie. the independent fragmentation starts from the $q\overline{q}g$ partonic state), no angle shift $\langle\Delta\phi(\mathbf{L1})\rangle$ can be seen (here, `MSTJ(2)=1` was set to have a gluon fragment like a d, u or s in the independent fragmentation. Setting `MSTJ(2)=3`, ie. assuming a gluon to fragment like a $d\overline{d}$, $u\overline{u}$ or $s\overline{s}$ pair, does not lead to $\langle\Delta\phi(\mathbf{L1})\rangle = 0$).

$\Delta\phi$ PS, IF		to hjet	to pjet	
flav	jet	$\langle\Delta\phi(\mathbf{L1})\rangle$	$\langle\Delta\phi(\mathbf{L1})\rangle$	$\langle\Delta\phi_{pj-hj}\rangle$
uds	q	−0.054	−0.040	−0.015
	$\overline{q}$	0.022	−0.046	0.068
	g	0.008	−0.010	0.019
c	q	−0.076	−0.052	−0.024
	$\overline{q}$	0.046	−0.041	0.087
	g	0.022	−0.012	0.034
b	q	−0.146	−0.042	−0.105
	$\overline{q}$	0.138	−0.016	0.153
	g	0.025	−0.005	0.028

$\Delta\phi$ no PS, IF		to hjet	to pjet	
flav	jet	$\langle\Delta\phi(\mathbf{L1})\rangle$	$\langle\Delta\phi(\mathbf{L1})\rangle$	$\langle\Delta\phi_{pj-hj}\rangle$
uds	q	0.003	0.004	−0.001
	$\overline{q}$	0.003	0.001	0.002
	g	−0.008	−0.006	−0.002
c	q	−0.019	−0.012	−0.007
	$\overline{q}$	−0.003	−0.007	0.004
	g	0.001	0.001	0.000
b	q	−0.047	−0.002	−0.045
	$\overline{q}$	0.039	0.000	0.039
	g	0.005	0.005	0.000

Chapter 3

3-Jet Events and Dalitz Plot

3.1 Synopsis

In the previous chapter, only samples of symmetric events generated by the JETSET Monte Carlo have been considered. Each of these samples had very similar kinematic configurations.

If one does not force the JETSET event generator to produce such special configurations, a wide variety of kinematic configurations emerge.

Compared to the TRISTAR events, only a smaller fraction will be found to be 3-jet events by the DURHAM cluster algorithm (see the next section for details on cluster finding algorithms), depending on the y_{cut} value used (for the standard choice around $y_{cut} = 0.01$, the fraction of 3-jet events is $\approx 30\%$).

Different y_{cut} values do also favour different kinematic configurations as 3-jets (see eg. sections 3.4 and 4.5).

In the previous chapter, it was observed that the strength of the string effect as measured by the angle shift observable $\langle \Delta\phi(\mathbf{L1}) \rangle$ does depend on the following properties of an event:

- The angle ϕ_{qg} between the quark jet and the gluon jet.
- The energy E_{cm} with which the event is generated.

If one has no information on which hadron jet originates from the hard gluon and if one has to rely on the assumption that the least energetic jet is the gluon jet, the probability for this third jet (ordered according to energy) to be the gluon jet ($P_{3=g}$) will also strongly influence the observable $\langle \Delta\phi(\mathbf{L1}) \rangle$.

It is thus necessary to restrict the study of the string effect to groups of events which have reasonably similar kinematic configurations.

3.2 Cluster Finding Algorithms

Hadronic events at LEP energies show a clear jet structure as can be seen from the example in figure 1.2. A jet can be understood as several particles that are directed into a small solid angle.

But only few events show such a clear 3-jet signature as the one in figure 1.2.

For quantitative studies it is necessary to define an algorithm that allows the grouping of particles into clusters (jets) based on firmer grounds than just visual ones.

The ingredients for such algorithms are:

- A resolution variable (or jet metric) y_{kl}.
- A cut-off y_{cut} for the clustering.
- A scheme for the combination of particle momenta to form a jet vector.

One of the first cluster finding algorithm used was the JADE algorithm (named after the JADE collaboration at DESY; see reference [22]) which used the resolution parameter

$$y_{kl} := \frac{2E_kE_l(1-\cos\theta_{kl})}{E_{vis}^2}.$$

This corresponds to the invariant mass squared of two (massless) particles k and l

$$m_{inv}^2 := (p_k+p_l)_\mu(p_k+p_l)^\mu = 2E_kE_l(1-\cos\theta_{kl}) \qquad \text{if} \quad m_k = m_l = 0$$

scaled with the visible energy squared of the events.

The basic idea behind the cluster algorithm is to determine the variable y_{kl} for all pairings (k,l) of the observed particles and to join those two particles together to form a pseudo-particle which have the smallest y_{kl}. The momentum of the newly formed pseudo-particle is usually taken as the sum of the 4-momenta of the two particles that are combined: $p_{ij} = p_i + p_j$. This combination scheme is usually referred to as the E-scheme. The new pseudo-particle is used just like an ordinary particle furtheron.

This process is iterated until the smallest y_{kl} determined from all pairings of particles (and pseudo-particles) exceeds a given cut-off y_{cut}.

The number of pseudo-particles left at this point gives the number of jets found (by a given algorithm, for a given y_{cut}) and their momenta give the jet axes. The jet momentum $\vec{p}_{jet}$ (or jet axis) is the momentum sum of the particles assigned to the jet.

The main disadvantage of the resolution variable of the JADE algorithm is its tendency to first cluster the low energy particles. A combination of two soft particles going into opposite directions is favoured over the combination of a soft particle with a hard particle going in the same direction. This leads to jets containing particles pointing into the hemisphere opposite to the jet direction.

The cluster finding algorithm that will be used in this analysis is the DURHAM (or $k_\perp$) algorithm (see reference [13]) which performs better in clustering soft particles.

It uses the resolution variable

$$y_{kl} := \frac{2\min(E_k^2,E_l^2)(1-\cos\theta_{kl})}{E_{vis}^2}$$

and the E-scheme for the combination of particle momenta.

The transverse momentum of a (massless) particle with energy E_k relative to a particle with larger energy E_l is defined as

$$k_\perp := 2\min(E_k,E_l)\sin\frac{\theta_{kl}}{2}$$

which gives with $\sin\theta \approx \theta$

$$k_\perp \approx 2\min(E_k, E_l)\frac{\theta_{kl}}{2} = E_k\theta_{kl}.$$

Thus, one can see that

$$k_\perp \approx E_k \sin\theta_{kl}.$$

Using

$$2\sin^2\frac{\theta_{kl}}{2} = 1 - \cos\theta_{kl}$$

it turns out that

$$\frac{k_\perp^2}{E_{vis}^2} = \frac{2\min(E_k^2, E_l^2)(1-\cos\theta_{kl})}{E_{vis}^2} = y_{kl}.$$

Thus, for small angles the resolution variable y_{kl} is the squared transverse momentum of the particle with the lower energy relative to the one with the larger energy, normed to the visible energy squared in the event.

This is a more natural choice for a clustering variable than the invariant mass that is used in the JADE algorithm.

The numerical values for the cut-off parameter are usually chosen as $y_{cut}^J = 0.04$ and $y_{cut}^D = 0.009$ which results in approximately the same 3-jet rates ($\approx 30\%$ at LEP energies). In this thesis, the string effect analysis will mainly be made for logarithmically spaced values of y_{cut}^D ranging from 0.001 in the soft limit to 0.1 in the hard limit.

The DURHAM algorithm performs better in resolving soft gluons (ie. the hadron jets stemming from them) due to the smaller value of its cut-off.

For a given y_{cut}, the minimum energy a cluster must have in order to be recognized as a separate jet can be calculated from the definition of the resolution variable:

$$\frac{2E_3^2}{E_{vis}^2}(1-\cos\theta_{23}) = y_{23} < y_{cut}$$

where E_3 denotes the energy of the least energetic jet in a 3 jet event and θ_{23} its angle with the second jet.

Setting $E_{vis} = E_{cm}$ and choosing $\theta_{23} = 90^\circ$ (this is a reasonable choice for events with kinematic configurations that are of interest), one gets

$$E_3 > \frac{E_{cm}}{\sqrt{2}}\sqrt{y_{cut}}.$$

The following table gives the minimum energy a cluster must have to be recognized as a jet for various y_{cut} values ($E_{vis} = E_{cm} = 91.2\,\mathrm{GeV}$):

y_{cut}	0.001	0.00316	0.01	0.0316	0.1
min E_3 (GeV)	2.0	3.6	6.4	11.4	20.3

This minimum energy can be seen in the distributions of E_3 for 3-jet events from ALEPH 1992 data at various y_{cut} values (see figure 4.23).

3.3 Dalitz Plot

The kinematics of events with 3-jet topology are characterized by the 3 jet axes. These 3 momentum vectors correspond to 9 degrees of freedom which are not independent of each other.

Defining the normalized energies of the 3 jets neglecting jet masses (see section 4.2 for the determination of E_i from the angles between the jets)

$$x_i := \frac{2E_i}{E_{cm}}, \qquad x_1 > x_2 > x_3$$

and using $\vec{p}_i$ to denote the momentum vector of jet i (in energy order), one has, due to energy and momentum conservation,

$$\sum_{i=1}^{3} x_i = 2,$$

$$\sum_{i=1}^{3} \vec{p}_i = \vec{0}.$$

These equations eliminate 4 degrees of freedom. Another 3 degrees of freedom are eliminated by the possibility to freely choose an orientation in space (Euler angles), leaving only 2 variables to fully describe the kinematics of a 3-jet event.

Accordingly, of the 3 normalized energies x_i, only 2 can be chosen independently.

It is practical to define

$$z := \frac{1}{\sqrt{3}}(x_2 - x_3)$$

as the normalized energy difference between the second and the third jet.

For events with approximate Y symmetry, z will be close to 0. For events with a third jet with very low energy, z will go to $1/\sqrt{3}$ (never reaching this extremal point of the phase space which marks the border to 2-jet configurations).

Since gluon jets are likely to have lower energy (see the model studies in section 3.4), the $P_{3=g}$ will be higher for 3-jet events with large z.

In the previous chapter, the strength of the angle shift effect was found to be dependent on the angle ϕ_{13} (or ϕ_{qg}, if it is known which jet is the gluon jet).

Thus, the variables z and ϕ_{13} are chosen to group the 3-jet events into classes of different kinematics. This is called the *Dalitz plot*. A binning of 6 by 6 in the z/ϕ_{13} plane is used to have good resolution while preserving sufficient statistics in each bin (see figure 3.1 for exemplaric configurations in each of the 36 Dalitz bins).

If a configuration is described by the variables z and ϕ_{13}, the normalized energies x_i can be calculated from them using the following relations:

$$\begin{aligned} x_3 &= \frac{-B \pm \sqrt{B^2 - 4AC}}{2A}, \\ x_2 &= \sqrt{3}z + x_3, \\ x_1 &= 2 - x_2 - x_3 \end{aligned}$$

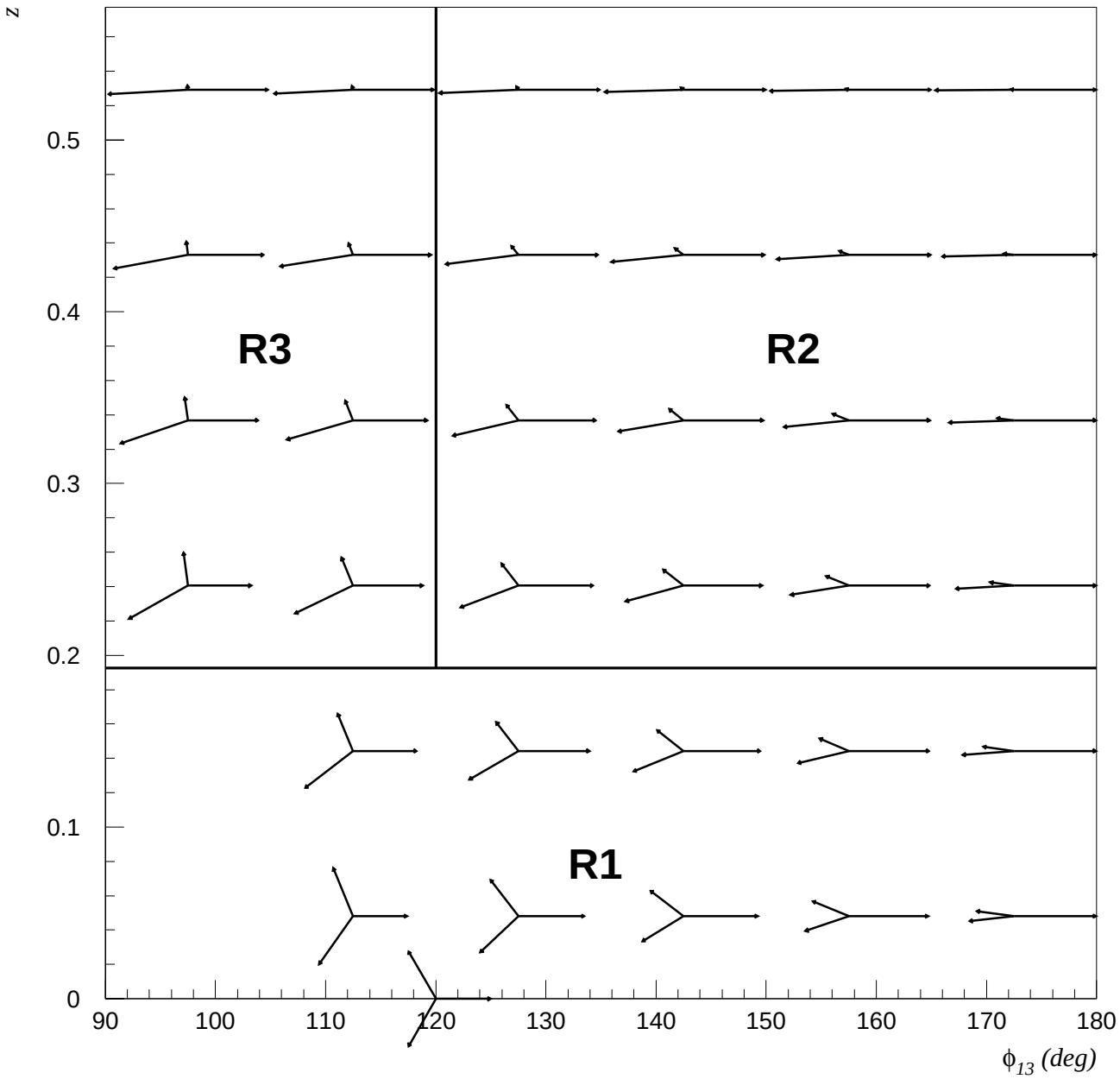

Figure 3.1: Classification of 3-jet events according to z and ϕ_{13} — the Dalitz plot. The length of the arrows corresponds to the jet energy. The configurations that would inhabit the lower left corner are unphysical. The position of the rare Mercedes events (on the $z = 0$ axis) is shown. The kinematic region **R1**, **R2** and **R3** are indicated.

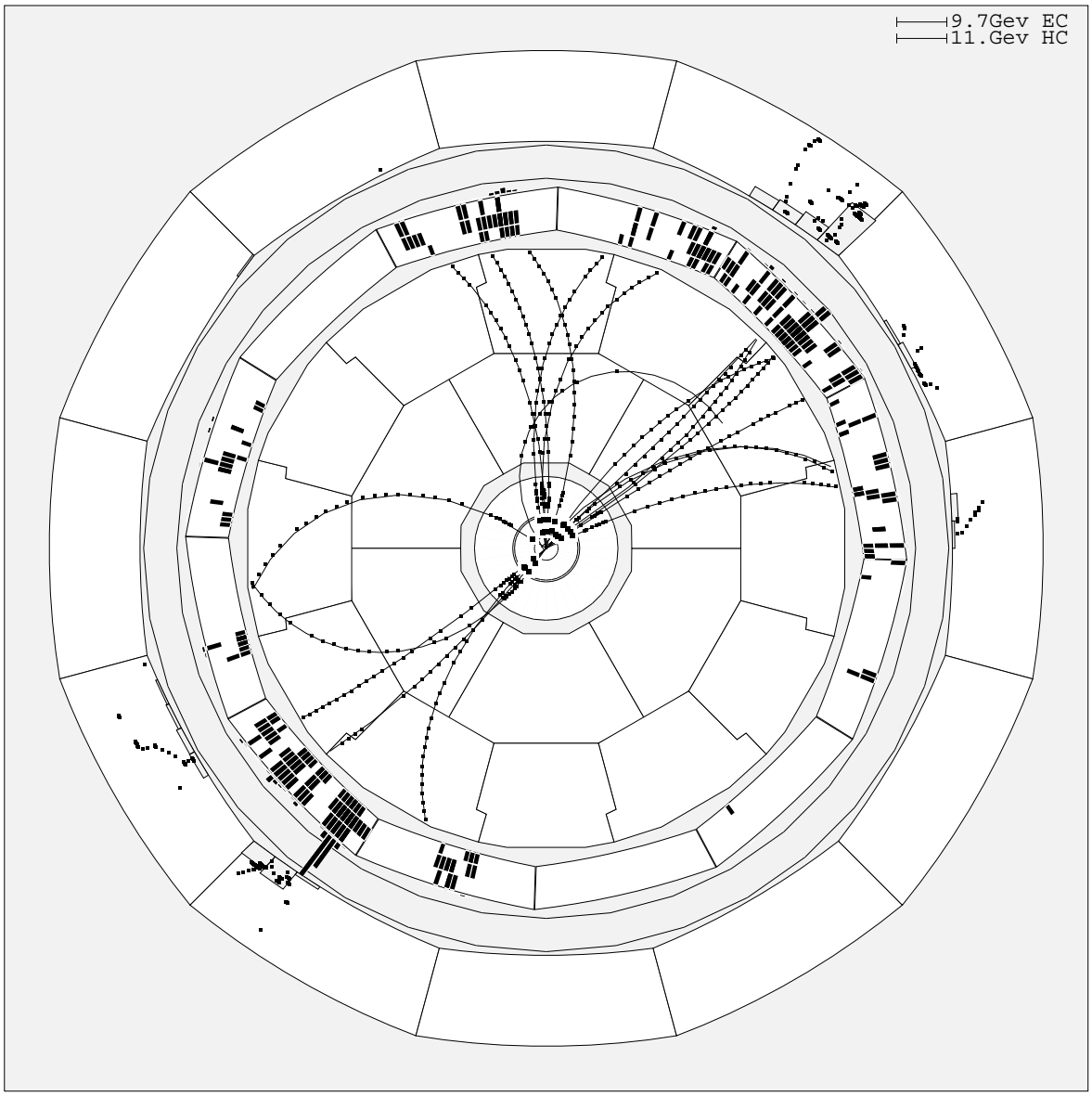

Figure 3.2: A 3-jet event belonging to kinematic region **R3** as seen in the ALEPH detector. The low energy third jet is going towards 12 o'clock.

where

$$\begin{aligned} A &= 4(\cos\phi_{13} - 1), \\ B &= 2\sqrt{3}z - 2(\sqrt{3}z - 2)(2 - \cos\phi_{13}), \\ C &= 4(\sqrt{3}z - 1). \end{aligned}$$

A division into just three kinematic regions, which is rougher but more easy to handle, is given by the definition of regions **R1**, **R2** and **R3**:

$$\begin{aligned} &\textbf{R1}\text{: } z < \tfrac{1}{3\sqrt{3}} \\ &\textbf{R2}\text{: } z \geq \tfrac{1}{3\sqrt{3}}, \phi_{13} > 120^\circ \\ &\textbf{R3}\text{: } z \geq \tfrac{1}{3\sqrt{3}}, \phi_{13} \leq 120^\circ \end{aligned}$$

Special attention is given to **R3**, since it contains the kinematic configurations which have the highest $P_{3=g}$ and well separated jets 2 and 3 with relatively small ϕ_{13}.

3.4 Gluon Jet Probability

For the symmetric 3-jet events considered in the previous chapter, it has been easy to identify the gluon jet due to the well separated jets originating from a 3 parton $q\overline{q}g$ configuration.

For 3-jet events with general kinematics produced by a Monte Carlo event generator with parton shower, it's not straightforward to identify the gluon jet.

The average number of partons (quarks and gluons) at the end of the parton shower is around 8.5 for JETSET 7.3 (using best fit parameters). In the $g \to q\overline{q}$ branchings, additional quark antiquark pairs (mainly of flavors u, d and s with very rare cases of c) are produced and the original quarks can occasionally acquire large virtualities and radiate very high energy gluons, leaving them with small 4-momentum.

It is therefore not obvious how to tag a hadron level jet in a parton shower Monte Carlo event as being a quark or gluon jet.

Several possibilities for the *definition* of a gluon jet (in PS events) were proposed in [14].

Since there is no canonical definition of a gluon jet, some deliberation is involved in selecting one special algorithm.

The *purity* of this tagging algorithm is unity, since the algorithm is the definition of a gluon jet. Its *efficiency*, ie. the ratio between the number of 3-jet events for which the gluon jet could be successfully identified to the total number of 3-jet events presented, may vary, though.

The algorithm that is used here works as follows:

- the partons at the end of the parton shower cascade (before hadronization) are grouped into exactly 3 jets (this requires that the partonic state must have at least 3 partons; cases where the original quarks did not radiate have to be excluded).

- for each quark assigned to a parton jet, the "baryon number" of the jet is increased by 1/3; for each antiquark, it is lowered by 1/3. A parton jet having baryon number equal to zero is taken as a gluon jet; parton jets with non-zero baryon number are tagged as quark jets.

- the hadron level jets are matched to the parton jets via minimum angle, starting with the most energetic hadron jet. A hadron jet matched to a parton jet that is tagged as gluon jet is taken to be a gluon jet.

- only events are considered which have 2 quark tags and 1 gluon tag.

This algorithm is named quark counting algorithm. Its efficiencies for several QCD models (see section 5.2 for an explanation of the abbreviations used for the QCD models) are given in table 1 in this section. They are based on all events with at least 3 partons.

The disadvantages of this algorithm are obvious:

- less than 100% efficiency; ambiguous events have to be rejected.

- jets containing an original quark and one antiquark produced in the parton shower are tagged as gluon jets.

- vice versa, a jet containing just one quark from a gluon splitting in the parton shower is tagged as quark jet.

If one only considers events with no additional quark antiquark pairs from the parton shower, the ambiguities are reduced. But the restriction to the subsample of these events also changes the probability $P_{3=g}$ — it is increased.

An alternative algorithm for the definition of the gluon jet in PS events, which has the disadvantage of being only applicable together with the JETSET event generator, has also been studied.

Here, the quark counting is replaced by a traceback of the quarks assigned to a parton jet through the history of the parton shower (using the mother-daughter relations available in the `LUJETS` COMMON block) to see if they come from a $g \to q\overline{q}$ branching or from the original $q\overline{q}$ pair. A parton jet that contains a quark which can be traced back to an original quark is tagged as a quark jet.

This algorithm has the advantage of having practically 100% efficiency (with the exception of the very rare cases where both quarks stemming from the original ones are assigned to the same jet).

It turns out that $P_{3=g}$ is not very sensitive to the gluon jet definition used.

In figures 3.3, 3.4 and 3.5, the values of $P_{3=g}$ (in %) are given for the kinematic configurations of the Dalitz plot. The underlaid squares have areas proportional to the number of events in the bin. Numbers are only given for bins with more than 1000 entries. For every model, 2 million events have been generated.

Especially for the **R3** configurations, $P_{3=g}$ is high (see also table 3 in this section).

In the vicinity of the symmetric configurations (with $z \approx 0$), $P_{3=g}$ is small. In order to study the string effect for such 3-jet configurations from the data, one would have to use other means to identify the gluon jet beyond the simple assumption that the third jet is the gluon jet. A possibility for this is the utilization of vertex detector (VDET)

information on secondary decay vertices from b decays to effectively tag the quark jets in a 3-jet event (see also section 5.4).

From figures 3.3, 3.4 and 3.5, one can easily see how different kinematic configurations are selected as 3-jet events for different values of y_{cut}.

The following tables give the probabilities for the least energetic hadron jet in a 3 jet event to be the gluon jet ($P_{3=g}$) and for the most energetic hadron jet to be a quark jet ($P_{1=q}$).

These numbers are based on events for which the quark jet identification algorithm yields exactly two quark jet tags. These events may contain secondary quark antiquark pairs. Separate results are given for events with no secondary quark antiquark pairs produced in the parton shower resp. color dipole cascade. $P_{3=g}$ and $P_{1=q}$ are higher for the subsample of these events. In the case of the ARIADNE model, which produces more such secondary quark antiquark pairs than JETSET, a restriction to events with only one quark antiquark pair results in higher values for $P_{3=g}$ and $P_{1=q}$ compared to JETSET, in contrast to the case without this restriction.

Events with initial flavor d show values of $P_{3=g}$ and $P_{1=q}$ a little below those for the normal mixture sample, while such with initial flavor b show values approximately 2% higher than the normal mixture.

$P_{3=g}$ is found to be strongly dependent on the value of y_{cut} used for the definition of 3-jet events — for a low value of the jet resolution parameter the overall $P_{3=g}$ is above 80%, whereas for hard y_{cut} values which require 3 jets of similar energy it drops to close to 55% (especially in the densely populated region 1).

For the JETSET parton shower Monte Carlo model, the traceback algorithm yields approximately 1% higher values for $P_{3=g}$ and practically the same for $P_{1=q}$. This gives confidence that the deliberation involved in choosing one algorithm for identification of quark/gluon jets does not very much bias the results for $P_{3=g}$ and $P_{1=q}$.

$P_{1=q}$ is close to 95% for all the QCD models considered (with a slight deviation for ARIADNE which can be explained by the higher rate for production of secondary quark antiquark pairs) and is much less dependent on y_{cut}.

Generally, the models considered show very similar $P_{3=g}$ and $P_{1=q}$, as one would expect, since they are all based on perturbative QCD.

The slight deviations shown, which are also dependent on the algorithm employed for quark/gluon jet identification, can not account for large differences in the predictions for the observable $\langle\Delta\phi(\mathbf{L1})\rangle$. Especially the variations of the JETSET parton shower model show no differences in $P_{3=g}$ and $P_{1=q}$ very much in contrast to their results for $\langle\Delta\phi(\mathbf{L1})\rangle$.

1. Efficiencies for the quark counting algorithm applied to different QCD models (note the high efficiency for the case of the restriction to events with only one $q\bar{q}$ pair found for PSAZ):

efficiency [%]	2 q jets tagged	2 q jets tagged + only one $q\bar{q}$ pair
PSCO2	96.8	74.4
PSAZ	97.4	83.0
HERWIG	98.1	81.9
ARIADNE	94.3	61.7

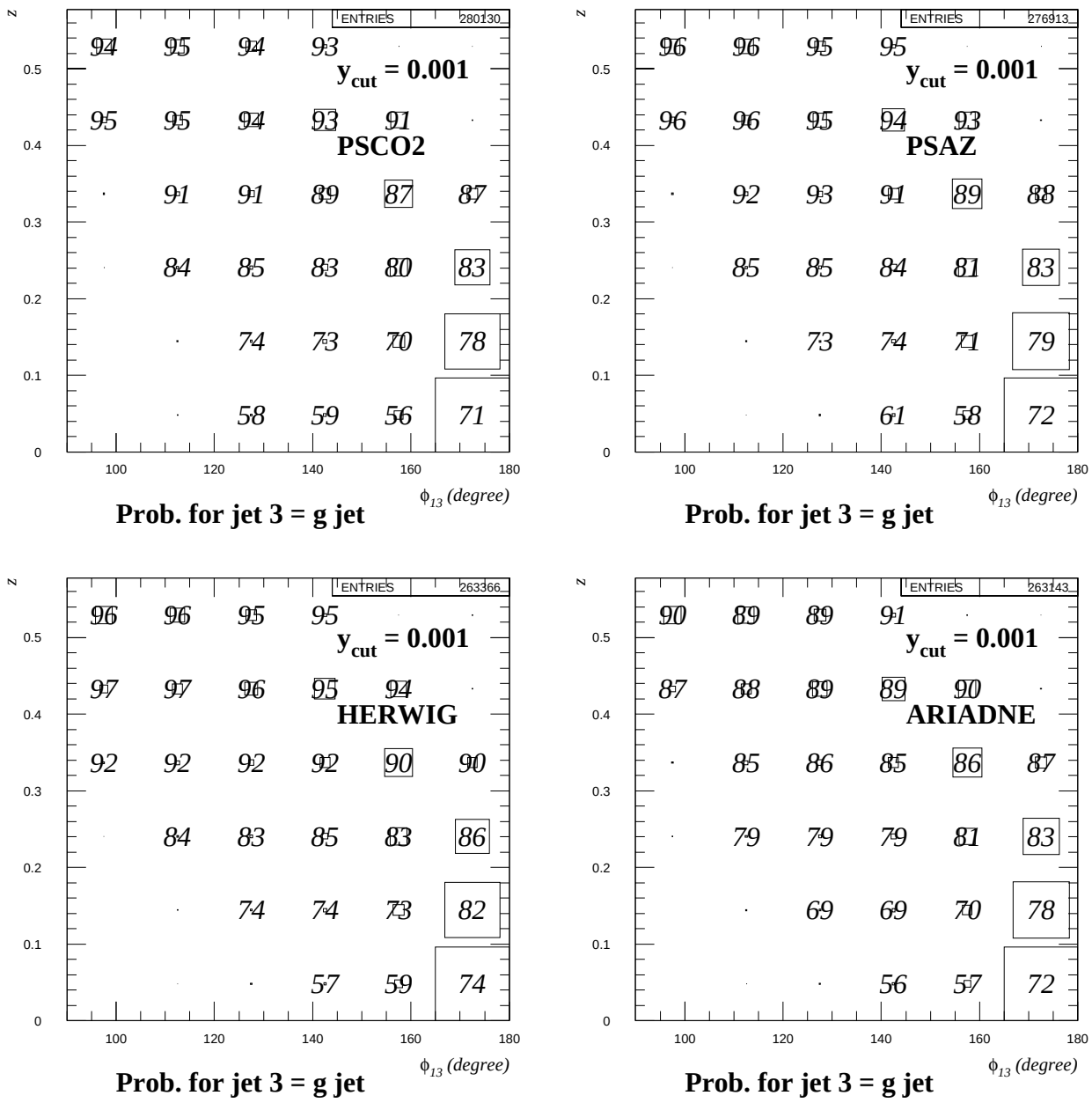

Figure 3.3: Probability $P_{3=g}$ (in %) for the third jet to be the gluon jet based on the quark counting algorithm. The values are given for the most important Monte Carlo models. 3-jet events were selected using the DURHAM algorithm with $y_{cut} = 0.001$. This value of y_{cut} gives a high 3-jet rate and selects 3-jet events mainly in **R2** and **R1** events with large ϕ_{13}.

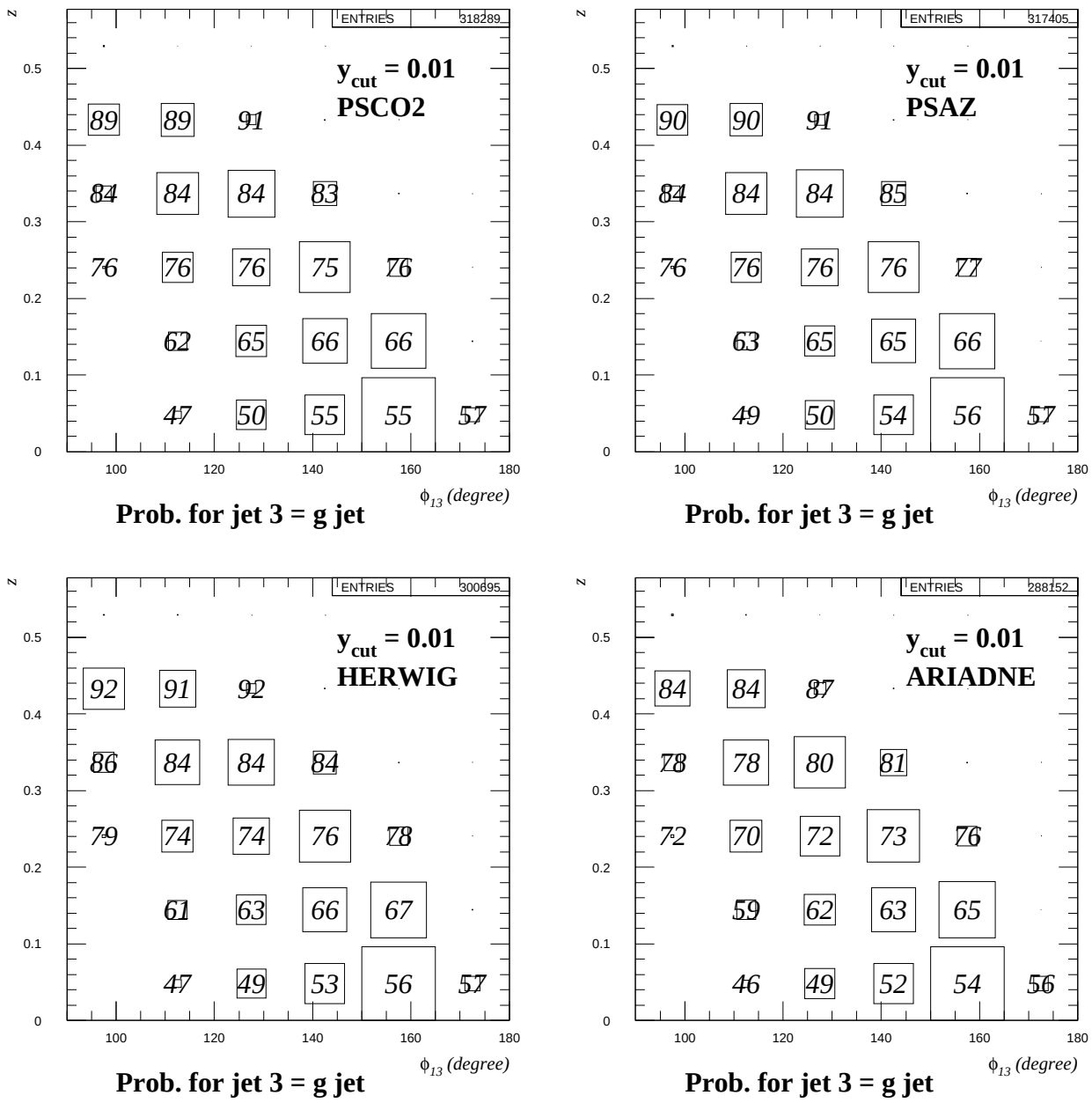

Figure 3.4: Probability $P_{3=g}$ (in %) for the third jet to be the gluon jet based on the quark counting algorithm. The values are given for the most important Monte Carlo models. 3-jet events were selected using the DURHAM algorithm with $y_{cut} = 0.01$. This value of y_{cut} gives a high rate of 3-jet events in **R3** which is of special interest for the string effect study. The values of $P_{3=g}$ are quite similar for the different models with ARIADNE showing somewhat lower values (due to the higher rate of secondary $q\overline{q}$ pairs, which lower $P_{3=g}$). The variations of the JETSET parton shower model are exemplified by PSCO2 and PSAZ, which both show very similar $P_{3=g}$, in contrast to the big difference in $\langle \Delta\phi(\mathbf{L1}) \rangle$.

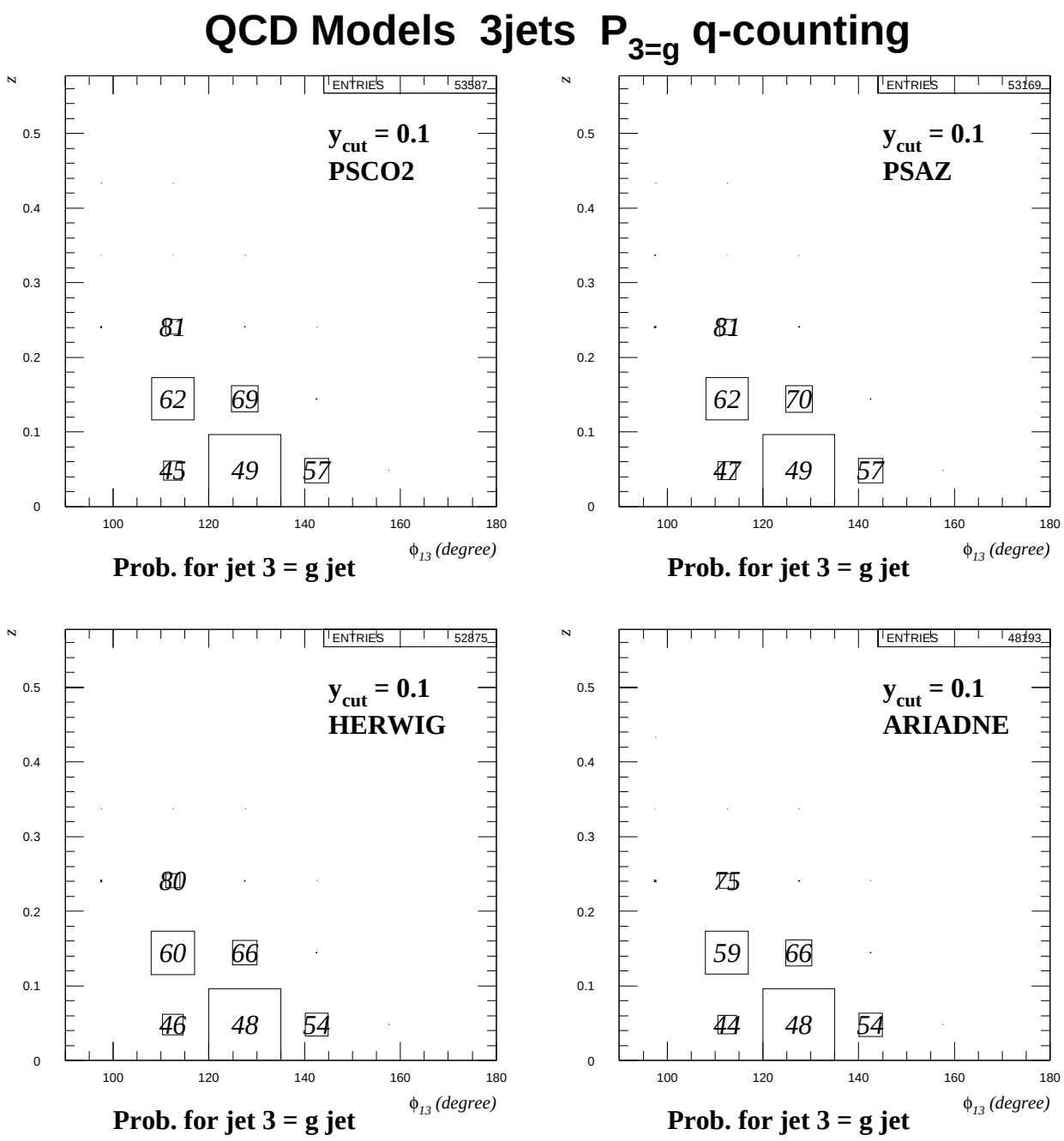

Figure 3.5: Probability $P_{3=g}$ (in %) for the third jet to be the gluon jet based on the quark counting algorithm. The values are given for the most important Monte Carlo models. 3-jet events were selected using the DURHAM algorithm with $y_{cut} = 0.1$. This value of y_{cut} selects 3-jet events almost exclusively in **R1** (symmetric configurations).

2. Overall $P_{3=g}$ and $P_{1=q}$ for JETSET PSCO2 for the two algorithms and for different initial flavors:

	$P_{3=g}$ [%]	$P_{1=q}$ [%]
q-counting flavor mix	71.0	95.3
traceback flavor mix	72.5	95.5
q-counting flavor d	70.1	95.2
q-counting flavor b	73.1	95.7

3. $P_{3=g}$ and $P_{1=q}$ for JETSET PSCO2 with q-counting algorithm for the different kinematic regions:

region	$P_{3=g}$[%]	$P_{1=q}$[%]
Rall	71.0	95.3
R1	59.3	94.8
R2	79.4	97.2
R3	84.4	94.2

4. Overall $P_{3=g}$ and $P_{1=q}$ for the different QCD models ("2 q jtag + 1 $q\bar{q}$" means events with 2 quark tags and only one $q\bar{q}$ pair):

QCD model	$P_{3=g}$[%]		$P_{1=q}$[%]	
	2 q jtag	2 q jtag + 1 $q\bar{q}$	2 q jtag	2 q jtag + 1 $q\bar{q}$
PSCO2	71.0	73.6	95.3	96.3
PSAZ	71.3	73.4	95.5	96.3
HERWIG	71.8	73.3	95.3	95.8
ARIADNE	68.5	75.0	92.6	96.3

5. Dependence of $P_{3=g}$ on y_{cut} for JETSET PSCO2:

y_{cut}	$P_{3=g}$[%]				$P_{1=q}$[%]			
	Rall	**R1**	**R2**	**R3**	**Rall**	**R1**	**R2**	**R3**
0.001	82.1	72.3	87.6	93.9	98.0	97.5	98.6	97.6
0.00316	76.2	63.4	83.0	89.5	97.5	97.2	98.3	96.2
0.01	71.0	59.3	79.4	84.4	95.3	94.8	97.2	94.2
0.0316	65.3	57.6	77.9	78.9	91.9	91.2	95.3	91.9
0.1	57.7	55.5	84.6	82.2	86.1	85.5	97.9	92.4

3.5 $\langle \Delta\phi \rangle$ for Events with General Kinematics

The observable $\langle \Delta\phi(\mathbf{L1}) \rangle$ chosen to study the string effect has still to be applied to Monte Carlo events with general kinematics.

For TRISTAR Y120 events, as they were studied in the previous chapter, the flavor dependence of $\langle \Delta\phi(\mathbf{L1}) \rangle$ was found to be small (20% difference between d and b events; see table 1 in section 2.9) compared to that of the momentum flow asymmetry. In figure 3.6, one can see that this also holds for jet 1 in events from **R3** for values of y_{cut} around the central value of 0.01. For jet 2, the difference in $\langle \Delta\phi(\mathbf{L1}) \rangle$ between flavors d and b is a little larger.

For the Monte Carlo events with general kinematics, the hadron jets are matched to the parton jets via minimum angle starting with the most energetic jet (for the third jet, large matching angles may occur). No cut on the maximum of the matching angles is performed.

Figure 3.7 shows that $\langle \Delta\phi(\mathbf{L1}) \rangle$ with respect to the parton jet axis is very close to zero. Thus, the leading particle **L1** closely approximates the parton jet direction also in configurations with general kinematics.

At least in **R3**, the values of $\langle \Delta\phi(\mathbf{L1}) \rangle$ are approximately the same (with reversed sign) for jet 1 and jet 2.

When comparing $\langle \Delta\phi(\mathbf{L1}) \rangle$, $\langle \Delta\phi(\mathbf{L2}) \rangle$ and $\langle \Delta\phi(\mathbf{L3}) \rangle$ with the angle $\langle \phi_{parton\ jet} - \phi_{hadron\ jet} \rangle$ in the case of Y120 events, $\langle \Delta\phi(\mathbf{L3}) \rangle$ still seemed to be a good approximation with the advantage of having a distribution with smaller RMS (closer resembling the RMS of the $\phi_{parton\ jet} - \phi_{hadron\ jet}$ distribution).

In figure 3.8 one can see that for general kinematics, $\langle \Delta\phi(\mathbf{L1}) \rangle$ gives the best approximation to the angle shift between parton and hadron jet, thus justifying its choice as an observable for the string effect.

After having prepared the ground with Monte Carlo model studies, the next chapter will deal with the actual measurement of the string effect using the observable $\langle \Delta\phi(\mathbf{L1}) \rangle$ on ALEPH data from 1992 and 1993.

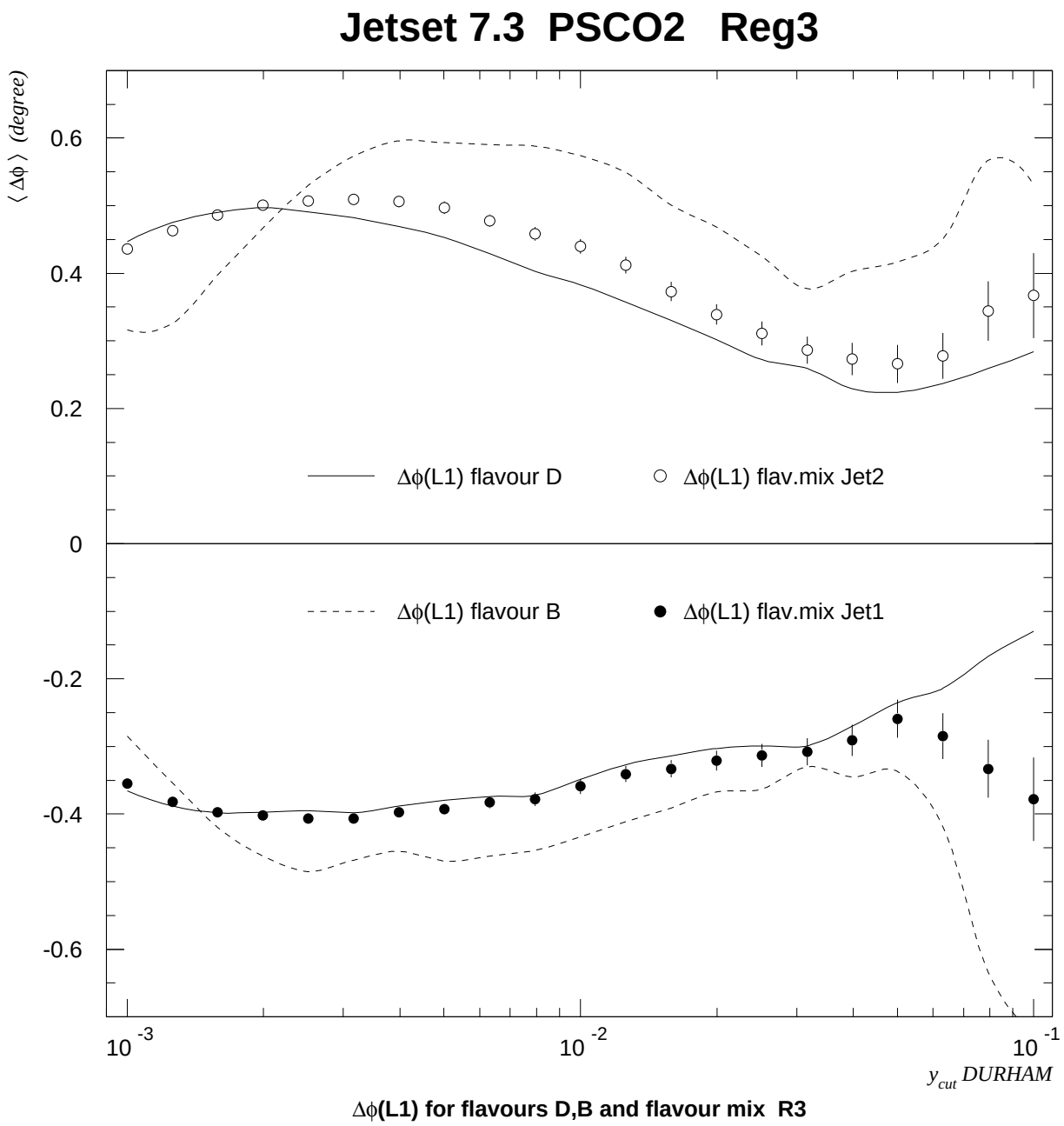

Figure 3.6: Flavour dependence of $\langle \Delta\phi(\mathbf{L1}) \rangle$ in $\mathbf{R3}$ for logarithmically spaced y_{cut} values.

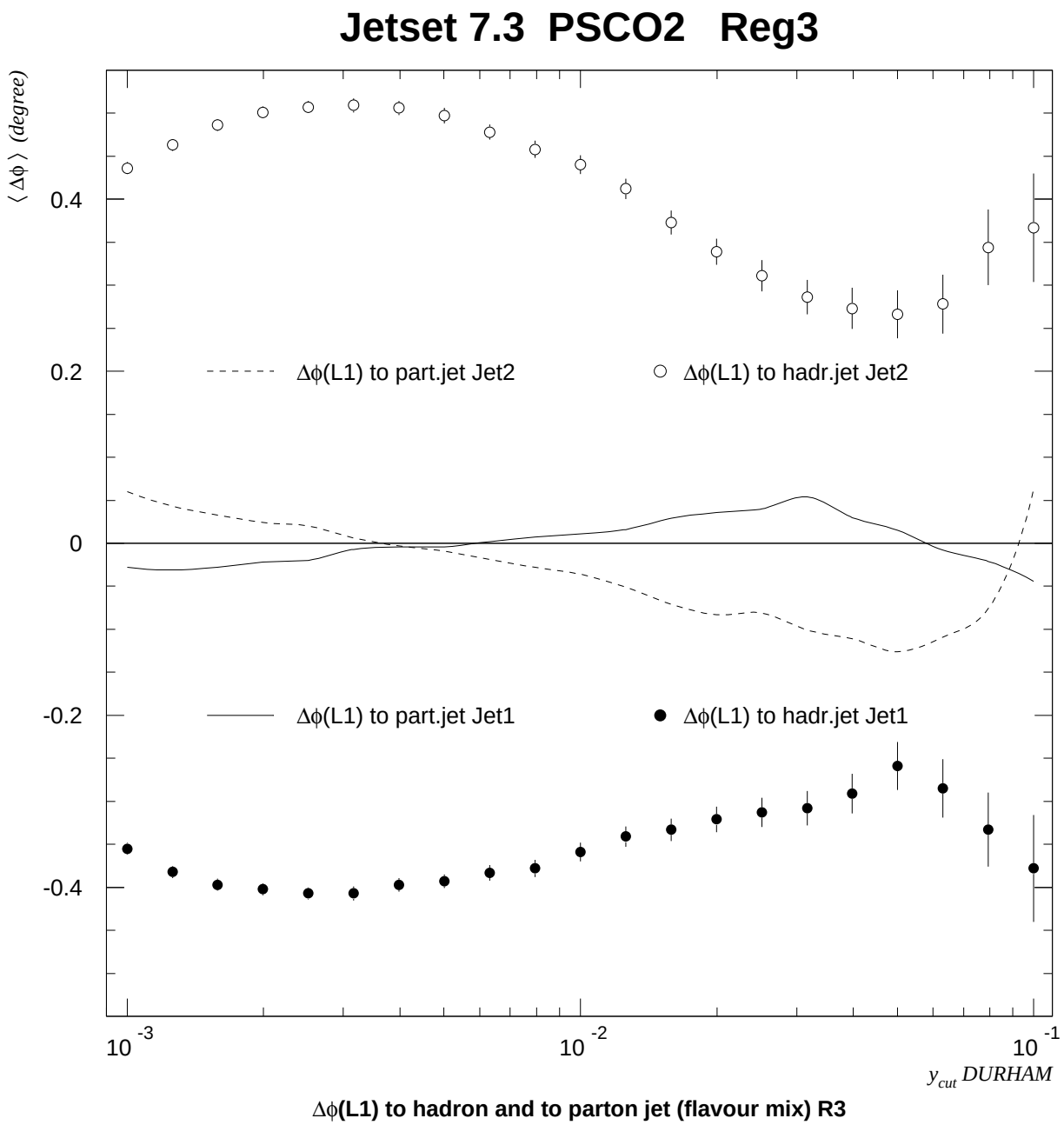

Figure 3.7: $\langle \Delta\phi(\mathbf{L1}) \rangle$ to parton and hadron jet in **R3** for logarithmically spaced y_{cut} values.

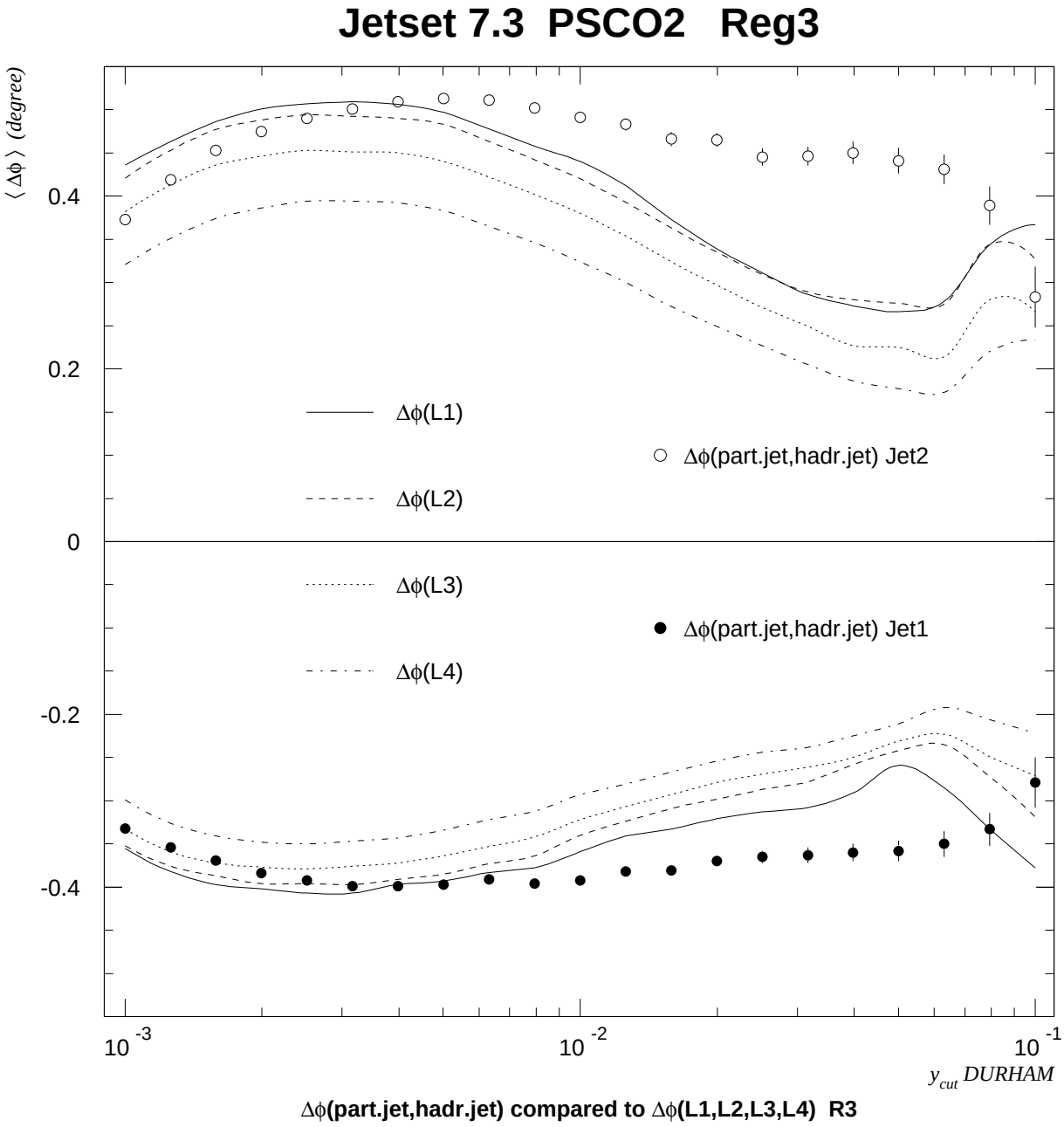

Figure 3.8: Comparison of $\langle\Delta\phi(\mathbf{L1})\rangle$, $\langle\Delta\phi(\mathbf{L2})\rangle$, $\langle\Delta\phi(\mathbf{L3})\rangle$ and $\langle\Delta\phi(\mathbf{L4})\rangle$ with $\langle\phi_{parton\ jet} - \phi_{hadron\ jet}\rangle$ for logarithmically spaced y_{cut} values.

Chapter 4

String Effect Measurement on ALEPH Data

4.1 Synopsis

A measurement of the string effect using the angle shift observable $\langle \Delta\phi(\mathbf{L1}) \rangle$ shall be made in this chapter. From the data sample of multihadronic Z^0 decays obtained by the ALEPH experiment (728421 events from 1992 and 650509 events from 1993), 3-jet events are selected for a range of 21 DURHAM y_{cut} values logarithmically spaced between 0.001 on the lower end and 0.1 on the upper end. Studying the string effect for different values of y_{cut} is interesting, since the kinematic configurations recognized as 3-jet events differ greatly for the extremal y_{cut} values used. In the soft limit, 3-jet configurations with low energetic third jet are prefered by the cluster algorithm, whereas in the hard y_{cut} region, events with very articulate 3-jet structure (having high energy third jets) are selected. It is found that the ability of parton shower Monte Carlo simulations to describe the distribution of kinematic configurations is not perfect; especially the region with $z \approx 0$ (which is densely populated on the Dalitz plot for harder y_{cuts}) is troublesome.

Events with 3-jet structure, which show one isolated high energy gamma particle (recognized as a jet on its own by the cluster algorithm) coming from final state photon radiation, are excluded from the analysis; the angle shift is studied separately for these $q\overline{q}\gamma$ events, displaying the opposite effect in full agreement with the conception of the string fragmentation process.

Using Monte Carlo methods, the measured values of $\langle \Delta\phi(\mathbf{L1}) \rangle$ for jet 1 and jet 2, separated in the kinematic regions **R1**, **R2** and **R3**, are corrected for effects of geometrical acceptance, detector efficiency and resolution, decays, secondary interactions and initial state photon radiation.

An estimate for the systematic error due to inefficiencies in the detector simulation is made by comparing the results of the standard measurement with those obtained under variation of some important cuts. Here, the cut on the energy of the neutral or the charged particles (particle specific cuts) or on the minimum angle between the jet axes and the beam direction (event specific cut) is varied.

The model bias error, which arises because the fully reconstructed Monte Carlo events (which are used to estimate the detector efficiency) are generated with one specific event generator only, is estimated using 7 Monte Carlo models, on which a simplified detector

simulation (SDS) is applied to approximate the effects of the real full featured detector simulation.

The statistical significance, ie. the deviation from the zero-hypothesis (here represented by the model MEIF; see section 5.2) in units of the statistical error, is presented for the angle shift observables $\langle \Delta\phi(\mathbf{L1}) \rangle$ and $\langle \Delta\phi(\mathbf{L3}) \rangle$ and a comparison is made with the results for the statistical significance of the standard string effect observable R_{string}. The angle shift variable $\Delta\phi(\mathbf{L1})$ is calculated once per event, whereas R_{string} is based on single particle counting. As expected, the significance of the former variable is smaller.

4.2 Event Selection

The data measured in the ALEPH detector is stored in electronic form on so-called data summary tapes (DST). Physics analysis is mainly done on a special form of DSTs, the miniDSTs, which only contain essential information (4-momenta, charges, dE/dx etc) of the measured particles. The extraction of special information from the miniDSTs, ie. the actual analysis or measurement, is made using the ALPHA program (ALEPH Physics Analysis, see [7]) and histogramming routines from the CERN program library (see [10]). The postprocessing and visualization of measurement results in histogram form are made with the PAW (Physics Analysis Workstation) program (see [11]). An overview over the highly complicated software systems for offline data analysis for the ALEPH experiment can be found in reference [12].

The data events on the miniDSTs are pre-classified in so-called EDIR (Event Directory) files.

In this analysis, only events that have been classified as belonging to EDIR selection class 16 are used for further analysis.

Class 16 selects events which are candidates for multihadronic Z^0 decays based on information from the TPC. The criteria used for class 16 selection are:

- A minimum of 5 charged tracks in the TPC with $|d_0| < 2$ cm and $|z_0| < 10$ cm (d_0 is the distance of closest approach of a fitted track to the vertex in the plane perpendicular to the beam; z_0 is the z distance at this point from the vertex). Each of these tracks must have at least 4 hits (N_{TPC}) in the TPC and $|\cos\theta| < 0.95$ with respect to the beam axis.

- The energy sum of all charged tracks (fulfilling the above cuts) has to be in excess of 10% of E_{cm} (91.2 GeV).

The cuts on d_0 and z_0 are used to select only particles from the primary interaction vertex and to exclude spiralling tracks and particles that suffered great energy loss due to interactions with the inner detector structure. The cuts on N_{TPC} and on $|\cos\theta|$ ensure good momentum measurement.

The information on the particles in an event is organized into so-called *sections* on the miniDST. Here, the EFLW (Energy Flow) section will be used. Its objects are the charged and neutral particles that have been measured in any of the subdetectors of ALEPH. The information from the TPC and from the calorimeters is matched and unified, thus avoiding the double-counting of particles that left a track in the TPC and

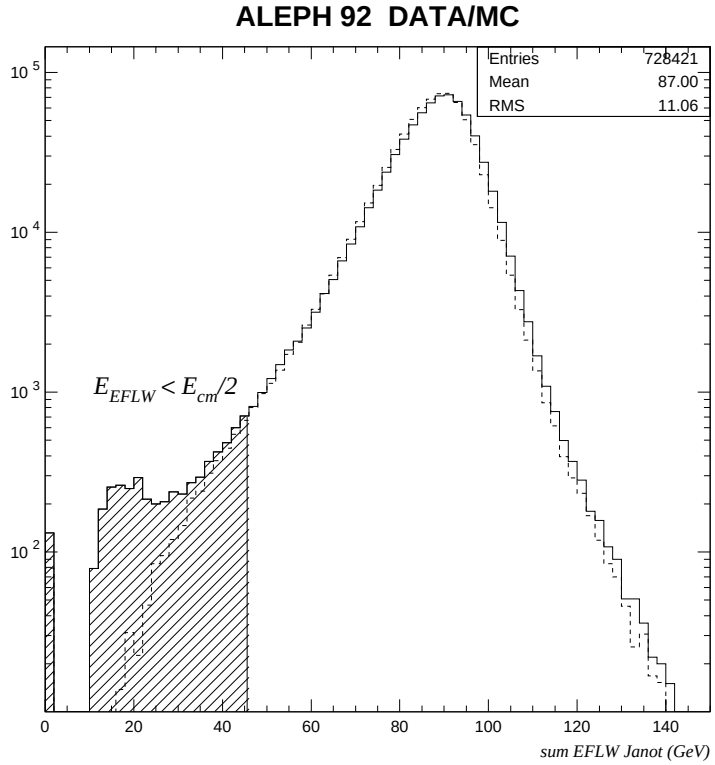

Figure 4.1: Energy flow sum for the ALEPH 1992 data. The area which is affected by the $\sum E_{\mathrm{EFLW}} > E_{cm}/2$ cut against the 2γ background is hatched. The energy flow sum for the fully reconstructed Monte Carlo events is superimposed as a dashed line.

deposited energy in the calorimeters (see reference [5] for a detailed account of the EFLW algorithm).

The EFLW objects are classified in the following categories:

- EFLW type 0: charged track.
- EFLW type 1: electron.
- EFLW type 2: muon.
- EFLW type 3: charged track from V0.
- EFLW type 4: electromagnetic (ie. gamma).
- EFLW type 5: neutral residual (ie. hadron)

In the following, EFLW objects with types ≤ 3 will be used as charged tracks for the analysis, such with type 4 as gammas and those with type 5 as neutral hadrons. It must be noted that a clear division between types 4 and 5 can not be made; the neutral EFLW objects should rather be considered together (see section 4.8.2, figure 4.24).

Based on the EFLW objects, further selection cuts are made on the events:

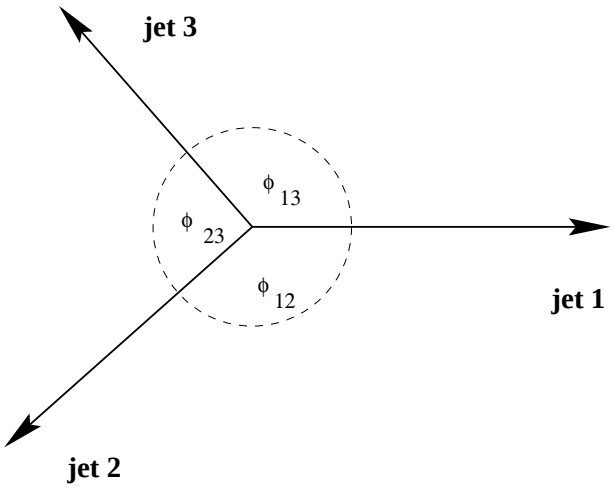

Figure 4.2: 3-jet event. The arrows represent the jet momentum vectors. The angles between the jets are indicated.

- Events containing a charged track with an energy $E > E_{cm}$ are discarded. Due to the errors in the momentum measurement for the very high energy charged particles in the TPC, a few cases occur where energies as high as 365 GeV are assigned to charged particles. Since the mere removal of the track would leave the event hopelessly unbalanced, the whole event is discarded.

- The EFLW energy sum $\sum_i E_i$ is required to be larger than $E_{cm}/2$. This cut is made in order to reduce the 2γ background (see figure 4.1 for the distribution of the energy sum and the fraction of events lost due to this cut). 2γ events come from the reaction $\gamma\gamma \to q\overline{q} \to$ hadrons, where the γ's are virtual photons from the electromagnetic field of the electrons and positrons circulating in the collider.

- The angle θ_{thrust} of the thrust axis with respect to the beam axis has to be larger than 30°. The thrust axis $\vec{v}_t$ is defined as the vector $\vec{n}$ for which the quantity thrust T is maximal:
$$T := \max_{|\vec{n}|=1} \frac{\sum_i |\vec{n} \cdot \vec{p}_i|}{\sum_i |\vec{p}_i|}$$
where i indexes all EFLW particles. If the thrust axis is found to lie closer than 20° to the beam axis, the total EFLW energy sum is strongly reduced due to the loss of particles in the insensitive region around the beam pipe.

From the events passing these cuts, 3-jets are selected using the DURHAM algorithm (see section 3.2) for 21 logarithmically spaced y_{cut} values ranging from 0.001 to 0.1. In section 4.5, the jet rates for these y_{cut} values are shown.

As one can see from figure 4.1, the visible energy can vary to a large extent for hadronic events. This is due to detector inefficiencies, energy resolution and to weak decays causing missing energy by the production of neutrinos.

A common event plane is defined in such a way, that the least energetic jet is contained in it; it is the plane perpendicular to the vector $\vec{n}$ defined by
$$\vec{n}_1 := \vec{p}_1 \times \vec{p}_3, \quad \vec{n}_2 := \vec{p}_3 \times \vec{p}_2, \quad \vec{n} := \frac{\vec{n}_1 + \vec{n}_2}{|\vec{n}_1 + \vec{n}_2|}$$

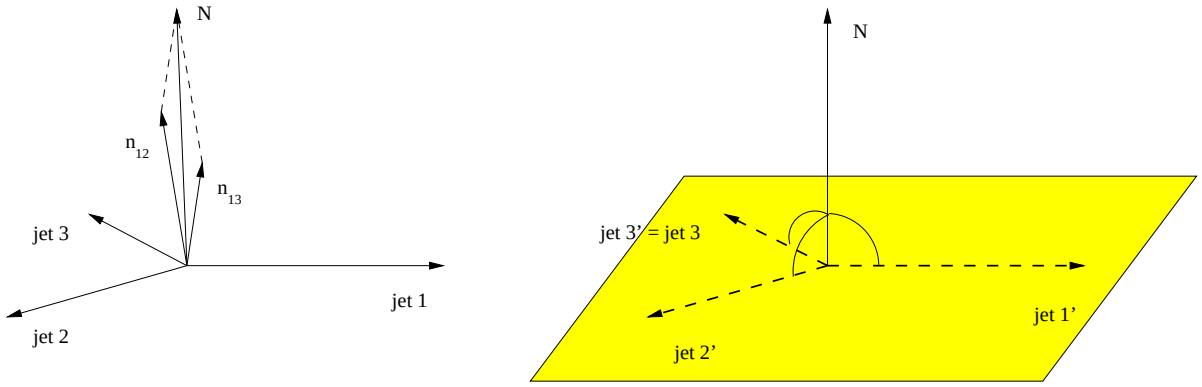

Figure 4.3: Construction of a common event plane for non-coplanar 3-jet events (caused by detector inefficiencies and missing energy).

where $\vec{p_i}$ are the jet momentum vectors ordered according to their visible energy (see figure 4.3 for the construction of the event plane). All azimuthal angles are measured in this event plane and the jet vectors are projected.

The angular resolution of the ALEPH detector is much better than the energy resolution. This fact can be utilized by reconstructing the jet energies from the angles between the jet axes (projected into the event plane) with the following relations (see also figure 4.2):

$$E_{i,rec} := E_{cm} \frac{\sin \phi_{jk}}{\sin \phi_{12} + \sin \phi_{23} + \sin \phi_{13}} \qquad (i,j,k \quad \text{cyclic}).$$

It can be easily shown using energy and momentum conservation, that these relations hold for 3-jet configurations with massless jets. It has been shown that including the measured jet masses does not significantly improve the energy resolution.

The energy ordering of the three jets will be with respect to these reconstructed energies.

As an extra quality cut to ensure that the events are "well contained" within the detector, all 3 jets are required to have measured jet axes not too close to the beam axis (see figure 4.4):

$$\theta_{jet,beam_i} > 30^\circ.$$

Events not fulfilling this condition will be discarded. See figure 4.6 for the distribution of $\theta_{jet,beam_i}$ and $\min(\theta_{jet,beam_i})$ in **R3**.

This cut will, amongst others, be varied to estimate the systematic error (section 4.8.2, figure 4.6).

Events which are unbalanced (see figure 4.5 for an example of an unbalanced event) will also be discarded, since they can not be dealt with in the coordinate system used which assumes balanced events (see figure 2.12) with the third jet oriented towards positive azimuthal angles.

Events with hard final state photon radiation ($q\overline{q}\gamma$ events) are also excluded from the standard angle shift analysis. The selection criterion for $q\overline{q}\gamma$ events is the following: one of the 3 jets must contain a photon (EFLW type 4) which has more than 85% of the jet's energy, ie. $x_\gamma > 0.85$. This cut performs very well in identifying $q\overline{q}\gamma$ events (see figure 4.10).

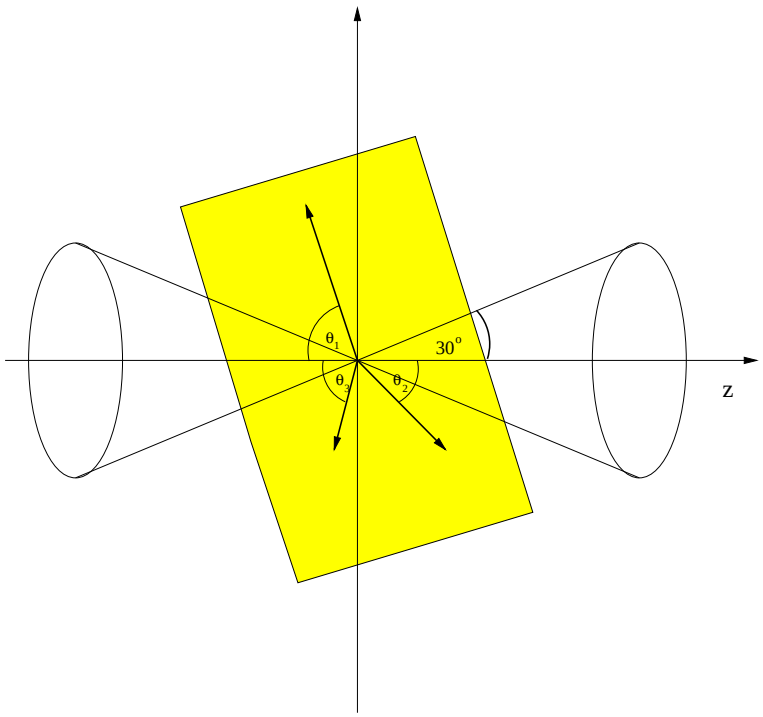

Figure 4.4: As an extra quality cut, the jet axes are required not to lie within a cone of 30° opening angle around the beam axis. This ensures that the event is well contained within the detectors fiducial volume.

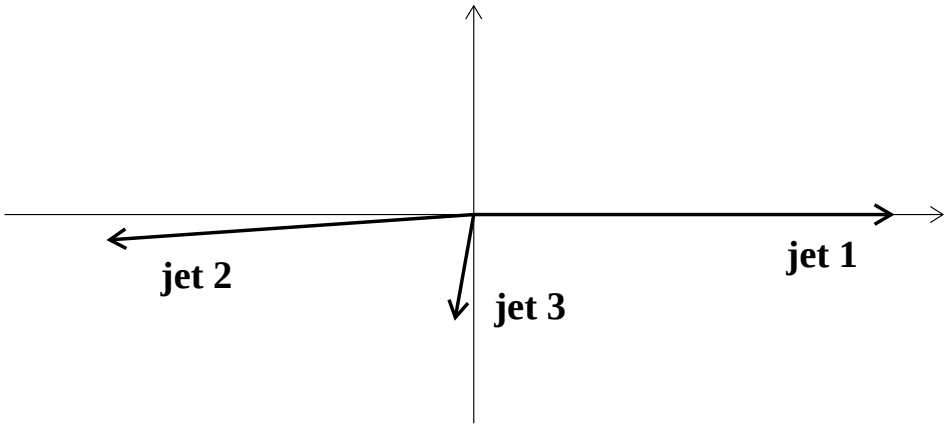

Figure 4.5: Example of an unbalanced jet configuration.

The remaining $q\overline{q}g$ events are classified according to their kinematics (Dalitz plot and regions 1,2 and 3).

The $\langle\Delta\phi(\mathbf{L1})\rangle$ angle shift analysis is only performed for jets containing 3 or more particles — there has to be a remaining jet vector to which the angle shift of the leading particle **L1** can be measured.

The number of events from 1992 and 1993 ALEPH data samples retained at the different stages of the event selection process are given in the next tables for the low, the central and the high value of the y_{cut} range chosen. For the purpose of performing the corrections, the ALEPH collaboration uses fully simulated Monte Carlo events generated with a special version of JETSET 7.3 ("HVFL")[1] and processed through the detector simulation program GALEPH and the event reconstruction JULIA.

For both data and fully reconstructed Monte Carlo, the complete statistics available for 1992 and 1993 has been used.

Note that events which contain a charged particle with a momentum in excess of 91 GeV are excluded from the analysis.

The number of events in the 3 kinematic regions is the number of events with more than 2 particles in the most energetic jet (only jets with more than 2 particles are used in the $\Delta\phi$ analysis) in that region.

ALEPH 1992	$y_{cut} = 0.001$		$y_{cut} = 0.01$		$y_{cut} = 0.1$	
requirement	DATA	GALEPH	DATA	GALEPH	DATA	GALEPH
CLAS 16 events	728421	1854562	728421	1854562	728421	1854562
all $\|p_i\| < 91$ GeV	728397	1854483	728397	1854483	728397	1854483
used for EFLW analysis	612184	1565832	612184	1565832	612184	1565832
3jets DURHAM	162179	419339	186743	508251	29661	83302
$\min(\theta_{jet,beam_i}) > 30^\circ$	146291	378254	152113	412091	22078	61885
unbalanced events rejected	1156	2765	196	424	8	7
$q\overline{q}\gamma$ events rejected	1174	2598	1102	2321	176	393
selected $q\overline{q}g$ 3jets	143959	372887	150815	409343	21894	61485
in region **R1**	51562	139168	69461	193775	19342	53998
in region **R2**	75508	193202	45921	122159	225	633
in region **R3**	16825	40335	35399	93296	2322	6827
energy sum [GeV]						
$\langle$sum EFLW$\rangle$, CLAS 16	87.004	86.570	87.004	86.570	87.004	86.570
$\langle$sum EFLW$\rangle$, 3-jets	89.637	88.875	88.402	87.977	87.905	87.571

[1]The HVFL03 generator is used for the generation of fully reconstructed events together with a simulation of the 1992 setup of the ALEPH detector. For the 1993 setup, HVFL04 is used which is also based on JETSET 7.3 but with different parameters.

ALEPH 1993	$y_{cut} = 0.001$		$y_{cut} = 0.01$		$y_{cut} = 0.1$	
requirement	DATA	GALEPH	DATA	GALEPH	DATA	GALEPH
CLAS 16 events	690509	1870602	690509	1870602	690509	1870602
all $\|p_i\| < 91\,\mathrm{GeV}$	690490	1870531	690490	1870531	690490	1870531
used for EFLW analysis	579465	1577766	579465	1577766	579465	1577766
3jets DURHAM	152306	427485	177416	515360	28069	84409
$\min(\theta_{jet,beam_i}) > 30°$	137027	384829	144473	418295	20821	62777
unbalanced events rejected	1201	2528	169	398	5	9
$q\overline{q}\gamma$ events rejected	1144	2612	1056	2429	182	425
selected $q\overline{q}g$ 3jets	134680	379686	143246	415465	20634	62343
in region **R1**	47409	142300	65630	197092	18109	54928
in region **R2**	71333	195364	43814	123620	224	615
in region **R3**	15869	41882	33759	94632	2285	6769
energy sum [GeV]						
$\langle$sum EFLW$\rangle$, CLAS 16	87.143	86.987	87.143	86.987	87.143	86.987
$\langle$sum EFLW$\rangle$, 3-jets	89.977	89.304	88.726	88.443	88.178	88.008

4.3 Angular Resolution of the ALEPH Detector

In the previous section, the reconstruction of jet energies via the kinematics of the 3-jet event was described. For this scheme to work successfully, a good angular resolution for the jet axes is of preeminent importance.

It is also important to know the accuracy of a single measurement of the angle shift of the leading particle $\Delta\phi(\mathbf{L1})$.

Due to statistics, the mean value of the $\Delta\phi(\mathbf{L1})$ distribution, which is the actual observable, has a much lower error as the one for a single measurement.

The smearing effect of the detector on $\Delta\phi(\mathbf{L1})$ can be described as the convolution of the $\Delta\phi$ distribution on the Monte Carlo truth level (MCT; ie. the event as it is generated by HVFL with no simulation of detector effects) with a gaussian detector response function with a width σ which gives the mean statistical error of a single measurement. The result of this convolution is the $\Delta\phi$ distribution as it is observed on the reconstructed level (eg. using EFWL objects).

To calculate the width σ of the gaussian from the distributions of $\Delta\phi(\mathbf{L1})$ on the reconstructed and on the MCT level, a deconvolution of $\Delta\phi(\mathbf{L1})$ could be made.

If one instead starts with the naïve assumption that the $\Delta\phi$ distributions are gaussians (which they are not, having non-gaussian tails; see eg. figure 4.37), one can calculate the width of the detector smearing function (ie. the angular resolution) via quadratic addition of the errors (ie. the RMS values of the $\Delta\phi$ distributions on the reconstructed and on

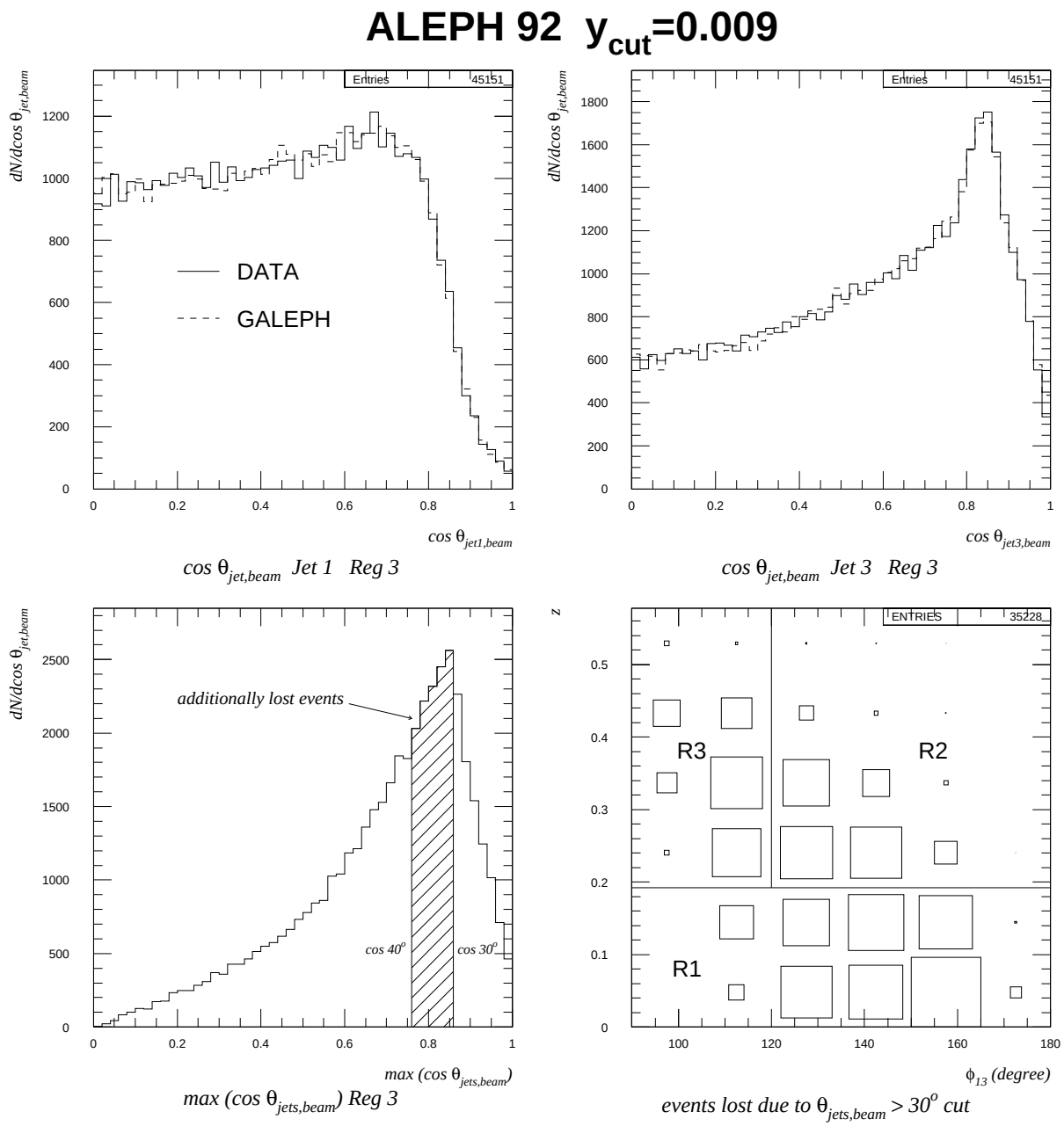

Figure 4.6: Distribution of $\cos\theta_{jet,beam_i}$. The region of events that are additionally lost when enforcing a harder cut on $\min\theta_{jet,beam_i}$ is shaded. The distribution over the Dalitz plot of the events which are discarded due to the $\theta_{jet,beam_i}$ cut is shown.

the MCT level):

$$\sigma_{ang\ res} = \sqrt{\sigma^2_{MC\ rec} - \sigma^2_{MC\ truth}}$$

where $\sigma_{MC\ rec}$ gives the RMS of the $\Delta\phi(\mathbf{L1})$ distribution as measured on the reconstructed level for fully simulated Monte Carlo events and $\sigma_{MC\ truth}$ denotes the RMS as it is found for the Monte Carlo truth level.

With values of $\sigma_{MC\ rec} = 4.46°$ (derived from $\approx 1.9 \cdot 10^6$ fully reconstructed 1992 Monte Carlo events) and $\sigma_{MC\ truth} = 4.24°$ (based on $3 \cdot 10^6$ HVFL03 events), one finds

$$\sigma_{ang\ res} = 1.38°$$

for jet 1 in **R3**.

Another way to study the angular resolution is to use the information on the matching between reconstructed objects and MCT objects (only available for charged tracks).

ALPHA defines two variables for every object `ITK` from the charged track section:

- `KNMTCH(ITK)` gives the number of matching candidates for charged track `ITK` in the MCT section.
- `KSMTCH(ITK,I)` gives the number of shared hits between charged track `ITK` and MCT object `I`.

`KSMTCH` is a measure for the goodness of the matching (see figure 4.7); for a successful matching, a minimum of 5 shared hits will be required.

The 3-dimensional matching angle

$$\alpha_{match} = \arccos \frac{\vec{p}_{rec} \cdot \vec{p}_{MCT}}{|\vec{p}_{rec}|\ |\vec{p}_{MCT}|}$$

is strongly dependent on the momentum of the particle; low energy particles easily suffer large deflection due to multiple scattering, whereas for high energy particles, the spread of α_{match} is small:

p [GeV]	mean	RMS
$0.0 \le p < 0.5$	3.163°	15.702°
$0.5 \le p < 1.0$	0.843°	2.365°
$1.0 \le p < 2.5$	0.461°	1.253°
$2.5 \le p < 5.0$	0.244°	0.668°
$5.0 \le p < 10.0$	0.144°	0.389°
$10.0 \le p$	0.088°	0.483°

For high energy charged particles, the angular resolution is obviously very good.

But the angular resolution for the actual observable $\langle\Delta\phi(\mathbf{L1})\rangle$ has still to be studied. Eventhough the leading particle **L1** in a jet will always have high momentum (see figure 4.20) and its direction will therefore be measured will high accuracy, the resolution for $\Delta\phi(\mathbf{L1})$ will strongly depend on the accuracy of the measurement of the jet direction (the jet axis is computed as the sum of the momenta of the particles assigned to the jet, of which many have low momenta or may escape the measurement).

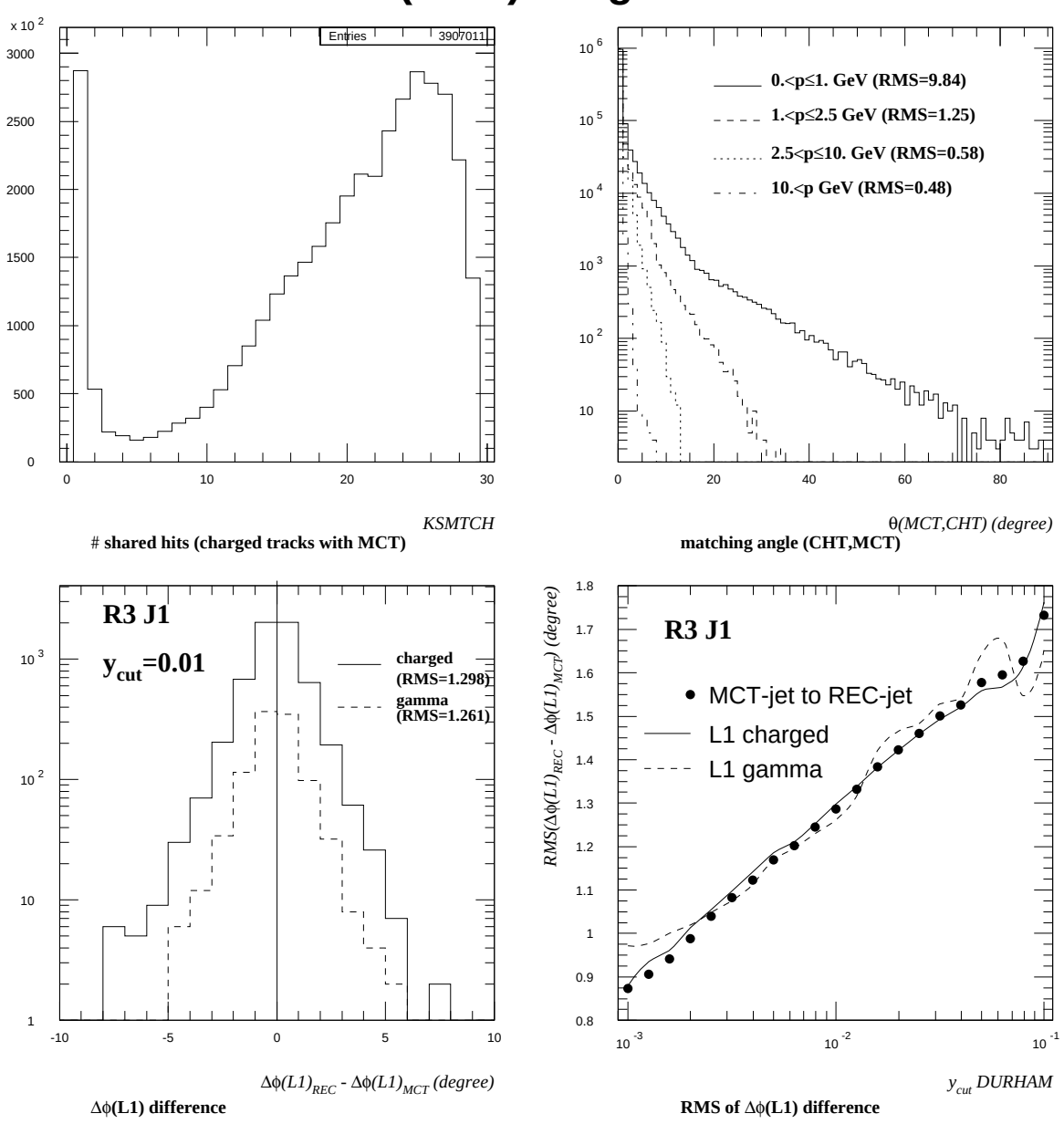

Figure 4.7: Angular resolution of the ALEPH detector. The number of shared hits between matched objects from the EFLW and from the MC truth section is shown. The 3-dimensional matching angle between EFLW and MCT objects depends on their energy. The distribution of the differences between $\Delta\phi(\mathbf{L1})$ on the MCT and reconstructed level for charged particles (TPC information) and photons (ECAL information) is shown. The RMS of the azimuthal angle difference between the jets defined using EFLW objects and MCT objects (which are assigned to each other via minimum angle matching) increases for harder y_{cut}; the RMS of the $\Delta\phi(\mathbf{L1})$ difference (for charged particles and gammas) is of the same size.

Since a considerable part of the **L1** particles are photons, the angular resolution of the ECAL must also be studied. An algorithm for matching EFLW type 4 objects (photons) to the MCT objects has not yet been build into ALPHA; thus a straightforward procedure to do this was designed for this task.

For every EFLW object of type 4, a comparison of its energy $E_{\gamma\,\mathrm{EFLW}}$ and its direction is made with all photons from the MCT section.

For a successful matching, a 3-dimensional angle between the momenta

$$\Delta\alpha < 5^\circ$$

and a difference in energy

$$\Delta E < 3(0.18\sqrt{E_{\gamma\,\mathrm{EFLW}}} + 0.009 E_{\gamma\,\mathrm{EFLW}})$$

corresponding to 3σ of the energy resolution of the ECAL (as given in [5]) is required. If more than one MCT photon fulfils the above requirements, the one with the smallest $\Delta\alpha$ is used.

The distribution of the differences of the azimuthal angle shift $\Delta\phi(\mathbf{L1})$

$$\Delta\left(\Delta\phi(\mathbf{L1})\right)_{match} = \Delta\phi(\mathbf{L1})_{rec} - \Delta\phi(\mathbf{L1})_{MCT}$$

for the leading particle **L1** in jet 1 of **R3** 3-jet events (at $y_{cut} = 0.01$) which are matched between Monte Carlo truth level and reconstructed level is shown in figure 4.7, having an RMS of $\sigma(\Delta(\Delta\phi(\mathbf{L1}))_{match}) = 1.30^\circ$ for charged particles and $\sigma(\Delta(\Delta\phi(\mathbf{L1}))_{match}) = 1.26^\circ$ for photons.

The angular resolution for $\Delta\phi(\mathbf{L1})$ for charged particles and photons is of the same size.

The angular resolution for the jet direction itself can be studied with

$$\Delta\phi_{jet,\,match} = \phi_{jet,\,rec} - \phi_{jet,\,MCT},$$

looking at the azimuthal angle difference between the jet axes derived from reconstructed objects and those derived from MCT objects, assigned to each other via minimum angle matching (for this, the common event plane of the reconstructed jet axes is used).

For jet 1 in **R3** 3-jet events at $y_{cut} = 0.01$ one finds $\sigma(\Delta\phi_{jet,\,match}) = 1.29^\circ$ (see also figure 4.7; these results are based on 200000 fully reconstructed Monte Carlo events for the 1993 setup).

The resolution for a single $\Delta\phi(\mathbf{L1})$ measurement is dominated by the resolution for the jet axis. Its value of $\approx 1.3^\circ$ is in good agreement with the naïve estimate obtained by approximating the $\Delta\phi$ distribution as being gaussian.

4.4 $q\overline{q}\gamma$ Events

Amongst the events selected as 3-jets from the data by the DURHAM cluster algorithm (using a central value of $y_{cut} = 0.01$), there are $\approx 0.7\%$ $q\overline{q}\gamma$ events.

An example of such a $q\overline{q}\gamma$ event as it was recorded in the ALEPH detector is shown in figure 4.8. Two hadronic jets are clearly visible and an energy deposition in the ECAL without associated track in the TPC indicating an isolated high energy photon.

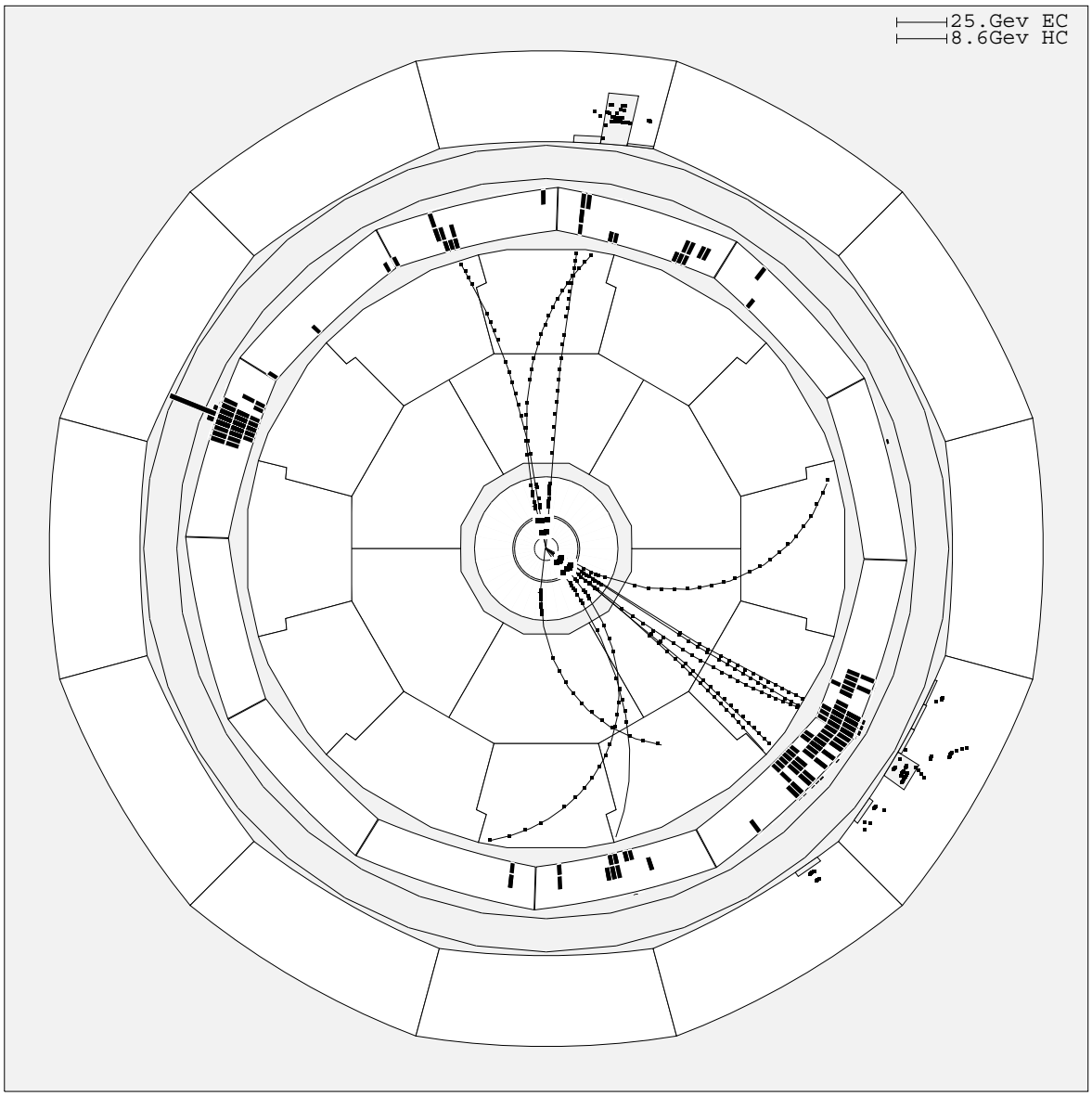

Figure 4.8: Example of a $q\overline{q}\gamma$ event as seen in the ALEPH detector. Two hadron jets and one isolated photon (energy deposition in the ECAL on the left hand side; no matching TPC tracks) are clearly visible. From the energy gauges in the upper right corner one can estimate $E_\gamma \approx 30\,\mathrm{GeV}$.

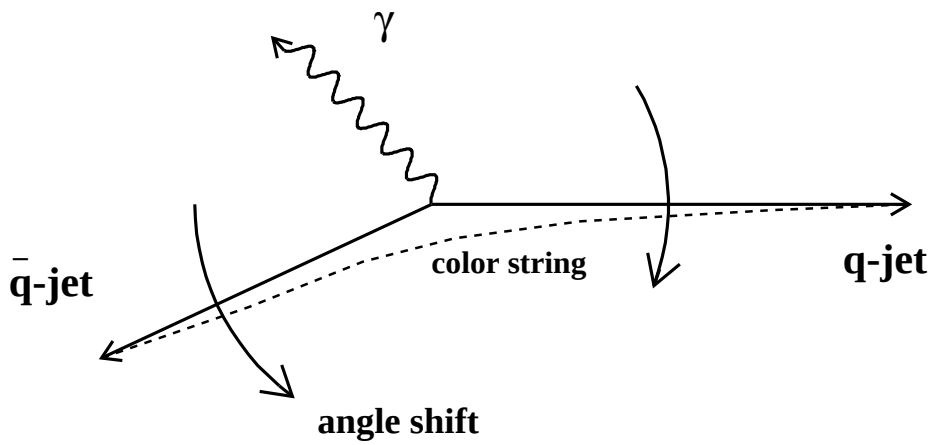

Figure 4.9: $q\overline{q}\gamma$ event according to the string fragmentation model. The color string stretches only between the two quarks, resulting in an angle shift in the opposite direction as in $q\overline{q}g$ events. The γ is pictured as the third jet here, since this is the case for $\approx 65\%$ of the $q\overline{q}\gamma$ events.

Such an isolated photon need not always be recognized as being the only particle in a jet — other (neutral and charged) particles may be assigned to the same cluster jet.

In order to select jets which are actually due to an isolated photon, it is required that the photon be the leading particle in the jet having a fraction larger than 85% of the total visible energy of the jet (see [6]):

$$x_\gamma = E_\gamma / E_{jet,\,vis} \geq 0.85.$$

From figure 4.10, one can see that this cut is effective to suppress the background from cases of jets with high energetic photons coming from other processes than final state bremsstrahlung.

The hard bremsstrahlung photons mainly constitute the least energetic jet (for $\approx 65\%$ of the 3-jet events for central y_{cut} values). In a substantial fraction of events, the photon is the sole particle in the jet, having $x_\gamma = 1$.

These $q\overline{q}\gamma$ events arise from hard electromagnetic bremsstrahlung emitted from one member of a quark antiquark pair produced in a Z^0 decay (FSR; see reference [3]).

In the framework of string fragmentation, a color string is thought to stretch between the quark and the antiquark (see figure 4.9) being the source for particle production in the hadronization process. Since the photon carries no color charge, it is not connected to the quarks with such a color string.

This leads to the assumption, that the hadronization will result in an angle shift from parton jet axes to hadron jet axes in the opposite direction as for the case of $q\overline{q}g$ events (this has also been investigated by the L3 collaboration, see reference [24]).

In figures 4.34, 4.35 and 4.36, the mean values $\langle\Delta\phi\rangle$ for particles with different momenta are shown for regular $q\overline{q}g$ events and for $q\overline{q}\gamma$ events.

The asymptotic (ie. for high particle momenta) behavior of $\langle\Delta\phi\rangle(p)$ is clearly visible to be reversed for $q\overline{q}\gamma$ events, confirming the above assumption. Since there is much less statistics for $q\overline{q}\gamma$ events, the momentum intervals had to be chosen larger for the $\langle\Delta\phi\rangle(p)$ plot.

The $\langle\Delta\phi\rangle$ effect seems to be stronger for $q\overline{q}\gamma$; this is not surprising, because the photon is clearly identified for $q\overline{q}\gamma$ 3-jets, whereas for $q\overline{q}g$ events only the assumption that the third jet is the gluon jet can be made, thus smearing the effect somewhat (eventhough $P_{3=g}$ is high in **R3**). This comes out clearly for harder values of y_{cut}, where kinematic configurations with high energetic third jet are favoured, for which $P_{3=g}$ is smaller.

The reversion of the string effect in $q\overline{q}\gamma$ events can be seen for the whole range of y_{cut} values studied.

The values for $\langle\Delta\phi(\mathbf{L1})\rangle$ obtained for $q\overline{q}\gamma$ events from ALEPH 1992 data are given in the following table, with a comparison to the values obtained from $q\overline{q}g$ events (note that these values are *not* corrected for detector effects etc.; the statistical errors are given):

y_{cut}	jet	$\langle\Delta\phi(\mathbf{L1})\rangle_{q\overline{q}\gamma}$ **R3** [deg]	$\langle\Delta\phi(\mathbf{L1})\rangle_{q\overline{q}g}$ **R3** [deg]
0.001	J1	0.111 ± 0.153	-0.327 ± 0.016
	J2	-0.324 ± 0.175	0.322 ± 0.017
0.003	J1	0.314 ± 0.213	-0.488 ± 0.016
	J2	-0.482 ± 0.212	0.557 ± 0.017
0.009	J1	0.737 ± 0.344	-0.578 ± 0.024
	J2	-1.001 ± 0.368	0.592 ± 0.025
0.030	J1	0.833 ± 0.642	-0.538 ± 0.046
	J2	-1.044 ± 0.591	0.433 ± 0.048

The statistical errors given are of course larger for the $q\overline{q}\gamma$ events due to the much smaller statistics (see section 4.8.2 for the definition of the statistical error on $\langle\Delta\phi(\mathbf{L1})\rangle$).

For all values of y_{cut}, $\langle\Delta\phi(\mathbf{L1})\rangle$ shows the opposite effect for $q\overline{q}\gamma$ as for $q\overline{q}g$ events; for harder y_{cut} values, the $\langle\Delta\phi(\mathbf{L1})\rangle$ effect gets stronger for $q\overline{q}\gamma$ events, whereas for $q\overline{q}g$ events, $\langle\Delta\phi(\mathbf{L1})\rangle$ decreases after showing maximum effect for the central y_{cut} values. But it has to be noted that the statistical errors for the $q\overline{q}\gamma$ events are too large to make definite statements.

4.5 Jet Rates and Dalitz Plot Studies

For the range of y_{cut} values considered here, the jet rates vary by a large extent. For soft y_{cut}, the higher multijet rates (4-jet, 5-jet, etc.) are large, whereas for harder y_{cut}, the 2-jet rate is predominant with only a small 3-jet fraction (see figure 4.11).

The 3-jet rate, which is of importance in the study of the string effect, reaches its maximum for $y_{cut} \approx 0.003$.

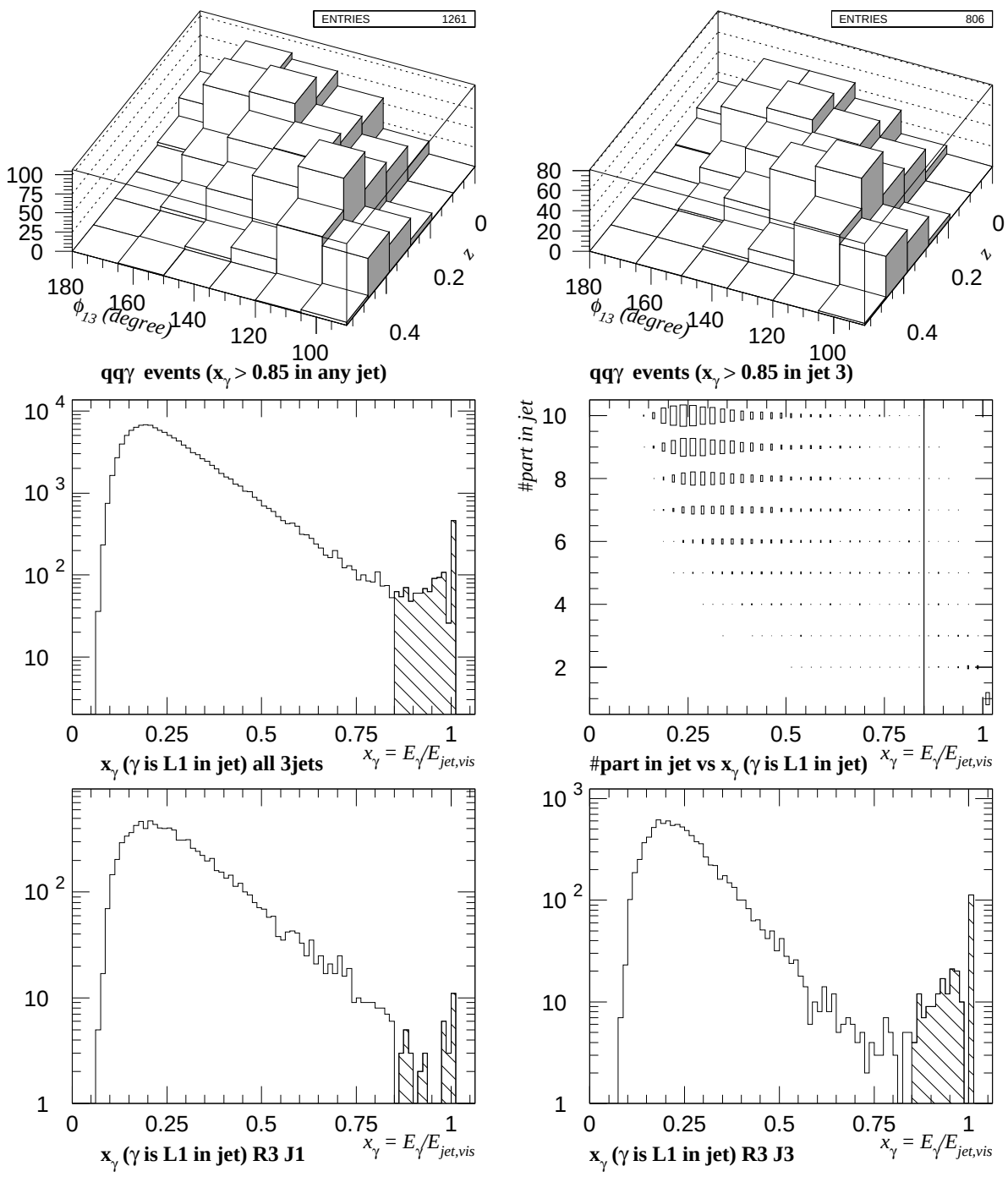

Figure 4.10: The distribution of $q\overline{q}\gamma$ events over the Dalitz plot is shown for the cases where any one jet in a 3-jet event is identified as an FSR photon and for the case where this photon is the least energetic jet. The distributions of $x_\gamma = E_\gamma/E_{jet,\,vis}$ for the photon (being the leading particle in its jet) are shown and the $x_\gamma > 0.85$ cut is indicated. Photons with $x_\gamma > 0.85$ are often isolated particles constituting a jet on their own.

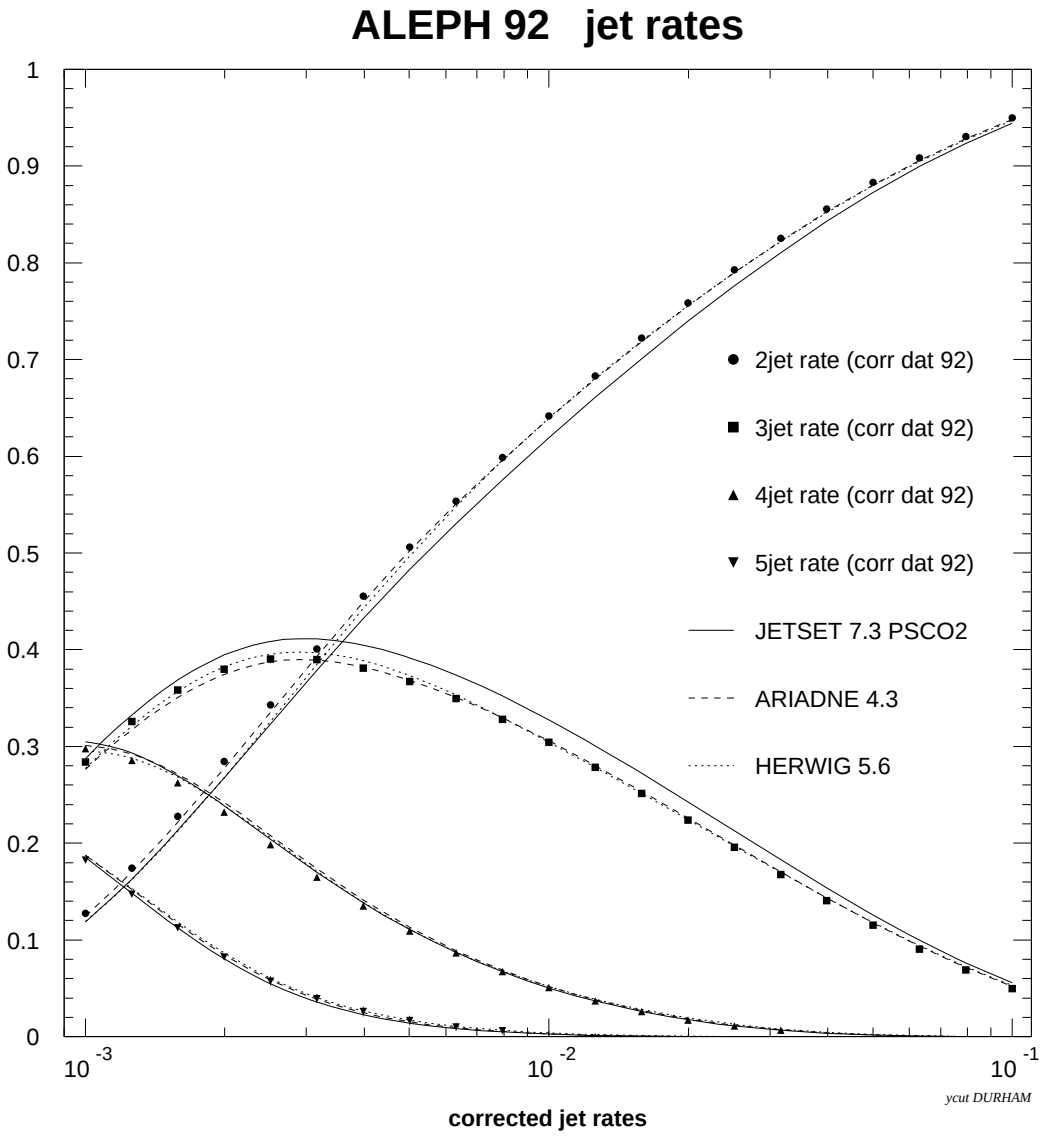

Figure 4.11: Corrected jet rates derived from ALEPH 1992 data. For hard y_{cut}, the 2-jet rate is dominant, whereas for soft y_{cut}, a large fraction of 4-jet and 5-jet events are found. The 3-jet rate peaks for $y_{cut} \approx 0.003$. For the standard value of the DURHAM cut-off $y_{cut} = 0.01$, the 3-jet rate is $\approx 30\%$. The predictions of the most important QCD models are superimposed. JETSET fails to describe the 2-jet and 3-jet rates observed on the data, while HERWIG and ARIADNE are in good agreement.

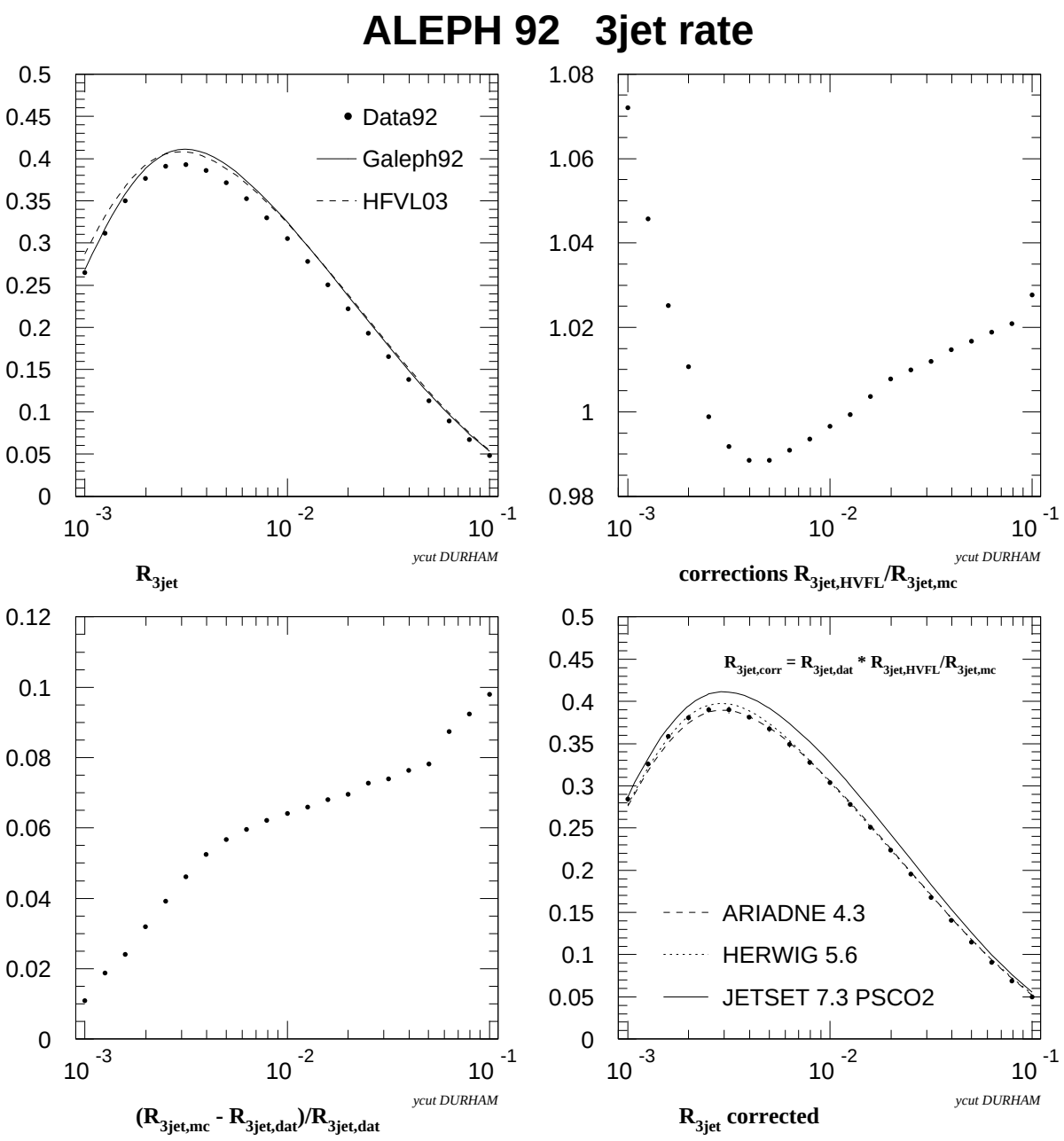

Figure 4.12: 3-jet rate for ALEPH 1992. The discrepancy between data and MC can be seen, reaching 10% for hard y_{cut}. The corrected 3-jet rates are also given with the predictions of the most important QCD models superimposed.

A problem for any analysis focussing on 3-jet events is the fact, that the 3-jet rate observed in the ALEPH data is not accurately reproduced by the Monte Carlo simulations (both on the plain event generator level and on the fully reconstructed level with detector simulation). This can be seen in figure 4.12.

The correction of the 3-jet rate against detector effects etc. is made in the following way (see section 4.7 for more details on the ideas behind the correction of data):

$$R_{3-jet}^{\text{corr}} := \frac{R_{3-jet}^{\text{had lev}}}{R_{3-jet}^{\text{rec lev}}} \, R_{3-jet}^{\text{raw DATA}}.$$

The multiplicative corrections $R_{3-jet}^{\text{had lev}}/R_{3-jet}^{\text{rec lev}}$ calculated from the Monte Carlo are also shown in figure 4.12.

The systematic error on R_{3-jet}^{corr} is estimated through a variation of some important cuts (only the particle specific cuts $E_{neutral} > 0.8\,\text{GeV}$ and $E_{charged} > 0.4\,\text{GeV}$ are used; the event specific cut on $\theta_{jet,beam_i}$ is useless in this context).

It is given by

$$\sigma_{syst} := \max_{\text{variations i}} (|R_{\text{3-jet, var i}}^{\text{corr}} - R_{\text{3-jet, std}}^{\text{corr}}|)$$

where $R_{\text{3-jet, var i}}^{\text{corr}}$ is the value for the 3-jet rate derived from the i-th variation of the cuts; $R_{\text{3-jet, std}}^{\text{corr}}$ is the value of the 3-jet rate with no extra cuts.

The results for the 3 jet rate corrected for geometrical acceptance, detector efficiency and resolution, decays, secondary interactions and initial state photon radiation derived from ALEPH 1992 data are given in the following table.

The estimate for the error due to the model bias is derived from the results obtained using the SDS algorithm on 7 different models (see section 4.8.3 for details on how the model bias error is computed).

y_{cut}	R_{3-jet}^{corr}	syst	mbias
0.00100	0.2840	$\pm$0.0001	$\pm$0.0035
0.00126	0.3255	$\pm$0.0005	$\pm$0.0034
0.00159	0.3587	$\pm$0.0011	$\pm$0.0026
0.00200	0.3803	$\pm$0.0019	$\pm$0.0028
0.00251	0.3903	$\pm$0.0026	$\pm$0.0026
0.00316	0.3899	$\pm$0.0024	$\pm$0.0034
0.00398	0.3812	$\pm$0.0019	$\pm$0.0026
0.00501	0.3671	$\pm$0.0012	$\pm$0.0036
0.00631	0.3492	$\pm$0.0020	$\pm$0.0032
0.00794	0.3278	$\pm$0.0014	$\pm$0.0028
0.01000	0.3040	$\pm$0.0012	$\pm$0.0017
0.01259	0.2781	$\pm$0.0016	$\pm$0.0025
0.01585	0.2511	$\pm$0.0015	$\pm$0.0019
0.01995	0.2235	$\pm$0.0011	$\pm$0.0020
0.02512	0.1952	$\pm$0.0008	$\pm$0.0012
0.03162	0.1674	$\pm$0.0005	$\pm$0.0012
0.03981	0.1405	$\pm$0.0005	$\pm$0.0009
0.05012	0.1149	$\pm$0.0006	$\pm$0.0009
0.06310	0.0906	$\pm$0.0002	$\pm$0.0006
0.07943	0.0689	$\pm$0.0001	$\pm$0.0005
0.10000	0.0498	$\pm$0.0002	$\pm$0.0007

The corrected values for the 3-jet rate are also shown in figure 4.12.

As one can also see from this figure, the size of the corrections varies strongly with y_{cut}. The strong rise for soft y_{cut} is due to the fact, that very low energetic jets (favoured as third jets for soft y_{cut}) especially suffer from detector effects.

The discrepancy between the 3-jet rate as found for raw data and for fully reconstructed Monte Carlo events also depends strongly on the y_{cut}; for hard y_{cut}, it goes as high as 10%. For large y_{cut}, events with high energy third jet are favoured; the rise of the discrepancy in the 3-jet rate with y_{cut} shows once more that the JETSET parton shower Monte Carlo has problems in describing hard gluon emission properly.

Other observables are also influenced by the insufficient description of the 3-jet rate. Figure 4.13 shows a comparison between the $z = (x_2 - x_3)/\sqrt{3}$ distributions from 1992 data and GALEPH for different values of y_{cut}. The distributions have been normalized to the total number of hadronic events (instead of the number of selected 3-jet events). This again makes the difference in the 3-jet rate visible, leading to the largest deviations for $y_{cut} = 0.1$. For $y_{cut} = 0.001$, the peak of the distribution for $z \approx 0.5$ is not reproduced by the MC.

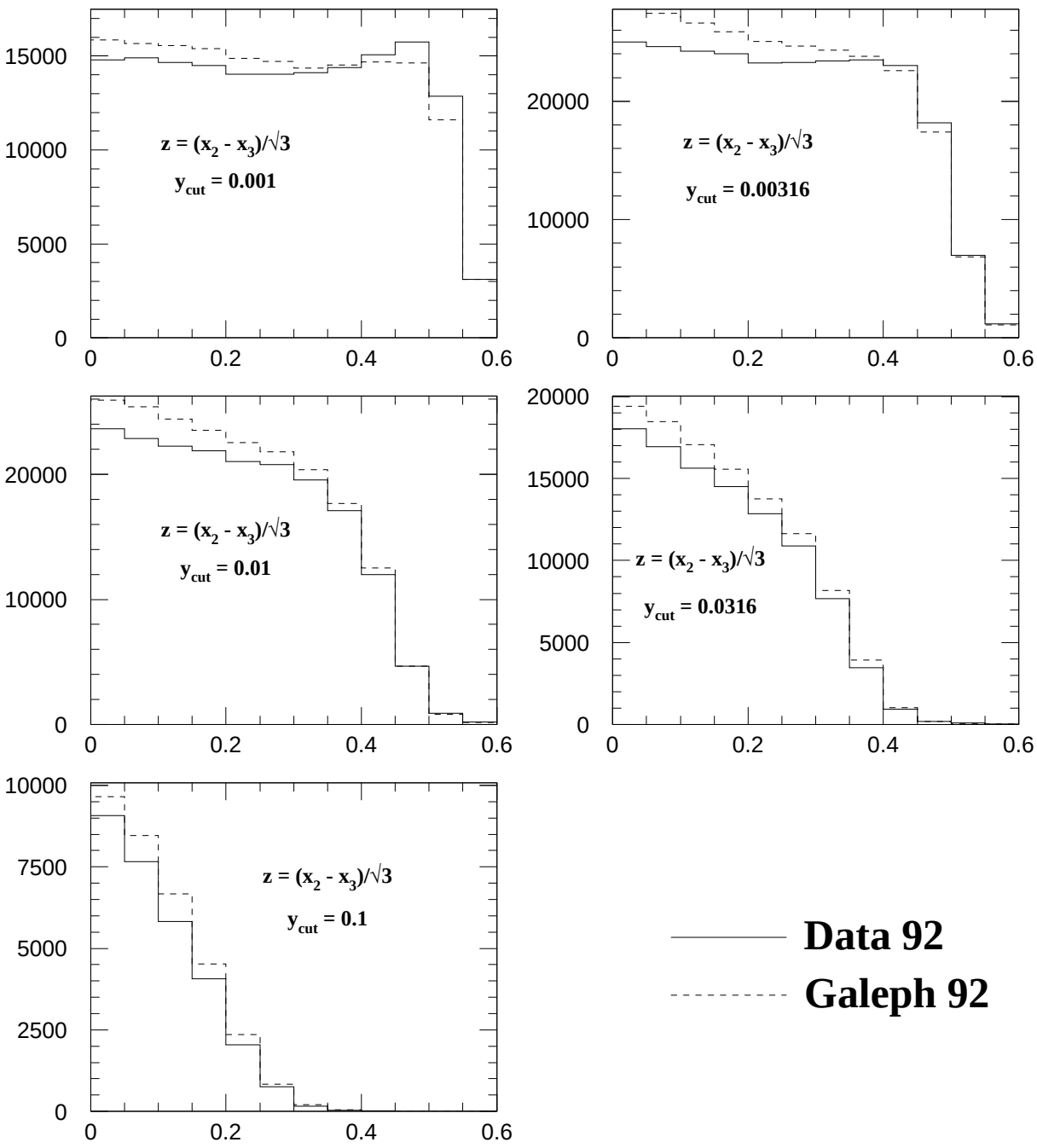

Figure 4.13: Comparison of the z distribution for data and MC at different y_{cut} values. The distributions are normalized to the total number of hadronic events — thus the discrepancy in the 3-jet rate between data and MC can be seen. For $y_{cut} = 0.1$ the discrepancy is maximal. The small peak around $z \approx 0.5$ of the data z distribution for $y_{cut} = 0.001$ is not reproduced by the MC.

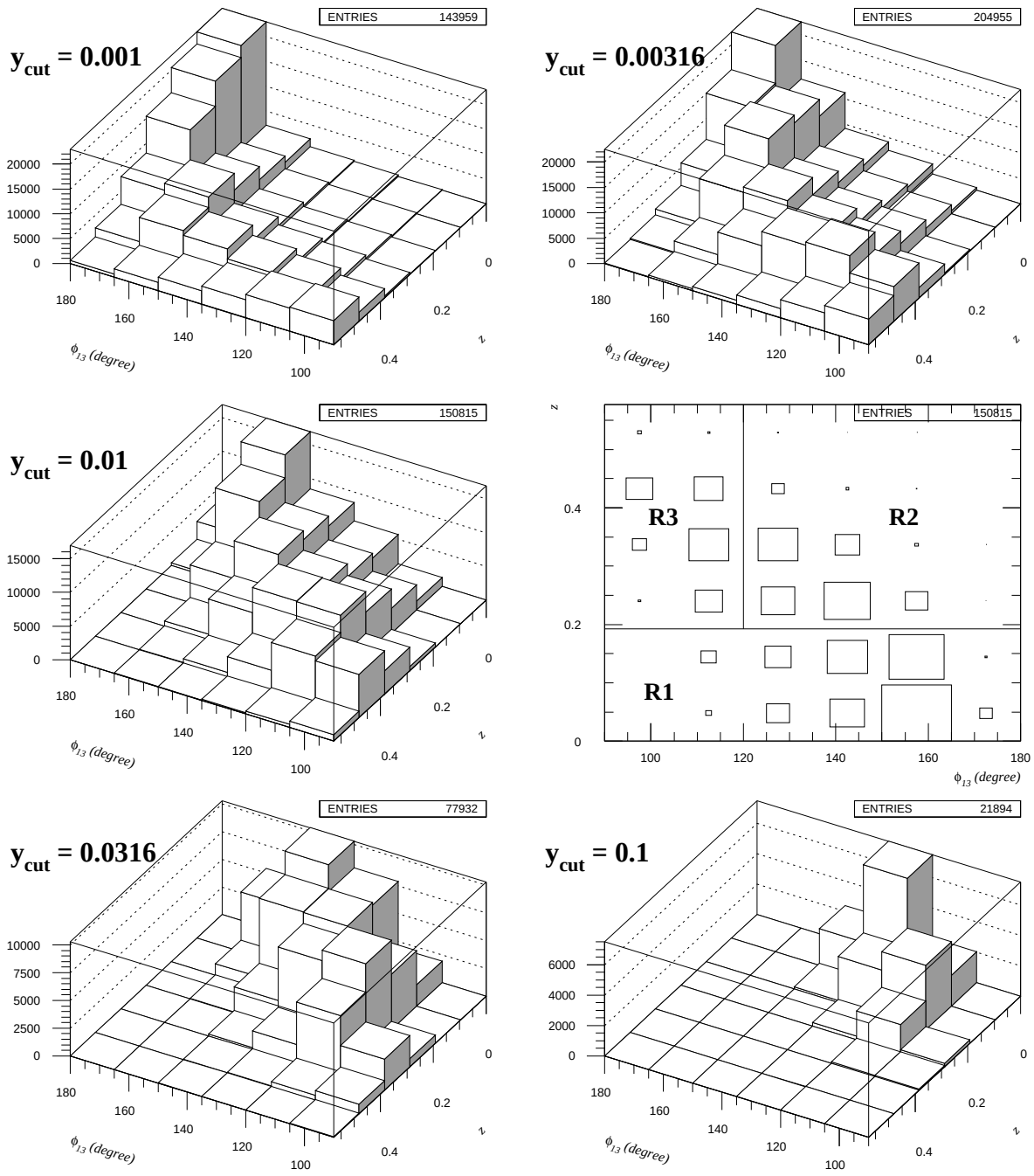

Figure 4.14: Dalitz plot for different values of y_{cut}. For the central $y_{cut} = 0.01$, both the lego and the box plot are shown. The kinematic regions are indicated in the box plot. For hard y_{cut} values, the selected 3-jets are close to the Mercedes-like configurations.

The spread of 3-jet events over the Dalitz plot for different values of y_{cut} (evenly spaced on the logarithmic scale) is shown in figure 4.14. The number of 3-jet events for the values of y_{cut} can be seen to vary. With increasing y_{cut}, the events selected as 3-jets move towards values of $z \approx 0$ and $\phi_{13} \approx 120^\circ$ (Mercedes configurations with 3 jets of approximately the same energy). At the same time, the jets become broader (see figure 4.37).

The overlap between different values of y_{cut}, ie. the events that are selected as 3-jets for a range of y_{cut} values, is shown in figure 4.15. The events which are 3-jets for the whole range of y_{cut} considered, must have very articulate 3-jet structure (ie. low z) and the jets must not have subjet structure (otherwise they would be found to be 4-jet or 5-jet events for soft y_{cut}). But the number of events which are 3-jets for all y_{cut} considered is less than 1% of all hadronic events. Nevertheless, the results (eg. for $\langle \Delta\phi(\mathbf{L1}) \rangle$) obtained for different values of y_{cut} can not be considered statistically independent, showing even far-reaching (on the y_{cut} scale) correlations.

The fraction $N_{\text{reg}}/N_{\text{3-jet}}$ of events assigned to the kinematic regions **R1**, **R2** and **R3** is shown in figure 4.16. Apart from the fact, that a higher percentage of 3-jets is found in the MCs, the kinematic regions are filled differently for soft y_{cut}.

For hard y_{cut}, **R1** (with its Mercedes-like events) is heavily populated.

The discrepancy in the 3-jet rate between the data and the MC can also be studied for the kinematic configurations of the Dalitz plot (see figure 4.17). Since the 3-jet rate predicted from the MC is higher than what is actually observed on the data, the difference

$$\delta_{ij} := \frac{N_{ij}^{\text{GALEPH}} - N_{ij}^{\text{DATA}}}{N_{ij}^{\text{DATA}}}$$

is used to have positive values (here (i, j) is the index of the Dalitz bin).

Only for very small y_{cut}, δ_{ij} becomes negative for $z \approx 0.5$ configurations. This corresponds to the peak in the z distribution of the data (see figure 4.13) which is not reproduced by the MC.

Once again, the main discrepancy between data and MC arises from the small-z events, ie. those events with all 3 jets being energetic, which are not well described by the parton shower MC. In the MC, too many events with Mercedes-like configurations are produced leaving the 2-jet rate too low (compare figure 4.11).

In the following tables, the variation over the Dalitz plot of the values of $\Delta\phi(\mathbf{L1})$ is given for ALEPH raw data from 1992 and GALEPH (only bins containing more than 1000 data events are shown). Note that these values are *not* corrected for detector effects.

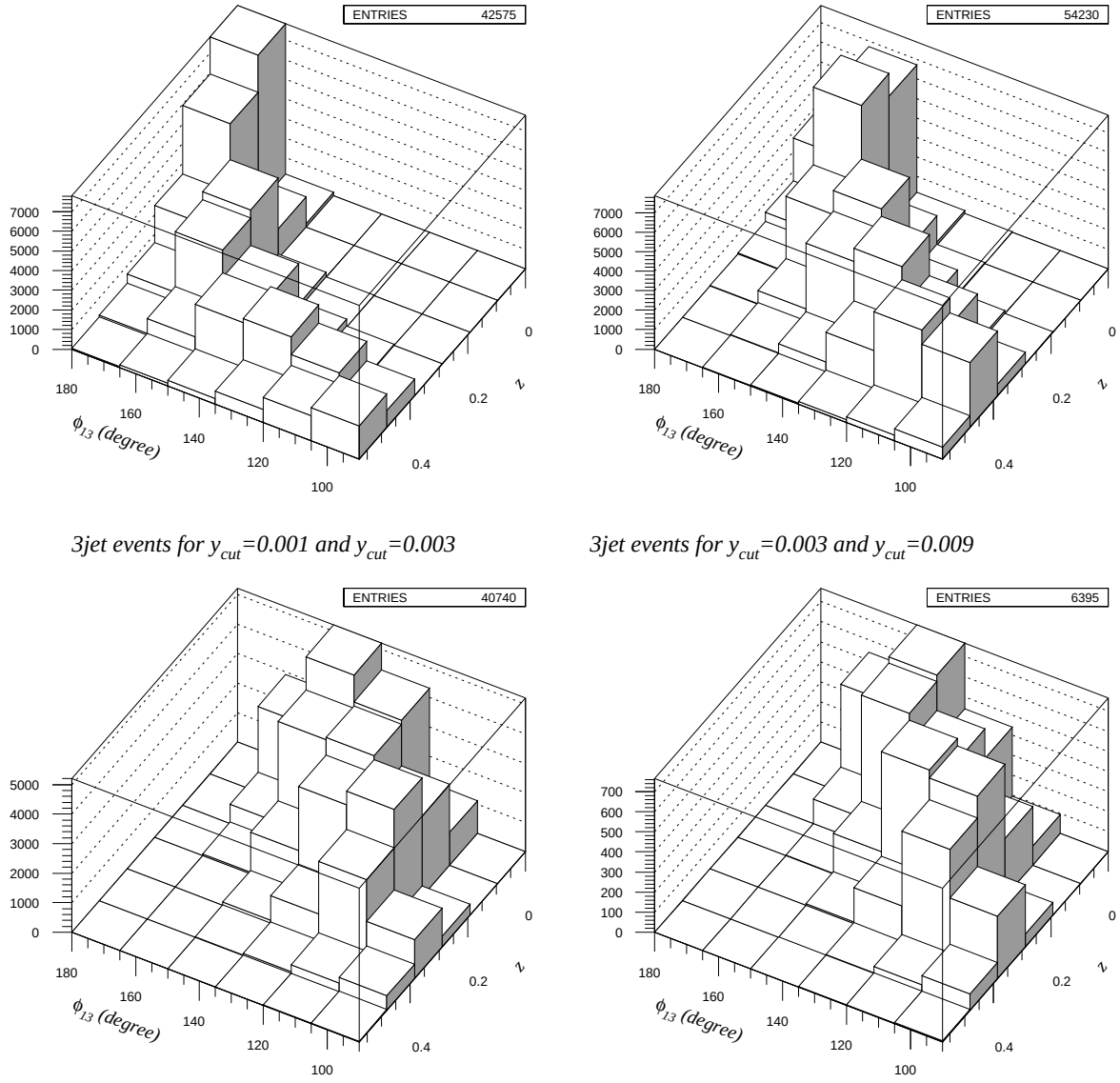

Figure 4.15: The overlap of events, which are recognized as 3-jets for a larger range of y_{cut} values is shown. Only $\approx 1\%$ of all hadronic events are selected as 3-jets for the whole y_{cut} range.

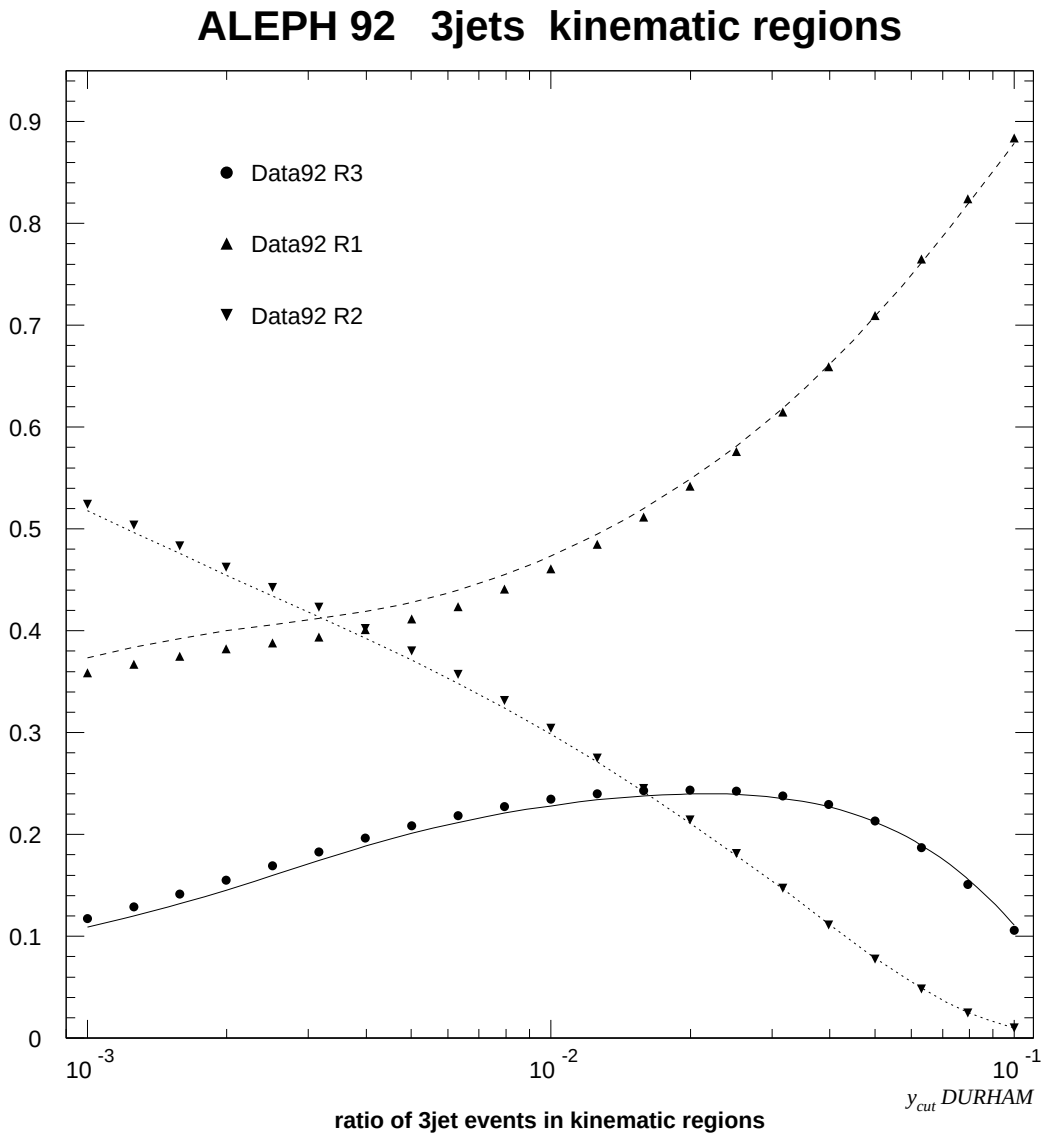

Figure 4.16: The fractions of 3-jets in the 3 kinematic regions for ALEPH data 1992. The results for fully reconstructed MC events are superimposed. For small y_{cut}, a discrepancy can be seen. For hard y_{cut}, the fractions agree between data and MC and **R1** (symmetric events) is predominant.

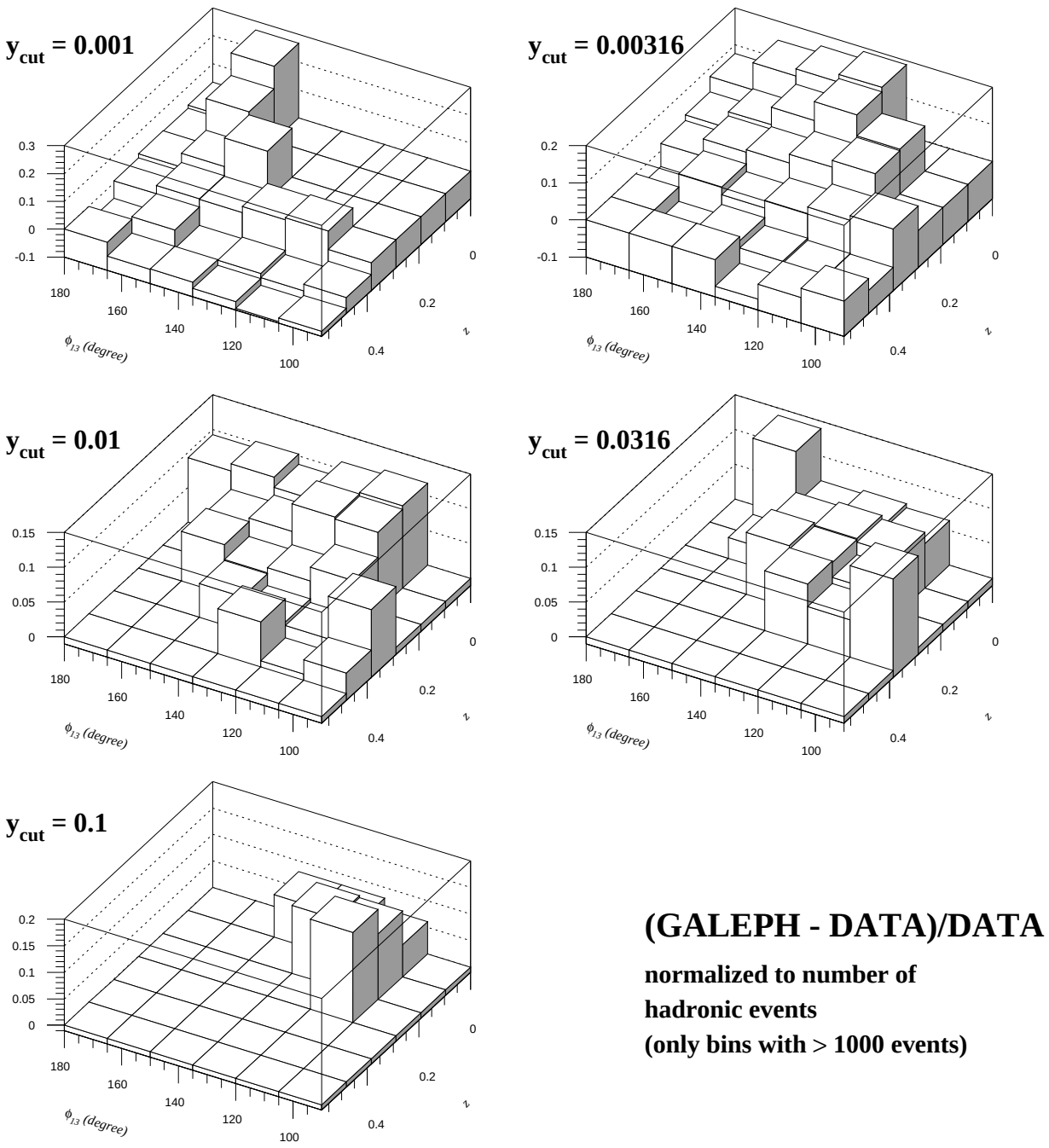

Figure 4.17: Difference of the occupation of Dalitz configurations between data and MC, normalized to the total number of hadronic events (thus showing the discrepancy in the 3-jet rate). The discrepancy can be seen to come from the Mercedes-like region of the Dalitz plot. These configurations are insufficiently described by parton shower MC.

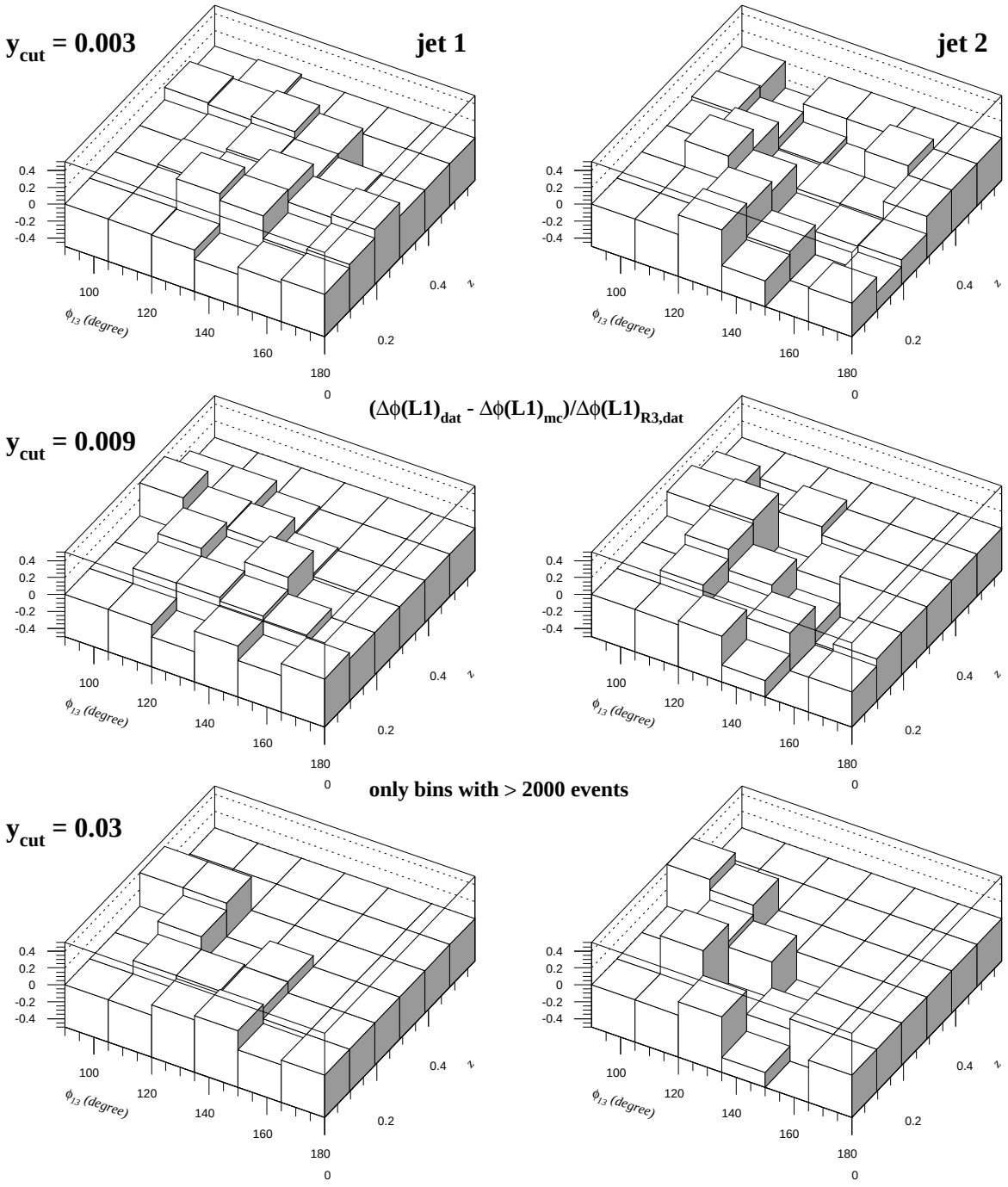

Figure 4.18: Difference between $\langle \Delta\phi(\mathbf{L1}) \rangle$ results from data (not corrected for detector effects) and MC for the Dalitz configurations.

- $\langle \Delta\phi(\mathbf{L1}) \rangle$ for **Jet 1** and $y_{cut} = 0.009$ (typical error bars are 0.03 to 0.1):

$\phi_{13} \rightarrow$		index of histogram channel					
$z \uparrow$		**1**	**2**	**3**	**4**	**5**	**6**
	# data events	1155					
6	$\langle \Delta\phi(\mathbf{L1}) \rangle_{Dat}$	$-0.855°$					
	$\langle \Delta\phi(\mathbf{L1}) \rangle_{MC}$	$-0.836°$					
	# data events	6918	7896	3701			
5	$\langle \Delta\phi(\mathbf{L1}) \rangle_{Dat}$	$-0.642°$	$-0.577°$	$-0.586°$			
	$\langle \Delta\phi(\mathbf{L1}) \rangle_{MC}$	$-0.553°$	$-0.486°$	$-0.569°$			
	# data events	3434	9645	10148	7173	1193	
4	$\langle \Delta\phi(\mathbf{L1}) \rangle_{Dat}$	$-0.604°$	$-0.542°$	$-0.400°$	$-0.378°$	$-0.564°$	
	$\langle \Delta\phi(\mathbf{L1}) \rangle_{MC}$	$-0.375°$	$-0.416°$	$-0.282°$	$-0.361°$	$-0.446°$	
	# data events		6443	8159	11448	6928	
3	$\langle \Delta\phi(\mathbf{L1}) \rangle_{Dat}$		$-0.459°$	$-0.338°$	$-0.283°$	$-0.240°$	
	$\langle \Delta\phi(\mathbf{L1}) \rangle_{MC}$		$-0.297°$	$-0.273°$	$-0.109°$	$-0.262°$	
	# data events		3583	6206	9693	14812	
2	$\langle \Delta\phi(\mathbf{L1}) \rangle_{Dat}$		$-0.407°$	$-0.312°$	$-0.225°$	$-0.162°$	
	$\langle \Delta\phi(\mathbf{L1}) \rangle_{MC}$		$-0.301°$	$-0.201°$	$-0.138°$	$-0.102°$	
	# data events		1293	5493	8164	17171	4350
1	$\langle \Delta\phi(\mathbf{L1}) \rangle_{Dat}$		$-0.325°$	$-0.032°$	$-0.115°$	$-0.008°$	$-0.075°$
	$\langle \Delta\phi(\mathbf{L1}) \rangle_{MC}$		$-0.173°$	$-0.115°$	$-0.056°$	$-0.047°$	$-0.033°$

- $\langle \Delta\phi(\mathbf{L1}) \rangle$ for **Jet 2** and $y_{cut} = 0.009$ (typical error bars are 0.05 to 0.15):

$\phi_{13} \rightarrow$		index of histogram channel					
$z \uparrow$		**1**	**2**	**3**	**4**	**5**	**6**
	# data events	1155					
6	$\langle \Delta\phi(\mathbf{L1}) \rangle_{Dat}$	$0.775°$					
	$\langle \Delta\phi(\mathbf{L1}) \rangle_{MC}$	$0.896°$					
	# data events	6918	7896	3701			
5	$\langle \Delta\phi(\mathbf{L1}) \rangle_{Dat}$	$0.641°$	$0.532°$	$0.592°$			
	$\langle \Delta\phi(\mathbf{L1}) \rangle_{MC}$	$0.553°$	$0.659°$	$0.533°$			
	# data events	3434	9645	10148	7173	1193	
4	$\langle \Delta\phi(\mathbf{L1}) \rangle_{Dat}$	$0.580°$	$0.589°$	$0.359°$	$0.180°$	$-1.647°$	
	$\langle \Delta\phi(\mathbf{L1}) \rangle_{MC}$	$0.407°$	$0.405°$	$0.545°$	$0.237°$	$-1.046°$	
	# data events		6443	8159	11448	6928	
3	$\langle \Delta\phi(\mathbf{L1}) \rangle_{Dat}$		$0.568°$	$0.407°$	$-0.043°$	$-1.168°$	
	$\langle \Delta\phi(\mathbf{L1}) \rangle_{MC}$		$0.409°$	$0.392°$	$0.148°$	$-0.884°$	
	# data events		3583	6206	9693	14812	
2	$\langle \Delta\phi(\mathbf{L1}) \rangle_{Dat}$		$0.404°$	$0.326°$	$-0.009°$	$-1.386°$	
	$\langle \Delta\phi(\mathbf{L1}) \rangle_{MC}$		$0.312°$	$0.392°$	$0.021°$	$-0.985°$	
	# data events		1293	5493	8164	17171	4350
1	$\langle \Delta\phi(\mathbf{L1}) \rangle_{Dat}$		$0.460°$	$0.133°$	$-0.156°$	$-1.685°$	$-2.998°$
	$\langle \Delta\phi(\mathbf{L1}) \rangle_{MC}$		$0.179°$	$0.107°$	$0.023°$	$-1.183°$	$-2.948°$

- $\langle \Delta\phi(\mathbf{L1}) \rangle$ for **Jet 1** and $y_{cut} = 0.003$ (typical error bars are 0.03 to 0.1):

$\phi_{13} \rightarrow$		index of histogram channel					
$z \uparrow$		**1**	**2**	**3**	**4**	**5**	**6**
	# data events	5314	3807	1943			
6	$\langle \Delta\phi(\mathbf{L1}) \rangle_{Dat}$	$-0.555°$	$-0.529°$	$-0.579°$			
	$\langle \Delta\phi(\mathbf{L1}) \rangle_{MC}$	$-0.547°$	$-0.513°$	$-0.553°$			
	# data events	6729	10132	9762	7218	2720	
5	$\langle \Delta\phi(\mathbf{L1}) \rangle_{Dat}$	$-0.532°$	$-0.455°$	$-0.401°$	$-0.358°$	$-0.188°$	
	$\langle \Delta\phi(\mathbf{L1}) \rangle_{MC}$	$-0.462°$	$-0.397°$	$-0.324°$	$-0.326°$	$-0.394°$	
	# data events	1981	5676	7369	11007	10734	1704
4	$\langle \Delta\phi(\mathbf{L1}) \rangle_{Dat}$	$-0.450°$	$-0.451°$	$-0.354°$	$-0.277°$	$-0.227°$	$-0.375°$
	$\langle \Delta\phi(\mathbf{L1}) \rangle_{MC}$	$-0.454°$	$-0.445°$	$-0.313°$	$-0.242°$	$-0.214°$	$-0.278°$
	# data events		3235	4371	7439	16025	6640
3	$\langle \Delta\phi(\mathbf{L1}) \rangle_{Dat}$		$-0.378°$	$-0.283°$	$-0.256°$	$-0.169°$	$-0.278°$
	$\langle \Delta\phi(\mathbf{L1}) \rangle_{MC}$		$-0.363°$	$-0.257°$	$-0.130°$	$-0.110°$	$-0.203°$
	# data events		1647	2982	5250	14145	16085
2	$\langle \Delta\phi(\mathbf{L1}) \rangle_{Dat}$		$-0.375°$	$-0.394°$	$-0.271°$	$-0.092°$	$-0.151°$
	$\langle \Delta\phi(\mathbf{L1}) \rangle_{MC}$		$-0.321°$	$-0.223°$	$-0.140°$	$-0.094°$	$-0.127°$
	# data events			2402	3946	10820	23561
1	$\langle \Delta\phi(\mathbf{L1}) \rangle_{Dat}$			$-0.112°$	$-0.052°$	$-0.022°$	$-0.039°$
	$\langle \Delta\phi(\mathbf{L1}) \rangle_{MC}$			$-0.116°$	$-0.108°$	$-0.037°$	$-0.037°$

- $\langle \Delta\phi(\mathbf{L1}) \rangle$ for **Jet 1** and $y_{cut} = 0.03$ (typical error bars are 0.07 to 0.15):

$\phi_{13} \rightarrow$		index of histogram channel					
$z \uparrow$		**1**	**2**	**3**	**4**	**5**	**6**
	# data events						
6	$\langle \Delta\phi(\mathbf{L1}) \rangle_{Dat}$						
	$\langle \Delta\phi(\mathbf{L1}) \rangle_{MC}$						
	# data events	1001					
5	$\langle \Delta\phi(\mathbf{L1}) \rangle_{Dat}$	$-0.880°$					
	$\langle \Delta\phi(\mathbf{L1}) \rangle_{MC}$	$-0.642°$					
	# data events	2977	6000	1988			
4	$\langle \Delta\phi(\mathbf{L1}) \rangle_{Dat}$	$-0.575°$	$-0.587°$	$-0.302°$			
	$\langle \Delta\phi(\mathbf{L1}) \rangle_{MC}$	$-0.360°$	$-0.373°$	$-0.605°$			
	# data events		8168	7503	2739		
3	$\langle \Delta\phi(\mathbf{L1}) \rangle_{Dat}$		$-0.435°$	$-0.329°$	$-0.411°$		
	$\langle \Delta\phi(\mathbf{L1}) \rangle_{MC}$		$-0.268°$	$-0.331°$	$-0.341°$		
	# data events		4990	8197	8699	1331	
2	$\langle \Delta\phi(\mathbf{L1}) \rangle_{Dat}$		$-0.333°$	$-0.215°$	$-0.180°$	$-0.108°$	
	$\langle \Delta\phi(\mathbf{L1}) \rangle_{MC}$		$-0.247°$	$-0.130°$	$-0.111°$	$-0.151°$	
	# data events		1913	7915	10379	6065	
1	$\langle \Delta\phi(\mathbf{L1}) \rangle_{Dat}$		$-0.224°$	$-0.191°$	$-0.115°$	$-0.066°$	
	$\langle \Delta\phi(\mathbf{L1}) \rangle_{MC}$		$-0.083°$	$-0.126°$	$-0.023°$	$-0.096°$	

The discrepancy in $\langle\Delta\phi(\mathbf{L1})\rangle$ between data and MC is also visualized in figure 4.18; the variable

$$\frac{\langle\Delta\phi(\mathbf{L1})\rangle_{ij}^{\text{DATA}} - \langle\Delta\phi(\mathbf{L1})\rangle_{ij}^{\text{GALEPH}}}{\langle\Delta\phi(\mathbf{L1})\rangle_{\mathbf{R3},\,\text{DATA}}},$$

with the normalization to $\langle\Delta\phi(\mathbf{L1})\rangle_{\mathbf{R3},\,\text{DATA}}$ to avoid large fluctuations is used.

For jet 1, the data gives a larger value of $\langle\Delta\phi(\mathbf{L1})\rangle$ for all kinematic configurations over the whole y_{cut} range. For jet 2, the MC shows a larger angle shift for certain configurations.

4.6 Momentum Spectrum of Leading Particles and Jet Energies

A comparison has to be made of the description of the momentum spectra, especially of the leading particles in the jet which are used for the $\langle\Delta\phi(\mathbf{L1})\rangle$ measurement, between the data and the fully reconstructed Monte Carlo.

The overall momentum spectrum of the charged and neutral particles is fairly well described by the MC up to the highest momenta (see figure 4.19). For low momentum charged particles, the agreement between data and MC is still good, whereas for neutral particles, a discrepancy is clearly visible.

The p and x distributions of the leading particles in the jets are also well described by the MC (see figure 4.20 and 4.21).

The values in the following tables are all for ALEPH 1992 data (not corrected for detector effects). For $y_{cut} = 0.01$ 3-jet events, the following mean values for the momenta of the leading particles are found:

	R1			**R2**			**R3**		
p [GeV]	jet 1	jet 2	jet 3	jet 1	jet 2	jet 3	jet 1	jet 2	jet 3
leading	11.90	7.73	5.81	12.17	9.52	4.02	11.53	10.83	3.22
second	6.52	4.43	3.42	6.68	5.37	2.38	6.36	5.99	1.96
third	4.41	3.11	2.42	4.51	3.72	1.70	4.32	4.10	1.42

The leading particle is well separated from the second particle in the jet, having approximately twice the energy in average. In **R3**, the leading particle in the third jet has less than one third of the energy of the leading particle in jet 1.

The fraction of the jet energy that the leading particles in $y_{cut} = 0.01$ 3-jet events carry in the mean is given in the next table:

	R1			**R2**			**R3**		
$x_l = E_l/E_{jet,\,vis}$	jet 1	jet 2	jet 3	jet 1	jet 2	jet 3	jet 1	jet 2	jet 3
leading	0.295	0.281	0.275	0.297	0.286	0.287	0.293	0.290	0.285
second	0.162	0.161	0.162	0.163	0.161	0.171	0.162	0.160	0.174
third	0.110	0.113	0.115	0.110	0.112	0.123	0.110	0.110	0.126

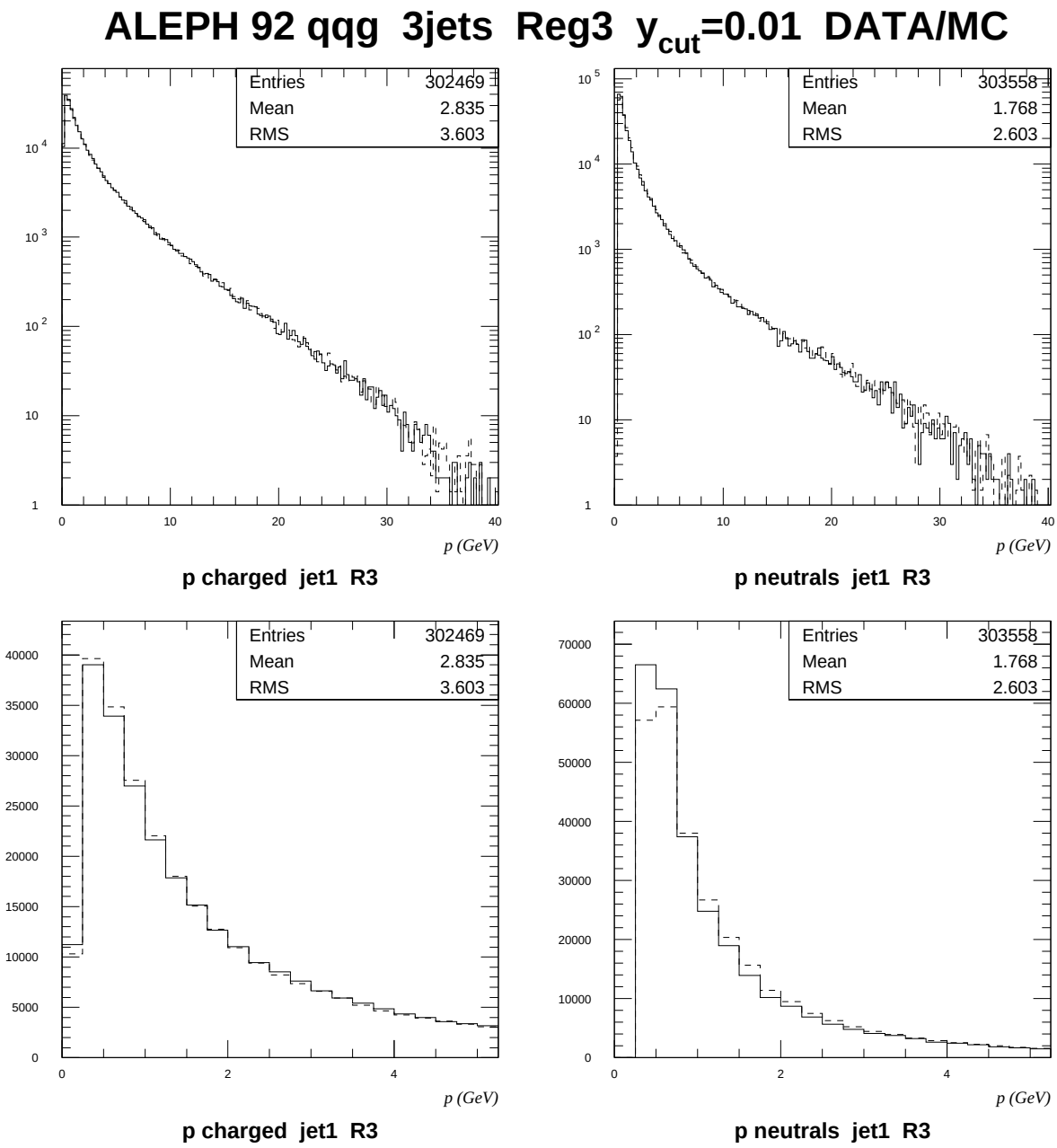

Figure 4.19: Momentum spectrum for charged and neutral particles for jet 1 of **R3** 3-jet events. Generally, the shape of the momentum distribution is well described by the MC (dashed line). But for low momentum neutral particles deviations are visible.

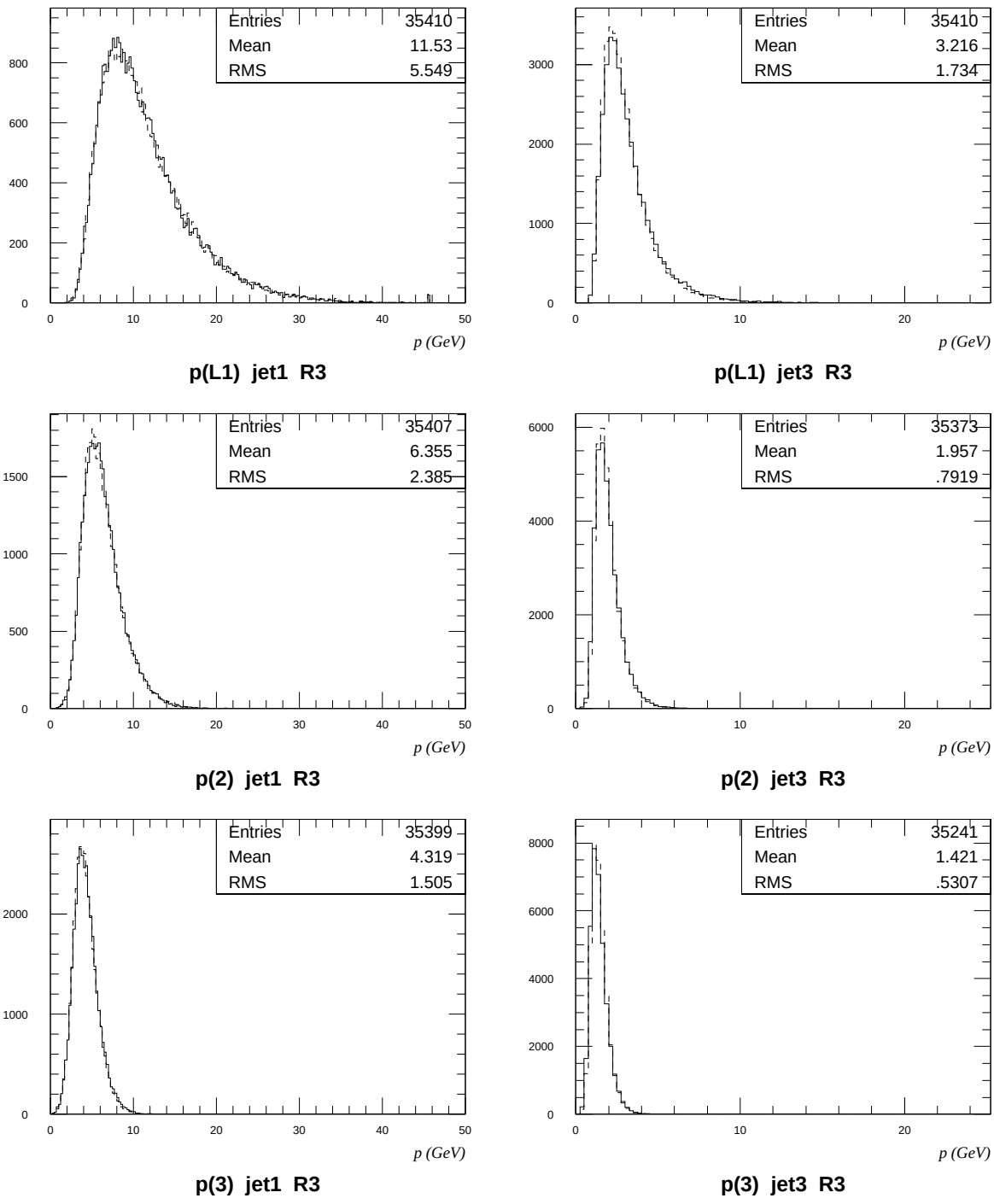

Figure 4.20: Momentum spectrum of the leading particle (L1), the second particle ($p(2)$) and the third particle ($p(3)$) in jet 1 and jet 3 of **R3** 3-jet events from ALEPH 1992 data and MC at $y_{cut} = 0.01$. The mean p of the first particle is almost twice as large as that of the second. For **R3**, the mean p of the leading particle in jet 3 is less than a third of that of the leading particle in jet 1 (note the different scale for jet 1 and jet 3).

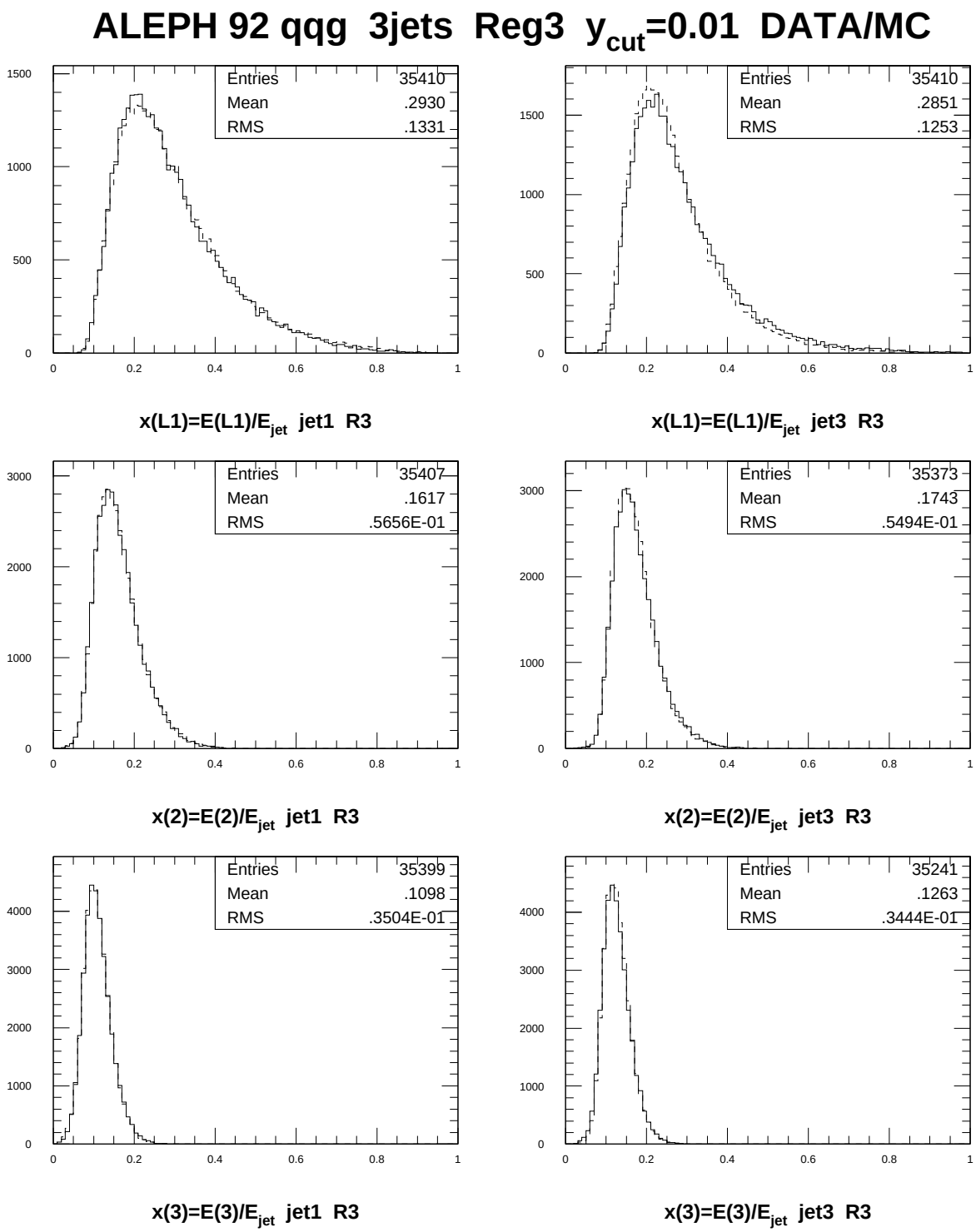

Figure 4.21: Fraction $x_{lead} = E_{lead}/E_{jet,\,vis}$ of the jet energy for the leading particles. The x distributions for jet 1 and jet 3 are very similar. For the leading particle in jet 3, a slight difference between data and MC is visible.

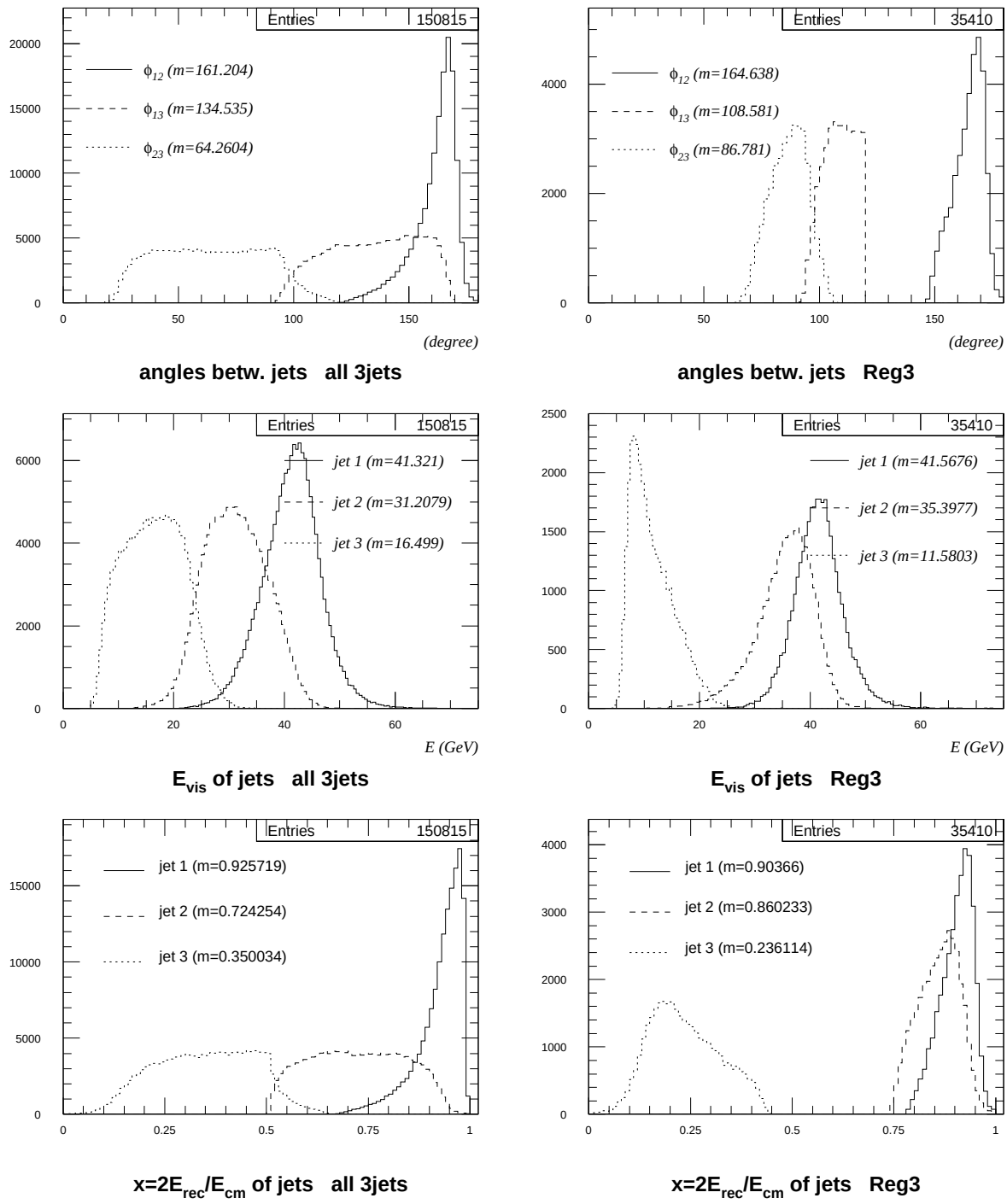

Figure 4.22: Distributions of the angles ϕ_{12}, ϕ_{13} and ϕ_{23} between the jets and of E_{vis} and $x = 2E_{rec}/E_{cm}$ for 3-jet events from ALEPH 1992 data at $y_{cut} = 0.01$ (m stands for the mean of the distributions). For **R3**, the jets are well separated. Due to the reconstruction of jet energies from the angles between the jets, these E_{rec} can go to zero, even if $E_{vis} > 5\,\mathrm{GeV}$ due to the cluster algorithm.

The fraction of the jet energy that the leading, the second and the third particle have is fairly independent of the kinematic region and of the jet number.

The azimuthal angles between the jet axes for 3-jet events for $y_{cut} = 0.01$ can be seen in figure 4.22. The following table gives the mean values for the kinematic regions:

	Rall	**R1**	**R2**	**R3**
$\langle\phi_{12}\rangle$	161°	156°	166°	165°
$\langle\phi_{13}\rangle$	135°	146°	137°	109°
$\langle\phi_{23}\rangle$	64°	58°	57°	87°

The visible energy distribution can also be seen in figure 4.22. For **R3**, the distributions for jet 1 and jet 2 are closer together, with jet 3 having a much lower mean energy. The mean values of the E_{vis} distributions are given in the following table ($y_{cut} = 0.01$):

E_{vis} [GeV]	**Rall**	**R1**	**R2**	**R3**
jet 1	41.3	40.8	41.9	41.6
jet 2	31.2	28.1	32.7	35.4
jet 3	16.5	20.6	14.1	11.6

The same can be seen in the $x = 2E_{jet\,rec}/E_{cm}$ distribution (also figure 4.22). Due to the reconstruction of the jet energies from the angles between the jets, the third jet can be assigned a very small energy, eventhough its visible energy has to be above a certain threshold (see section 3.2) for the event to be selected as a 3-jet. The mean values for x are given in the next table ($y_{cut} = 0.01$):

$x = 2E_{rec}/E_{cm}$	**Rall**	**R1**	**R2**	**R3**
jet 1	0.926	0.921	0.950	0.904
jet 2	0.724	0.622	0.775	0.860
jet 3	0.350	0.458	0.275	0.236

The visible energies of the jets are strongly dependent on the value of y_{cut} used, since different y_{cut} favour different kinematic configurations as 3-jets (see figure 4.23). The dependence of E_{vis} of the jets on the value of y_{cut} can be seen from the next table:

E_{vis} [GeV]		$y_{cut} = 0.001$	$y_{cut} = 0.00316$	$y_{cut} = 0.01$	$y_{cut} = 0.0316$	$y_{cut} = 0.1$
R1	J1	43.8	42.3	40.8	38.8	36.0
	J2	27.0	27.2	28.1	28.8	29.3
	J3	19.0	19.8	20.6	21.7	23.9
R2	J1	44.3	43.2	41.9	39.9	34.8
	J2	34.0	33.4	32.7	31.3	27.7
	J3	11.4	12.4	14.1	16.9	22.3
R3	J1	45.2	43.3	41.6	39.6	36.3
	J2	39.1	37.1	35.4	33.4	30.2
	J3	5.6	8.6	11.6	15.2	20.5

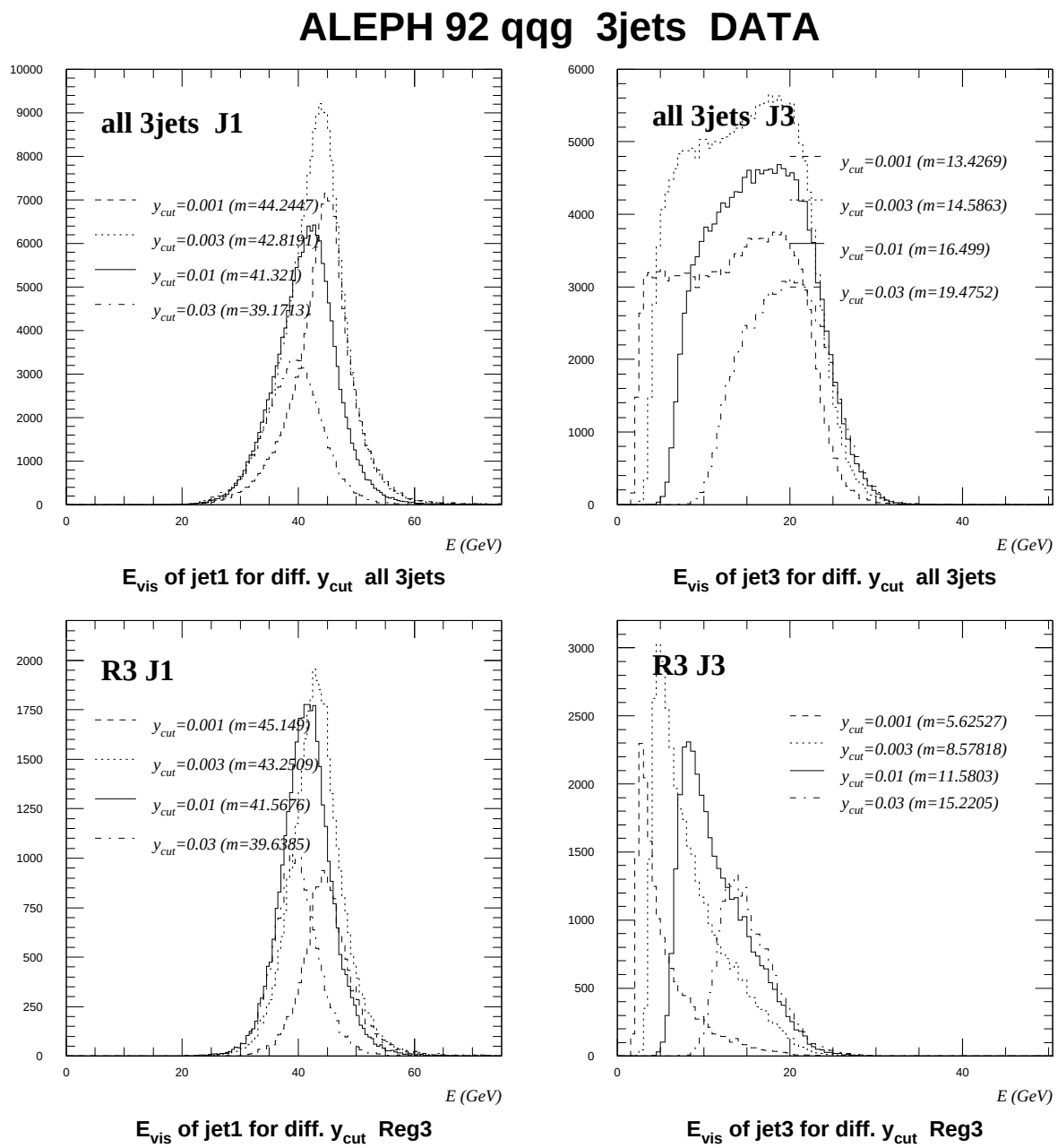

Figure 4.23: Energy distribution for jet 1 and jet 3 for different values of y_{cut}. For jet 3, the minimum energy required to be clustered as a separate jet is clearly visible, varying with y_{cut}. The solid line shows the distribution for the central $y_{cut} = 0.01$.

4.7 Correction of $\langle\Delta\phi(\mathbf{L1})\rangle$

The results for $\langle\Delta\phi(\mathbf{L1})\rangle$ that have been given up to now have not been corrected for effects of geometrical acceptance, detector efficiency and resolution, decays, secondary interactions and initial state photon radiation.

In order to have a result for $\langle\Delta\phi(\mathbf{L1})\rangle$ which can be compared to the predictions of Monte Carlo models, a correction for these effects has to be made.

The usual procedure employed is the following: the values for the observable are determined for both the hadron level Monte Carlo without detector simulation and for fully reconstructed Monte Carlo events. The detector effects can be estimated from the difference in those values.

For the 3-jet rate, a multiplicative correction scheme was used:

$$R_{3-jet}^{\text{corr}} := C_{\text{corr}}\, R_{3-jet}^{\text{raw DATA}} \qquad \text{where} \quad C_{\text{corr}} := \frac{R_{3-jet}^{\text{had lev}}}{R_{3-jet}^{\text{rec lev}}}.$$

For $\langle\Delta\phi(\mathbf{L1})\rangle$, an additive correction scheme seems more appropriate, since the detector effects can be seen to cause a smearing and a shift of the $\Delta\phi$ distribution, thus also resulting in a shift of the mean value $\langle\Delta\phi(\mathbf{L1})\rangle$ of the distribution.

The corrected values $\langle\Delta\phi(\mathbf{L1})\rangle^{\text{corr}}$ of the angle shift are computed in the following way:

$$\langle\Delta\phi(\mathbf{L1})\rangle^{\text{corr}} := \langle\Delta\phi(\mathbf{L1})\rangle_{\text{DATA}}^{\text{raw}} + C^{\text{corr}}$$

where

$$C^{\text{corr}} := \langle\Delta\phi(\mathbf{L1})\rangle_{\text{MC}}^{\text{had lev}} - \langle\Delta\phi(\mathbf{L1})\rangle_{\text{MC}}^{\text{rec lev}}.$$

Here, $\langle\Delta\phi(\mathbf{L1})\rangle_{\text{DATA}}^{\text{raw}}$ stands for the raw results from ALEPH data; $\langle\Delta\phi(\mathbf{L1})\rangle_{\text{MC}}^{\text{had lev}}$ stands for the results from plain HVFL runs without detector simulation and $\langle\Delta\phi(\mathbf{L1})\rangle_{\text{MC}}^{\text{rec lev}}$ comes from the analysis of fully reconstructed Monte Carlo events.

The size and the variation of the corrections C^{corr} with y_{cut} for jet 1 in the 3 kinematic regions can be seen in figures 4.39, 4.41 and 4.43 (the error bars shown are from the propagation of statistical errors from hadron level and reconstructed level MC). Note that the corrections are rather small for jet 1 and central y_{cut} values.

The determination of $\langle\Delta\phi(\mathbf{L1})\rangle_{\text{MC}}^{\text{had lev}}$ is made using the HVFL event generator (in versions HVFL03 and HVFL04, according to which data (from 1992 or 1993) is to be corrected; see also section 4.3). The event selection for hadron level MC events is described in section 5.1. The Monte Carlo truth information of the fully reconstructed events could also be used (it is nothing but the results of HVFL runs); but using HVFL directly has several advantages:

- Higher statistics can be generated: for each 1992 and 1993, about 2 million fully reconstructed events are available. For this study, a sample of 3 million hadron level events generated with both HVFL03 and HVFL04 were used to minimize statistical errors.

- In the generation of the HVFL events, no ISR (initial state radiation) and FSR (final state photon radiation off the quarks; see section 4.4) were allowed. The results $\langle\Delta\phi(\mathbf{L1})\rangle^{\text{corr}}$ are thus corrected against these processes.

The fraction of 2γ events left after the cut $\sum E_{\mathrm{EFLW}} > E_{cm}/2$ is negligible and need not be accounted for in the correction.

Neutrinos were considered as not measurable and were excluded from the analysis of the hadron level Monte Carlo events; the results $\langle \Delta\phi(\mathbf{L1}) \rangle^{\mathrm{corr}}$ are thus not corrected for missing energy due to neutrino production. The same procedure was therefore also employed on the QCD models, with which the corrected values $\langle \Delta\phi(\mathbf{L1}) \rangle^{\mathrm{corr}}$ were compared (see chapter 5).

The same procedure for reconstructing the jet energies from the angles and for the determination of the common event plane that was used on the data (see section 4.2) was also employed on the HVFL events.

4.8 Determination of Errors

To have information on the reliability of the results of the string effect measurement, the errors on that measurement have to be estimated.

Various sources of errors exist. The statistical errors are due to the limited statistics of the measurement. From the 1992 and 1993 data, about 1.4 million events were used, with about 1.9 million fully reconstructed Monte Carlo events and 3 million hadron level Monte Carlo events for each year, making the statistical errors very small.

The systematic error gives the uncertainty of the corrected result due to imperfections in the simulation of the detector effects. It can not be reduced through higher statistics. One part of the systematic error is the error due to the model bias; this comes from the fact that the detector effects are estimated via the detector simulation of events from one specific event generator, only. The systematic error is found to be of the same size as the statistical error for the whole range of y_{cut} values; variations in the size of the systematic error are due to statistical fluctuations.

The total error given in the error bands of figures 4.38, 4.40 and 4.42 are the quadratic sum of the statistical error and the systematic errors:

$$\delta_{\mathrm{tot}} = \sqrt{(\delta_{\mathrm{stat}})^2 + (\delta_{\mathrm{syst}})^2 + (\delta_{\mathrm{mbias}})^2}.$$

The values of the errors on $\langle \Delta\phi(\mathbf{L1}) \rangle$ for all y_{cut} values considered are listed in tables 1 and 2 at the end of section 4.10.

4.8.1 Statistical Error

The single measurements of the angle shift $\Delta\phi(\mathbf{L1})$ of the leading particle in a jet spread around the mean value $\langle \Delta\phi(\mathbf{L1}) \rangle$ with a certain RMS (see the tables in section 4.10).

The statistical error of the observable $\langle \Delta\phi(\mathbf{L1}) \rangle$ is given by

$$\delta_{\mathrm{stat}} = \frac{\mathrm{RMS}\,(\Delta\phi(L1))}{\sqrt{N_{3-jet}}}$$

where N_{3-jet} is the number of 3-jet events (with more than 2 particles in the jet considered) from which the $\Delta\phi(\mathbf{L1})$ distribution was derived.

This statistical error is calculated for the raw data ($\delta_{\text{stat}}^{\text{raw DATA}}$), the hadron level MC ($\delta_{\text{stat}}^{\text{had lev}}$) and for the fully reconstructed MC ($\delta_{\text{stat}}^{\text{rec lev}}$), and decreases with the square root of the number of events used for the analysis.

In figures 4.39, 4.41 and 4.43 the statistical errors can be seen for the range of y_{cut} values used.

For $y_{cut} = 0.01$ in jet 1 **R3**, the statistical error is $\approx 0.02°$.

4.8.2 Systematic Error

The systematic error on $\langle \Delta\phi(\mathbf{L1}) \rangle$ arises from the correction term and is due to possible inefficiencies in the detector simulation; in figure 4.24 one can see that low momentum neutral particles are very badly simulated. The corrected values $\langle \Delta\phi(\mathbf{L1}) \rangle^{\text{corr}}$ will have some uncertainty caused by this inaccurate description of the detector response through the corrections that are applied to the raw values.

To estimate these uncertainties, $\langle \Delta\phi(\mathbf{L1}) \rangle$ was determined from both data and fully reconstructed MC using the following variations of the cuts, which were applied additionally to those described in section 4.2:

1. $E_{neutral} > 0.8\,\text{GeV}$.
2. $E_{charged} > 0.4\,\text{GeV}$.
3. $\min(\theta_{jet,beam_i}) > 40°$ instead of $\min(\theta_{jet,beam_i}) > 30°$ (see figure 4.6).

The former two are particle specific cuts, whereas the latter is an event specific cut.

The $\langle \Delta\phi(\mathbf{L1}) \rangle$ result for each of these runs on ALEPH data was corrected (using the corresponding GALEPH results and the standard HVFL results with the procedure described in section 4.7). The maximum of the absolute values of the differences between $\langle \Delta\phi(\mathbf{L1}) \rangle^{\text{corr}}$ taken from the standard analysis with those from the variations of the cuts is used as an estimate of the systematic error (this is done for each value of y_{cut}):

$$\delta_{\text{syst}} = \max_{\text{variations i}} \left(\left| \langle \Delta\phi(\mathbf{L1}) \rangle_{\text{std}}^{\text{corr}} - \langle \Delta\phi(\mathbf{L1}) \rangle_{\text{var i}}^{\text{corr}} \right| \right).$$

So the single differences between the results from the standard analysis and those with varied cuts are

$$\langle \Delta\phi(\mathbf{L1}) \rangle_{\text{std}}^{\text{corr}} - \langle \Delta\phi(\mathbf{L1}) \rangle_{\text{var i}}^{\text{corr}} =$$

$$\left(\langle \Delta\phi(\mathbf{L1}) \rangle_{\text{std}}^{\text{raw data}} - \langle \Delta\phi(\mathbf{L1}) \rangle_{\text{std}}^{\text{galeph}} \right) - \left(\langle \Delta\phi(\mathbf{L1}) \rangle_{\text{var i}}^{\text{raw data}} - \langle \Delta\phi(\mathbf{L1}) \rangle_{\text{var i}}^{\text{galeph}} \right).$$

These values can be seen for the three variations of the cuts in figures 4.39, 4.41 and 4.43.

It should be noted, that the combined value for 1992 and 1993 of the total detector simulation systematic error that is shown there is computed as

$$\delta_{\text{syst, 92+93}}^{\text{det sim}} = \left(\delta_{\text{syst, 92}}^{\text{det sim}} + \delta_{\text{syst, 93}}^{\text{det sim}} \right) / 2$$

where

$$\delta_{\text{syst, 92}}^{\text{det sim}} = \max \left(|\delta_{\text{neut, 92}}|, |\delta_{\text{char, 92}}|, |\delta_{\theta_{jet}, \text{92}}| \right).$$

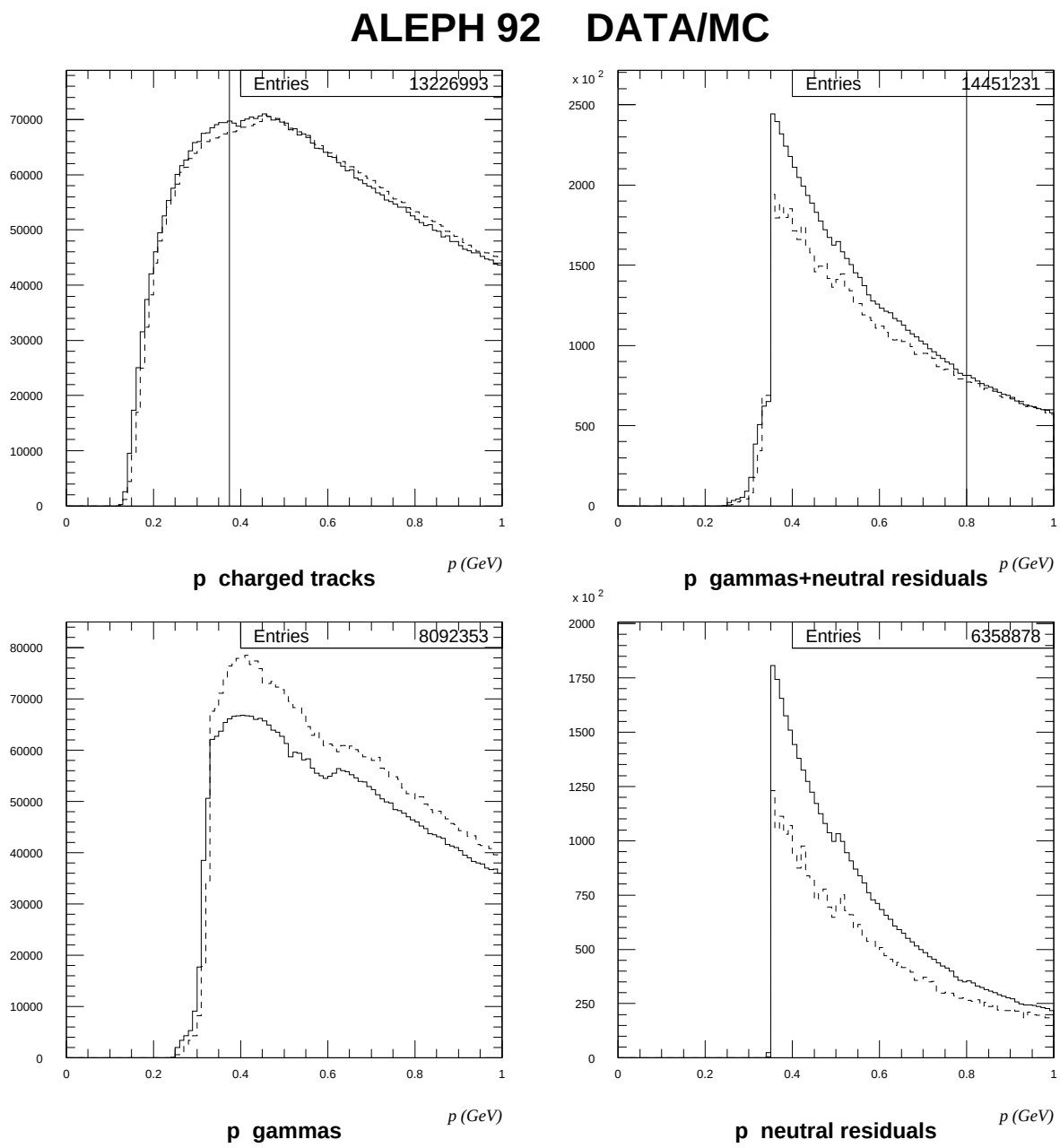

Figure 4.24: Detail of the p distribution for small momenta (MC superimposed as dashed line). The p distribution of the charged particles is well described starting from $p \approx 0.4\,\mathrm{GeV}$. The distributions for all neutral particles are in good agreement starting from $p \approx 0.8\,\mathrm{GeV}$. The separate distributions for gammas and neutral residuals are badly described by the MC. Note that the cut for the systematics analysis is made on the energy of charged and neutral particles and that neutrals are assumed as massless whereas all charged particles are assigned the $\pi^{\pm}$ mass. Thus the cut $E_{charged} > 0.4\,\mathrm{GeV}$ corresponds to $p_{charged} > 0.375\,\mathrm{GeV}$.

The curves giving the systematic errors from the cuts on $E_{neutral}$, $E_{charged}$ and $\min(\theta_{jet,beam_i})$ are calculated as

$$\delta_{\text{neut, 92+93}} = (\delta_{\text{neut, 92}} + \delta_{\text{neut, 93}})\,/2 \qquad \text{etc } \ldots .$$

Due to this interchange of calculating the mean and the maximum, the combined total systematic error can be larger than the maximum of the combined errors from the three variations of the cuts.

The systematic error is of about the same size as the statistical error for most y_{cut}, becoming twice as large for the central values of y_{cut}. It is $\approx 0.04°$ for jet 1 of **R3** for $y_{cut} = 0.01$.

4.8.3 Model Bias Error and Simplified Detector Simulation

Apart from the fact that the detector simulation is not perfect, it is only performed on events produced with one specific event generator — the HVFL Monte Carlo based on JETSET. All the fully reconstructed MC events (GALEPH events) used for the correction of the results for $\langle\Delta\phi(\mathbf{L1})\rangle$ were generated with HVFL.

But the HVFL generator is, after all, just a QCD model with inherent imperfections. This could lead to a systematic error on the corrected results. Computing the corrections with other QCD models might result in different values for $\langle\Delta\phi(\mathbf{L1})\rangle^{\text{corr}}$.

To estimate the systematic error coming from this model bias, it would be appropriate to compute $\langle\Delta\phi(\mathbf{L1})\rangle^{\text{corr}}$ using corrections from several QCD models and to take the maximum deviation for all these models from the results of a reference model (which should be chosen as the one in which one has the most trust) as the error:

$$\delta_{\text{mbias}} = \max_{\text{models i}} \left(\left| \langle\Delta\phi(\mathbf{L1})\rangle^{\text{corr}}_{\text{ref}} - \langle\Delta\phi(\mathbf{L1})\rangle^{\text{corr}}_{\text{model i}} \right| \right)$$

where $\langle\Delta\phi(\mathbf{L1})\rangle^{\text{corr}}_{\text{ref}}$ denotes the $\langle\Delta\phi(\mathbf{L1})\rangle$ value corrected using the reference model and $\langle\Delta\phi(\mathbf{L1})\rangle^{\text{corr}}_{\text{model i}}$ is the $\langle\Delta\phi(\mathbf{L1})\rangle$ value corrected with the i-th QCD model.

The single differences between $\langle\Delta\phi(\mathbf{L1})\rangle$ corrected with the reference model and $\langle\Delta\phi(\mathbf{L1})\rangle$ corrected with the i-th QCD model are

$$\langle\Delta\phi(\mathbf{L1})\rangle^{\text{corr}}_{\text{ref}} - \langle\Delta\phi(\mathbf{L1})\rangle^{\text{corr}}_{\text{model i}} =$$

$$\left(\langle\Delta\phi(\mathbf{L1})\rangle^{\text{had lev}}_{\text{ref}} - \langle\Delta\phi(\mathbf{L1})\rangle^{\text{rec lev}}_{\text{ref}} \right) - \left(\langle\Delta\phi(\mathbf{L1})\rangle^{\text{had lev}}_{\text{model i}} - \langle\Delta\phi(\mathbf{L1})\rangle^{\text{rec lev}}_{\text{model i}} \right).$$

But the complete detector simulation is very demanding in terms of computer time and storage space requirements for the output files. The generation of an event sample with sufficient statistics for several QCD models is beyond possibilities.

Nevertheless, an easy to implement simplified detector simulation (SDS; see reference [16]) which describes the most important aspects of the full-featured detector simulation can be employed to study the model bias error.

This simplified detector simulation is applied on the output of an event generator and works in the following way:

- Neutrinos are removed since they are unobservable.
- On the charged particles, the following cuts are applied:

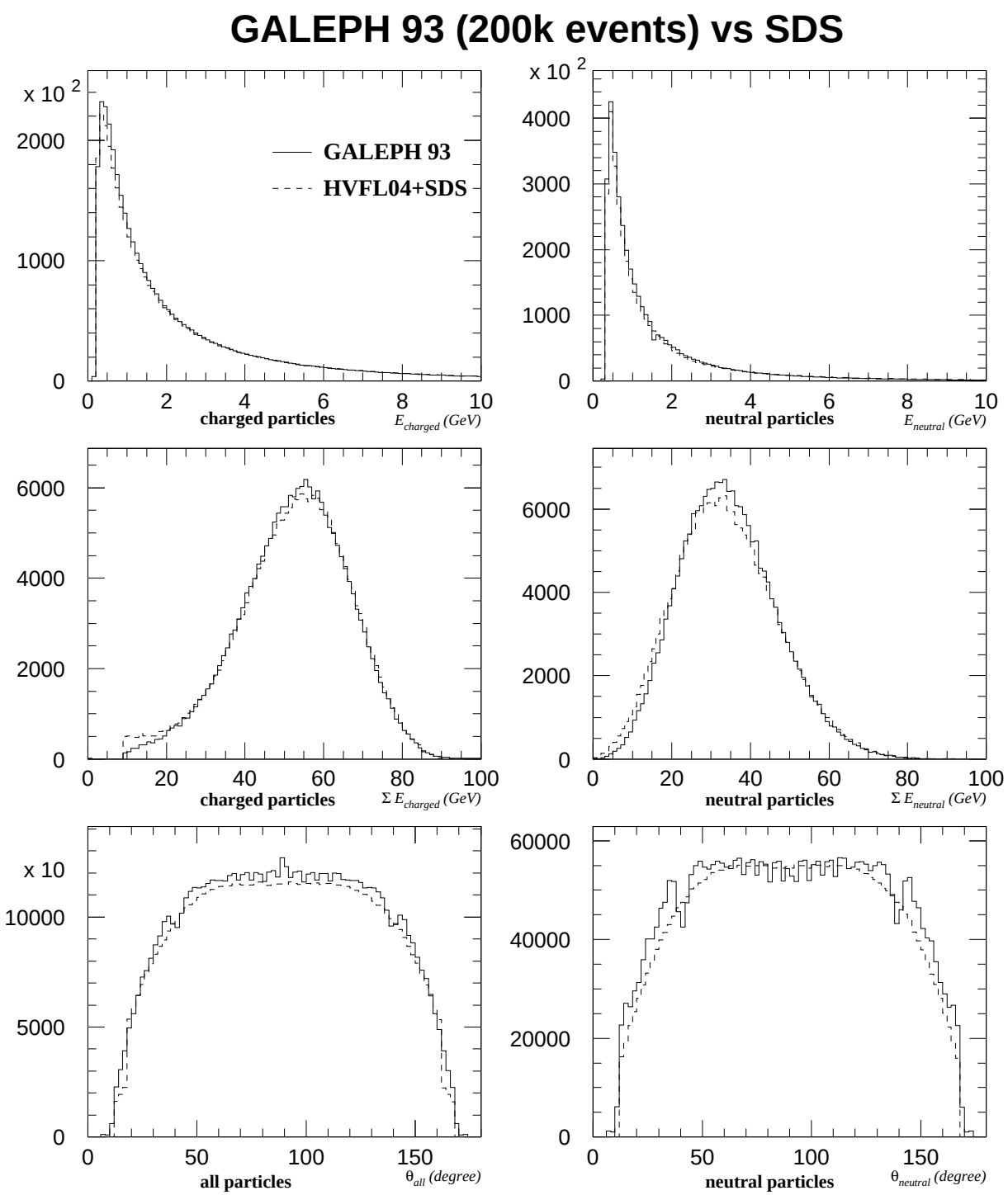

Figure 4.25: Comparison of some global distributions for fully reconstructed MC events and events from the simplified detector simulation (SDS). These shapes are not perfectly reproduced but fairly well approximated.

1. $|p_{charged_\perp}| > 0.16\,\mathrm{GeV}$ (momentum perpendicular to the beam axis)
2. $\theta_{charged} > 14.5^\circ$ (polar angle to the beam axis)
3. $N_{charged} \geq 5$ (number of charged particles in an event)
4. $\sum E_{charged} > 0.1 E_{cm}$ (sum of charged energy in an event)
5. $|d_0| < 2.5\,\mathrm{cm}$ ($|d_0|$ is the smallest distance to the interaction point for decay products from K^0_S and strange baryon decays)

These cuts approximate the geometric acceptance for charged tracks and the cuts used for class 16 selection (see section 4.2).

The absolute value of the momentum is furthermore smeared with a gaussian whose standard deviation is typical for the errors for momentum measurements in ALEPH (see references [1] or [5]):

$$|p'| = |p| + \Delta|p|,$$

where

$$\Delta|p| = R_{\mathrm{rand}} \cdot 0.0008 \cdot |p|^2.$$

R_{rand} is a normal distributed random number (with mean 0 and variance 1).

All charged particles are assigned the $\pi^\pm$ mass (for ALEPH data, the assumption of the pion mass for all charged particles is made by default).

The energies and absolute values of the momenta are rescaled, preserving the original momentum directions. The smearing of the momenta and the pion mass assignment is made before the above cuts are applied.

- All neutral particles are treated together — a separate simulation of EFLW types 4 (photons) and 5 (residuals) is difficult (see figure 4.24). The following procedure is used on all neutral particles:

  1. The cut $\theta_{neutral} > 12^\circ$ is made to describe the angular distribution of the neutrals.
  2. The description of the energy distribution is complicated, since in the hadron level MC, photon energies down to 0 GeV occur,whereas for the detector, the lower limit for measurable energies is $\approx 0.3\,\mathrm{GeV}$. A simple cut on $E_{neutral} > 0.3\,\mathrm{GeV}$ does not satisfactorily reproduce the number of neutral particles.

     The alternative used is to make for all neutral particles with $E < 2\,\mathrm{GeV}$ the substitution

     $$E \longrightarrow E + 0.2\,\mathrm{GeV}$$

     with probability $p = E/(2\,\mathrm{GeV})$. Particles with small energies are shifted more often than such with higher energies. Particles with energies above 2 GeV are left unaffected.
  3. The energies of the neutral particles (after the above substitution) are smeared in the following way:

     $$E'_{neutral} = E_{neutral} + \Delta E_{neutral}$$

where

$$\Delta E_{neutral} = R_{\text{rand}} \cdot 0.19 \cdot \sqrt{E_{neutral}}.$$

R_{rand} is again a normal distributed random number (with mean 0 and variance 1). The smearing is inspired by the energy resolution of the ECAL (see [5]; the term $0.017 E_{neutral}$ is neglected). Subsequently, the cut $E_{neutral} > 0.3\,\text{GeV}$ is applied.

- Finally, the normal event selection cuts described in section 4.2 are applied (ie. the cuts on $\sum E_{\text{EFLW}}$, θ_{thrust} and $\theta_{jet,beam_i}$).

In figure 4.25, a comparison is made for some global particle distributions between fully reconstructed MC events and events from the simplified detector simulation. For this comparison, the SDS was applied to events generated with HVFL04 (the 1993 GALEPH events are generated with the same generator).

For the estimation of the model bias error, the following QCD models were used together with SDS (for more details on these models, see section 5.2):

1. JS73 PSCO2: JETSET 7.3 coherent parton shower with string fragmentation.
   The latest best fit parameters ([29]) are used. This model is used as the reference model.

2. JS73 PSCO2 LLLA: JETSET 7.3 coherent parton shower with string fragmentation.
   The same best fit parameters as for PSCO2 are used, with the exception:
   `PARJ(81)`$= \Lambda_{LLA} = 0.304\,\text{GeV}$: the lower error bound (see reference [4] for the estimate of the errors of the best fit parameters) around the default value (`PARJ(81)`$= 0.329\,\text{GeV}$) is used.

3. JS73 PSCO2 MMIN: JETSET 7.3 coherent parton shower with string fragmentation.
   The same best fit parameters as for PSCO2 are used, with the exception:
   `PARJ(82)`$= M_{min} = 1.37\,\text{GeV}$: the upper error bound around the default value (`PARJ(82)`$= 1.21\,\text{GeV}$) is used.

4. JS73 PSAS1: JETSET 7.3 coherent parton shower with string fragmentation.
   With `MSTJ(44)=1`, α_s is chosen to run with $Q^2 = m^2/4$ (where m is the mass of the decaying parton).

5. HERWIG 5.6: HERWIG 5.6 coherent parton shower with cluster fragmentation.

6. ARIADNE 4.3: ARIADNE 4.3 color dipole cascade with string fragmentation.

7. JS73 MESF: JETSET 7.3 optimized matrix element with string fragmentation.

In figures 4.39, 4.41 and 4.43, the contributions of the models PSAS1, HERW56, ARIADNE and MESF to the model bias error can be seen.

For jet 1 of **R3** at $y_{cut} = 0.01$ as a typical example, a systematic error due to the model bias of $\approx 0.03^\circ$ is found.

4.9 Results from the Momentum Flow Analysis

The azimuthal momentum flow in the reconstructed event plane has been studied for ALEPH data (with the selection cuts from section 4.2) using the asymmetries defined in section 2.4.

In figure 4.26 the momentum flow for some typical kinematic configurations from the Dalitz plot is shown. In **R3**, the third jet can be seen to have low momentum flow whereas in **R1** configurations with even sharing of momentum flow between jet 2 and jet 3 can be seen (symmetric events).

For kinematic configurations from the Dalitz plot centered around $\phi_{13} = 112.5°$ and $z = 0.24$, the jet profiles of the 3 jets are shown in figure 4.27.

The reassignment of particles to the jet axes via minimum angle (see figure 4.28 which shows the jets from the same Dalitz configurations as before) shows the same characteristic jet profiles with unphysically steep edges that could already be seen for the TRISTAR events (figure 2.5).

In figure 4.29 the momentum flow distributions for jet 1 and jet 2 in **R3** and for jet 1 in the three kinematic regions are compared between uncorrected data and MC. The momentum flow asymmetry can be seen to be stronger in **R3** compared to **R2** and especially **R1**. The MC predicts more momentum flow in the jet core than is observed from the data (the distributions are normalized to the number of 3-jet events in the corresponding kinematic region).

The following table gives the (uncorrected) values of $A_{LR}^{\pm 8}$ for data and MC (1992) at $y_{cut} = 0.009$:

$A_{LR}^{\pm 8}$		DATA 92	GALEPH 92
R1	J1	−0.025	−0.020
	J2	−0.060	−0.035
R2	J1	−0.059	−0.054
	J2	0.024	0.048
R3	J1	−0.087	−0.086
	J2	0.094	0.093

The results for **R3** are fairly close to the expectations from TRISTAR Y120, where asymmetries around ±0.100 were observed for jet 1 and jet 2 respectively.

The detailed asymmetries (defined as in section 2.4) are shown in figure 4.30 for the three kinematic regions and for the interjet exclude case (with smaller asymmetries in the jet core for jet 1; see section 4.10 for the 30° interjet exclude scheme used for the analysis of the data).

The momentum flow distributions for particles from different p intervals for jet 1 in **R3** show the change of the sign of the mean values from positive to negative when going to larger p, reaching an asymptotic value of ≈ -0.54 (see figure 4.31).

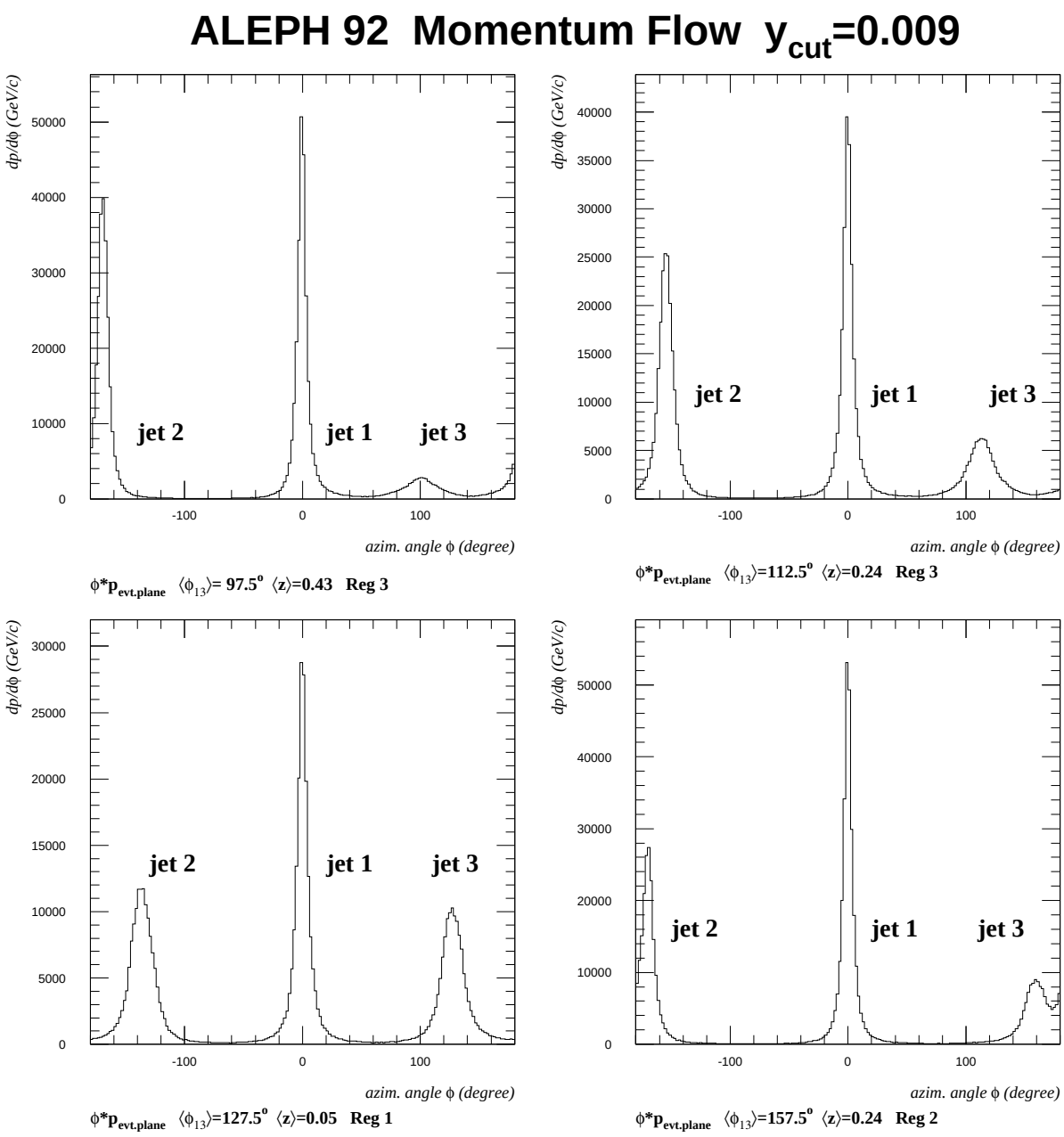

Figure 4.26: Momentum flow in the event plane for typical 3-jet kinematic configurations. The momentum flow and the mean azimuthal angle of the jets can be seen to vary for the configurations.

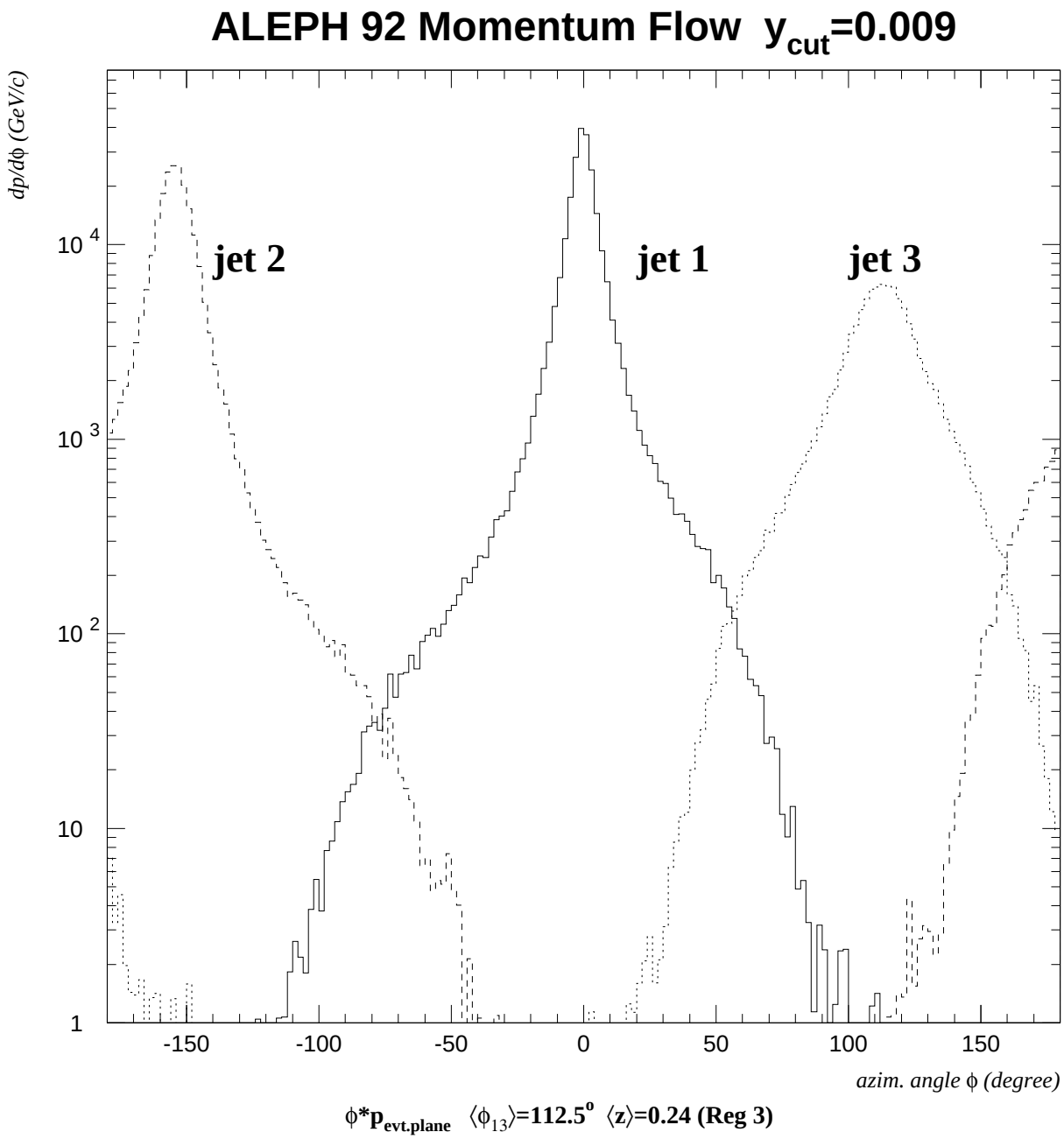

Figure 4.27: Momentum flow for a Dalitz configuration from **R3**.

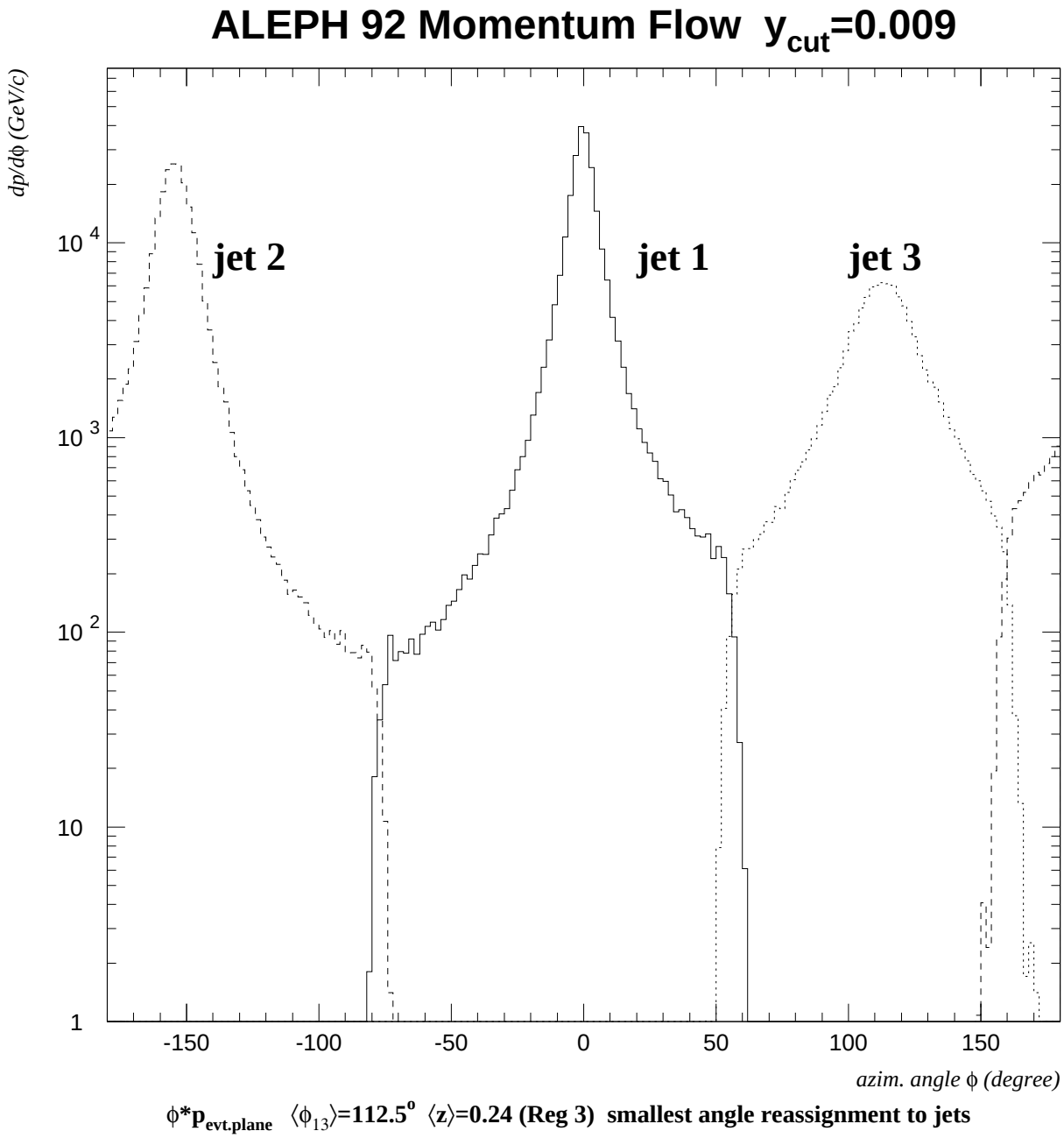

Figure 4.28: Momentum flow for a Dalitz configuration from **R3** after reassignment of the particles to the closest jet. The jet borders are very steep.

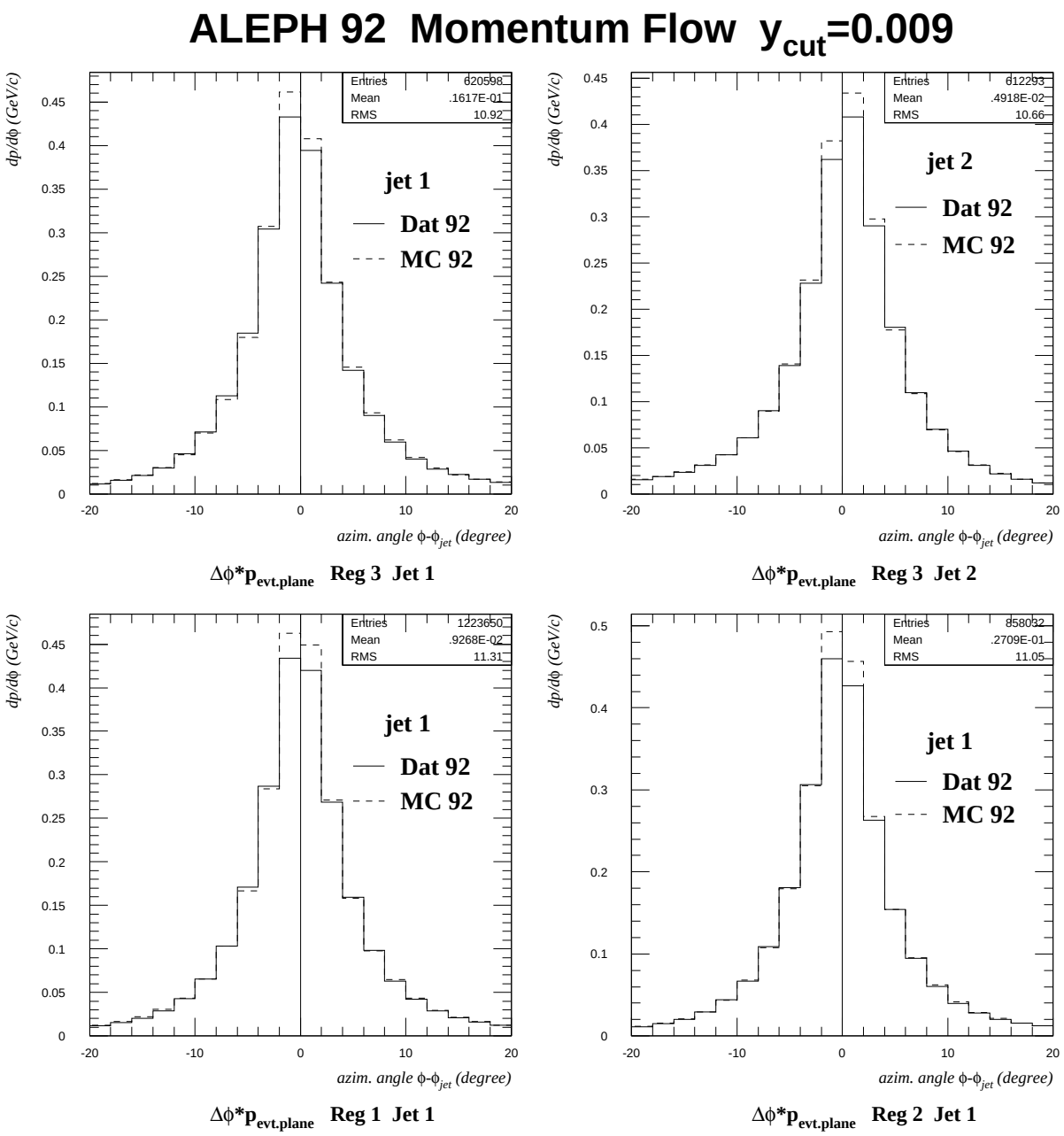

Figure 4.29: Comparison of momentum flow around the jet axes between data and Monte Carlo (1992). The MC predicts a slightly higher momentum flow in the jet core. The asymmetries are larger for **R3**.

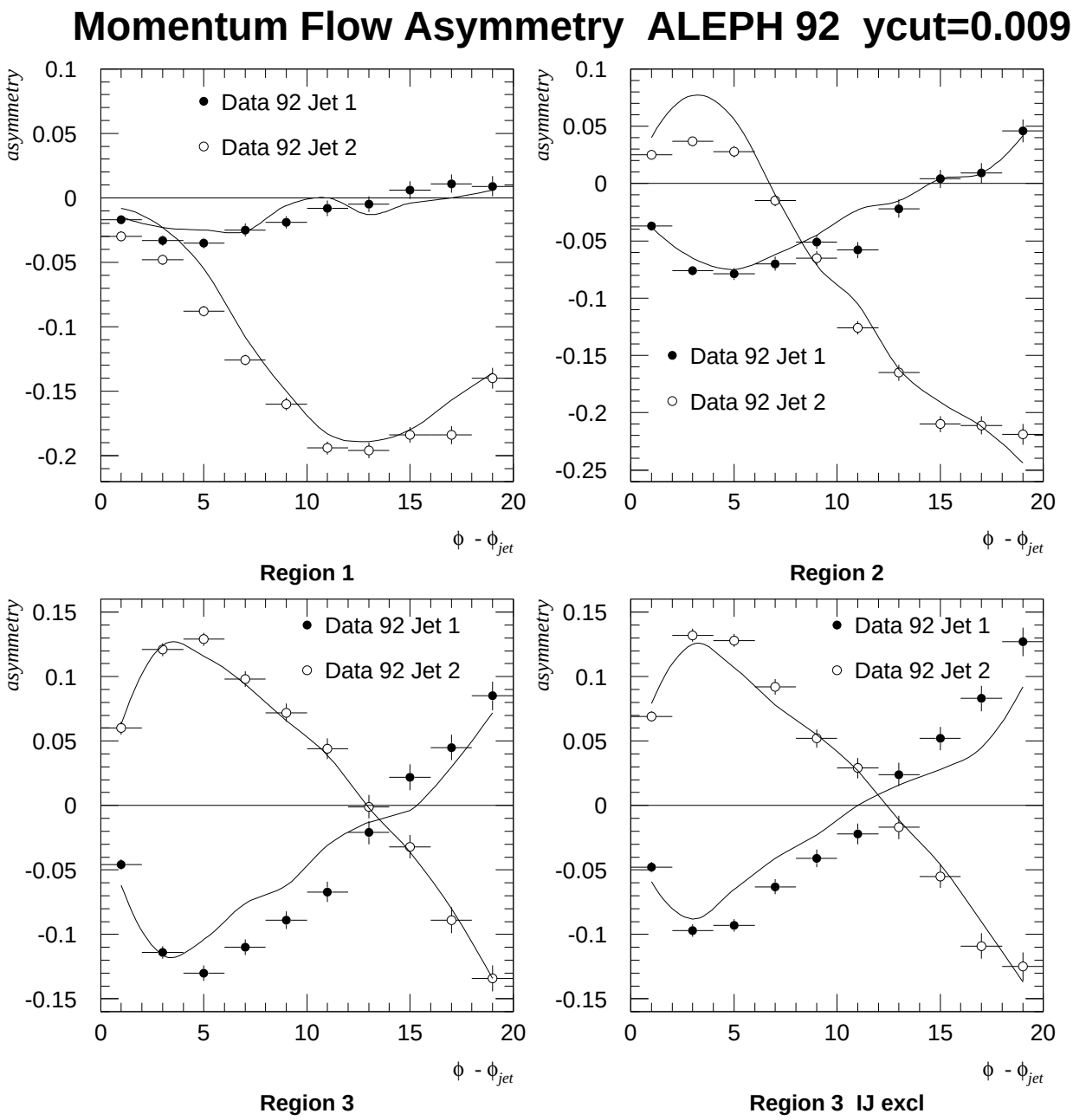

Figure 4.30: Detailed asymmetries for jet 1 and jet 2 in the three kinematic regions. The asymmetries are almost mirror symmetric between jet 1 and jet 2 for **R3**. The exclusion of interjet particles reduces the asymmetry especially in the core of jet 1.

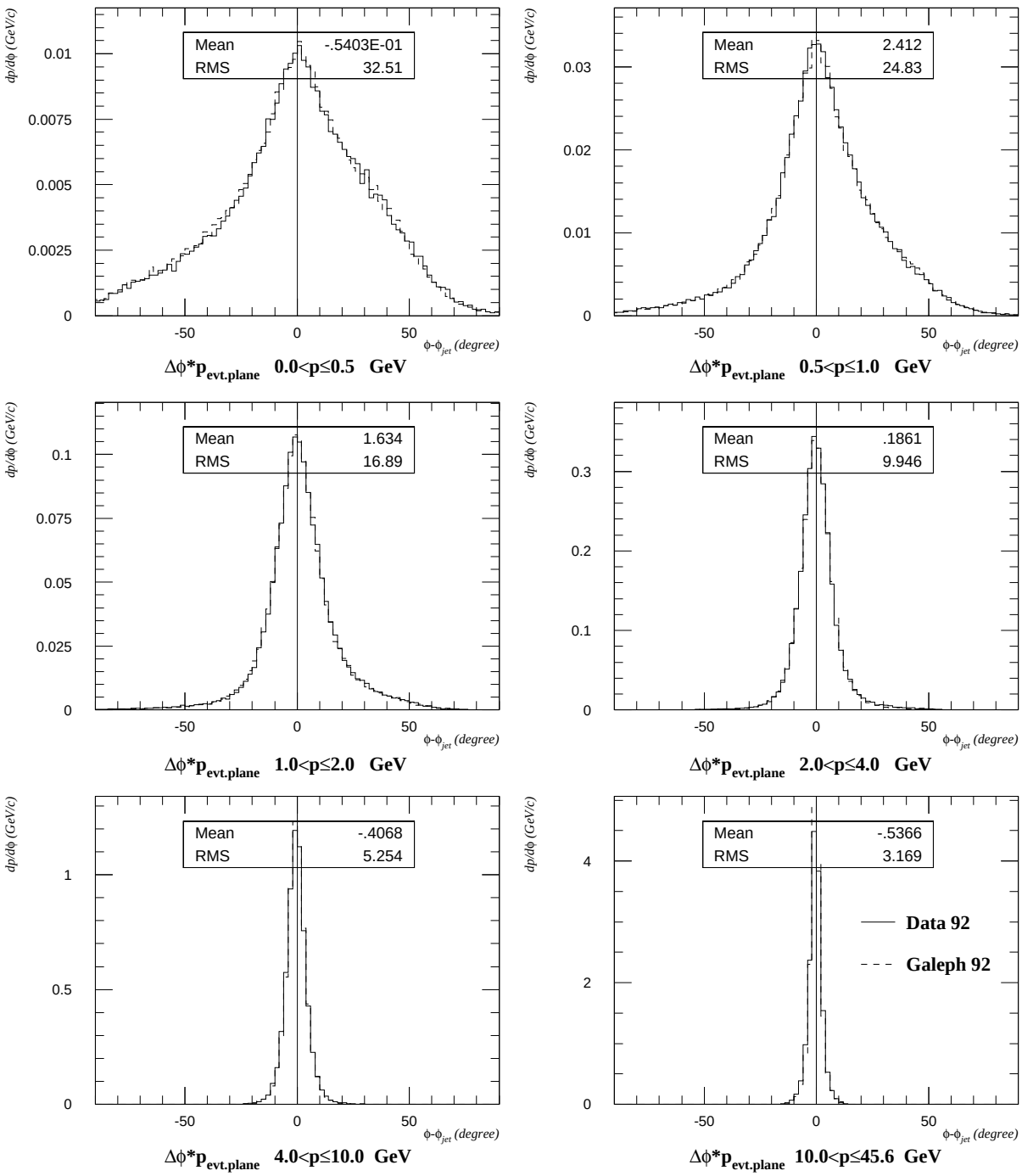

Figure 4.31: The momentum flow distributions for particles from different p intervals. As observed for the TRISTAR events, the mean has a maximum for low p particles and reaches an asymptotic value of $\approx -0.54^\circ$ for high p particles, motivating the $\langle \Delta\phi(\mathbf{L1}) \rangle$ analysis.

4.10 Results from the Angle Shift Analysis

The angle shift of the mean of the $\Delta\phi$ distributions for particles from different p intervals is shown in figure 4.32. It shows the same behavior as was observed for Y120 TRISTAR events in section 2.8 (figure 2.14).

The mean values go to an asymptotic value of $\approx -0.55^\circ$ for jet 1 **R3** at $y_{cut} = 0.009$ (a problem with the description of the number of low momentum particles in the MC can be seen; the normalization is made to the number of 3-jet events in the kinematic region). The distributions become narrower with increasing momentum. In chapter 2 it was shown that this approximates the angle shift between parton jet and hadron jet caused by the fragmentation process.

The dependence of $\langle\Delta\phi\rangle$ on the momentum of the particles is also shown in figures 4.34, 4.35 and 4.36 for **R3** at different values of y_{cut}. The angle shift $\langle\Delta\phi\rangle$ can be seen to be approximately the same for jet 1 and jet 2 with reversed signs. It becomes smaller with increasing y_{cut} (especially for the low momentum particles; but also the asymptotic values are affected — compare tables 1 and 2 in this section).

The predictions of the Monte Carlo for $\langle\Delta\phi\rangle$ fit the data results for soft $y_{cut} = 0.003$ quite well; for (commonly used) larger values of y_{cut}, the Monte Carlo predictions are too small (see also section 4.5).

For $q\overline{q}\gamma$ events, the angle shift can be seen to be reversed with respect to that in $q\overline{q}g$ events (see section 4.4 for details).

The angle shift of the charged particles can be seen to be larger for low momentum particle than that of the neutral particles (gammas and residuals together). Nevertheless, the asymptotic values agree quite well.

The following table gives the uncorrected $\langle\Delta\phi(\mathbf{L1})\rangle$ results for ALEPH data from 1992 at $y_{cut} = 0.009$ (statistical errors only; the RMS of the distributions is given in brackets):

$\langle\Delta\phi(\mathbf{L1})\rangle$		all part	charged	neutrals
R1	J1	$-0.147 \pm 0.017(4.483)$	$-0.140 \pm 0.020(4.452)$	$-0.163 \pm 0.031(4.555)$
	J2	$-0.862 \pm 0.024(6.466)$	$-0.870 \pm 0.028(6.382)$	$-0.840 \pm 0.048(6.683)$
R2	J1	$-0.359 \pm 0.019(4.301)$	$-0.350 \pm 0.023(4.284)$	$-0.378 \pm 0.036(4.341)$
	J2	$-0.021 \pm 0.024(5.323)$	$-0.028 \pm 0.028(5.291)$	$-0.004 \pm 0.046(5.406)$
R3	J1	$-0.578 \pm 0.024(4.527)$	$-0.574 \pm 0.028(4.510)$	$-0.587 \pm 0.045(4.569)$
	J2	$0.592 \pm 0.025(4.736)$	$0.566 \pm 0.029(4.736)$	$0.655 \pm 0.046(4.735)$

The next table gives the (uncorrected) values for $\langle\Delta\phi(\mathbf{L1})\rangle$ for ALEPH data and MC (1992) at $y_{cut} = 0.009$ (statistical errors only; the RMS of the distributions is given in brackets):

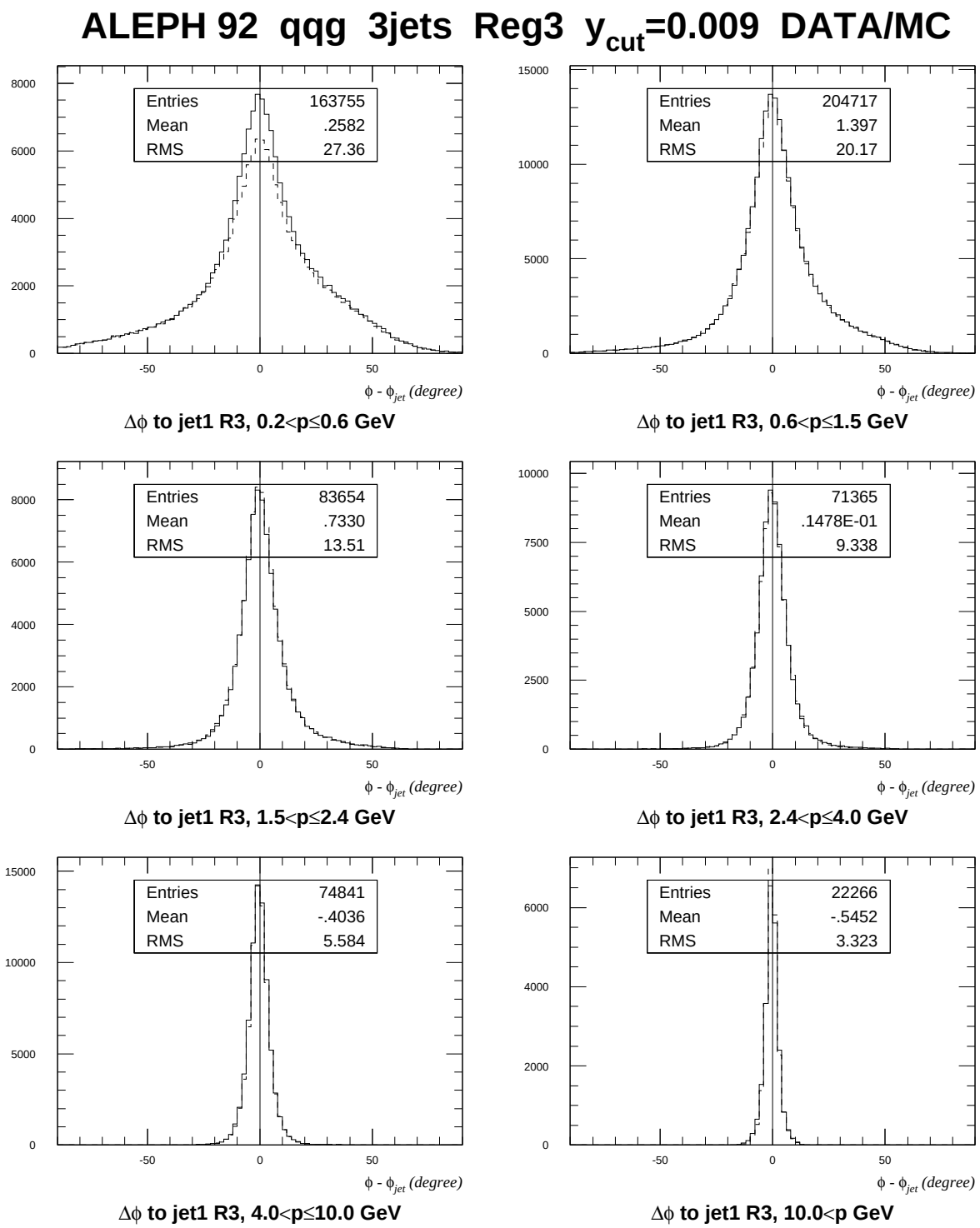

Figure 4.32: The distribution of $\Delta\phi$ for particles from different p intervals — comparison between data and MC. For high p, the distribution is very narrow with mean $\approx -0.55^\circ$. For low p, the description by the MC is bad in the core region.

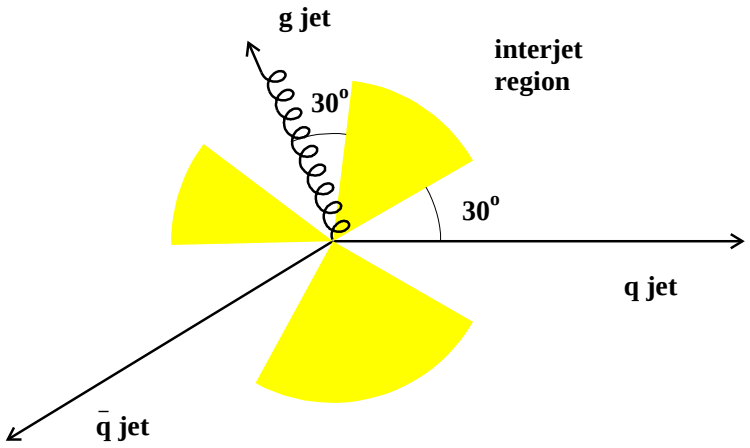

Figure 4.33: Symmetric definition of the interjet region. The 40% definition used for the TRISTAR studies cuts asymmetrically around the jet axes and obscures the angle shift effect.

$\langle\Delta\phi(\mathbf{L1})\rangle$		DATA 92	GALEPH 92
R1	J1	$-0.147 \pm 0.017(4.483)$	$-0.110 \pm 0.013(4.332)$
	J2	$-0.862 \pm 0.024(6.466)$	$-0.631 \pm 0.019(6.170)$
R2	J1	$-0.359 \pm 0.019(4.301)$	$-0.282 \pm 0.016(4.171)$
	J2	$-0.021 \pm 0.024(5.323)$	$0.122 \pm 0.019(5.088)$
R3	J1	$-0.578 \pm 0.024(4.527)$	$-0.444 \pm 0.019(4.319)$
	J2	$0.592 \pm 0.025(4.736)$	$0.510 \pm 0.020(4.467)$

The effects of the interjet particles and the cluster algorithm on the observable $\langle\Delta\phi(\mathbf{L1})\rangle$ have also been studied. For the reassignment of particles to the closest jet, the same procedure was used that was described in section 2.5. For the definition of the interjet region, a different scheme was used. The 40% definition cuts asymmetrically around the jet axes, obscuring the angle shift effect. For this reason, an alternative 30° definition visualized in figure 4.33 was introduced. The 40% definition of the interjet region could be used for symmetric events — but for a successful analysis of the string effect on symmetric events, the gluon jet must be identified (eg. using b tagging).

The next table compares the uncorrected results for $\langle\Delta\phi(\mathbf{L1})\rangle$ for the exclusion of interjet particles and for the reassignment with the standard results (ALEPH data 1992; $y_{cut} = 0.009$; statistical errors only; the RMS of the distributions is given in brackets):

$\langle\Delta\phi(\mathbf{L1})\rangle$		standard	IJ exclude	reassign
R1	J1	$-0.147 \pm 0.017(4.483)$	$-0.084 \pm 0.014(3.761)$	$-0.141 \pm 0.017(4.409)$
	J2	$-0.862 \pm 0.024(6.466)$	$-0.051 \pm 0.021(5.512)$	$-0.701 \pm 0.024(6.415)$
R2	J1	$-0.359 \pm 0.019(4.301)$	$-0.193 \pm 0.016(3.626)$	$-0.326 \pm 0.019(4.221)$
	J2	$-0.021 \pm 0.024(5.323)$	$0.493 \pm 0.021(4.752)$	$-0.016 \pm 0.023(5.216)$
R3	J1	$-0.578 \pm 0.024(4.527)$	$-0.392 \pm 0.020(3.847)$	$-0.498 \pm 0.023(4.410)$
	J2	$0.592 \pm 0.025(4.736)$	$0.540 \pm 0.022(4.166)$	$0.475 \pm 0.024(4.612)$

The exclusion of interjet particle reduces the $\langle\Delta\phi(\mathbf{L1})\rangle$ effect by $\approx 30\%$ (compared to $\approx 50\%$ for TRISTAR Y120 configurations). The $\langle\Delta\phi\rangle$ distribution is narrower. One should note that here, the reduction was given with respect to $\langle\Delta\phi\rangle = 0$; if one takes the $\langle\Delta\phi(\mathbf{L1})\rangle$ value from MEIF ($\approx 0.2°$; see section 5.3) to give the "zero string effect" value, then the reduction due to the exclusion of interjet particles gets even smaller.

In contrast to the expectations from TRISTAR (where an increase by 15%) was observed), the reassignment reduces the effect by some 15% when applied on **R3** configurations from the data.

Figure 4.44 shows the y_{cut} dependence of $\langle\Delta\phi(\mathbf{L1})\rangle$ for raw data and MC 1992. For soft y_{cut} values, data and MC show an angle shift effect of the same size; for larger y_{cut} values, the data shows a larger string effect than the MC. The results from the exclusion of interjet particles and from the reassignment are also shown.

The uncorrected $\Delta\phi(\mathbf{L1})$ distributions for jet 1 and jet 2 in **R3** for $y_{cut} = 0.01$ can be seen in figure 4.37. The data distribution is wider and has a larger mean. For calculating the average values, the range $\pm 50°$ has been used.

The $\langle\Delta\phi(\mathbf{L1})\rangle^{\text{corr}}$ angle shift measurement was carried out on the ALEPH data from 1992 and 1993 for a range of 21 (logarithmically spaced) y_{cut} values between 0.001 and 0.1.

The results from the analysis of 1992 and 1993 data (which had to be processed separately, due to the need to apply different corrections) were statistically combined in the following way:

$$\langle\Delta\phi(\mathbf{L1})\rangle^{\text{corr}}_{92+93} = \left(\langle\Delta\phi(\mathbf{L1})\rangle^{\text{corr}}_{92} + \langle\Delta\phi(\mathbf{L1})\rangle^{\text{corr}}_{93}\right)/2.$$

Since the data samples for 1992 and 1993 are of about the same size, this seems justified.

The errors for the combined $92 + 93$ results were computed in the following way:

- statistical error: since the combined data sample is twice as large as the ones for the individual years, $\delta^{92+93}_{\text{stat}}$ is defined as

$$\delta^{92+93}_{\text{stat}} = \left(\delta^{92}_{\text{stat}} + \delta^{93}_{\text{stat}}\right)/(2\sqrt{2}).$$

- systematic error: the systematic error can not be lowered with increasing statistics. The mean of the systematic errors from 1992 and 1993 is used:

$$\delta^{92+93}_{\text{syst}} = \left(\delta^{92}_{\text{syst}} + \delta^{93}_{\text{syst}}\right)/2.$$

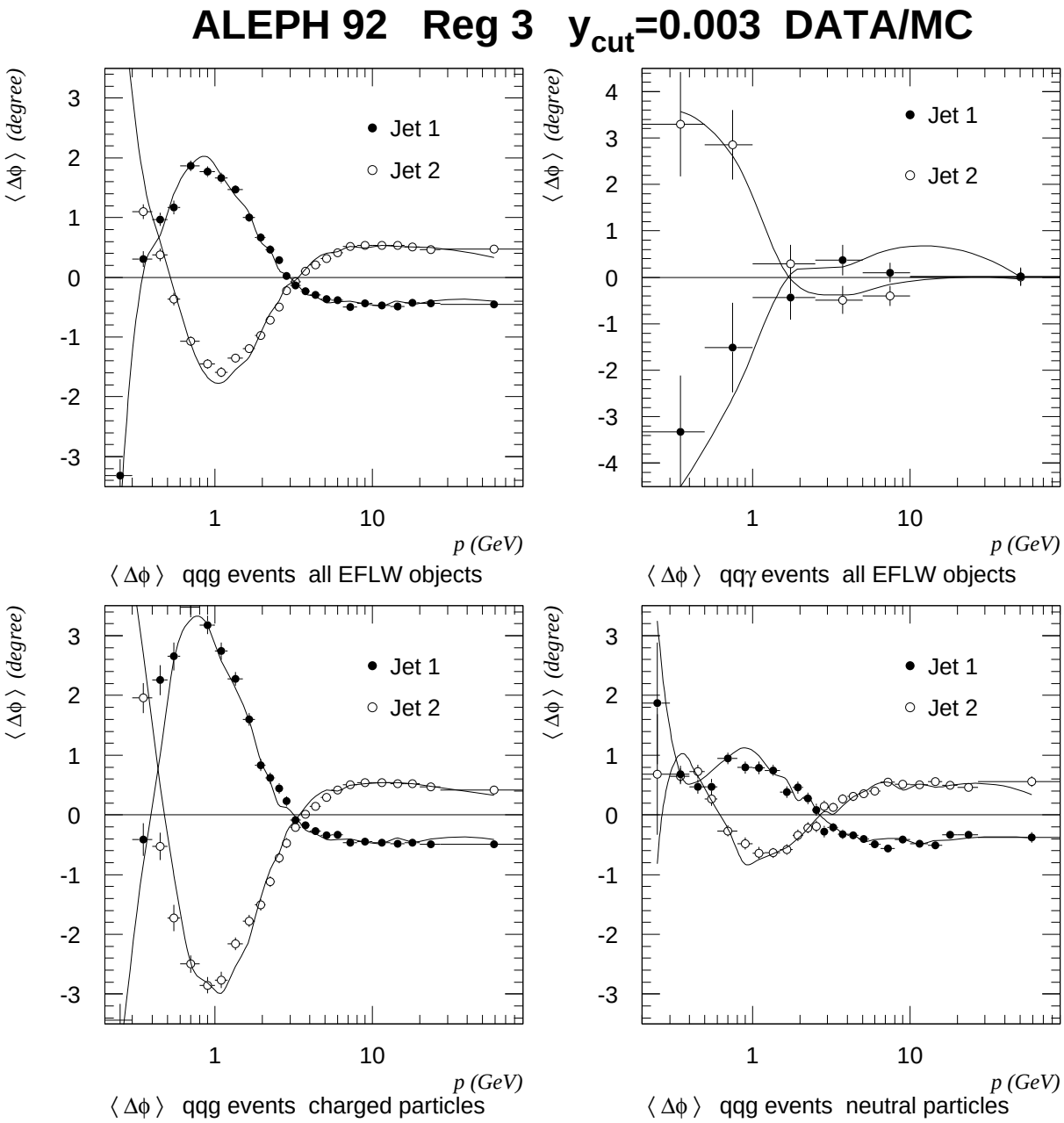

Figure 4.34: Dependence of $\langle\Delta\phi\rangle$ on p for **R3** events from ALEPH 1992 data at $y_{cut} = 0.003$. The results from the fully reconstructed MCs are superimposed as solid lines.

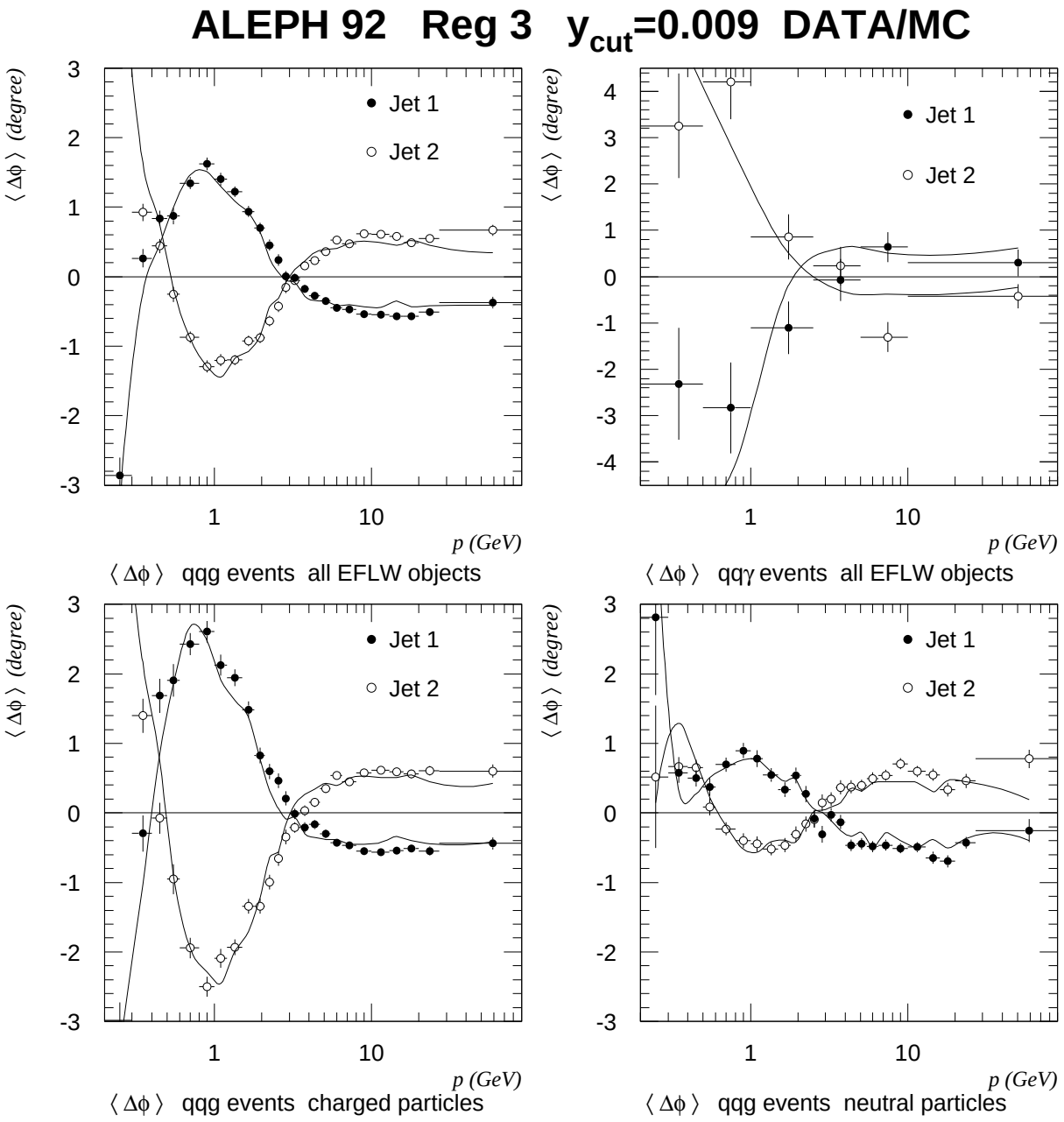

Figure 4.35: Dependence of $\langle\Delta\phi\rangle$ on p for **R3** events from ALEPH 1992 data at $y_{cut} = 0.009$. The results from the fully reconstructed MCs are superimposed as solid lines.

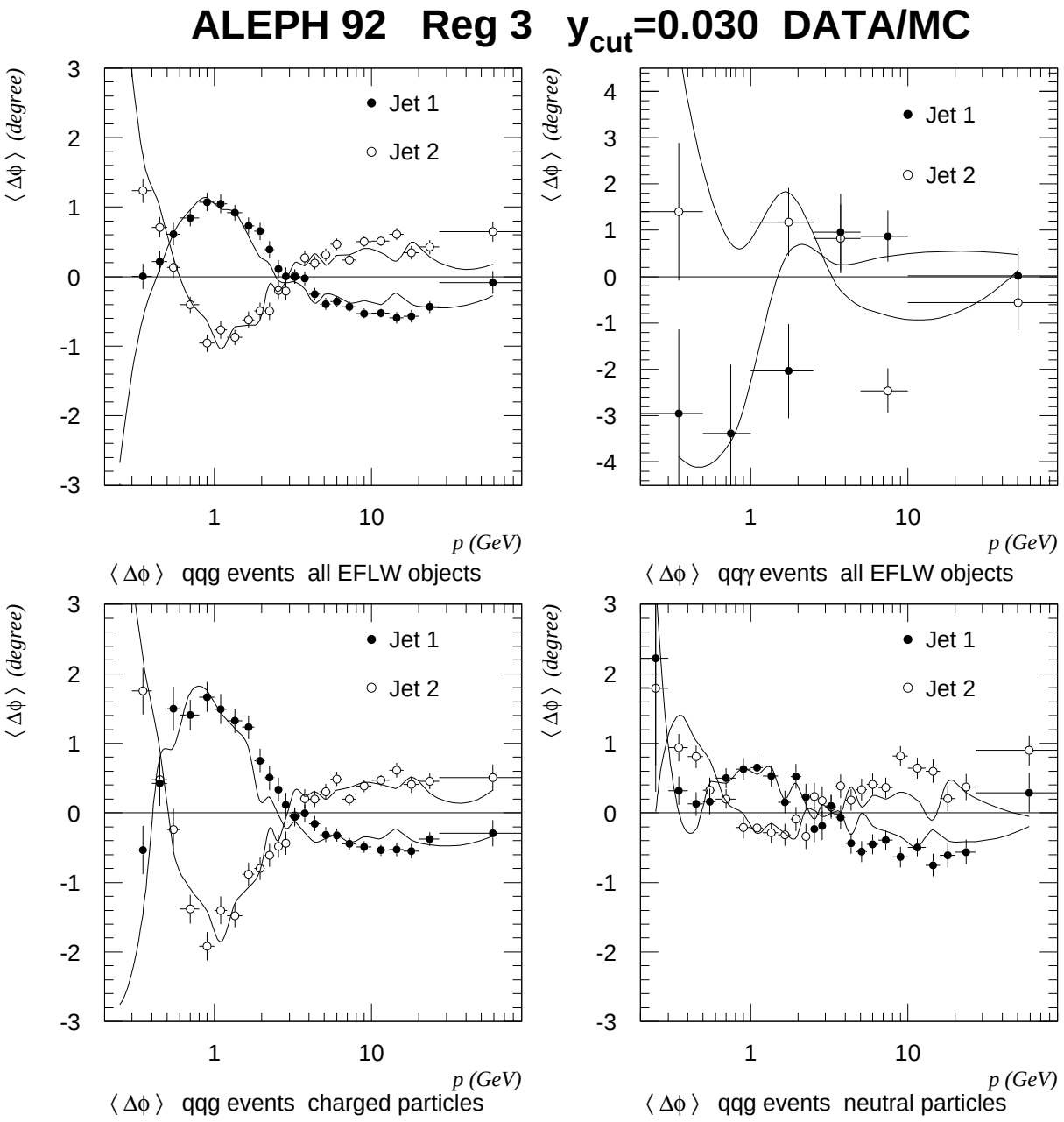

Figure 4.36: Dependence of $\langle\Delta\phi\rangle$ on p for **R3** events from ALEPH 1992 data at $y_{cut} = 0.030$. The results from the fully reconstructed MCs are superimposed as solid lines.

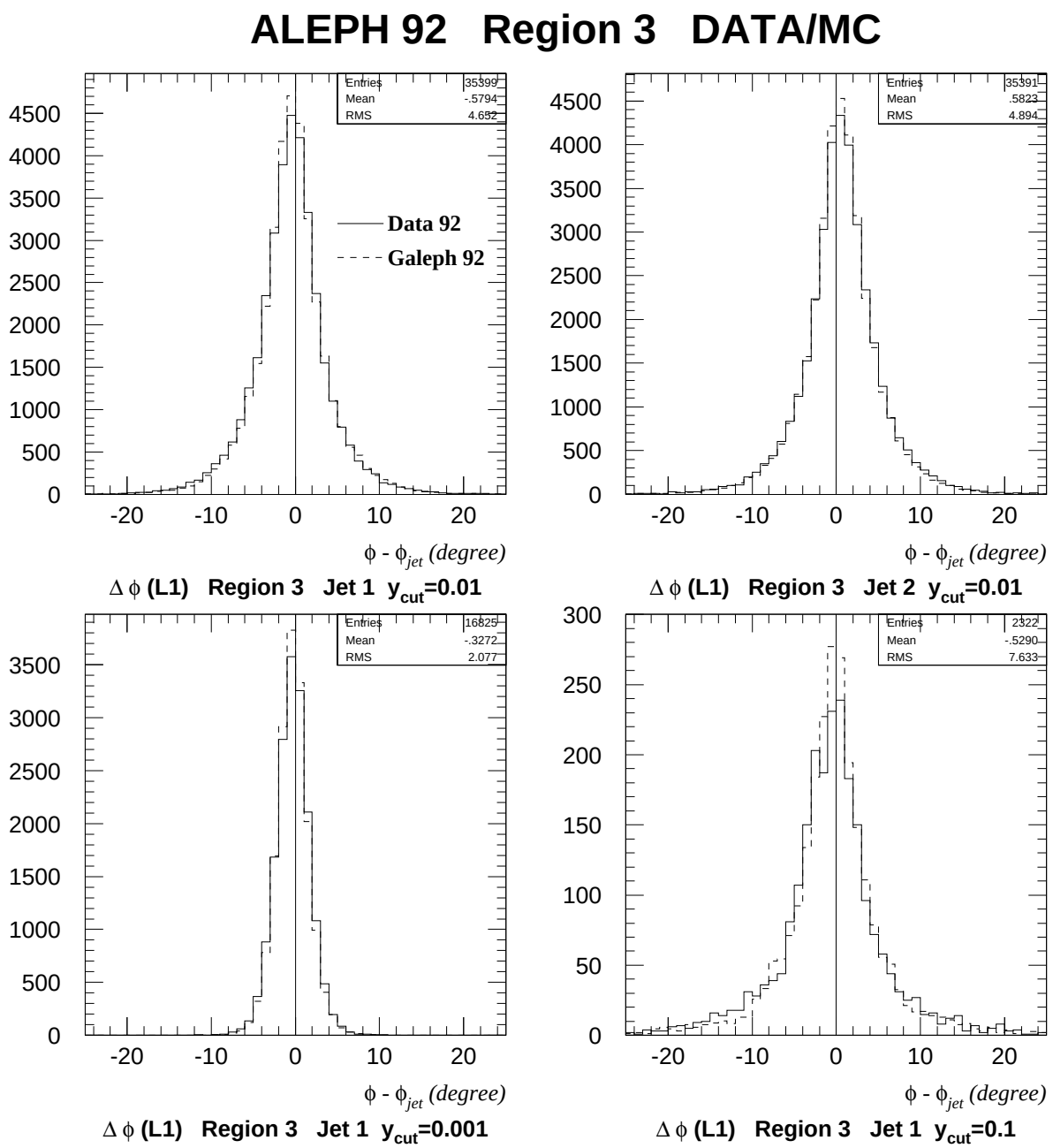

Figure 4.37: Comparison of the $\Delta\phi(\mathbf{L1})$ distributions around jet 1 and jet 2 (in $\mathbf{R3}$ for $y_{cut} = 0.01$) between (uncorrected) data and MC. The data distributions are broader with a larger mean value. The $\Delta\phi(\mathbf{L1})$ distributions for jet 1 at $y_{cut} = 0.1$ and $y_{cut} = 0.001$ are also shown; for harder y_{cut}, the distributions become broader.

The results for $\langle\Delta\phi(\mathbf{L1})\rangle^{\rm corr}_{92+93}$ for jet 1 and jet 2 in the three kinematic regions are shown in figures 4.38, 4.40 and 4.42 (the grey bands show the total error; see section 4.8) with details on the corresponding errors in figures 4.39, 4.41 and 4.43.

The predictions of the most important QCD models are superimposed (see chapter 5 for the detailed model comparison). The parameter-set PSAZ of the JETSET 7.3 event generator is found to describe the string effect for jet 1 very well and is thus considered an important QCD model here.

For jet 1 and jet 2 in **R3**, the corrected results and the errors are given in tables 1 and 2.

4.11 Statistical Significance

It is important to know how significant the string effect (defined via the angle shift $\langle\Delta\phi(\mathbf{L1})\rangle$) is, ie. how large the difference between the observed results $\langle\Delta\phi(\mathbf{L1})\rangle^{\rm corr}$ and the predictions for the zero-effect is.

For the symmetric TRISTAR configurations studied in chapter 2 (especially for Y120) the angle shift observed when no string fragmentation was involved (using independent fragmentation instead), and which shall be called the zero-effect, was found to be $\langle\Delta\phi\rangle = 0$.

But for general kinematic configurations the equivalence of "no string effect" and $\langle\Delta\phi\rangle = 0$ need not hold.

In the following, the predictions of the model MEIF (see section 5.2 for details) is considered as the zero-effect.

The statistical significance is defined as

$$\text{sig} := \frac{\langle\Delta\phi\rangle^{\rm corr} - \langle\Delta\phi\rangle^{\rm MEIF}}{\sigma_{\rm stat}},$$

giving the deviation of the corrected result from the zero-effect hypothesis in units of the statistical error of the measurement (in the previous sections, $\delta_{\rm stat}$ was used to denote the statistical error).

In figure 4.45, the statistical significances depending on y_{cut} are shown for the three kinematic regions. For soft y_{cut} the significance is largest due to the higher $P_{3=g}$ which is essential for the measurement (see section 3.4; soft y_{cut} values lead to low energy third jets which stem from gluon radiation with high probability). This is also the reason for the enhanced statistical significance in **R3**.

The significance for $\langle\Delta\phi(\mathbf{L3})\rangle$ is higher than for $\langle\Delta\phi(\mathbf{L1})\rangle$ due to the smaller spread of the distribution. It was already observed that $\langle\Delta\phi(\mathbf{L3})\rangle$ would be a more desirable observable than $\langle\Delta\phi(\mathbf{L1})\rangle$ due to its higher significance (not merely relying on only one particle in a jet) — but it had to be dropped because it does not sufficiently approximate the angle shift between parton and hadron jets for general kinematic configurations.

A comparison between the statistical significance of $\langle\Delta\phi(\mathbf{L1})\rangle$ and of R_{string} is also made in figure 4.45 (where the corrected values of R_{string} are also shown). Since R_{string} is a "particle based" observable, its significance is much higher than that of the "jet/event based" observable $\langle\Delta\phi(\mathbf{L1})\rangle$.

Nevertheless, $\langle\Delta\phi(\mathbf{L1})\rangle$ can be said to be statistically significant with a 25σ deviation from the zero-effect hypothesis for central y_{cut}.

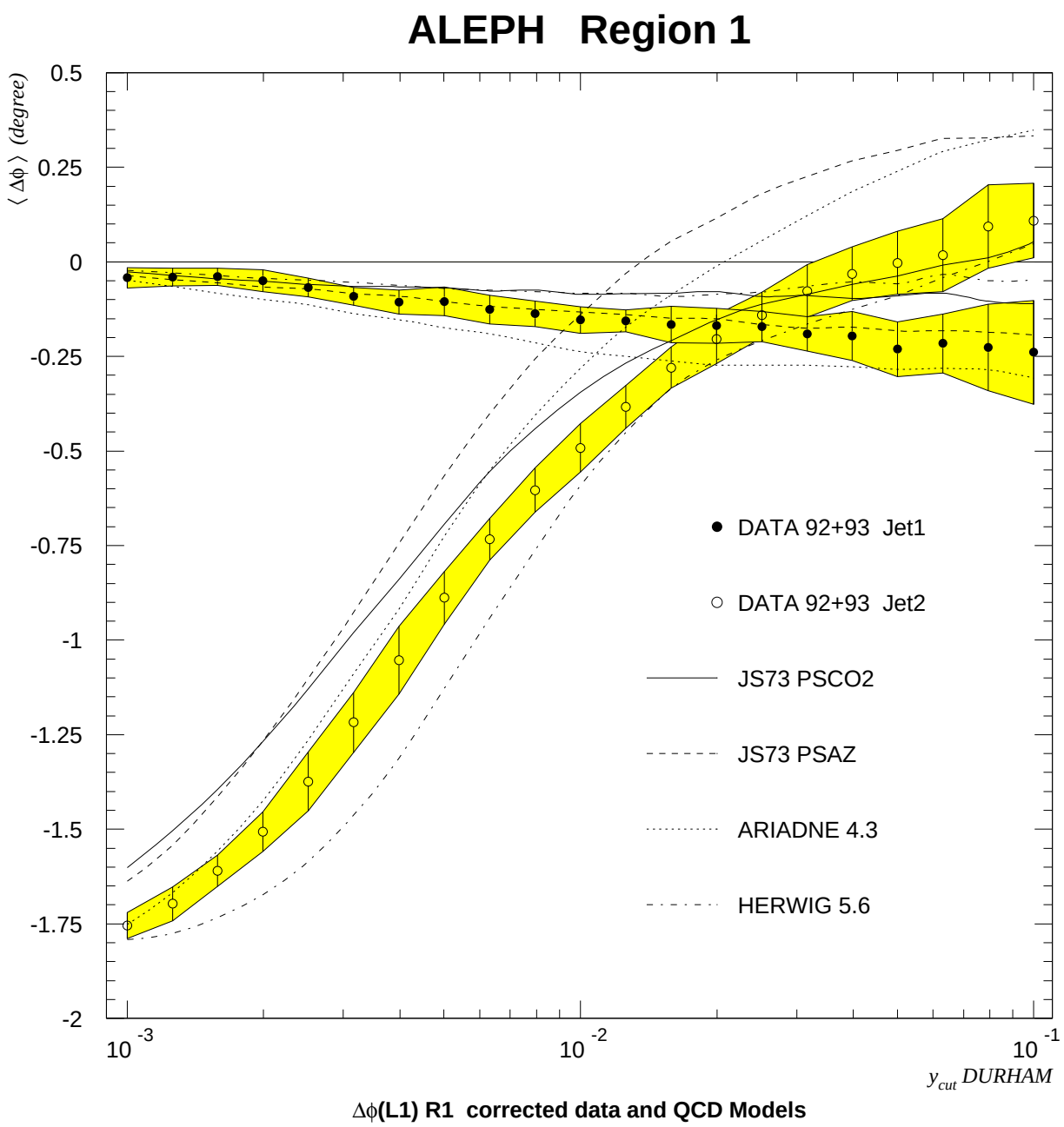

Figure 4.38: Dependence of $\langle \Delta\phi(\mathbf{L1}) \rangle$ on y_{cut} DURHAM. Corrected results for jet 1 and jet 2 from **R1** derived from ALEPH 1992 and 1993 data. The predictions of the most important QCD models are superimposed. JS73 stands for JETSET 7.3.

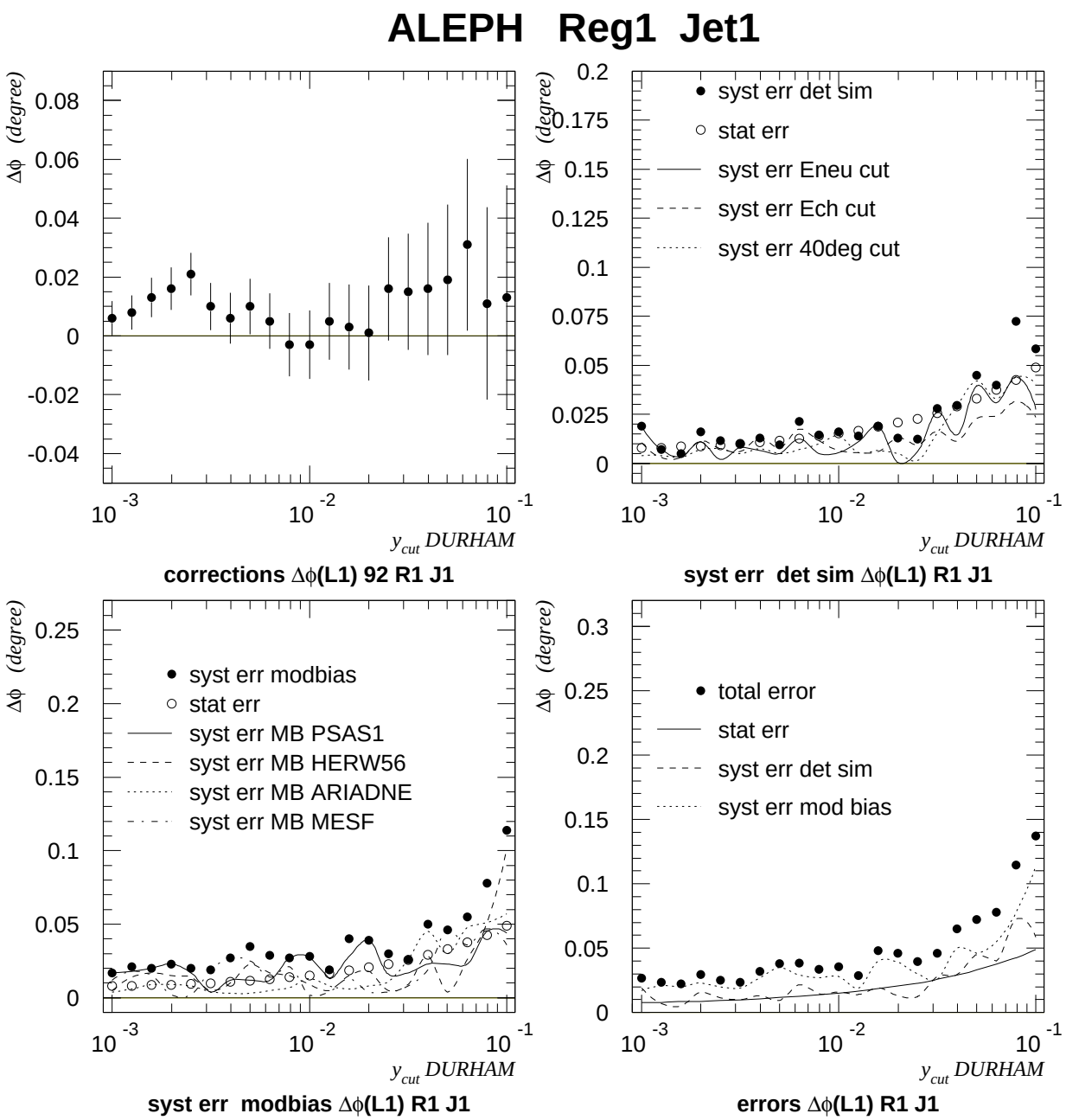

Figure 4.39: Corrections applied to the data and contributions to the systematic error from the simulation of the detector acceptance and from the model bias. The dependence on y_{cut} for jet 1 from **R1** events. The corrections are those for 1992; the errors are statistical combinations of 1992 and 1993 errors.

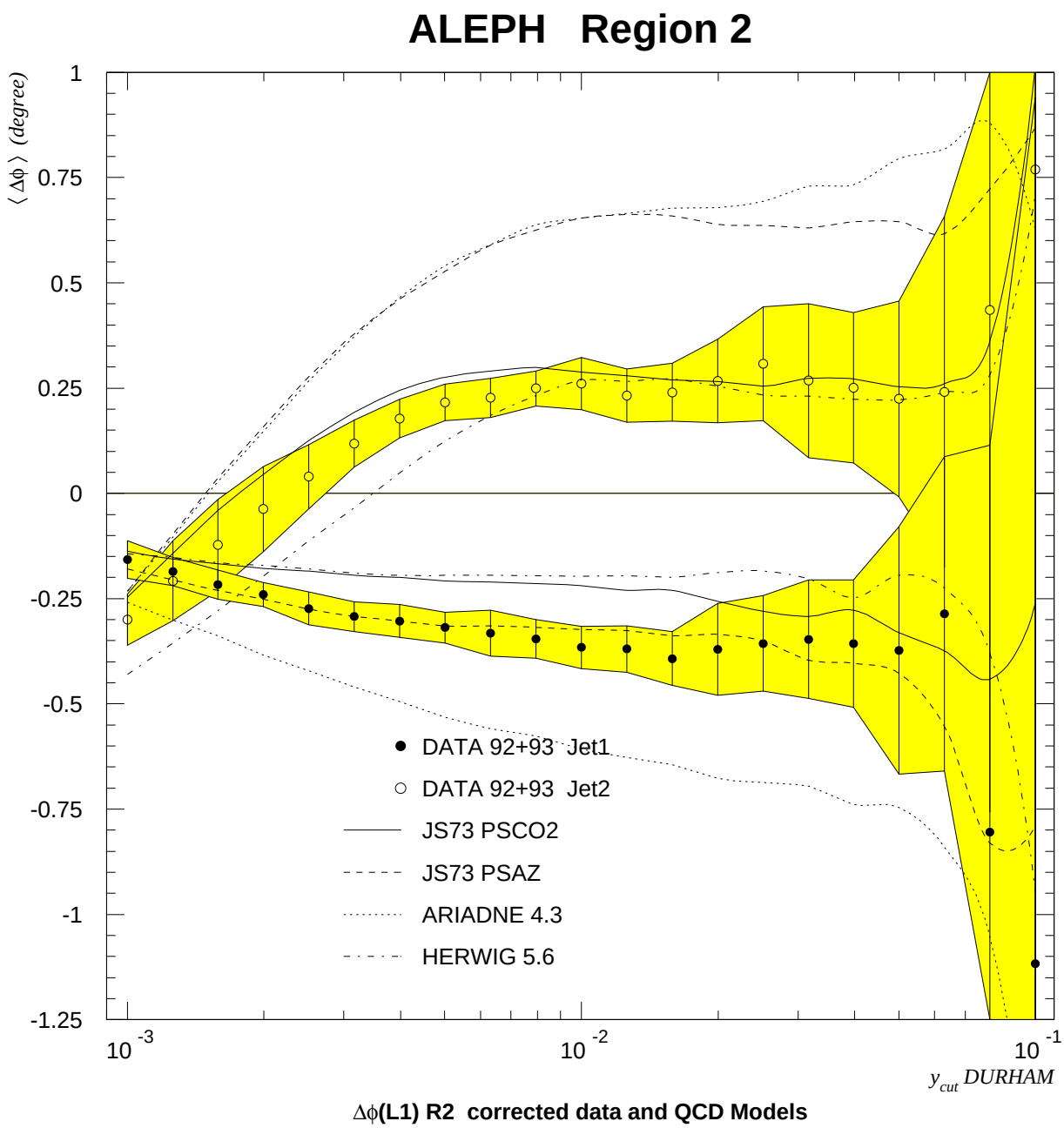

Figure 4.40: Dependence of $\langle \Delta\phi(\mathbf{L1}) \rangle$ on y_{cut} DURHAM. Corrected results for jet 1 and jet 2 from **R2** derived from ALEPH 1992 and 1993 data. The predictions of the most important QCD models are superimposed. For hard y_{cut} values, **R2** is scarcely populated; the errors become very large. JS73 stands for JETSET 7.3.

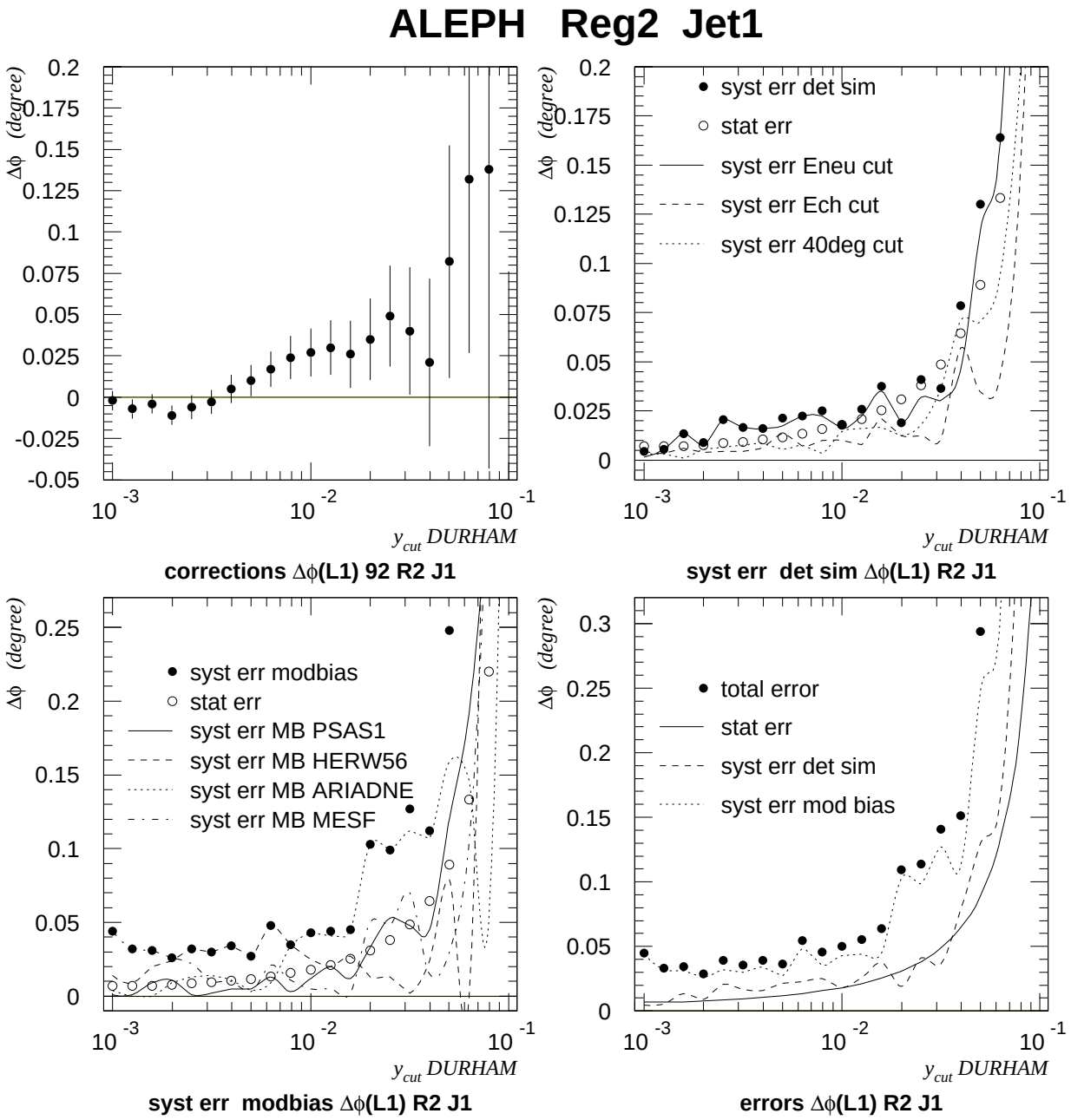

Figure 4.41: Corrections applied to the data and contributions to the systematic error from the simulation of the detector acceptance and from the model bias. The dependence on y_{cut} for jet 1 from **R3** events. The corrections are those for 1992; the errors are statistical combinations of 1992 and 1993 errors. **R2** is scarcely populated for hard y_{cut} and thus the errors become huge.

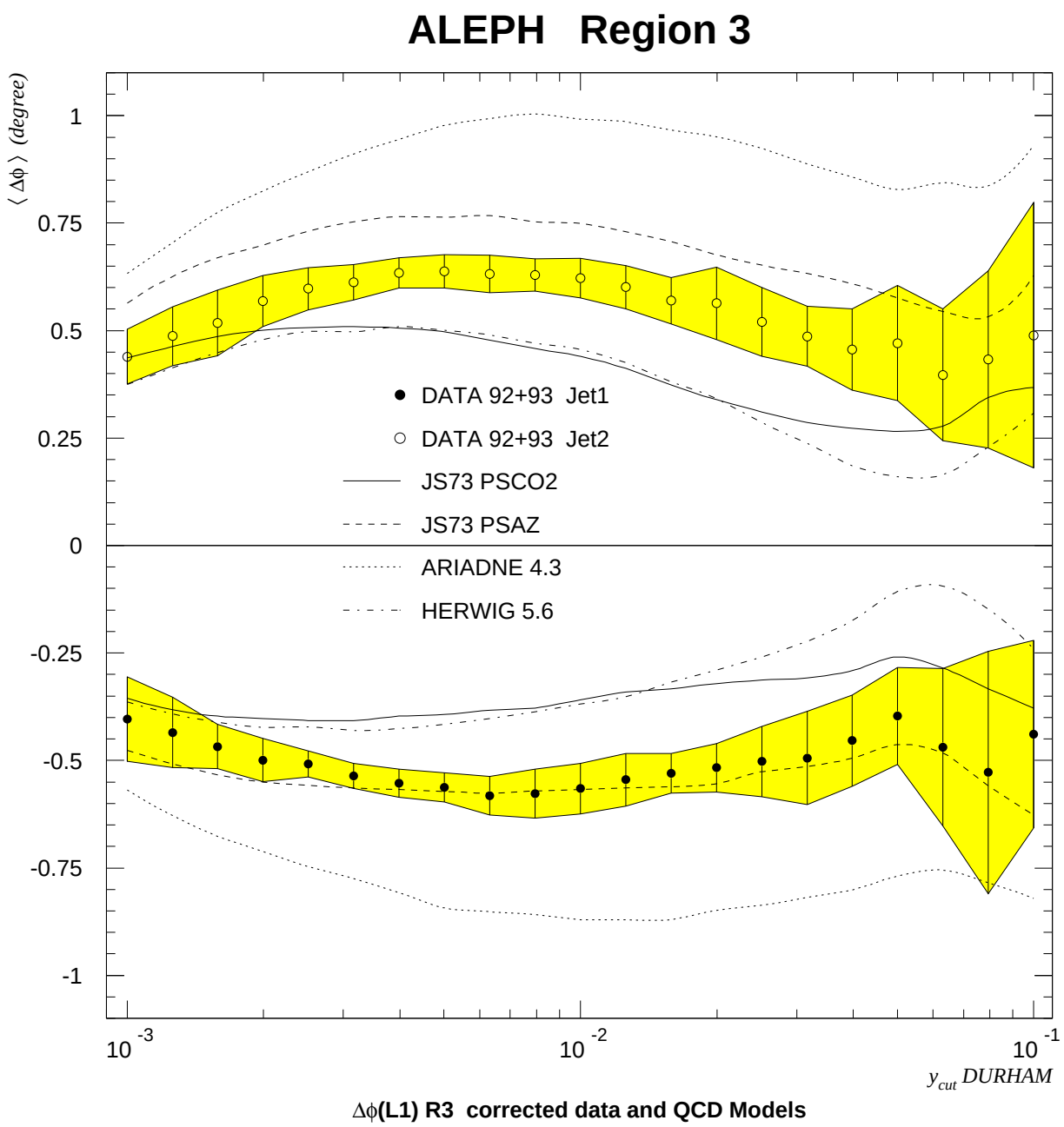

Figure 4.42: Dependence of $\langle \Delta\phi(\mathbf{L1}) \rangle$ on y_{cut} DURHAM. Corrected results for jet 1 and jet 2 from **R3** derived from ALEPH 1992 and 1993 data. The predictions of the most important QCD models are superimposed. JS73 stands for JETSET 7.3.

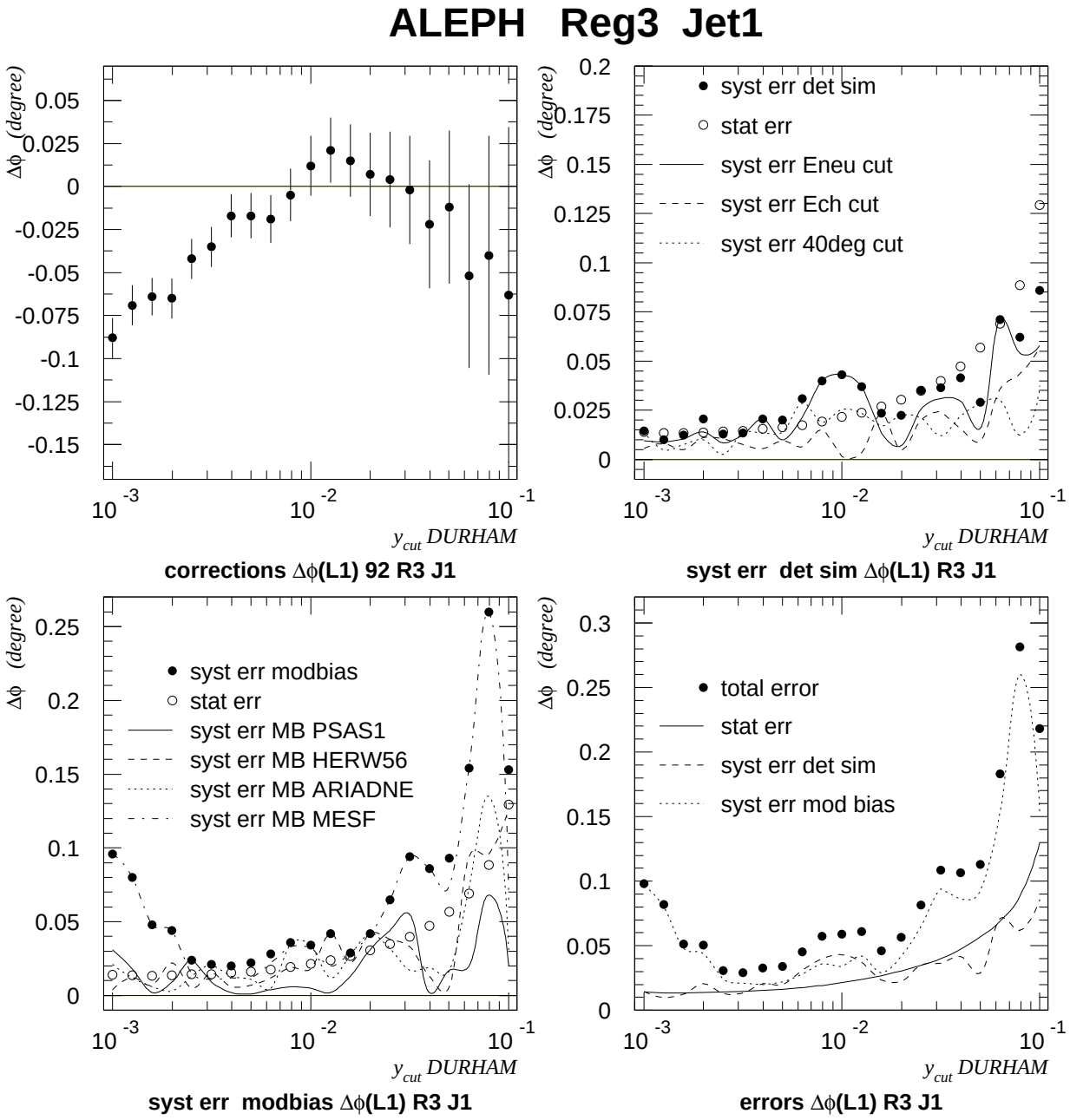

Figure 4.43: Corrections applied to the data and contributions to the systematic error from the simulation of the detector acceptance and from the model bias. The dependence on y_{cut} for jet 1 from **R3** events. The corrections are those for 1992; the errors are statistical combinations of 1992 and 1993 errors. Statistical fluctuations of the systematic errors can be seen.

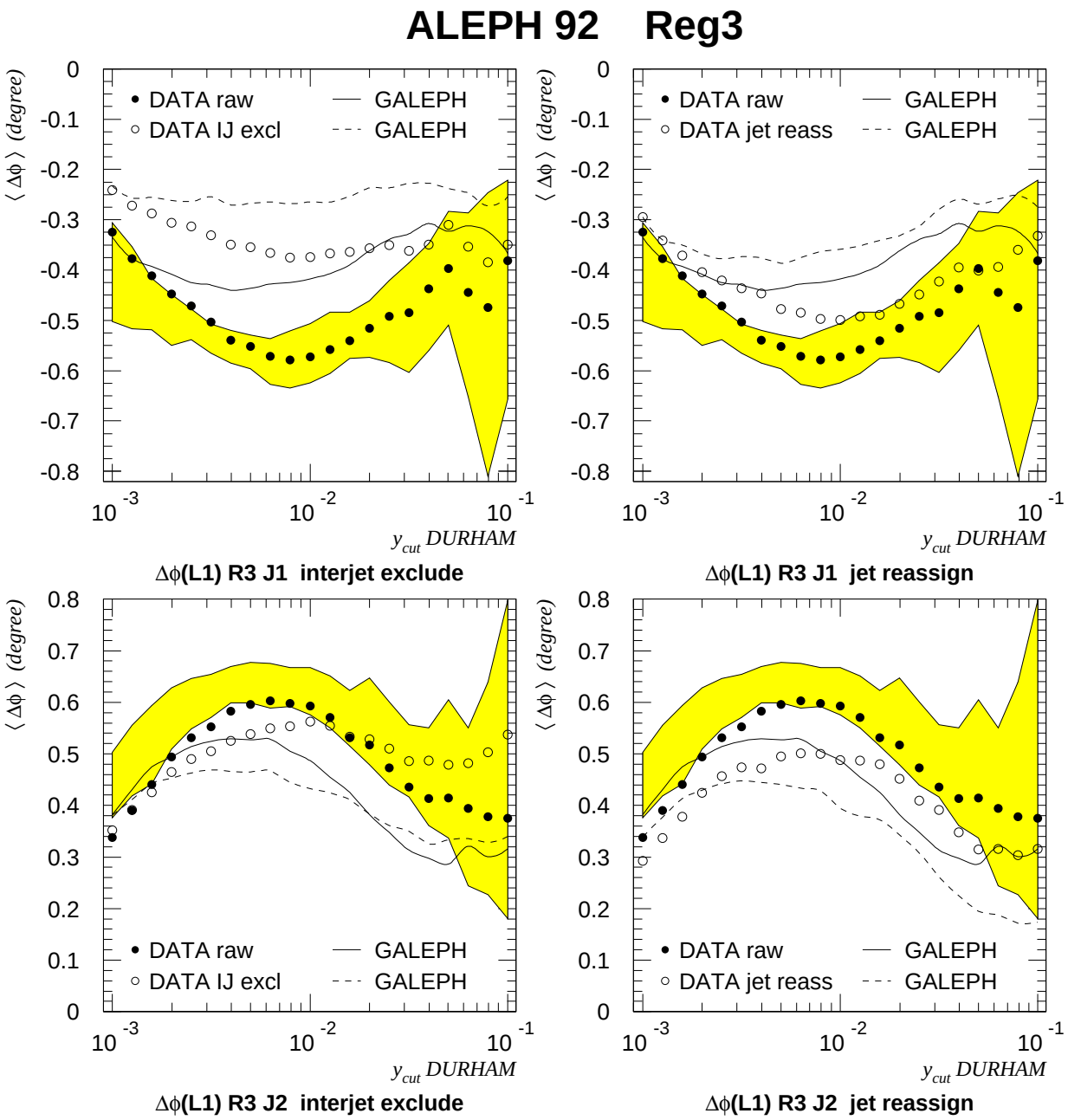

Figure 4.44: Uncorrected results for $\langle \Delta\phi(\mathbf{L1}) \rangle$ from the standard analysis and for the exclusion of interjet particles and the reassignment of particles to the closest jet axis, superimposed on the error band of the corrected data. The corresponding MC results are shown, giving smaller values for $\langle \Delta\phi(\mathbf{L1}) \rangle$ throughout, except for the smallest y_{cut}. In contrast to the observations from the TRISTAR events, the reassignment leads to a $\approx 15\%$ smaller $\langle \Delta\phi(\mathbf{L1}) \rangle$ effect for general kinematic configurations. The dependence on the interjet particles is smaller than for TRISTAR Y120 events (30% instead of 50%).

Results for the $\langle \Delta\phi(\mathbf{L1}) \rangle$ measurement for jet 1 in R3 from ALEPH 1992 and 1993 data.

y_{cut}	$\langle \Delta\phi(\mathbf{L1}) \rangle^{\text{corr}}$	stat	syst	mbias
0.00100	$-0.404°$	$\pm 0.014°$	$\pm 0.015°$	$\pm 0.096°$
0.00126	$-0.435°$	$\pm 0.014°$	$\pm 0.010°$	$\pm 0.080°$
0.00159	$-0.467°$	$\pm 0.013°$	$\pm 0.012°$	$\pm 0.048°$
0.00200	$-0.499°$	$\pm 0.014°$	$\pm 0.021°$	$\pm 0.044°$
0.00251	$-0.508°$	$\pm 0.014°$	$\pm 0.013°$	$\pm 0.024°$
0.00316	$-0.536°$	$\pm 0.015°$	$\pm 0.014°$	$\pm 0.021°$
0.00398	$-0.553°$	$\pm 0.016°$	$\pm 0.021°$	$\pm 0.020°$
0.00501	$-0.563°$	$\pm 0.016°$	$\pm 0.020°$	$\pm 0.022°$
0.00631	$-0.582°$	$\pm 0.018°$	$\pm 0.031°$	$\pm 0.028°$
0.00794	$-0.577°$	$\pm 0.019°$	$\pm 0.040°$	$\pm 0.036°$
0.01000	$-0.566°$	$\pm 0.022°$	$\pm 0.043°$	$\pm 0.034°$
0.01259	$-0.545°$	$\pm 0.024°$	$\pm 0.037°$	$\pm 0.042°$
0.01585	$-0.530°$	$\pm 0.027°$	$\pm 0.024°$	$\pm 0.029°$
0.01995	$-0.517°$	$\pm 0.030°$	$\pm 0.023°$	$\pm 0.042°$
0.02512	$-0.502°$	$\pm 0.035°$	$\pm 0.035°$	$\pm 0.065°$
0.03162	$-0.494°$	$\pm 0.040°$	$\pm 0.037°$	$\pm 0.094°$
0.03981	$-0.454°$	$\pm 0.047°$	$\pm 0.041°$	$\pm 0.086°$
0.05012	$-0.396°$	$\pm 0.057°$	$\pm 0.029°$	$\pm 0.093°$
0.06310	$-0.469°$	$\pm 0.069°$	$\pm 0.071°$	$\pm 0.154°$
0.07943	$-0.528°$	$\pm 0.089°$	$\pm 0.062°$	$\pm 0.260°$
0.10000	$-0.439°$	$\pm 0.129°$	$\pm 0.086°$	$\pm 0.153°$

Table 1: Results of the string effect measurement using the observable $\langle \Delta\phi(\mathbf{L1}) \rangle$ of jet 1 in kinematic region **R3** for logarithmically spaced values of y_{cut} DURHAM between 0.001 and 0.1. These results are statistical combinations of the measurements on 1992 and 1993 ALEPH data. The systematic error is estimated using variations of the particle and event selection cuts. The model bias error is estimated by applying a simplified detector simulation on 7 QCD models. The string effect is maximal for $y_{cut} \approx 0.006$ and falls off for softer and harder values. The errors become large for hard y_{cut}. Variations in the size of the systematic error are due to statistical fluctuations.

Results for the $\langle \Delta\phi(\mathbf{L1}) \rangle$ measurement for jet 2 in R3 from ALEPH 1992 and 1993 data.

y_{cut}	$\langle \Delta\phi(\mathbf{L1}) \rangle^{\text{corr}}$	stat	syst	mbias
0.00100	0.439°	±0.015°	±0.027°	±0.056°
0.00126	0.487°	±0.014°	±0.022°	±0.063°
0.00159	0.517°	±0.014°	±0.042°	±0.062°
0.00200	0.569°	±0.014°	±0.027°	±0.051°
0.00251	0.597°	±0.015°	±0.031°	±0.035°
0.00316	0.613°	±0.015°	±0.031°	±0.023°
0.00398	0.635°	±0.016°	±0.023°	±0.022°
0.00501	0.638°	±0.017°	±0.021°	±0.028°
0.00631	0.632°	±0.019°	±0.025°	±0.030°
0.00794	0.630°	±0.020°	±0.022°	±0.022°
0.01000	0.622°	±0.022°	±0.020°	±0.035°
0.01259	0.601°	±0.025°	±0.020°	±0.039°
0.01585	0.570°	±0.028°	±0.022°	±0.040°
0.01995	0.563°	±0.032°	±0.043°	±0.065°
0.02512	0.520°	±0.036°	±0.042°	±0.058°
0.03162	0.487°	±0.043°	±0.032°	±0.045°
0.03981	0.455°	±0.050°	±0.030°	±0.075°
0.05012	0.471°	±0.059°	±0.087°	±0.083°
0.06310	0.397°	±0.072°	±0.073°	±0.114°
0.07943	0.433°	±0.094°	±0.130°	±0.129°
0.10000	0.489°	±0.135°	±0.225°	±0.162°

Table 2: Results of the string effect measurement using the observable $\langle \Delta\phi(\mathbf{L1}) \rangle$ of jet 2 in kinematic region **R3** for logarithmically spaced values of y_{cut} DURHAM between 0.001 and 0.1. These results are statistical combinations of the measurements on 1992 and 1993 ALEPH data. The systematic error is estimated using variations of the particle and event selection cuts. The model bias error is estimated by applying a simplified detector simulation on 7 QCD models. The string effect is maximal for $y_{cut} \approx 0.005$ and falls off for softer and harder values. The errors become large for hard y_{cut}.

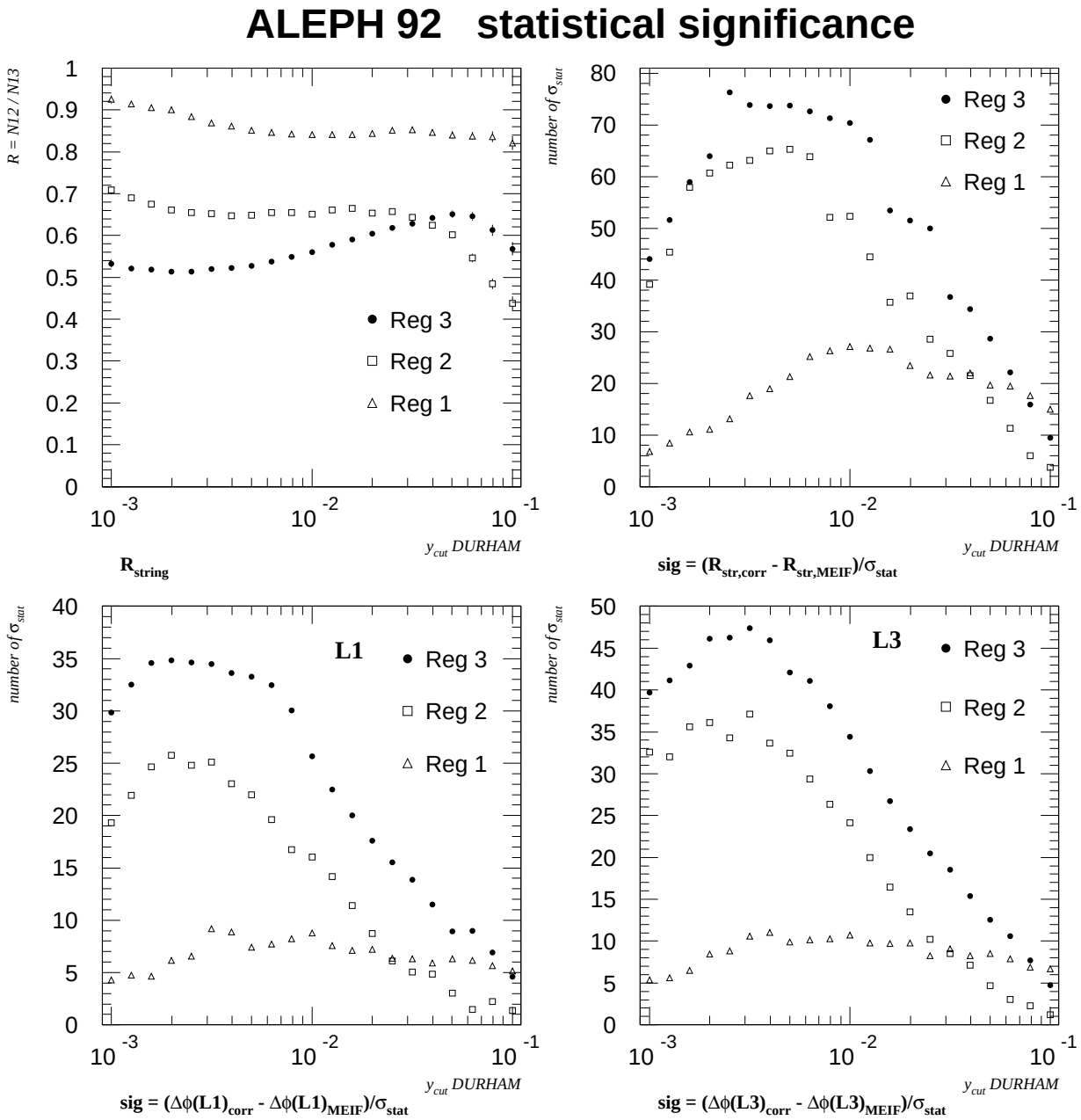

Figure 4.45: Statistical significance dependent on y_{cut} for $\langle\Delta\phi(\mathbf{L1})\rangle$ and $\langle\Delta\phi(\mathbf{L3})\rangle$ in the three kinematic regions compared to that of the ordinary string effect variable $R_{string} = N_{12}/N_{13}$. $\langle\Delta\phi(\mathbf{L1})\rangle$ as a jet specific observable is statistically less significant than R_{string} but nevertheless shows a pronounced ($\approx 25\sigma$ for central y_{cut}) deviation from the zero hypothesis (here represented by MEIF, ie. JETSET matrix element with independent fragmentation). The corrected results for R_{string} in the three kinematic configurations are also shown.

Chapter 5

Comparison with QCD models

5.1 Synopsis

In the previous chapter, a measurement of the string effect using the observable $\langle \Delta\phi(\mathbf{L1}) \rangle$ was performed.

A comparison is now to be made between the results from the data and predictions from the various QCD models. This is necessary to see which features of the different models have influence on the description of the string effect.

A graphical visualization of the $\langle \Delta\phi(\mathbf{L1}) \rangle$ results of the different models is given for the range of y_{cut} values and the three kinematic regions, superimposed on the corrected data.

For easier comparison, the results for all models for $y_{cut} = 0.01$ are collected in one representation for jet 1 and jet 2 in each region.

The 15 QCD models used are variations of JETSET 7.3, HERWIG (5.6 and 5.8) and ARIADNE 4.3. The parameters for these models are derived from multiparameter fits on global event properties ([4], [29]). For each of the models, 2 million events were generated at $E_{cm} = 91.25\,\mathrm{GeV}$.

Neutrinos are excluded from the analysis (compare section 4.7) and no ISR and FSR is allowed. Particles with mean lifetimes in excess of $10^{-9}s$ are treated as stable. 3-jet events are clustered using the DURHAM algorithm for a range of y_{cut} values. The energies of the jets are reconstructed from the angles between the jets and a common event plane is defined (see section 4.2).

5.2 QCD Models

Most of the models studied are versions of JETSET 7.3 with parton shower and string fragmentation. Aspects of the parton shower and fragmentation process are varied. Besides the parton shower models, also JETSET 7.3 with $O(\alpha_s^2)$ matrix elements is used, together with either string fragmentation or independent fragmentation. The HERWIG event generator, which uses coherent parton shower and cluster fragmentation, and the ARIADNE model, using color dipole cascades and string fragmentation (which is adopted from JETSET 7.3), are also studied.

For the PSCO2 (standard) parameter set for JETSET parton shower, the following switches are set:

```
MSTJ(  1)  =  1       ! fragmentation scheme (1=string)
MSTJ(101)  =  5       ! parton shower (5)
MSTJ( 42)  =  2       ! coherent (2)
MSTJ( 43)  =  4       ! z definition (4=global unconstrained)
MSTJ( 47)  =  2       ! correction at first branching (qqg) (2)
MSTJ( 44)  =  2       ! alpha_s scale z(1-z)m^2  (2)
MSTJ( 46)  =  0       ! no azimuthal correlations (0)
```

For the other JETSET 7.3 parton shower models, only those switches which differ from the above values will be explicitly shown.

If not otherwise stated, the models using string fragmentation (ie. JETSET PS) differ in the following parameters from the JETSET 7.3 default:

```
MSTJ( 11)  =  3       ! heavy flavor fragmentation
PARJ( 54)  =  -0.050  ! epsilon c
PARJ( 55)  =  -0.0045 ! epsilon b
```

5.2.1 JS73 PSCO2

This is the reference model of the analysis (see also section 4.8.3). The events are generated using JETSET 7.3 with coherent parton shower and string fragmentation. The best fit parameters used are those from the latest multiparameter fit on 1992 data (see reference [29]), fitting more parameters than in previous fits. The following parameter settings were made to change the JETSET 7.3 default parameters:

```
PARJ( 81)  =  0.329   ! Lambda LLA
PARJ( 82)  =  1.21    ! M min
PARJ( 21)  =  0.353   ! sigma
PARJ( 41)  =  0.50    ! A
PARJ( 42)  =  1.08    ! B
PARJ( 11)  =  0.48    ! V_ud
PARJ( 12)  =  0.46    ! V_s
PARJ( 13)  =  0.60    ! V_cb
PARJ( 17)  =  0.16    ! higher meson nonets (tensor...)
PARJ( 14)  =  0.096
PARJ( 16)  =  0.096
PARJ( 15)  =  0.032
PARJ( 26)  =  0.40    ! eta-prime suppress.
PARJ(  2)  =  0.295   ! s/u
PARJ(  1)  =  0.092   ! qq/q
PARJ(  3)  =  0.51    ! su/du
```

5.2.2 JS73 PSCO

This model uses JETSET 7.3 coherent parton shower and string fragmentation with best fit parameters determined from a smaller 1989 and 1990 data sample (see [4]). The following parameter settings were made to change the JETSET 7.3 default parameters:

```
PARJ( 81)  =  0.319   ! LLA
PARJ( 82)  =  1.57    ! M min
PARJ( 21)  =  0.359   ! sigma
PARJ( 41)  =  0.5     ! a
PARJ( 42)  =  0.88    ! B
```

5.2.3 JS73 PSCO2 LLLA

This is a slight modification of model PSCO2, setting `PARJ(81)`$= \Lambda_{LLA} = 0.304\,\mathrm{GeV}$. This is the lower error bound around the default value `PARJ(81)`$= 0.329\,\mathrm{GeV}$ (see reference [4] for the estimate of the errors of the best fit parameters).

5.2.4 JS73 PSCO2 MMIN

This is a slight modification of model PSCO2, setting `PARJ(82)`$= M_{min} = 1.37\,\mathrm{GeV}$. This is the upper error bound around the default value `PARJ(82)`$= 1.21\,\mathrm{GeV}$ (see reference [4] for the estimate of the errors of the best fit parameters).

5.2.5 JS73 PSLU

In this version of the parton shower in JETSET 7.3, a "local unconstrained" definition of variable z is used — the energy fraction in the particles grandmother's rest frame is used (assuming massless daughters; for massive ones, energy and momentum are reshuffled).

```
MSTJ( 43)  =  2       ! z definition (2=local unconstrained)

PARJ( 81)  =  0.378   ! LLA
PARJ( 82)  =  1.05    ! M min
PARJ( 21)  =  0.374   ! sigma
PARJ( 41)  =  0.5     ! a
PARJ( 42)  =  0.73    ! B
```

5.2.6 JS73 PSAZ

In this JETSET 7.3 model, the azimuthal distribution in the gluon decay shower branchings is chosen anisotropically due to interferences with nearest neighbours.

```
MSTJ( 46)  =  2       ! azimuthal interference with n.n., gluon decay

PARJ( 81)  =  0.294   ! LLA
PARJ( 82)  =  1.7025  ! M min
```

```
PARJ( 21)  =  0.3665  ! sigma
PARJ( 41)  =  0.5     ! a
PARJ( 42)  =  0.753   ! B
```

5.2.7 JS73 PSA1

In this second JETSET 7.3 model with nonhomogeneous azimuthal angle distribution in gluon decays, this anisotropy is due to a kinematics-dependent effective gluon polarization.

```
MSTJ( 46)  =  1       ! azimuthal interference due to gluon polarization

PARJ( 81)  =  0.315   ! LLA
PARJ( 82)  =  1.63    ! M min
PARJ( 21)  =  0.36    ! sigma
PARJ( 41)  =  0.5     ! a
PARJ( 42)  =  0.85    ! B
```

5.2.8 JS73 PSAS1

For this model, the α_s scale $Q^2 = m^2/4$ is used for the shower (m is the mass of the decaying parton) which is different from the standard choice $Q^2 = z(1-z)m^2$.

```
MSTJ( 44)  =  1       ! alpha_s scale m^2/4

PARJ( 81)  =  0.349   ! Lambda LLA
PARJ( 82)  =  1.78    ! M min
PARJ( 21)  =  0.377   ! sigma
PARJ( 41)  =  0.50    ! A
PARJ( 42)  =  0.72    ! B
```

5.2.9 JS73 PSIN

No angular ordering is performed in the branching of the time-like shower, resulting in an incoherent parton shower evolution for this variation of JETSET 7.3.

```
MSTJ( 42)  =  1       ! incoherent (1)
MSTJ( 44)  =  1       ! alpha_s scale m^2/4

PARJ( 81)  =  0.38    ! LLA
PARJ( 82)  =  1.59    ! M min
PARJ( 21)  =  0.414   ! sigma
PARJ( 41)  =  0.5     ! a
PARJ( 42)  =  1.23    ! B
```

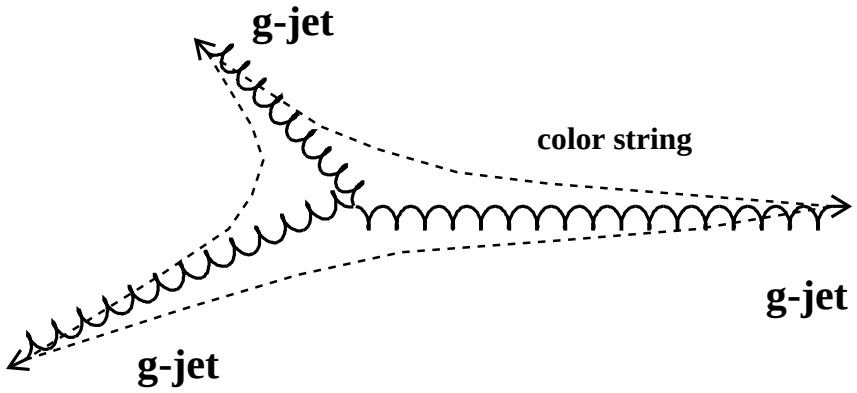

Figure 5.1: String fragmentation view of a 3-jet configuration originating from a gg state through hard gluon radiation. The closed color string can be seen. The angle shift $\langle \Delta\phi(\mathbf{L1}) \rangle$ for jet 1 is expected to be small due to the strings on either side, mutually compensating the shift effect of each other.

5.2.10 JS73 PSGG

This is a toy model based on JETSET 7.3, starting the coherent parton shower not from a $q\overline{q}$ state, but from a gg state. Due to the larger color charge of the gluon (compared to the quark), the leading log scale Λ_{LLA} has to be chosen unphysically small to compensate for the higher rate of radiation off the evolving gluons by reducing the strength of α_s (see the first equation in chapter 1). This helps to preserve reasonable multiplicities.

From the events generated from this gg state, 3-jets are selected giving a sample of event configurations similar to the one shown in figure 5.1, having a closed color string stretching between the three hard gluons. 3 gluon configurations like this with a closed color string are possible as decay modes for onia ($c\overline{c}$, $b\overline{b}$) decays.

One can expect the angle shift $\langle \Delta\phi(\mathbf{L1}) \rangle$ (eg. for jet 1) to be small, since there is hadron production from the color strings on either side.

The parameters are more or less those of PSCO2, with the big exception of `PARJ(81)`.

```
PARJ( 81)  =  0.001   ! Lambda LLA  (very small!)
PARJ( 82)  =  1.20    ! M min
PARJ( 21)  =  0.350   ! sigma
PARJ( 41)  =  0.00    ! A
PARJ( 42)  =  1.10    ! B
PARJ( 11)  =  0.51    ! V_ud
PARJ( 12)  =  0.54    ! V_s
PARJ( 13)  =  0.60    ! V_cb
```

```
PARJ( 17)  =  0.16    ! higher meson nonets (tensor...)
PARJ( 14)  =  0.096
PARJ( 16)  =  0.096
PARJ( 15)  =  0.032
PARJ( 26)  =  0.40    ! eta-prime suppress.
PARJ(  2)  =  0.305   ! s/u
PARJ(  1)  =  0.102   ! qq/q
PARJ(  3)  =  0.43    ! su/du
```

5.2.11 ARIADNE 4.3

The ARIADNE Monte Carlo model (version 4.3 is used here; see reference [25] for details) generates the partonic final state of the Z^0 decay with a parton shower formalism completely different from the time-like branching description used in JETSET.

The idea behind this color dipole cascade is to view the emission of a gluon as an emission off a color dipole constituted by the two initial quarks. The emission of a further gluon can then come from the two dipoles qg and $\overline{q}g$.

The cut-off for the emission cascade is given by the minimum transverse momentum $p_{\perp\,min}$ limiting the range of the evolution variable $z = p_\perp^2$.

The color dipole formalism implicitly incorporates interference effects between the initial quarks and the subsequently emitted gluons.

ARIADNE does not have a hadronization scheme of its own but uses the JETSET string fragmentation.

```
PARA(  1)  =  0.225   ! LAMBDA
PARA(  3)  =  0.730   ! Pt-min (cd cascade cut-off)
MSTA( 20)  =  0       ! elmag dipole rad (0 = off, 1 = on)
MSTA( 11)  =  0       ! phase space restr. (0=def,4=no restr.)

MSTJ(  1)  =  1       ! fragmentation scheme (string)

PARJ( 21)  =  0.354   ! sigma
PARJ( 41)  =  0.5     ! a
PARJ( 42)  =  0.800   ! B

MSTJ( 11)  =  3       ! heavy flavor fragmentation
PARJ( 54)  =  -0.050  ! epsilon c
PARJ( 55)  =  -0.006  ! epsilon b
```

5.2.12 HERWIG 5.6

The HERWIG Monte Carlo model (see reference [26]) is a coherent parton shower model completely independent of JETSET. Its parton shower prescription differs in the choice of the evolution variable. For the hadronization, the cluster fragmentation scheme is used. Here, the gluons that were created in the parton shower are at the end forced to decay into $q\overline{q}$ pairs which are then grouped together into color neutral clusters, which

can decay into hadrons or further clusters. The parameter of importance for the cluster fragmentation is the lower limit for the cluster mass.

The following parameter settings are used for the generation of events with the HERWIG 5.6 Monte Carlo event generator.

```
PROCESS CODE (IPROC)   =     100
NUMBER OF FLAVOURS     =    5
STRUCTURE FUNCTION SET =    5
AZIM SPIN CORRELATIONS =    T
AZIM SOFT CORRELATIONS =    T
QCD LAMBDA (GEV)       =     .1620
DOWN     QUARK  MASS   =     .3200
UP       QUARK  MASS   =     .3200
STRANGE  QUARK  MASS   =     .5000
CHARMED  QUARK  MASS   =    1.8000
BOTTOM   QUARK  MASS   =    5.2000
TOP      QUARK  MASS   =  100.0000
GLUON EFFECTIVE MASS   =     .8350
EXTRA SHOWER CUTOFF (Q)=     .4800
EXTRA SHOWER CUTOFF (G)=     .0000
PHOTON SHOWER CUTOFF   =   91.2500
CLUSTER MASS PARAMETER =    3.6700
SPACELIKE EVOLN CUTOFF =    2.5000
INTRINSIC P-TRAN (RMS) =     .0000
```

5.2.13 HERWIG 5.8

This model uses the HERWIG 5.8 event generator together with the best fit parameters for HERWIG 5.6 (by the time of writing, no best fit parameters have yet been determined for version 5.8 of HERWIG). As a warning it should be noted that version 5.8 at present fails to describe the spectrum of high momentum particles.

5.2.14 JS73 MESF

This model is also based on the JETSET 7.3 event generator, but uses the $O(\alpha_s^2)$ QCD matrix elements for the differential 3-jet and 4-jet cross sections to calculate the partonic final state of the Z^0 decay.

The hadronization starting from this partonic state is performed using string fragmentation.

```
MSTJ(  1)  =   1       ! fragmentation scheme (string)
MSTJ(101)  =   2       ! matrix element (2)

PARJ(122)  =   0.14    ! Lambda
PARJ(125)  =   0.01    ! ymin
PARJ( 21)  =   0.44    ! sigma
```

```
PARJ( 41)  =   1.0     ! a
PARJ( 42)  =   0.496   ! B

MSTJ( 11)  =   3       ! heavy flavor fragmentation
PARJ( 54)  =   -0.055  ! epsilon c
PARJ( 55)  =   -0.012  ! epsilon b

MSTJ(110)  =   2       ! Zhu parametrisation
MSTJ(111)  =   1       ! optimized scale, i.e. Q^2 = f * E_cm^2
PARJ(129)  =   0.00136 ! optimized Q^2 scale for the 3- and 4-jet rate
```

5.2.15 JS73 MEIF

This JETSET 7.3 based model uses also the $O(\alpha_s^2)$ matrix elements for the generation of the partonic final state, but performs the hadronization by means of the independent fragmentation algorithm. This model has no string-like features and is used for the zero effect hypothesis.

```
MSTJ(  1)  =    2       ! fragmentation scheme (independent)
MSTJ(  2)  =    3       ! g jet fragments like u,d,s pair in indep. frag.
MSTJ(  3)  =    1       ! particles share IF momentum imbalance
MSTJ(101)  =    2       ! matrix element (2)

PARJ(122)  =    0.123   ! Lambda
PARJ(125)  =    0.01    ! ymin
PARJ( 21)  =    0.473   ! sigma
PARJ( 41)  =    1.0     ! a
PARJ( 42)  =    0.516   ! B

MSTJ( 11)  =    3       ! heavy flavor fragmentation
PARJ( 54)  =    -0.055  ! epsilon c
PARJ( 55)  =    -0.012  ! epsilon b

MSTJ(110)  =    2       ! Zhu parametrisation
MSTJ(111)  =    1       ! optimized ME
PARJ(129)  =    0.0023  ! renormalization mass
```

5.3 Results of the QCD Model Comparison

The results of the model comparison are collected in figures 5.2 through 5.7 and 5.8 through 5.13.

In the first six figures, the corrected results for $\langle \Delta\phi(\mathbf{L1}) \rangle$ (combined from 1992 and 1993 data) and the corresponding error bands (total error; see section 4.8) are given for the whole range of y_{cut} values, separated for jet 1 and jet 2 and for the three kinematic regions. The results for the various QCD models are superimposed as lines with different line styles.

Groups of four models are collected together in one representation, since PAW has only four different line styles which can be well discriminated.

The most important models PSCO2, HERW56 and ARIADNE as well as PSAZ, the variation of JETSET 7.3 PS which best describes the string effect observed on the data, are once again collected in one representation (see also figures 4.38, 4.40 and 4.42).

For a direct simultaneous comparison between all 15 QCD models, figures 5.8 through 5.13 give the $\langle \Delta\phi(\mathbf{L1}) \rangle$ results for the central $y_{cut} = 0.01$.

The different kinematic situations and probabilities $P_{3=g}$ in the three regions **R1**, **R2** and **R3** can be seen to have a substantial impact on the value of $\langle \Delta\phi(\mathbf{L1}) \rangle$ for the data and the QCD model predictions. Region **R3** is the one most sensitive to the string effect.

The results for jet 1, which is expected to be a quark jet in $\approx 95\%$ of all cases, are considered more reliable than those for jet 2, since this jet by definition has the largest angular separation from the other two jets. In the following, the central y_{cut} region (around 0.01) is considered first.

The standard version of the JETSET 7.3 coherent parton shower and string fragmentation model with the most recent tuned parameter set (PSCO2) predicts an angle shift that is consistently smaller than the data values, especially in the sensitive region **R3**.

A slight dependence on the parameter tuning can also be seen. For example, the version PSCO has a higher value for the parton shower cut-off M_{min} than PSCO2, thus reducing the dilution effect from the parton shower.

The other JETSET models considered are variations of the parton shower. PSA1 gives almost identical results as the standard PSCO version. The versions PSAZ (azimuthal anisotropy due to gluon interference), PSLU (z-definition changed to "local") and PSAS1 (change of α_s argument) predict, in general, somewhat higher values, in reasonable agreement with the jet 1 data.

The JETSET incoherent parton shower version (PSIN) predicts an even smaller angle shift than the standard version, in disagreement with the data.

The JETSET toy model (PSGG) with its closed color string shows the smallest angle shift of all models considered (except MEIF). This serves as a test of the string fragmentation picture. The angle shifts of the color strings on both sides of jet 1 and 2 do not completely cancel due to the asymmetric kinematics.

The HERWIG 5.6 predictions are very similar to those of JETSET PSCO2 in all regions. This is surprising since parton shower and hadronization scheme are very different.

A striking feature is the large $\langle \Delta\phi(\mathbf{L1}) \rangle$ value predicted by ARIADNE, larger than the data value by several times the error bar. The reason seems to be some sort of synergetic effect of the color dipole cascade and the color string fragmentation.

The MESF model using $O(\alpha_s^2)$ QCD matrix elements (both $q\overline{q}g$ and $q\overline{q}gg$ states contribute to the 3-jet event sample) together with string fragmentation gives too large values throughout. This observation goes into the same direction as the one made in chapter 2, where the string effect was found to get diluted with the introduction of parton shower.

The independent fragmentation model MEIF shows the largest deviation from the data. Its predictions may be viewed as a "zero string effect", which for general kinematic configurations however does not mean $\langle \Delta\phi \rangle = 0$.

The results for jet 2 are seen to be almost mirror symmetric, at least in region **R3**, with JETSET PSAZ giving a somewhat too high value.

When going towards smaller y_{cut} values, the model predictions are seen to come closer to each other and to the data.

Figure 5.14 shows an attempt to get some insight into the question of how much of the "string effect" is contributed by the perturbative and the non-perturbative phases, respectively. Modification of the parton shower obviously has an effect, as is exemplified by comparing the JETSET PSCO2 versions without and with azimuthal correlations. It becomes also clear that ARIADNE produces a significant effect already at the partonic level. The situation with HERWIG is not yet clarified.

5.4 Conclusion and Outlook

In this work an analysis of the so-called "string effect" in $Z^0 \to$ 3-jet events (ie. $q\overline{q}$ events with a hard gluon radiated) is performed. A new variable, $\langle \Delta\phi(\mathbf{L1}) \rangle$, the azimuthal angle shift of the leading particle with respect to the jet axis, has been proposed and a measurement of that quantity has been carried out on data gathered by the ALEPH experiment in 1992 and 1993.

3-jet events were selected for a range of values of the cluster algorithm cut-off y_{cut}. The results of the measurement were corrected for detector effects. The systematic errors due to the detector simulation and to the model bias were estimated. They are roughly of the same size as the statistical error. The systematic error from the detector simulation shows strong statistical fluctuations.

It should be noted that the effect is rather small ($|\langle \Delta\phi(\mathbf{L1}) \rangle| \approx 0.5^\circ$ for jet 1 in the most sensitive kinematic region), roughly 10 times smaller than the average spread of the $\Delta\phi(\mathbf{L1})$ distribution. It is also smaller than the estimated error for a single $\Delta\phi(\mathbf{L1})$ measurement ($\approx 1.3^\circ$). Nevertheless, the mean of the distribution can be accurately determined.

Model studies using JETSET 3-jet events with threefold symmetry show that the angle shift of the leading particle in a jet with respect to the hadron jet axis approximates the angle shift from the parton jet axis to the hadron jet axis caused by the hadronization performed using the string fragmentation scheme.

The angle shift expected from these model studies can actually be seen for data events from kinematic region **R3**, which is especially sensitive for string effect observations due to the high probability $P_{3=g}$ for the least energetic jet to be the gluon jet and to the relatively small angle ϕ_{13} between the first and the third jet (the angle shift was found to decrease with increasing ϕ_{13} in the MC studies on symmetric events).

In this definition of the string effect, the influence of the jet core on the effect is studied whereas in the usual definition via R_{string}, only the interjet particles are involved. Since the angle shift $\langle \Delta\phi(\mathbf{L1}) \rangle$ relies heavily on the definition of the jet axis, all particles in jet 1 and jet 2 are used for the analysis of the string effect. The particles in the third (gluon) jet are not used, apart from their total momentum sum which defines the jet axis. The structure and particle multiplicity of the third jet does not influence $\langle \Delta\phi(\mathbf{L1}) \rangle$. In the definition of the string effect using R_{string}, the particles of the interjet region which are assigned to the third jet do contribute to the effect. For this reason, the string effect observables $\langle \Delta\phi(\mathbf{L1}) \rangle$ and R_{string} need not always conform in their predictions.

By excluding the interjet particles from the analysis, it could be seen that they con-

tribute less than 30% to the angle shift effect.

For the $q\overline{q}\gamma$ events selected from the data, the reversed angle shift effect could be seen. This is in agreement with the expectations from the string fragmentation picture.

The fully reconstructed Monte Carlo events based on JETSET show a smaller string effect than the uncorrected data. The measurement of $\langle\Delta\phi(\mathbf{L1})\rangle$ also suffers from an uncertainty due to the inability of the JETSET parton shower Monte Carlo to correctly describe the 3-jet rate and the distribution of 3-jet events among the kinematic configurations. The JETSET parton shower event generator especially fails in describing the rate of symmetric events (with three energetic jets) from **R1** which are due to very hard gluon radiation.

The comparison of the data with QCD models shows that the string effect in its definition via the angle shift $\langle\Delta\phi(\mathbf{L1})\rangle$ is not entirely due to non-perturbative effects from the hadronization. The assumption that it is exclusively a hadronization effect seemed plausible relying on the results of the TRISTAR study on symmetric events. For events with general kinematics generated with the JETSET event generator it can be noted that variations in the parton shower influence the quantity $\langle\Delta\phi(\mathbf{L1})\rangle$.

Considering jet 1 and central y_{cut} values, the standard version of JETSET (PSCO2) predicts significantly smaller values than the corrected data. Certain variants of the coherent parton shower however (PSAZ, PSLU, PSAS1) yield a satisfactory description.

A closer examination of the influence of the single model parameters (which are usually treated collectively in the multiparameter fit) on the string effect would still be of some interest.

Whereas the HERWIG predictions are very similar to those of JETSET PSCO2, the generator ARIADNE shows a much too large effect in all kinematic regions.

The observable $\langle\Delta\phi(\mathbf{L1})\rangle$ shows some dependence on the cluster algorithm cut-off y_{cut} (depending on the value of y_{cut}, either the soft or the hard perturbative regime is probed). Especially for jet 2 in **R1** and **R2**, this dependence is strong, whereas it is fairly small for both jet 1 and jet 2 in the sensitive region **R3**. For soft y_{cut} values, the differences between the predictions of the QCD models considered become small.

The interpretation of the measurement in terms of the color string effect is strongly influenced by the probability $P_{3=g}$ for the least energetic jet to be the gluon jet which is given by the QCD models. It is also influenced by the asymmetry of the kinematics of the 3-jet events in **R3**.

It would be of great interest to study the $\langle\Delta\phi(\mathbf{L1})\rangle$ effect on events with symmetric topology using a means of identifying the gluon jet in a 3-jet event:

- The effect of the interjet particles could be better studied.
- No asymmetric kinematics would obscure the angle shift.
- For events with threefold symmetry, the symmetry $\langle\Delta\phi(\mathbf{L1})\rangle_{q-jet} \approx -\langle\Delta\phi(\mathbf{L1})\rangle_{\overline{q}-jet}$ could be studied.

As methods for the identification of the gluon jet in 3-jet events, the reconstruction of secondary decay vertices for B mesons (b tagging) or the classification with neural networks could be used.

Since the number of events with b tag is comparatively small, an expansion of the string effect analysis using the angle shift observable $\langle\Delta\phi(\mathbf{L1})\rangle$ on the data samples of

the 1994 and forthcoming 1995 LEP runs seems highly desirable. This would also lead to more accurate results for the string effect measurement in $q\overline{q}\gamma$ events.

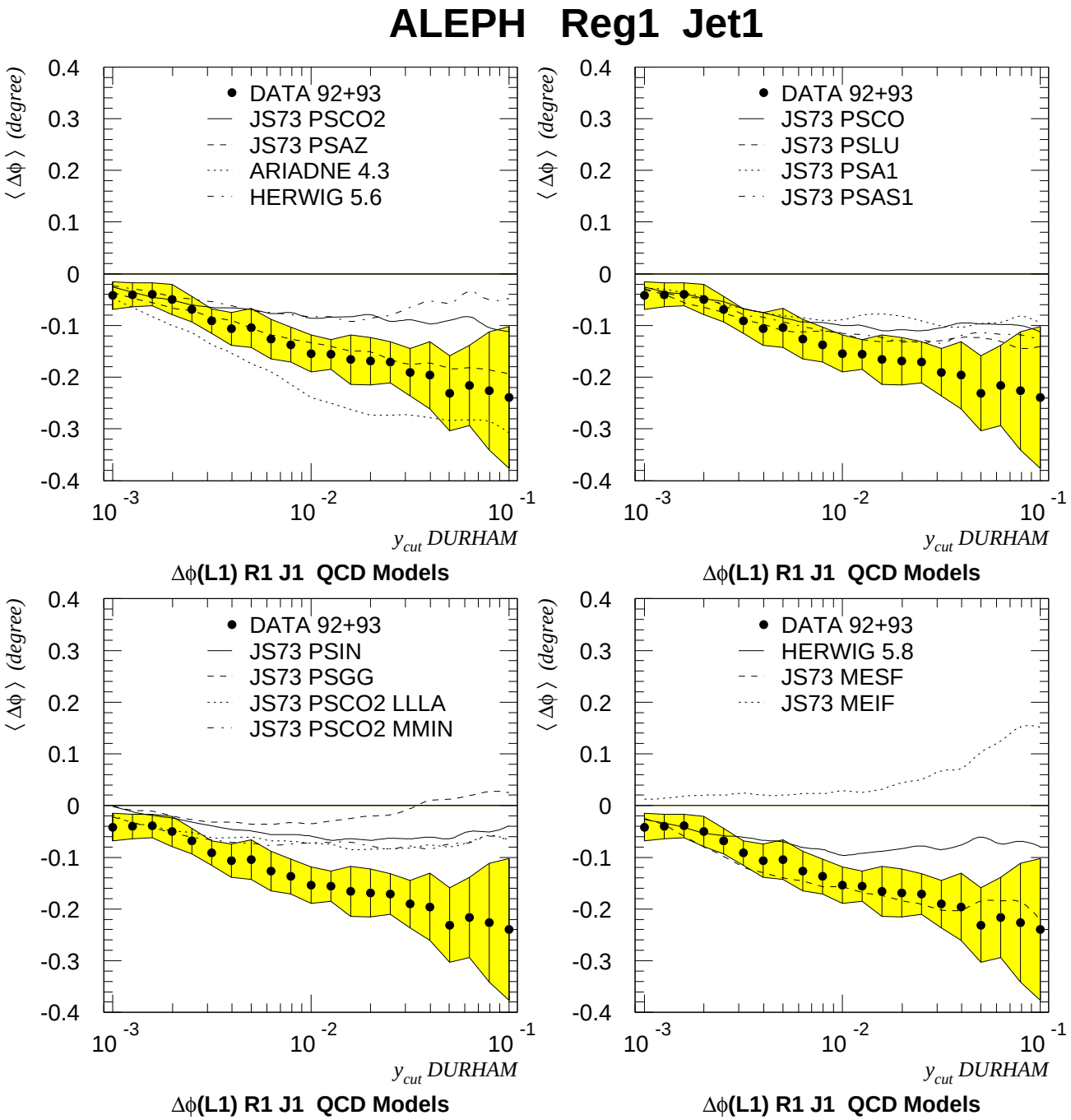

Figure 5.2: Results for $\langle \Delta\phi(\mathbf{L1}) \rangle$ of jet 1 from **R1** for the QCD models considered, superimposed on the corrected data (1992+1993) with error bands, are shown for the logarithmically spaced y_{cut} values between 0.001 and 0.1.

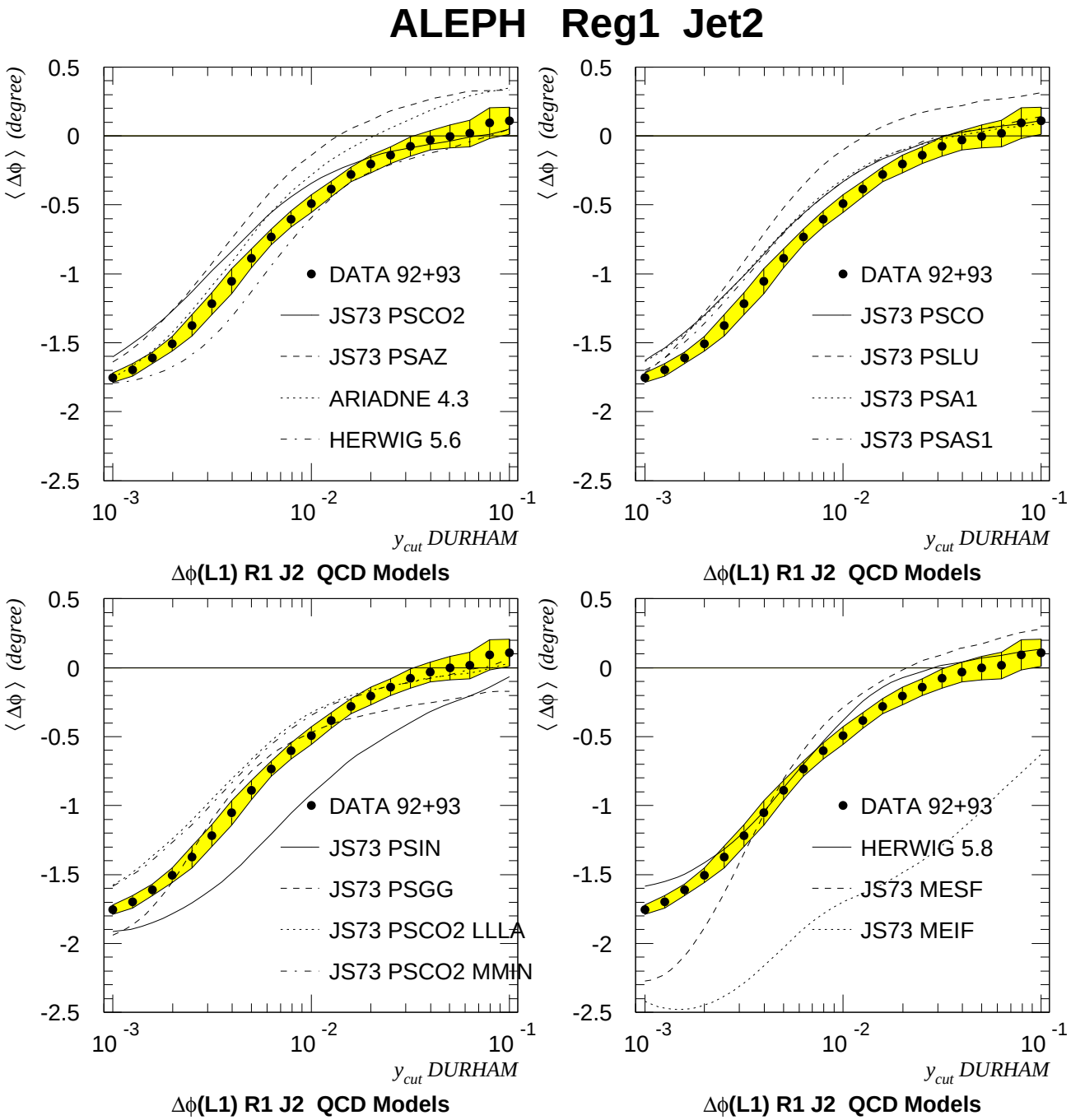

Figure 5.3: Results for $\langle \Delta\phi(\mathbf{L1}) \rangle$ of jet 2 from **R1** for the QCD models considered, superimposed on the corrected data (1992+1993) with error bands, are shown for the logarithmically spaced y_{cut} values between 0.001 and 0.1.

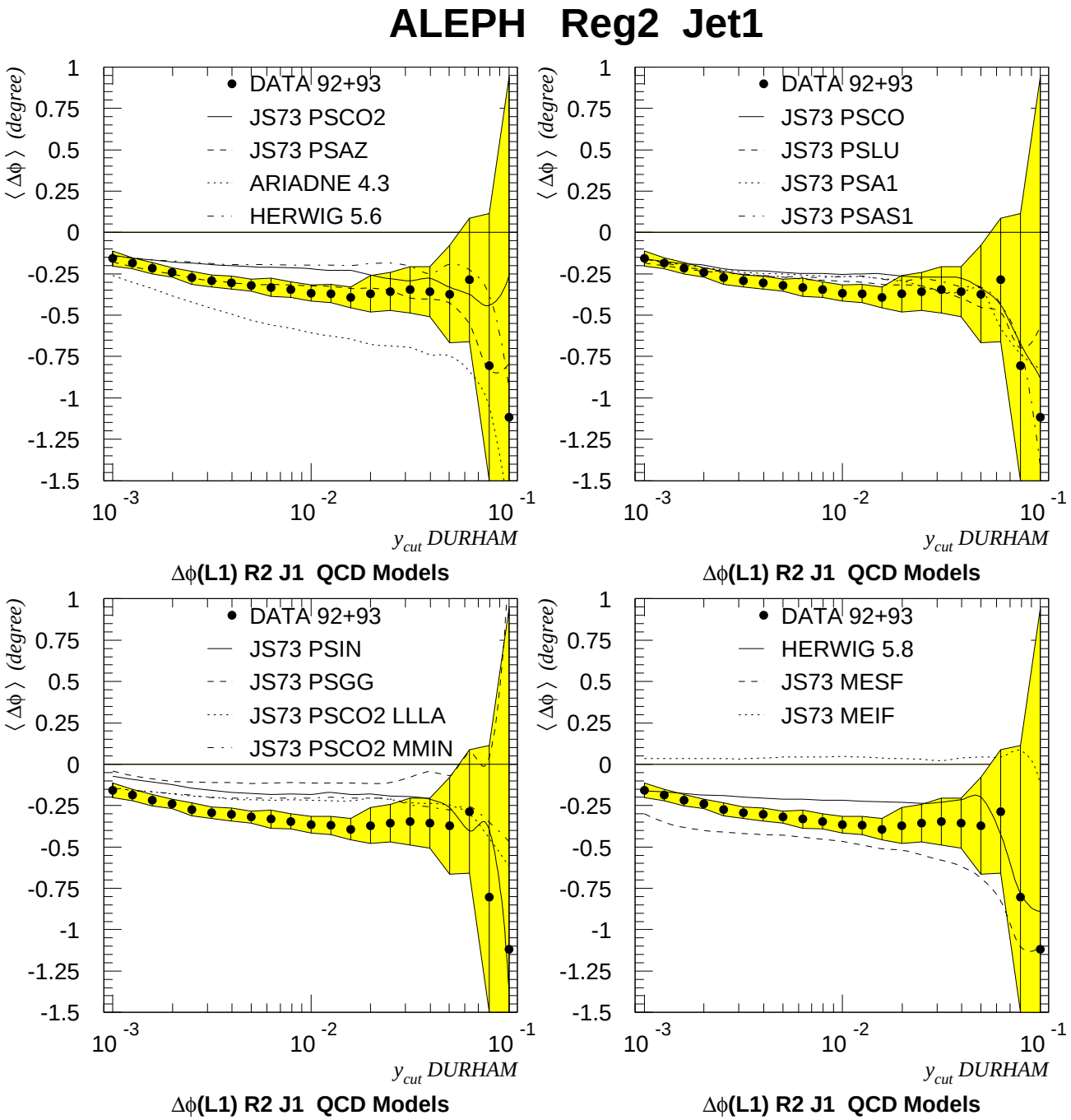

Figure 5.4: Results for $\langle \Delta\phi(\mathbf{L1}) \rangle$ of jet 1 from **R2** for the QCD models considered, superimposed on the corrected data (1992+1993) with error bands, are shown for the logarithmically spaced y_{cut} values between 0.001 and 0.1.

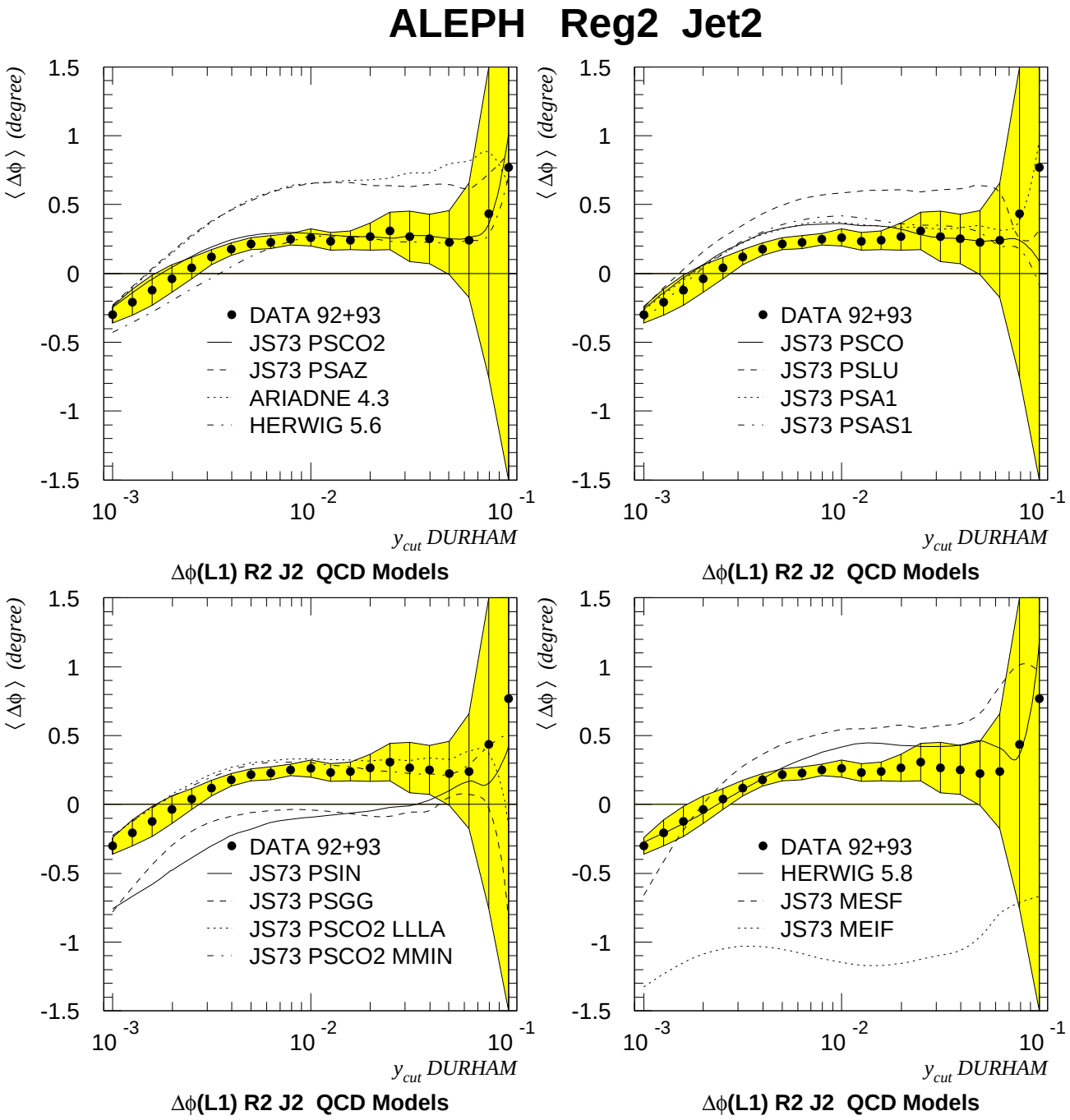

Figure 5.5: Results for $\langle \Delta\phi(\mathbf{L1}) \rangle$ of jet 2 from **R2** for the QCD models considered, superimposed on the corrected data (1992+1993) with error bands, are shown for the logarithmically spaced y_{cut} values between 0.001 and 0.1.

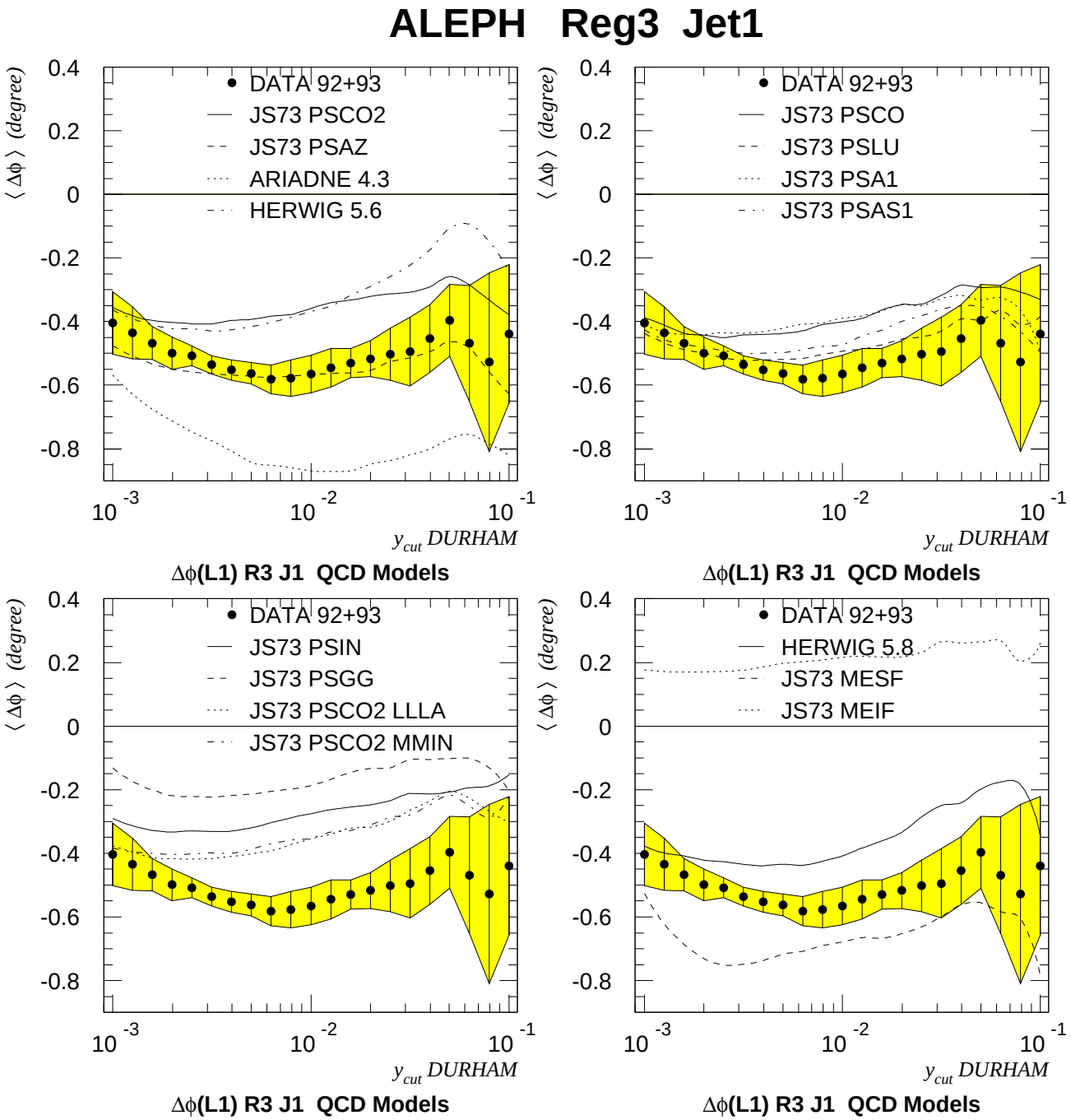

Figure 5.6: Results for $\langle \Delta\phi(\mathbf{L1}) \rangle$ of jet 1 from **R3** for the QCD models considered, superimposed on the corrected data (1992+1993) with error bands, are shown for the logarithmically spaced y_{cut} values between 0.001 and 0.1.

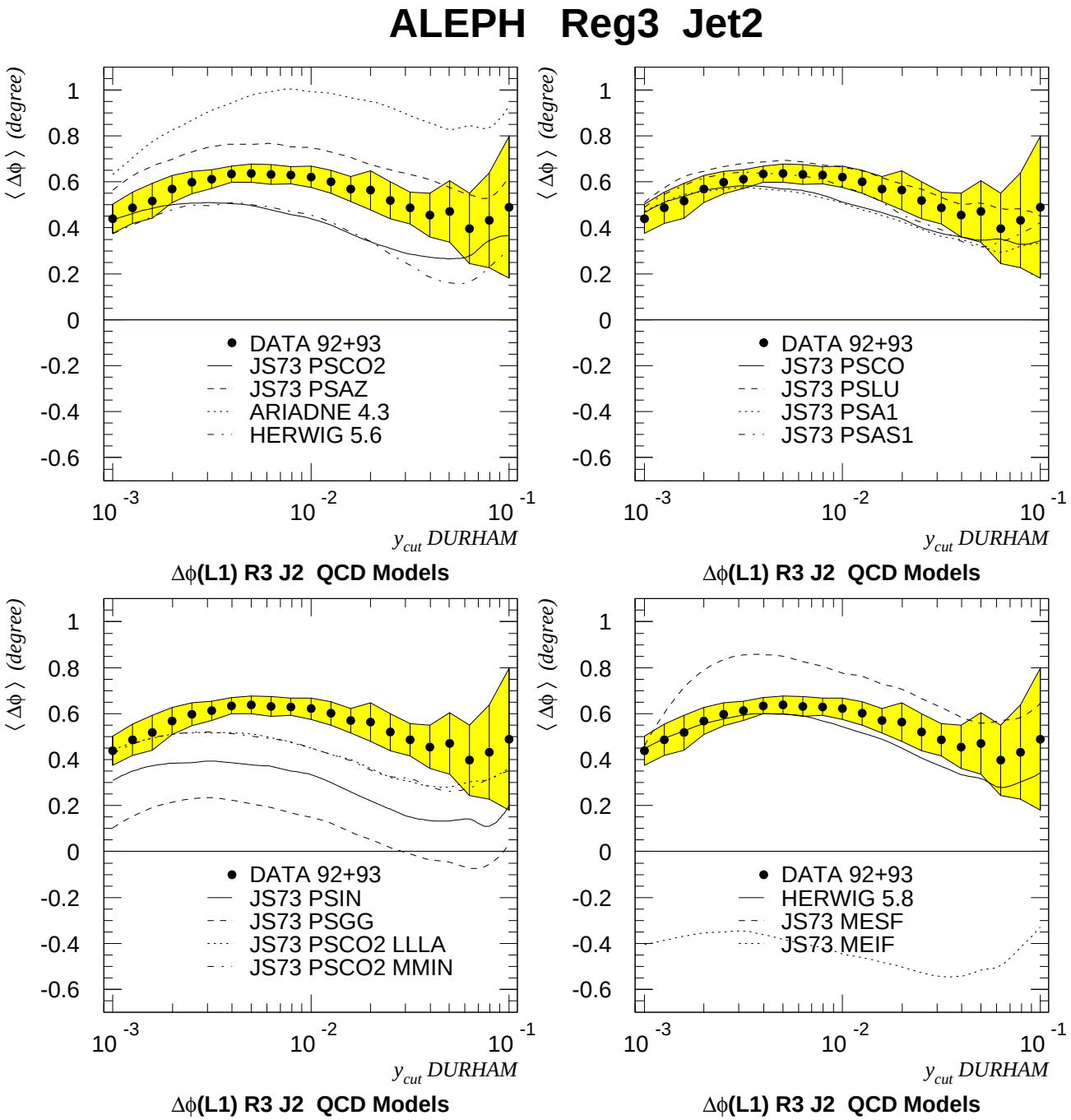

Figure 5.7: Results for $\langle \Delta\phi(\mathbf{L1}) \rangle$ of jet 2 from **R3** for the QCD models considered, superimposed on the corrected data (1992+1993) with error bands, are shown for the logarithmically spaced y_{cut} values between 0.001 and 0.1.

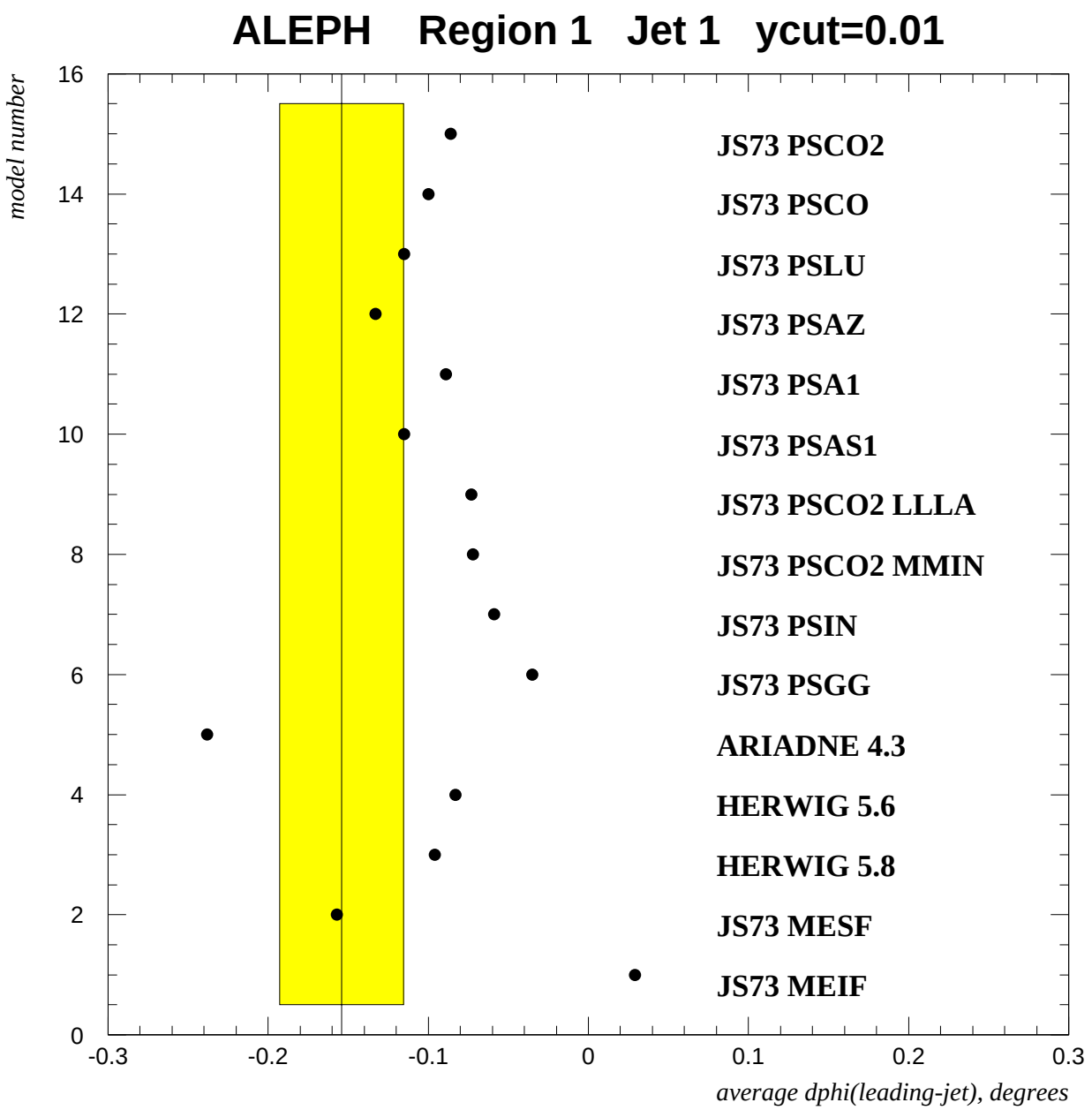

Figure 5.8: Results for $\langle \Delta\phi(\mathbf{L1}) \rangle$ of jet 1 from **R1** for the QCD models considered, superimposed on the corrected data (1992+1993) with error bands, are shown for the central $y_{cut} = 0.01$.

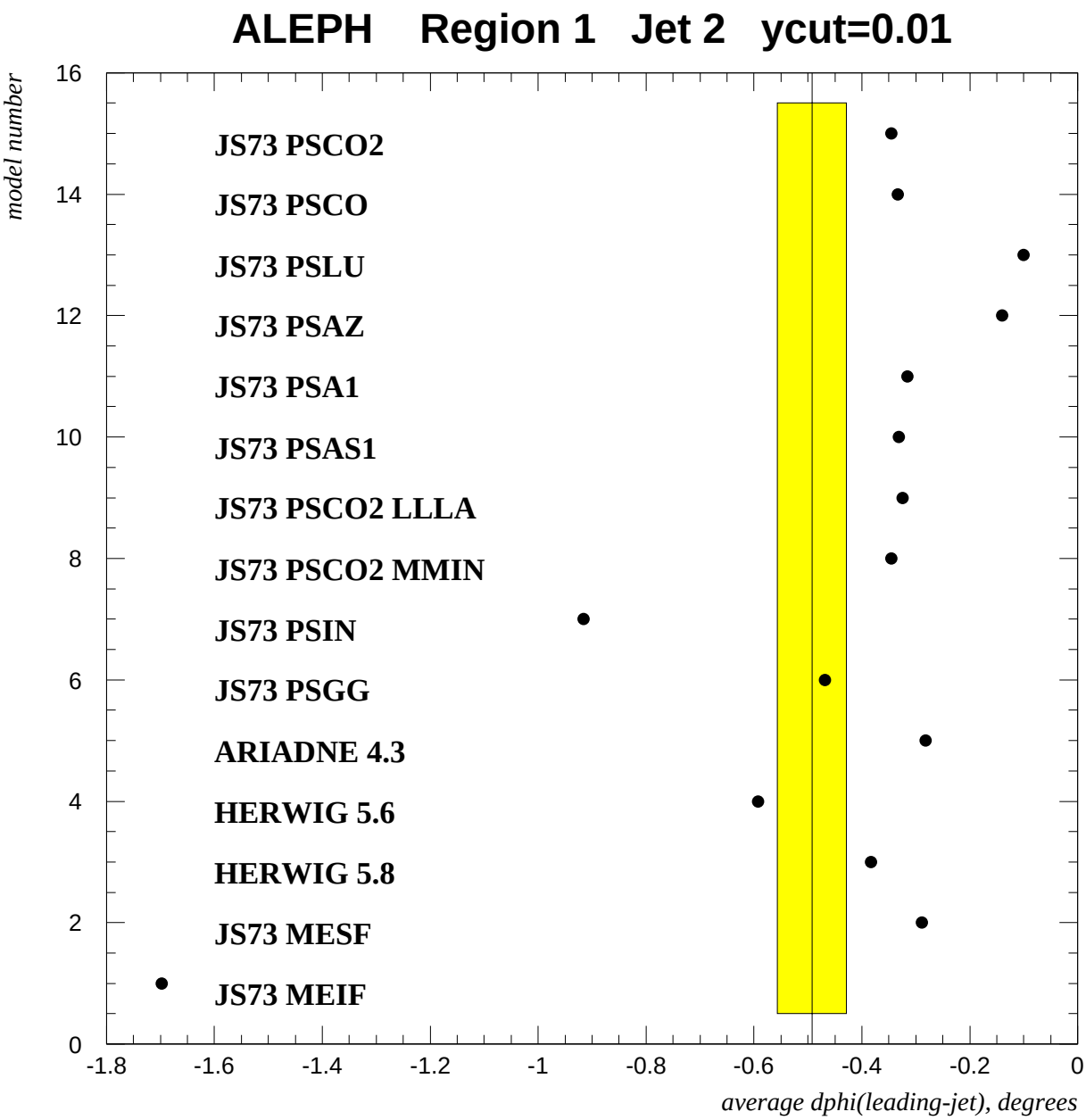

Figure 5.9: Results for $\langle \Delta\phi(\mathbf{L1}) \rangle$ of jet 2 from **R1** for the QCD models considered, superimposed on the corrected data (1992+1993) with error bands, are shown for the central $y_{cut} = 0.01$.

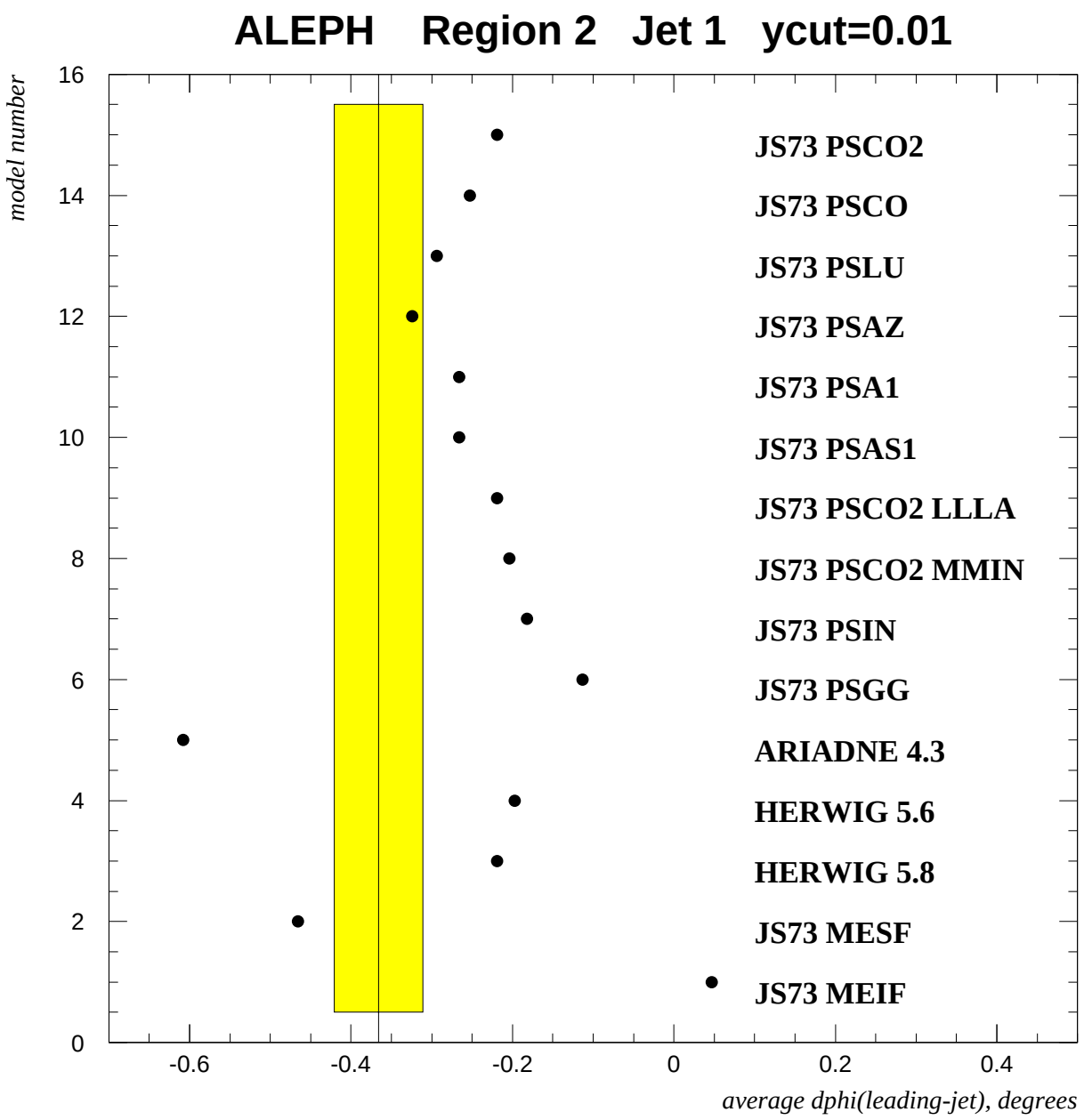

Figure 5.10: Results for $\langle \Delta\phi(\mathbf{L1}) \rangle$ of jet 1 from **R2** for the QCD models considered, superimposed on the corrected data (1992+1993) with error bands, are shown for the central $y_{cut} = 0.01$.

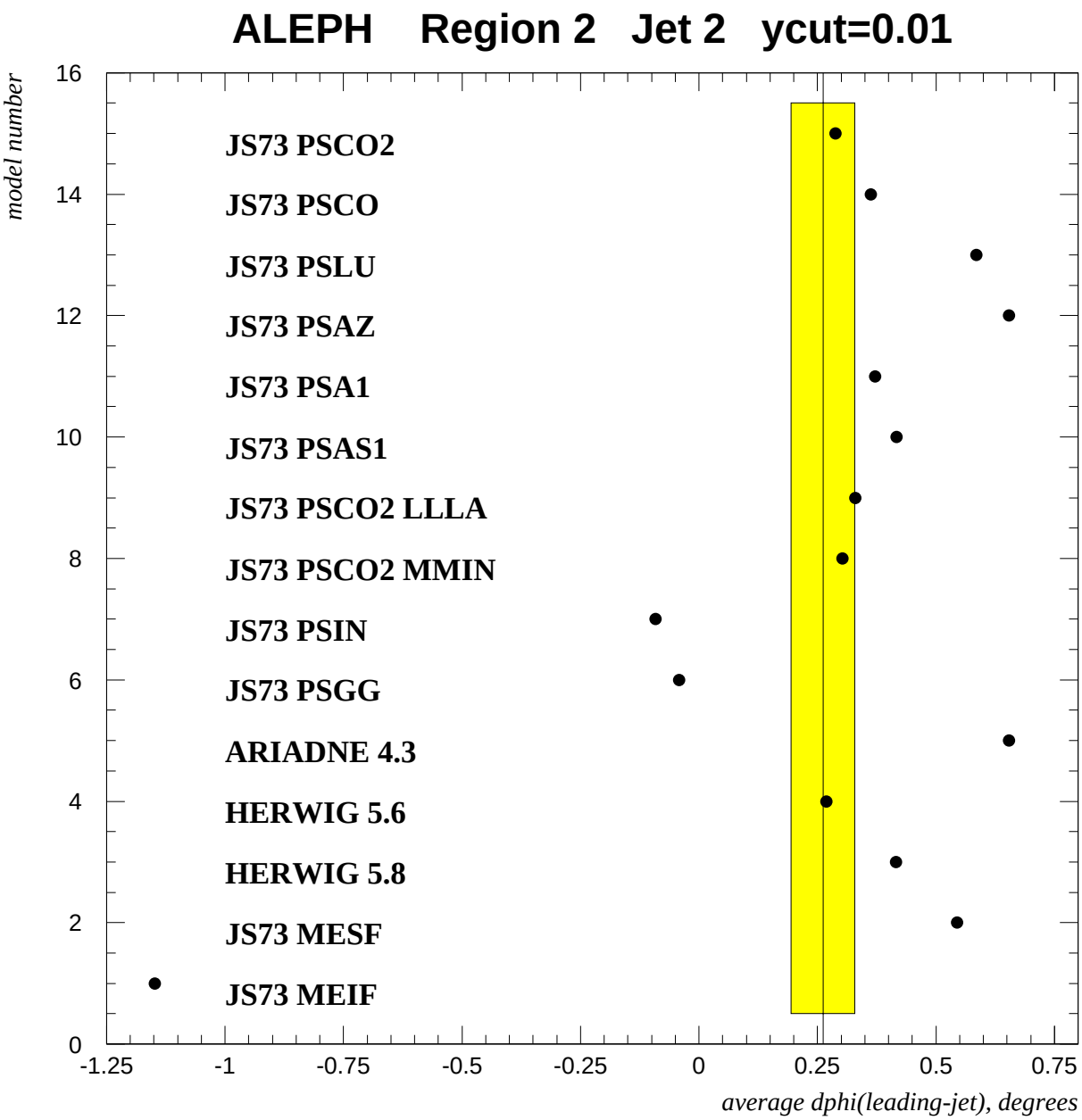

Figure 5.11: Results for $\langle \Delta\phi(\mathbf{L1}) \rangle$ of jet 2 from **R2** for the QCD models considered, superimposed on the corrected data (1992+1993) with error bands, are shown for the central $y_{cut} = 0.01$.

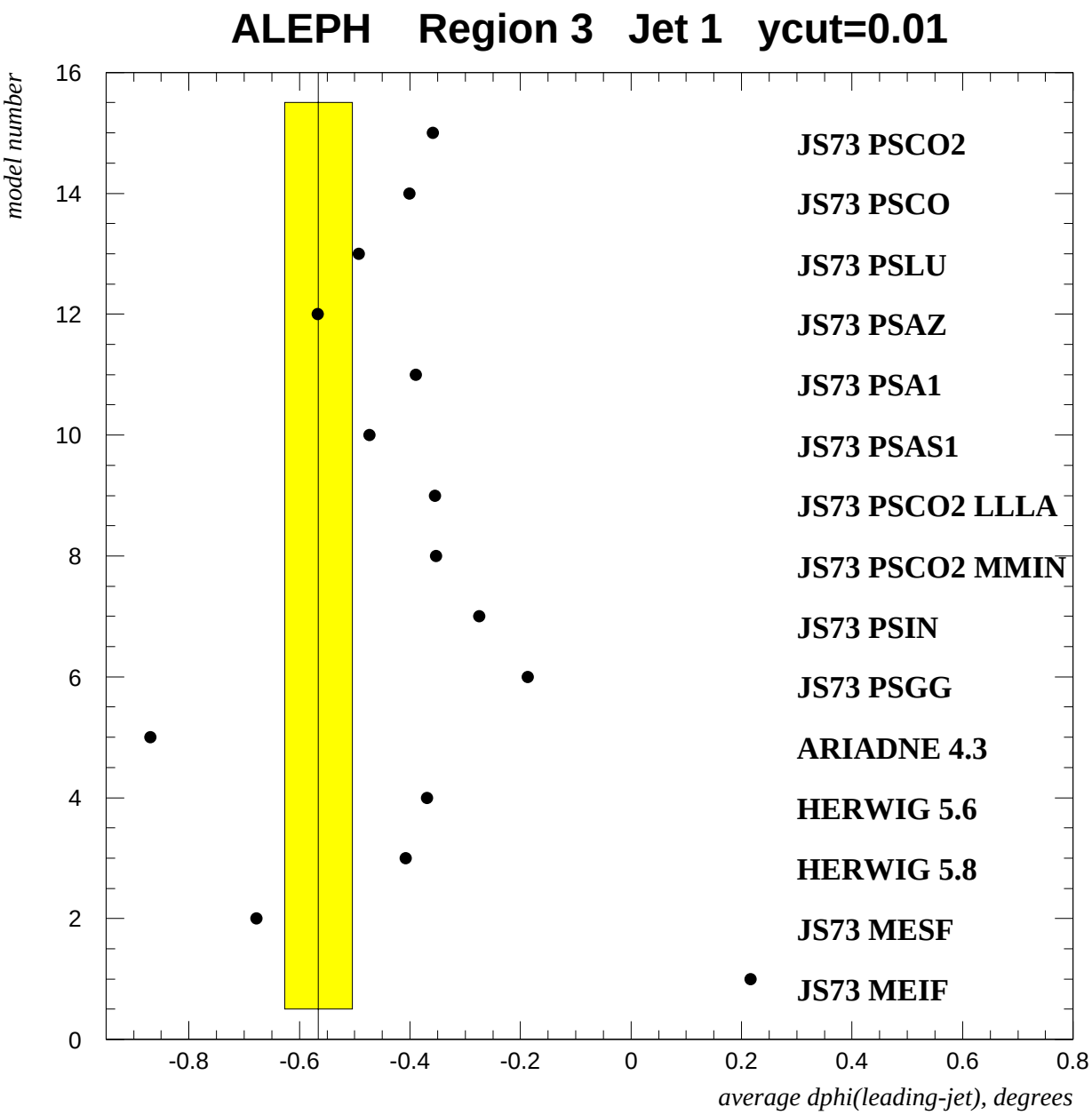

Figure 5.12: Results for $\langle \Delta\phi(\mathbf{L1}) \rangle$ of jet 1 from **R3** for the QCD models considered, superimposed on the corrected data (1992+1993) with error bands, are shown for the central $y_{cut} = 0.01$.

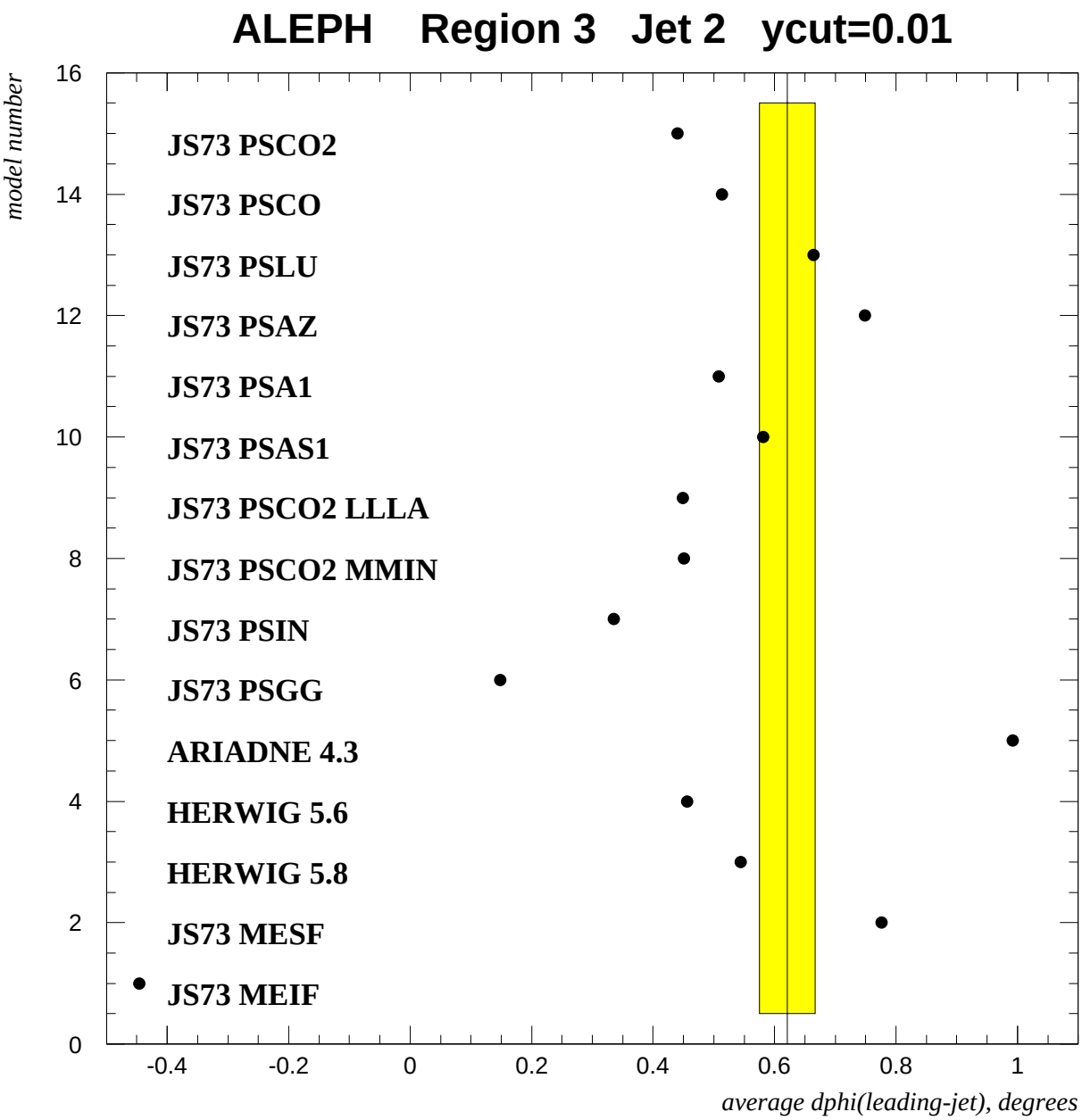

Figure 5.13: Results for $\langle \Delta\phi(\mathbf{L1}) \rangle$ of jet 2 from **R3** for the QCD models considered, superimposed on the corrected data (1992+1993) with error bands, are shown for the central $y_{cut} = 0.01$.

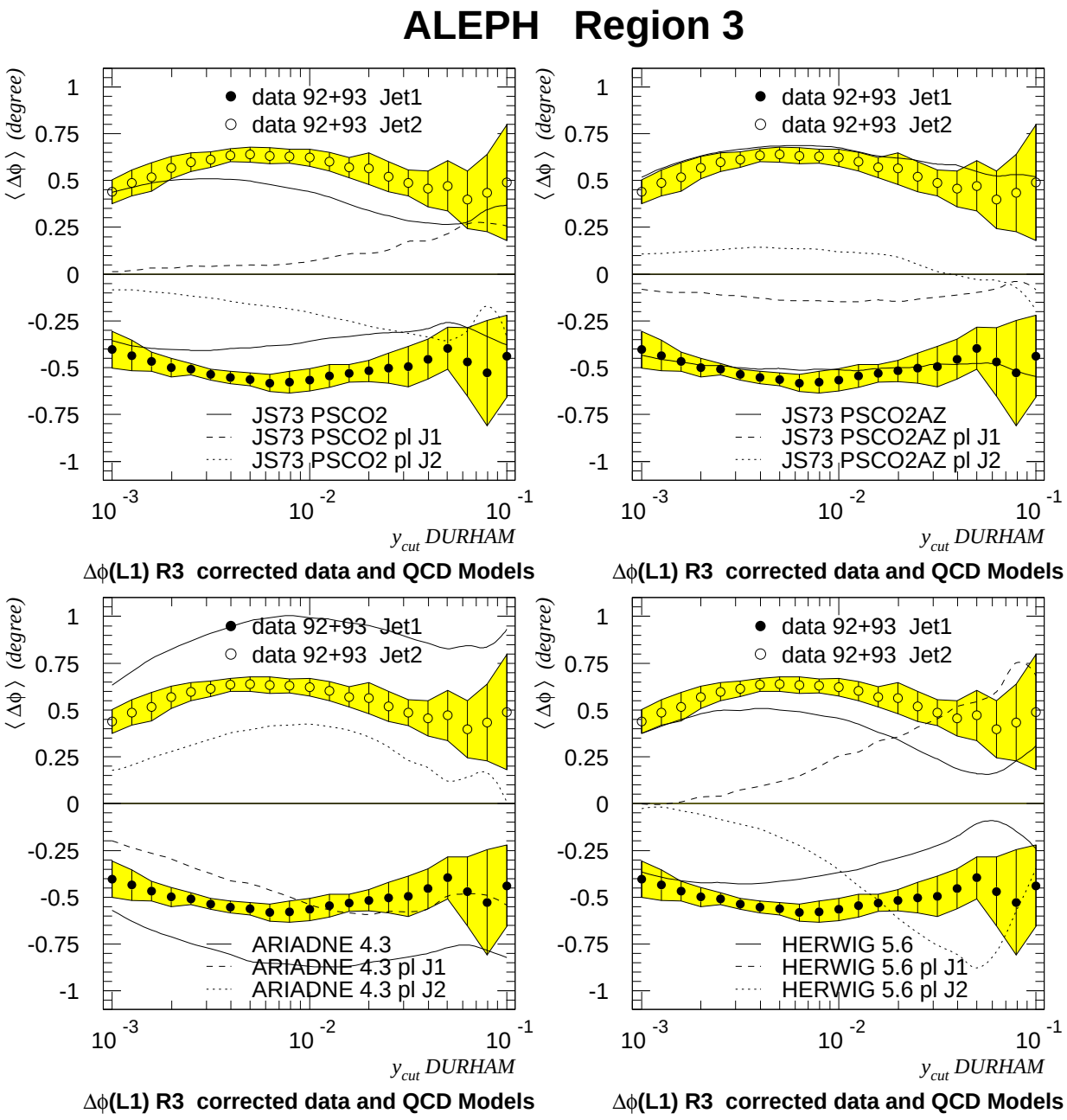

Figure 5.14: Results for $\langle\Delta\phi(\mathbf{L1})\rangle$ of jet 1 and jet 2 from **R3** for special QCD models, superimposed on the corrected data (1992+1993) with error bands, are shown for the logarithmically spaced y_{cut} values between 0.001 and 0.1. The $\langle\Delta\phi(\mathbf{L1})\rangle$ results on the hadron level and on the parton level are shown for the QCD models (`pl` stands for parton level). For PSCO2 and HERWIG, jet 1 has positive $\langle\Delta\phi(\mathbf{L1})\rangle$ values on the parton level. Since HERWIG has low multiplicity (≈ 6.2) on the parton level, the parton level $\langle\Delta\phi(\mathbf{L1})\rangle$ results are atypical. JETSET PSCO2 with azimuthal correlations (PSCO2AZ) yields negative $\langle\Delta\phi(\mathbf{L1})\rangle$ on the parton level for jet 1 and perfectly describes both jet 1 and jet 2 on the hadron level. ARIADNE shows $\langle\Delta\phi(\mathbf{L1})\rangle$ values close to those observed on the data already on the parton level.

Bibliography

[1] The ALEPH Collaboration, W. Blum (editor), *The ALEPH Handbook*, ALEPH 89-77, CERN, 1989.

[2] The ALEPH Collaboration, D. Decamp et al., Nucl. Instr. Meth. **A294** (1990) 121.

[3] The ALEPH Collaboration, D. Buskulic et al., *Measurement of Prompt Photon Production in Hadronic Z Decays*, Z. Phys. C **57**, 17-35 (1993).

[4] The ALEPH Collaboration, D. Buskulic et al., *Properties of Hadronic Z Decays and Test of QCD Generators*, Z. Phys. C **55** (1992) 209–234.

[5] The ALEPH Collaboration, *Performance of the ALEPH Detector at LEP*, CERN-PPE-94-170, submitted to Nucl. Instr. Meth. A, 1994.

[6] The ALEPH Collaboration, *Study of the Subjet Structure of Quark and Gluon Jets*, Phys. Lett. **B346** (1995) 389–398.

[7] H. Albrecht, E. Blucher, *ALPHA User's Guide, Version 114/115*, ALEPH 93-1, CERN, 1993.

[8] G. Altarelli, R. Kleiss, C. Verzegnassi, *Z Physics at LEP 1*, CERN 89-08, CERN, 1989.

[9] B. Anderson et al., *Parton Fragmentation and String Dynamics*, Phys. Rep. **97** (1983) 31-145.

[10] Application Software Group, CN Division, *HBOOK Reference Manual, Version 4.17*, CERN Program Library Long Writeup Y250, CERN, 1993.

[11] Application Software Group, CN Division, *PAW Physics Analysis Workstation, The Complete Reference, Version 1.14*, CERN Program Library Long Writeup Q121, CERN, 1992.

[12] D. Casper, *An Introduction to the ALEPH Offline System, Version 1.0*, ALEPH 93-26, CERN, 1993.

[13] S. Catani, Yu. L. Dokshitzer, M. Olsson, G. Turnock, B. Webber, Phys. Lett. **269B** (1991) 432.

[14] G. Cowan, *How to define a Gluon Jet in a three Jet Event (Suggestion)*, Minutes of the QCD/IPP meeting: 17-12-1992, ALEPH 92-189, 1992.

[15] H. Drevermann, C. Grab, B.S. Nilsson, R.K. Vogl *Graphical Concepts for the Representation of Events in High Energy Physics*, Int. J. Mod. Phys. C, Phys. Comput., 1991, Vol 2, Iss 1, pp 328–30.

[16] G. Dissertori, *Eine Untersuchung von Parton Schauer Modellen der perturbativen Quantenchromodynamik*, Diplomarbeit, Univ. Innsbruck, 1993.

[17] Yu. L. Dokshitzer, V. A. Khoze, A. H. Mueller, S. I. Troyan, *Basics of Perturbative QCD*, Edition Frontieres, Gif-sur-Yvette, 1991.

[18] R. D. Field, *Applications of Perturbative QCD*, Addison-Wesley, 1989.

[19] C. Itzykson, J.–B. Zuber, *Quantum Field Theory*, McGraw–Hill, Singapore, 1980.

[20] The JADE Collaboration, W. Bartel et al., Phys. Lett. **101B** (1981) 129.

[21] The JADE Collaboration, W. Bartel et al., Z. Phys. **C21** (1983) 37.

[22] The JADE Collaboration, W. Bartel et al., Z. Phys. **C33** (1986) 23.

[23] E. Kneringer, *String Effekt in hadronischen Z^0 Zerfällen*, Dissertation, Univ. Innsbruck, 1995.

[24] The L3 Collaboration, *Energy and Particle Flow in Three-Jet and Radiative Two-Jet Events from Hadronic Z Decays*, CERN PPE/94-164.

[25] L. Lönnblad, *Ariadne Version 4, A Program for Simulation of QCD-Cascades Implementing the Colour Dipole Model*, Comput. Phys. Commun. **71** (1992) 15.

[26] G. Marchesini, B. Webber, G. Abbiendi, I. Knowles, M. Seymour, L. Stanco, *HERWIG, a Monte Carlo event generator for simulating Hadron Emission Reactions With Interfering Gluons*, Comput. Phys. Commun. **67** (1992) 465.

[27] O. Nachtmann, *Elementarteilchenphysik, Phänomene und Konzepte*, Vieweg Verlag, 1986.

[28] The Particle Data Group, *Review of Particle Properties*, Phys.Rev.D **45**, Number 11, Part II, 1992.

[29] G. Rudolph, private communications.

[30] H. Schmidt, *Bestimmung der Eichkopplungen der Quantenchromodynamik aus 3-Jet-Ereignissen im Aleph-Detektor*, Dissertation, Mainz, 1994.

[31] T. Sjöstrand, PYTHIA *5.6 and* JETSET *7.3 Physics and Manual*, CERN-TH.6488/92, 1992.

[32] T. Spickermann, *"String Effect" in 3-Jet Events*, Moriond Conference, March 1993.

[33] W. J. Stirling, *QCD and Collider Physics*, Lecture Notes from CERN Academic Training Programme, CERN, 1990.

[34] B.R. Webber, *Quantum Chromodynamics*, Proceedings of the 1993 European School of High-Energy Physics, CERN report 94-04, 1994.

Danksagung

Mein besonderer Dank gilt dem Betreuer dieser Dissertation, Herrn Univ.-Doz. Dr. Gerald Rudolph, für die Vergabe des interessanten Themas und die kompetente und geduldige Betreuung. Unter seiner Anleitung konnte ich sehr viele Erfahrungen auf dem Gebiet der Hochenergiephysik und der wissenschaftlichen Methodik sammeln. Seine präzise Arbeitsweise und kritische Analyse werden mir stets ein Vorbild sein.

Auch Herrn Univ.-Doz. Dr. Peter Girtler bin ich zu großem Dank verpflichtet für viele hilfreiche Gespräche und Diskussionen, die mir viel bei der Erschließung des Stoffgebietes geholfen haben.

Herrn Univ.-Prof. Dr. Dietmar Kuhn danke ich für sein stets Interesse am Fortgang dieser Arbeit und für die finanzielle Unterstützung durch die Beschäftigung als Vertragsassistent, ohne die das Entstehen dieser Arbeit nicht möglich gewesen wäre.

Herrn Univ.-Doz. Mag. Dr. Gebhard Grübl, der mich schon bei meiner Diplomarbeit ausgezeichnet betreut hat, möchte ich dafür danken, daß er stets ein offenes Ohr für die wissenschaftlichen Probleme, mit denen ich befaßt war, hatte und mir manchen hilfreichen Ratschlag gab.

Herrn Univ.-Ass. Mag. Emmerich Kneringer danke ich besonders für seine Hilfe beim Erlernen des Umgangs mit den Programmen und Bibliotheken der CERN Library, insbesondere mit der Physics Analysis Workstation (PAW), und seine Unterstützung bei der Verwendung der Monte Carlo Generatoren und der Datenanalyseeinrichtungen des ALEPH Experiments (shift).

Ihm und Herrn Mag. Günther Dissertori möchte ich auch für viele hilfreiche Diskussionen danken.

Herrn OR. Dr. Herbert Oberguggenberger bin ich dafür zu Dank verpflichtet, daß durch seine Unterstützung sich meine Lehrverpflichtungen nicht in allzu großem Zeitaufwand niederschlugen.

Vorallem aber gilt mein Dank meinen Eltern, die immer Vertrauen zu mir hatten und mich durch die langen Jahre des Studiums moralisch und finanziell unterstützt haben.

Diese Arbeit wurde vom Fonds zur Förderung der wissenschaftlichen Forschung im Rahmen des Projekts P9737PHY unterstützt.